

**Exclusive and Inclusive Electron Scattering
from ${}^{40}_{18}\text{Ar}$ and ${}^{48}_{22}\text{Ti}$ to Obtain the Spectral
Function of Argon**

Daniel L. Abrams
New York City, New York

B.S. Pure Mathematics
B.A. Physics
University of Vermont, 2012

A Dissertation Presented to the Graduate Faculty
of the University of Virginia in Candidacy for the Degree of
Doctor of Philosophy

DEPARTMENT *of* PHYSICS
UNIVERSITY *of* VIRGINIA

January, 2022

to my mother

Preface

As my course work in college and graduate school focused on theoretical condensed matter physics, I began research in experimental nuclear physics with almost no experience in the field, and hence faced a steep learning curve. However, my research on nuclear magnetic resonance in nano-structured diamond conducted at The City College of New York before graduate school persuaded me to join the Polarized Target Group at UVA.

Given my educational background, this dissertation is written as an introduction to electron-nucleus scattering assuming little background knowledge of nuclear physics and experimental techniques. Knowledge of quantum field theory is assumed, as I derive the inclusive and exclusive differential cross sections from the Feynman rules of QED. I believe that it is important for an experimentalist to understand the theory behind their experiment. Thus, this dissertation has more of a focus on the theoretical aspect of electron scattering than most experimental dissertations.

In the initial stages of the experiment, I found it difficult to learn how to do the experimental analysis. Almost everything I learned about the experimental analysis was conveyed to me by conversations with fellow grad students, and I found that very few written sources existed that described in detail the methods of experimental data analysis. Many of the sources I consulted, including some books and Ph.D. dissertations, were either out-dated or contained broad statements that never really explained how the analysis was done. Thus, one of the goals of this dissertation is to explain in detail the exact methods used to analyze the data.

Another goal of this dissertation is to try to explain and elucidate the inner workings of the codes used to analyze the data. I had almost zero coding experience upon joining the E12-14-012 experiment, so understanding the codes was a major struggle for me. Some of the codes are so dense, complex, and often poorly commented, that they are incredibly difficult to understand. I did a deep dive into the inclusive cross section codes and Monte-Carlo simulation codes, and have tried my best to explain in detail how the codes performed the calculations.

A brief note on notation. It is common notation in the literature to denote the inclusive cross section as $d^2\sigma/d\Omega'dE'$, and call it *doubly-differential*, while simultaneously denoting the exclusive cross section as $d^6\sigma/d\Omega'dE'd\Omega_{p'}dE_{p'}$, and calling it *six-fold differential*. This notation is clearly inconsistent, as the

differential $d\Omega$ is *two-fold*, containing differentials for the polar and azimuthal angles. Thus, in this dissertation, the notation $d^3\sigma/d\Omega'dE'$ is used to denote the inclusive differential cross section.

I hope that this dissertation, especially the sections covering the data analysis, can be used as a reference for future graduate students studying nuclear phenomenon using electron scattering. Definitions of quantities important to the data analysis are written in a general form using logic statements which can be applied to any analysis framework and coding language.

This dissertation is the culmination of over four years of work on the E12-14-012 experiment at Jefferson Lab. Its been a long journey to reach this point, filled with trials and tribulations along the way. From the August 12th, 2017, UTR rally and subsequent terrorist attack, to the COVID-19 pandemic still ravaging the world, times have been tough. However, the years since I began my graduate studies at UVA back in late August of 2013 have also been filled with unforgettable good times. I have had incredible opportunities to study physics across the country, even across the world. I learned so much during my time at UVA, and am incredibly proud of all the work that has gone into this dissertation.

Daniel L. Abrams

New York, New York
October, 2021

Acknowledgements

I would like to take this opportunity to acknowledge and thank the many people who supported me during the process of completing this Ph.D. There are so many people who deserve thanks, but unfortunately, not everybody can be listed here. To those not explicitly acknowledged, your contributions did not go unnoticed. Thank you!

To my New York City friends, I've missed you all! Thanks for keeping our friendships through my absence.

To my Charlottesville friends, thank you for all the good times. I will never forget the over eight years I spent in Charlottesville, and I will miss you all dearly.

To the members of Ghost Logic, Edwin, Ross, and Josh, thank you for the music! From our first gig in the parking lot of 3 B's Bar and Grill in Orange, to our last gig at Tucked Away Brewing in Manassas just before the COVID-19 lockdown, and our two studio recording sessions, I will always remember the good times spent making and playing music with you guys!

Special thanks to Edwin and Ross, the additional members of the Ghost Logic core tripod. We played in three bands together over seven years, the unnamed Nirvana-Offspring cover band, Ghost Logic, and most recently Hollow Point. Thanks for the good times! I'm glad to count you among my friends.

Special thanks to my colleagues at Virginia Tech! Thanks to Hongxia Dai, one of the original graduate students on E12-14-012, for keeping me company during the owl shifts at the JLab accelerator, and for help with the data analysis. Thanks to Linjie Gu for helping me with the data analysis, especially for helping me understand the codes. Thanks to professor Camillo Mariani for helping me understand the process of experimental data analysis.

Special thanks to my colleagues at the University of Virginia! To my friends, Raza, Evan, and Alex, thank you for keeping me company during the all-night homework sessions in the TA lounge. Our conversations during problem solving sessions were invaluable, and I couldn't have completed this degree without your help. Thanks to Mikhail Yurov for his help and advice with coding and data analysis. Very special thanks to Dien Nguyen for helping me during the initial phases of the experiment, and keeping me calm and centered when learning ROOT. Thanks to professor Genya Kolomeisky for

supervising my early research in theoretical condensed matter physics.

Of course, very special thanks goes to my academic advisor, professor Donal Day, for guiding me through my Ph.D. Thank you for allowing me the extra time needed to complete this dissertation properly, and for being a good advisor in general. I learned so much during our conversations, and appreciate all that you have done for me.

Special thanks to my family, especially my aunt Ruthie, for always being there for me.

Very special thanks to my mother, Beryl Abrams! Thank you for your unwavering support during my entire life. I appreciate everything that you do for me, and none of my achievements, academic or otherwise, would have been possible without you. Thank you for proofreading the entire manuscript at the last minute! I love you, Mom!

Additionally, I would like to thank the following people for their help before I began my Ph.D. Thanks to my long-time tutor Jim Kennis, for tutoring me in mathematics during high school before I was interested in the subject. Thanks to professor Valeri Kotov of the University of Vermont for inspiring my interest in theoretical condensed matter physics as an undergraduate. Thanks to professor Carlos Meriles of The City College of New York, for accepting my request to join his research group during my gap year before graduate school. The research experience I gained at CCNY was crucial for my acceptance and success at UVA.

Finally, I would like to acknowledge the dearly departed friends and family who were unable to complete this journey with me. Even though you are gone, you have not been forgotten.

To my dog Abby, I miss you and will always remember you fondly.

To my cousin Jeff Stern, I hope you would have enjoyed reading this dissertation.

To my friend Adam Bratcher, who inspired me to play the guitar. I will always remember the times we spent hanging out at “the spot”, and the music we made in Casket Sacrifice.

To Bradley Joyce, my friend and founding member of Ghost Logic. We all miss you. I played your guitar at every Ghost Logic show, and promise to use it in my future bands.

To Johnette Ravenell, my childhood nanny and friend. Thank you for all the childhood memories. I will always remember your constant enthusiasm and joy for life.

To my Uncle Bobby. You were like a father to me, and I always admired you. I will always remember our fishing trips, visiting you and aunt Ruthie in Florida, and playing Medal of Honor and Left 4 Dead online together. Thank you for everything.

זְכוּרֵנוּם לְבָרָכָה.

Contents

Preface	v
Acknowledgements	vii
List of Symbols	xv
List of Figures	xvii
List of Tables	xxiii
1 Experiment E12-14-012 at Jefferson Lab	1
1.1 Motivation	1
1.2 Nuclear Physics of E12-14-012	2
1.3 Neutrino Oscillations	3
1.3.1 Connection to Neutrino Oscillation Experiments	5
1.4 Existing Experimental Data	8
2 Electron Scattering As A Probe of Nuclear Structure	9
3 Electron Scattering Theory	10
3.1 Scattering Kinematics	11
3.2 Derivation of the Cross Sections	13
3.3 The Hadronic Target Response Tensor	17
3.4 The (e, e') Cross Section	19
3.5 The $(e, e'p)$ Cross Section	21
3.5.1 Plane Wave Impulse Approximation	21
3.5.2 $(e, e'p)$ Kinematics and PWIA Cross Section	22
3.5.3 Distorted Wave Impulse Approximation	24
3.5.4 The Spectral Function	27
3.6 Scaling in (e, e') Cross Sections	33
3.6.1 y -Scaling in PWIA	38
3.6.2 ψ -Scaling in RFG	40
3.7 Radiative Corrections	43
3.8 Off-Shell Corrections	51
4 E12-14-012 Experimental Setup	53
4.1 CEBAF Accelerator and Beam	53
4.2 Experimental Hall A	54
4.3 Targets	55
4.3.1 Argon Target Cell	58

4.3.2	Titanium Target	60
4.3.3	Target Density Study	60
4.3.4	Carbon Target	60
4.3.5	Optics Target	62
4.4	Experimental Kinematics	62
4.5	Coordinate Systems	63
4.5.1	Hall Coordinate System	63
4.5.2	Detector Coordinate System	65
4.5.3	Transport Coordinate System	66
4.5.4	Focal Plane Coordinate System	67
4.5.5	Target Coordinate System	68
5	Hall A High Resolution Spectrometers	70
5.1	Scintillators	71
5.2	Vertical Drift Chambers	72
5.3	Gas Cherenkov Detector	75
5.3.1	Cherenkov PMT Calibration	76
5.4	Lead Glass Calorimeters	77
5.4.1	Calorimeter Calibration	79
5.5	Triggers	80
6	Modeling the Physics and the HRS	83
6.1	The Inclusive Cross Section Model	83
6.1.1	Calculating the Cross Section	89
6.1.2	Corrections to the Cross Section	90
6.2	Phenomenological Modeling of Final State Interactions	92
6.3	The HRS Monte-Carlo Model	96
6.3.1	Single Arm Monte-Carlo	96
6.3.2	SIMC	97
6.3.3	Comparing Data to Monte-Carlo Simulation	97
7	E12-14-012 Data Analysis	104
7.1	Data Acquisition	104
7.2	Event Selection Criterion	105
7.2.1	Acceptance Cuts	105
7.2.2	Beam Trip Cut	109
7.3	Particle Identification	109
7.3.1	Coincidence Time	111
7.3.2	DR.t1 Cut	113
7.4	Weighting the Data	114
7.5	Analysis of the Background	115

7.5.1	Charge Symmetric Background	115
7.5.2	Pion Contamination	116
7.5.3	Background Subtraction	118
8	Detector Efficiency Calculations	119
8.1	Scintillator/Trigger Efficiency	121
8.2	Cherenkov Cut Efficiency	123
8.3	Calorimeter Cut Efficiency	124
8.4	VDC/Tracking Efficiency	128
8.5	Coincidence Time Cut Efficiency	131
8.6	Beta Cut Efficiency	135
9	Extracting Cross Sections From Experimental Data	136
9.1	The Inclusive Cross Section	136
9.1.1	Acceptance Correction Method	136
9.1.2	Yield Ratio Method	137
9.1.3	Carbon Comparison Method	138
9.2	The Exclusive Cross Section	139
9.2.1	Extraction of the Spectral Function	139
10	Uncertainty and Error Analysis	139
10.1	Statistical Uncertainty	140
10.1.1	Restricted Binomial Error	140
10.1.2	The Wilson Score Interval	141
10.2	Systematic Uncertainty	142
10.2.1	Systematics from Radiative Corrections	144
10.2.2	Systematics from Final State Interactions	149
10.3	Propagation of Error	151
10.4	Uncertainty in the Cross Section	152
11	E12-14-012 Experimental Results	153
11.1	Inclusive Cross Sections	153
11.2	Scaling Functions	153
11.3	Exclusive Cross Sections	160
12	Summary and Conclusions	162
A	Supplementary Mathematics	169
A.1	The Dirac Delta Function	169
A.2	The Dilogarithm Function	169
A.3	The Gamma Function	170

B	Supplementary Theoretical Analysis	170
B.1	Three-Flavor Neutrino Oscillations	170
B.2	The Rosenbluth Cross Section	172
B.3	Calculating The Inclusive Cross Section	173
B.4	y -Scaling in PWIA Supplement	174
B.5	Correlated Spectral Function	175
B.6	Radiative Corrections Supplement	176
B.7	The SIMC Cross Section as a Surface	177
	B.7.1 Calculation of the Generated Phase Space	177
C	Supplementary Data Analysis	179
C.1	ROOT Tree/NTUPLE Histograms	179
C.2	Data to SIMC Comparison	180
	Index	199

List of Symbols

ADC	Analog-to-Digital Converter
BCS	Bardeen-Cooper-Schrieffer pairing mechanism
CCQE	Charged-Current Quasi-Elastic
CDWBA	Complete Distorted Wave Born Approximation
CEBAF	Continuous Electron Beam Accelerator Facility
CODA	CEBAF On-line Data Acquisition system
DAQ	Data Acquisition software
DCS	Detector Coordinate System
DEM	Democratic fit for the optical potential
DHB	Dirac-Hartree-Bogoliubov pairing mechanism
DIS	Deep Inelastic Scattering
DUNE	Deep Underground Neutrino Experiment
DWIA	Distorted Wave Impulse Approximation
EDAD	Energy-Dependent and A-Dependent fits for the optical potential
ESPACE	Event Scanning Program for Hall A Collaboration Experiments
FSI	Final State Interactions
FPCS	Focal Plane Coordinate System
HCS	Hall Coordinate System
HRS	High Resolution Spectrometer
IPSM	Independent Particle Shell Model
LAMPF	Los Alamos Meson Physics Facility
LArTPC	Liquid Argon Time Projection Chamber
LBNE	Long Baseline Neutrino Experiment
LDA	Local Density Approximation
LHRS	Left arm of the HRS
LNF	Laboratori Nazionali di Frascati
MC	Monte-Carlo
MF	Mean Field
PID	Particle Identification
PMNS	Pontecorvo-Maki-Nakagawa-Sakata matrix
PMT	Photomultiplier Tube
PWIA	Plane Wave Impulse Approximation
RFG	Relativistic Fermi Gas
RHRS	Right arm of the HRS
TCS	Target Coordinate System
TRCS	Transport Coordinate System
TPC	Time Projection Chamber
VDC	Vertical Drift Chamber

\mathbb{R}	The set of real numbers
\mathbb{C}	The set of complex numbers
\wedge	Logical AND
\vee	Logical OR
\neg	Logical NOT
\in	Is an element of
\subset	Is a proper subset of
$\text{Li}_2(z)$	Dilogarithm function
$\Gamma(z)$	Gamma function
$\Theta(x)$	Step function
σ_{eN}	Electron-nucleon cross section
σ_{red}	Reduced cross section
σ_M	Mott cross section
$S(\vec{\mathbf{p}}, E)$	Spectral function
$S(E_m)$	Missing energy distribution function
$n(p_m)$	Missing momentum distribution function
$H_X(m, L, U)$	Histogram of quantity X on the interval $[L, U]$ with m -bins
ε_X	Efficiency of quantity X
\mathfrak{B}	Base-cut for efficiency calculations
\mathfrak{C}	Selection cut applied to experimental data
$N(\mathfrak{C})$	Number of events that pass the cut \mathfrak{C}

List of Figures

1	Diagram comparing the shell model level structure for argon and titanium	2
2	Neutrino oscillation probabilities for an initial electron neutrino	4
3	Depiction of the LBNE/DUNE neutrino oscillation experiment	6
4	Diagrams of CCQE neutrino- and anti-neutrino-nucleus scattering in the Born approximation	7
5	Inclusive cross sections per-nucleon for ^{40}Ar and ^{16}O from the existing LNF data	8
6	Diagram depicting the kinematics for the $A(e, e'N)B$ reaction in the Born Approximation	12
7	Feynman diagram for single-photon-exchange $(e, e'p)$ scattering	13
8	Depiction of a general (e, e') differential cross section spectrum versus energy loss, at constant three-momentum transfer . . .	19
9	Diagrammatic representation of the processes that contribute to the strength of the inclusive cross section	21
10	Diagrammatic depiction of assumption (b) of PWIA	22
11	Feynman diagram of $A(e, e'p)X$ scattering in the plane wave impulse approximation	23
12	Feynman diagram depicting final state interactions between the knocked-out proton and recoiling nuclear $(A - 1)^*$ system	25
13	Diagram of the CDWBA	26
14	Plot showing the effects of the distorting optical potential \tilde{V} on the $\text{Ar}(e, e')$ cross section	27
15	Weighted proton missing momentum distributions for argon and titanium	31
16	Proton missing energy distributions showing individual shell contributions for argon and titanium	32
17	Surface plots of the argon and titanium model spectral functions used in the E12-14-012 analysis	34
18	Surface plots of the argon and titanium weighted model spectral functions used in the E12-14-012 analysis	35
19	Plots of inclusive cross sections and y -scaling functions from aluminum (e, e') data, showing the effects of y -scaling analysis on the cross section data	41
20	Plots of the ψ -scaling function for several nuclei extracted from experimental data	43
21	Feynman diagrams depicting bremsstrahlung from the electron and hadron	44

22	Feynman diagrams of the leptonic and hadronic self-energy correction	45
23	Feynman diagrams of the leptonic and hadronic vertex corrections.	46
24	One-loop correction diagrams depicting the two photon exchange correction and the vacuum polarization correction . . .	46
25	SLAC NE3 carbon data showing the effects of radiative corrections	50
26	The CEBAF accelerator at JLab, post 12 GeV upgrade	54
27	Top-down view of the high-resolution spectrometer arms in Hall A	56
28	Photograph of JLab's experimental Hall A	56
29	Cross-sectional schematic of JLab's experimental Hall A . . .	57
30	Photograph of the Hall A target ladder	58
31	Computer generated image of the argon gas target cell	59
32	Overlay of argon and aluminum dummy target y_{tg}^e histograms	59
33	Normalized yield versus CEBAF beam current, argon target .	61
34	Normalized yield versus CEBAF beam current, titanium target	61
35	Histogram of the z_{tg}^e distribution from the carbon optics target	62
36	Vector diagrams depicting parallel and anti-parallel kinematics	64
37	Diagram of the Hall Coordinate System	65
38	Diagram of the Detector Coordinate System	66
39	Diagram of the Transport Coordinate System	67
40	Diagram of the rotating Focal Plane Coordinate System	68
41	Diagram of the Target Coordinate System	68
42	Top and side views of the Target Coordinate System	69
43	Diagram of the QQDQ HRS magnetic transport system	72
44	Schematic diagrams of the detector packages of the High Resolution Spectrometers	73
45	Drawing of a portion of the scintillator paddles	74
46	Diagram showing the relative orientation of the VDC wire planes with respect to the nominal particle trajectory	74
47	Schematic diagram of the upper and lower VDC wire planes with a nominal particle trajectory	75
48	Computer rendered model of the Hall A CO ₂ gas Cherenkov detector	76
49	Histograms of the LHRS Cherenkov PMT ADC spectra	78
50	Diagrams of the lead glass calorimeters	79
51	Diagram of the singles trigger logic	82
52	Diagram of the coincidence trigger logic	83

53	Components of the titanium inclusive differential cross section model	84
54	Inclusive differential cross sections-per-nucleon calculated from the model	85
55	Depiction of a discretized (E', θ) phase-space	90
56	$^{40}\text{Ar}(p, p')$ cross section versus scattering angle, with cross sections derived from DEM, EDAD1, and EDAD2 optical potentials for comparison	94
57	Reduced cross sections for $1d_{3/2}$ proton knockout from argon in PWIA and DWIA, showing the calculation of the missing momentum shift Δ	95
58	Reduced cross sections for $1d_{3/2}$ proton knockout from argon in PWIA and DWIA, showing the calculation of the cross section ratio $\sigma_{DWIA}/\sigma_{PWIA}$	95
59	Histogram of the SIMC quantity Weight (argon Kin2)	98
60	Histograms of the missing energy spectra for argon and titanium, Kin2 and Kin4	100
61	Histograms of the missing momentum spectra for argon and titanium, Kin2 and Kin4	101
62	Histograms of the missing energy spectra for argon and titanium at Kin2, showing the three shell-cut regions	102
63	Histograms of the missing momentum for argon Kin2 with the shell cuts applied	102
64	Histograms of the missing momentum for argon Kin4 with the shell cuts applied	103
65	Histograms of the missing momentum for titanium Kin2 with shell cuts applied	103
66	Histograms of the missing momentum for titanium Kin4 with shell cuts applied	104
67	Histograms of the LHRS acceptance variables from the argon inclusive delta scan	106
68	Histograms of the LHRS acceptance variables from the titanium inclusive delta scan	107
69	Histogram of z_{tg}^e from the argon inclusive delta scan	108
70	Histogram of y_{tg}^e from the inclusive delta scan	108
71	Plot of the electron beam current versus run number	110
72	Histogram of $\Delta\beta(m)$ showing peaks corresponding to protons, deuterons, and tritons	111
73	Histograms of the coincidence time spectra for argon at Kin2 and Kin4	112

74	Increased resolution histogram of Δt_{coinc} for argon Kin5, showing the discrete nature of the CEBAF electron beam	113
75	Histograms of the DR.τ1 spectra for titanium Kin4	114
76	Histograms of the DR.τ1 spectra for argon Kin5	115
77	Yield correction factor for the charge symmetric background correction	116
78	Scatter plots of the LHRS calorimeter showing the effects of different cuts on the data	117
79	Histogram of Δt_{coinc} showing the background-sample and coincidence-peak selection cuts	118
80	Histograms of θ_{tg}^e showing the background subtraction process	119
81	Histograms of β_{HRS}^R distributions for argon and titanium at Kin2 and Kin4	120
82	Plot of the scintillator efficiency versus LHRS central momentum from the inclusive delta scan	122
83	Plot of the T1 trigger/scintillator efficiency versus run number for all kinematic settings	123
84	Plots of the inclusive Cherenkov cut efficiency for carbon, titanium, and argon targets	125
85	Plot of the Cherenkov cut efficiency versus LHRS central momentum from the inclusive delta scan	126
86	Plot of the Cherenkov cut efficiency versus run number for all kinematic settings	126
87	Histograms of E/p from the carbon, titanium, and argon inclusive delta scans	127
88	Plots of the calorimeter cut efficiency for the argon, titanium, and carbon inclusive delta scans	129
89	Plot of the calorimeter cut efficiency versus LHRS central momentum for $E/p \geq 0.3$, from the inclusive delta scan	130
90	Plot of the calorimeter cut efficiency versus run number for all kinematic settings	130
91	Plots of the VDC efficiency components, R_1 and R_2 , as a function of LHRS central momentum	132
92	Plot of the LHRS VDC efficiency versus LHRS central momentum from the inclusive (Kin5) delta scan	133
93	Plot of the RHRS VDC efficiency versus run number for all kinematic settings	133
94	Plot of the LHRS VDC efficiency as a function of the electron fractional momentum dp_{tg}^e	134
95	Plot of the coincidence time cut efficiency versus run number .	135

96	Plot of the RHRS β -cut efficiency versus run number for all kinematic settings	136
97	Depiction of the Wilson score interval on a number line	142
98	Change in RHRS β -cut efficiency for each variation of the cut interval	145
99	Change in coincidence time cut efficiency for each variation of the RHRS β -cut interval (Argon Kin4)	145
100	$^{12}\text{C}(e, e')$ differential cross section from the yield ratio method at $E_0 = 2.222 \text{ GeV}$, $\theta = 15.541^\circ$ (inclusive Kin5)	154
101	$^{48}\text{Ti}(e, e')$ differential cross section from the yield ratio method at $E_0 = 2.222 \text{ GeV}$, $\theta = 15.541^\circ$ (inclusive Kin5)	154
102	$^{40}\text{Ar}(e, e')$ differential cross section from the yield ratio method at $E_0 = 2.222 \text{ GeV}$, $\theta = 15.541^\circ$ (inclusive Kin5)	155
103	$^{27}\text{Al}(e, e')$ differential cross section from the yield ratio method at $E_0 = 2.222 \text{ GeV}$, $\theta = 15.541^\circ$ (inclusive Kin5)	155
104	Inclusive differential cross sections-per-nucleon from the experimental data	156
105	Inclusive differential cross sections normalized to the sum of the elementary cross sections	156
106	Carbon y -scaling function extracted from the E12-14-012 inclusive data, compared with previous results at different values of Q^2 . Figure inset shows the momentum-transfer dependence of the scaling function at fixed y	158
107	Aluminum y -scaling function extracted from the E12-14-012 inclusive data, compared with previous results from D. Day <i>et al.</i> at different values of Q^2	158
108	Plot showing the Q^2 dependence of the aluminum scaling function at $y = -0.2 \text{ GeV}$	159
109	Scaling functions of the first kind obtained from the E12-14-012 inclusive data with the LNF argon result for comparison	159
110	Scaling functions of the second kind obtained from the E12-14-012 inclusive data	160
111	Argon ψ -scaling functions obtained from the E12-14-012 inclusive data and the LNF data (with E12-14-012 carbon data for comparison)	161
112	$^{40}\text{Ar}(e, e'p)$ differential cross section as a function of missing energy (Kin1)	163
113	$^{48}\text{Ti}(e, e'p)$ differential cross section as a function of missing energy (Kin1)	163
114	$^{40}\text{Ar}(e, e'p)$ differential cross section as a function of missing momentum (Kin1)	164

115	$^{48}\text{Ti}(e, e'p)$ differential cross section as a function of missing momentum (Kin1)	164
116	$^{40}\text{Ar}(e, e'p)$ differential cross sections versus missing momentum for the three E_{miss} regions (Kin1)	165
117	$^{48}\text{Ti}(e, e'p)$ differential cross sections versus missing momentum for the three E_{miss} regions (Kin1)	166
118	Neutrino oscillation probabilities assuming an initial muon-neutrino	172
119	Neutrino oscillation probabilities assuming an initial tau-neutrino	173
120	Histograms of z_{tg}^e distributions for argon and titanium at Kin2	183
121	Histograms of β_{HRS}^R distributions for argon and titanium at Kin2	183
122	Histograms of argon data and SIMC acceptance variables at Kin2	184
123	Histograms of titanium data and SIMC acceptance variables at Kin2	185

List of Tables

1	Parametrization of the missing energy distributions of the shell-model states in argon and titanium	33
2	Key parameters of CEBAF beam quality, before and after the 12 GeV upgrade	54
3	List of previous $(e, e'p)$ experiments in Hall A	55
4	Target thickness and radiation lengths	57
5	Kinematic settings used in the E12-14-012 experiment	63
6	Momentum delta-scan run numbers and corresponding spectrometer central momentum	63
7	Summary of the scattering data collected by the E12-14-012 experiment	64
8	Main design characteristics of the Hall A high resolution spectrometers	71
9	Parameters for the longitudinal momentum distribution $f(y)$ used in the code	87
10	Layout of the inclusive cross section table generated by the code	91
11	Missing momentum shifts and DWIA to PWIA reduced cross section ratios calculated from the three optical potential fits for $p_m > 0$	96
12	Definitions of the shell-cuts (E_{miss} regions) applied to the missing energy spectrum	99
13	Acceptance cuts used in the inclusive data analysis	109
14	Sources of systematic uncertainty with associated cut variations	146
15	Sources and contributions to the systematic uncertainty from the aluminum, argon, carbon, and titanium inclusive data	147
16	Sources and contributions to the systematic uncertainty from the argon and titanium Kin1 exclusive data	147
17	Sources and contributions to the systematic uncertainty from the argon exclusive data at Kin2 through Kin5	148
18	ESPACE histogram names with descriptions used in the analysis	181
19	ESPACE histogram names with corresponding symbolic representations used in the data analysis	182
20	Histogram cuts with definitions used in the data analysis	182

1 Experiment E12-14-012 at Jefferson Lab

Experiment E12-14-012 was an electron scattering experiment conducted at the Thomas Jefferson National Accelerator Facility (TJNAF), also known as Jefferson Lab (JLab). The proposal outlining the experiment was submitted to the JLab Program Advisory Committee in July of 2014. The request for nine days of beam-time was quickly approved, with a scientific rating of A–, and the experiment was conducted during the months of February and March of 2017.

1.1 Motivation

The goal of E12-14-012 is to extract the differential cross section and the spectral function of argon from the scattering data. Moreover, the motivation for E12-14-012 can be viewed from two perspectives, from that of nuclear physics, and that of neutrino physics.

From the perspective of a nuclear physicist, the motivation behind E12-14-012 is to obtain information on the ground state of the argon (and titanium) nucleus to help constrain theoretical models of electron-nucleus scattering in the impulse approximation. Existing theoretical models of electron-nucleus scattering, such as the Fermi Gas model, have been shown experimentally to be inadequate in describing the complexity of nuclear dynamics[1]. Knowledge of the nuclear ground state is needed for the description of all interactions involving a single nucleon, independent of the final state[1]. This knowledge is obtained from the coincidence $(e, e'p)$ data, and is essential to accurately describe binding energies, spectroscopic factors, and the width of shell model states[1].

From the perspective of a neutrino physicist, the primary motivation behind E12-14-012 is to help increase the accuracy of accelerator based neutrino oscillation experiments. Recent neutrino experiments such as MINER ν A at FermiLab have found that all existing monte-carlo models fail to accurately reproduce experimental data[1]. Thus, accurate lepton-nucleus scattering data, like that collected during E12-14-012, can be used to reduce systematic uncertainty and pave the way for a reliable estimate of the neutrino cross sections[1]. The association of E12-14-012 with neutrino physics is elaborated on further in §1.3.1.

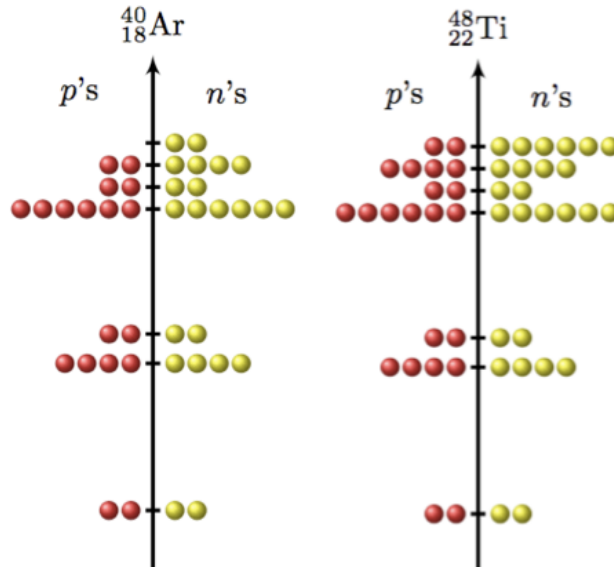


Figure 1: Diagram comparing the shell model level structure for argon and titanium[3]. Note the symmetry between the argon neutron and titanium proton shells.

1.2 Nuclear Physics of E12-14-012

In the *shell model* of the nucleus, a nucleon is described as moving in a central potential $V(r)$ with nucleon-nucleon (NN) interactions treated as a perturbation. The states allowed by this potential are described by a set of energy levels characterized by a principal quantum number n and an orbital angular momentum quantum number ℓ . Some of these levels have the same energy, and each degenerate group of levels is called a *shell*. Each shell can be occupied by a definite number of nucleons of one specific type[2].

The information on the nuclear ground state is contained in a quantity known as the *spectral function* $S(\vec{p}, E)$, defined in §3.5.4. The nucleon-specific spectral function for a certain nucleus can be accessed experimentally through general coincidence $(e, e'N)$ scattering. Considering the specific case of an argon nucleus, its *proton* spectral function can be obtained through an $\text{Ar}(e, e'p)$ scattering experiment. Similarly, the *neutron* spectral function can be obtained via $\text{Ar}(e, e'n)$ scattering. However, detecting the neutron is difficult experimentally, and not possible with the current spectrometer equipment in JLab's Hall A. As direct measurement of the neutron is not feasible, an indirect way is needed to obtain the argon *neutron* spectral function, without detecting the neutron itself.

If NN-correlations are ignored, the spectral function depends only on the

shell model structure of the nucleus. This property of the spectral function can be used to work around the neutron detection problem. Since the protons and neutrons in ^{40}Ar have different shell structure, they will each have their own spectral functions. If the proton and neutron shells are filled identically, a single spectral function can describe the nucleus.

Since the mean field part of the spectral function depends only on the shell model structure, the spectral function for one shell configuration should be valid for another nucleus with the same shell structure. The diagram in Fig. 1 shows the shell model structure for ^{40}Ar and ^{48}Ti . We can see that the *protons* in titanium have the same shell structure as the *neutrons* in argon. Hence, their spectral functions should be identical, that is,

$$S_n^{\text{Ar}}(\vec{\mathbf{p}}, E) = S_p^{\text{Ti}}(\vec{\mathbf{p}}, E). \quad (1.1)$$

Exploiting the correspondence of the level structures in argon and titanium allows us to obtain the *neutron* spectral function for *argon* through regular $(e, e'p)$ scattering on *titanium*.

1.3 Neutrino Oscillations

A neutrino is an extremely light, electrically neutral, leptonic particle that interacts via the weak force (and gravity) only. There are three types, or flavors, of neutrino: electron, muon, and tau, corresponding to the three generations of charged leptons (e, μ, τ) . First postulated by Wolfgang Pauli in 1930 to explain the apparent violation of energy conservation in β -decay reactions, the neutrino remains one of the most mysterious particles to date.

Initially thought to be massless, it is now known that neutrinos do carry mass, but the exact value of the masses are still unknown. Cosmological arguments put a rough upper bound on the sum of the neutrino masses at $m_{tot} < 11 \text{ eV}$, a mere 0.002% of the electron mass $m_e \approx 0.5 \text{ MeV}$ [4]. So far, neutrino experiments have only been able to obtain the squared mass differences $\Delta m_{ji}^2 = m_j^2 - m_i^2$. Determination of the order of the neutrino masses, known as the neutrino mass hierarchy problem, is still an unresolved question in neutrino physics.

Each type of neutrino ν has a corresponding anti-neutrino, $\bar{\nu}$. However, because they have no electric charge, it is possible that the neutrino and anti-neutrino are actually the same particle, distinguishable only by chirality. Fermions that are their own anti-particles are known as Majorana fermions, while (charged) fermions with distinct anti-particles are called

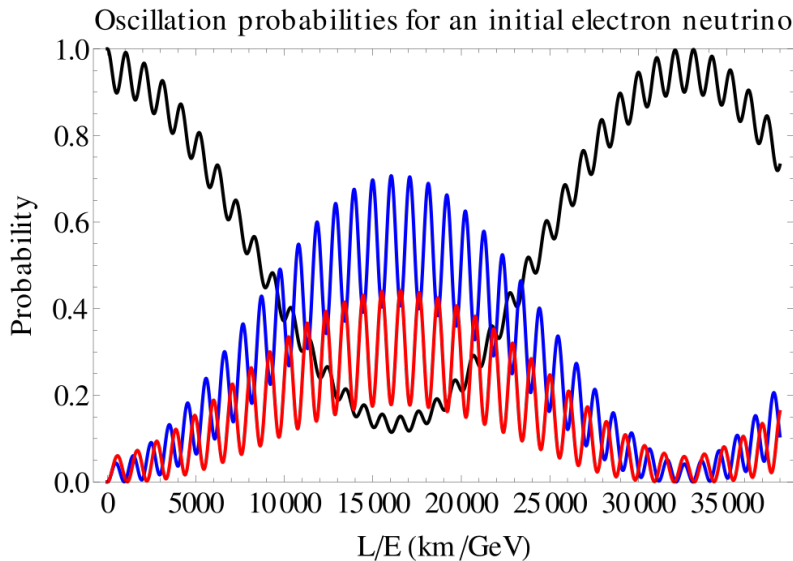


Figure 2: Neutrino oscillation probabilities from Eq. B.4 for an initial electron-neutrino[5]. The blue line is the probability to oscillate into a muon-neutrino $P(\nu_e \rightarrow \nu_\mu)$, and the red line the probability to oscillate into a tau-neutrino $P(\nu_e \rightarrow \nu_\tau)$. The black line is the survival probability $P(\nu_e \rightarrow \nu_e)$.

Dirac fermions. It is still an open question as to whether neutrinos are Majorana fermions.

Weak interactions create neutrinos in definite flavor eigenstates $|\nu_\ell\rangle$, along with their corresponding charged lepton ℓ . Similarly, if a neutrino of a specific flavor interacts weakly with matter, a charged lepton is produced with the same flavor as the interacting neutrino. However, neutrinos can also be classified as mass eigenstates $|\nu_i\rangle$ of their free Hamiltonian. Thus, the flavor eigenstates can be written as linear combinations of the mass eigenstates, and vice versa. Differences between the neutrino masses cause mixing of the flavor eigenstates as the neutrino propagates through space (or matter). That is, a neutrino of a specific flavor could transform into a neutrino of another flavor after traveling for some time. The matrix \mathbb{U} that describes the mixing is known as the PMNS matrix (see §B.1). This mixing phenomenon is known as neutrino oscillation.

The probability for a neutrino initially in the flavor eigenstate $|\nu_\ell\rangle$ to oscillate into the state $|\nu_{\ell'}\rangle$ after propagating a for a time t (over a distance $L \approx ct$) is calculated as

$$P(\nu_\ell \rightarrow \nu_{\ell'}) = |\langle \nu_{\ell'} | \nu_\ell(t) \rangle|^2 \quad (1.2)$$

The result of the calculation of Eq. 1.2 for three neutrino flavors is shown in

§B.1. There are three probabilities that can be calculated from Eq. 1.2. Assuming an initial electron-neutrino, there is the probability to oscillate into a muon-neutrino $P(\nu_e \rightarrow \nu_\mu)$, the probability to oscillate into a tau-neutrino $P(\nu_e \rightarrow \nu_\tau)$, and the survival probability $P(\nu_e \rightarrow \nu_e)$, or the probability for no oscillation to occur. These probabilities are plotted as functions of L/E in Fig. 2.

1.3.1 Connection to Neutrino Oscillation Experiments

The results of E12-14-012 are connected to neutrino oscillation experiments through the type of detector used. Upcoming neutrino oscillation experiments, such as the Long Baseline Neutrino Experiment (LBNE)/Deep Underground Neutrino Experiment (DUNE) at FermiLab and the Sanford Underground Research Facility will employ Liquid Argon Time Projection Chamber (LArTPC) detectors to detect neutrino-nucleus interactions. An illustration of the DUNE/LBNE experiment is shown in Fig. 3. In a long baseline neutrino oscillation experiment, neutrinos are generated and allowed to propagate over a great distance, before ultimately being detected. The long distance increases the probability of observing oscillations in neutrino flavor.

A Time Projection Chamber (TPC) detector is essentially a large vat containing a liquid or gas medium in which particle interactions occur. Unlike the spectrometers used in E12-14-012, which consist of a series of smaller detectors, a TPC detector contains no other constructional elements, minimizing multiple scattering and other unwanted interactions[6]. The LArTPC detectors can hold up to 70,000 tons of ultra-pure liquid argon (contaminants < 0.1 ppb)[7, 6]. The enormous size of the TPC is necessary, as the cross section for neutrino-nucleus interactions is small[6].

Inside the LArTPC detectors, the neutrinos and anti-neutrinos interact with the argon nuclei via the charged-current quasi-elastic (CCQE) weak processes,

$$\nu_\ell + A \rightarrow \ell^- + p + X \quad (1.3a)$$

$$\bar{\nu}_\ell + A \rightarrow \ell^+ + n + X. \quad (1.3b)$$

In these reactions, a neutrino ν_ℓ (or antineutrino $\bar{\nu}_\ell$) interacts with the nucleus through the exchange of a charged W^\mp boson, turning into its specific lepton flavor ℓ^\mp . For CCQE processes, the inclusive differential cross section is given by[8]

$$\frac{d^3\sigma}{d\Omega_\ell dE_\ell} = \frac{G_F^2 \cos^2 \theta_c}{32\pi^2} \frac{|\vec{\mathbf{k}}'|}{|\vec{\mathbf{k}}|} L_{\mu\nu} W^{\mu\nu}, \quad (1.4)$$

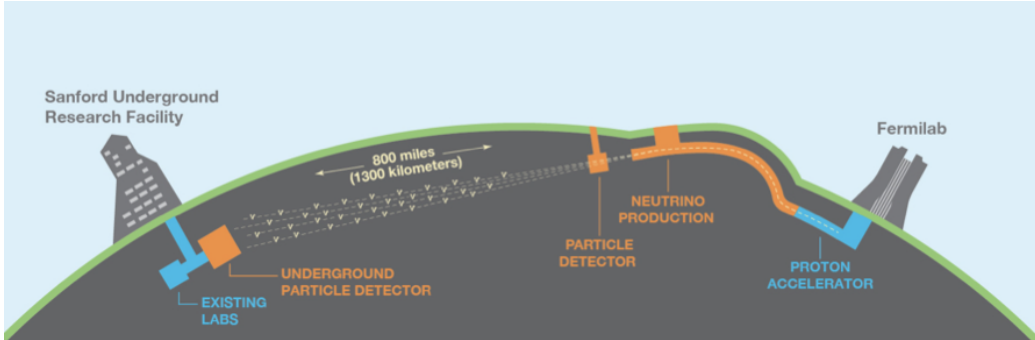


Figure 3: Depiction of the LBNE/DUNE neutrino oscillation experiment[7]. Neutrinos are generated at FermiLab and then pass through the near detector. The neutrinos propagate underground over a great distance before being observed in the far LArTPC detector.

where G_F is Fermi's coupling constant and θ_c is the Cabbibo angle. The vectors $\vec{\mathbf{k}}$ and $\vec{\mathbf{k}}'$ are the initial momentum of the neutrino and final momentum of the scattered lepton, respectively. The cross section also factors into two tensors, $L_{\mu\nu}$ and $W^{\mu\nu}$, which are similar to those derived in §3.2 for electron-nucleus scattering, but contain additional terms from axial-vector components in the current four-vectors[8]. Upon visual inspection of Eq. 1.4, it is clear that the inclusive neutrino-nucleus cross section has the same form as the cross section derived for electron scattering (see §3.2 Eq. 3.17). Transitioning to exclusive neutrino-nucleus scattering will change the form of the response tensor, but does not change the overall mathematical structure of the cross section, namely the factorization into purely leptonic and hadronic terms. Thus, in the impulse approximation, the exclusive neutrino-nucleus cross section factors analogously, and hence depends on a spectral function,

$$\left(\frac{d^6\sigma_\nu}{d\Omega_\ell dE_\ell d\Omega_N dE_N} \right)_{IA} \propto S(\vec{\mathbf{p}}, E). \quad (1.5)$$

Since the spectral function is an intrinsic property of the target ground state, the spectral function extracted from electron scattering data applies to the neutrino cross sections as well.

Accelerator based neutrino oscillation experiments obtain neutrino beams as decay products, mainly of pions, which are in turn produced by interactions of a separate proton beam with a chosen target material. Neutrino beams produced in this manner are not monochromatic, meaning the beam consists of particles that have a wide range of energies. This means that the incident neutrino energy has to be determined on an event-by-event basis,

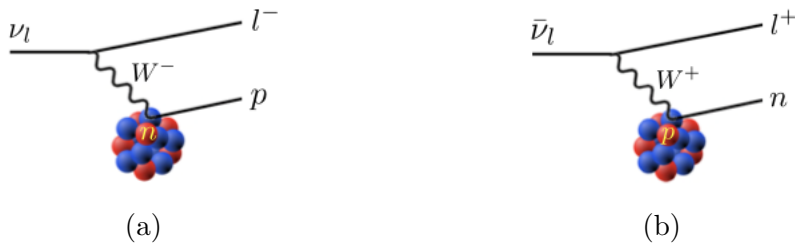


Figure 4: Diagrams of CCQE (a) neutrino- and (b) anti-neutrino-nucleus scattering in the Born approximation. The neutrino interacts with the nucleus via exchange of a W boson, transforming into its specific lepton flavor and ejecting a bound nucleon.

and must be reconstructed from the final state lepton and nucleon kinematics at the interaction point. It is the determination of the incident neutrino energy that leads to the largest source of systematic uncertainty in both long and short baseline neutrino oscillation experiments.

For CCQE scattering events, the reconstructed neutrino energy is given by[9]

$$E_\nu = \frac{m_N^2 - m_\ell^2 - E_N^2 + 2E_\ell E_N - 2(\vec{\mathbf{k}}_\ell \cdot \vec{\mathbf{p}}_N) + |\vec{\mathbf{p}}_N|^2}{2(E_N - E_\ell + |\vec{\mathbf{k}}_\ell| \cos \theta_\ell - |\vec{\mathbf{p}}_N| \cos \theta_N)}. \quad (1.6)$$

The momentum $\vec{\mathbf{k}}_\ell$ and angle θ_ℓ of the final-state lepton can be measured by the detectors. However, the quantities $|\vec{\mathbf{p}}_N|$ and E_N , the momentum and energy of the knocked-out nucleon, are unknown. Many current neutrino CCQE simulation codes calculate the reconstructed neutrino energy by making the approximations

$$|\vec{\mathbf{p}}_N| = 0 \quad (1.7a)$$

$$E_N = m_N - \epsilon, \quad (1.7b)$$

where ϵ is defined as the single-nucleon separation energy[9, 10]. Fortunately, the distribution of possible values of $|\vec{\mathbf{p}}_N|$ and E_N is determined by the spectral function, thus making knowledge of the nucleon energy and momentum distributions essential in constraining the incident neutrino beam energy. Increased accuracy of reconstructed neutrino energies can lead to increased accuracy in measurements of quantities of import to neutrino physics, such as the possible CP-violating phase $e^{-i\delta}$ in the PMNS-matrix and the squared mass difference $\Delta m_{ij}^2 = m_i^2 - m_j^2$ in the oscillation probability (see §B.1).

As the lepton-nucleus interaction is intrinsic to the operation of the LArTPC, it is important to have a fundamental understanding of the momentum and energy distribution of nucleons in the ground state of the argon

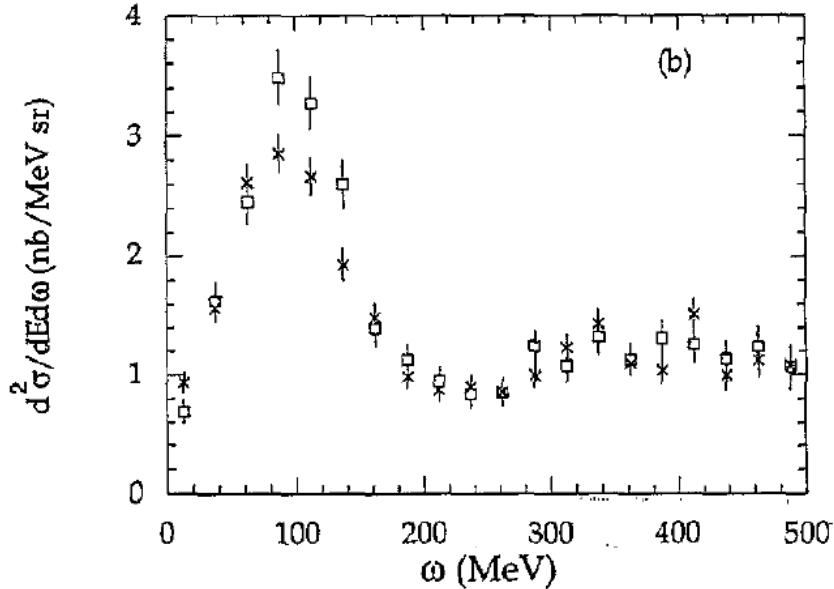


Figure 5: Inclusive cross sections per-nucleon for ^{40}Ar (asterisk) and ^{16}O (box) at $E' = 700$ MeV and $\theta = 32^\circ$ from the existing LNF argon data[11].

nucleus. E12-14-012 is designed to provide that knowledge.

1.4 Existing Experimental Data

Before E12-14-012 at JLab, there was only one previous experiment where inclusive electron scattering data was collected on ^{40}Ar . The experiment, conducted at the ADONE storage ring at the Laboratori Nazionali di Frascati (LNF), scattered 0.5 GeV – 1.5 GeV electrons from ^{16}O and ^{40}Ar at scattering angles of 32° and 83° [11]. The extracted per-nucleon inclusive cross sections for ^{40}Ar and ^{16}O are shown in Fig. 5. When comparing the $^{16}\text{O}(e, e')$ cross sections to previous experimental results, the experimenters found an overall correction factor of 1.19 had to be applied to the cross section to match the previous data.

Additionally, E12-14-012 is the first measurement of inclusive *quasi-elastic* electron scattering on ^{48}Ti . However, there have been *elastic* and *inelastic* electron scattering experiments on multiple isotopes of titanium, such as that of Refs. [12, 13, 14].

2 Electron Scattering As A Probe of Nuclear Structure

In order to study the atomic nucleus, a probe that can adequately resolve the nucleus and its components is required. Although many types of particles can in theory be used as nuclear probes, it will become apparent that the electron is best suited for the task. This is due to the fact that the electron possesses advantages as a probe of nuclear structure and dynamics that other particles lack.

The electron interacts with the nucleus via the electromagnetic force; the interaction strength being on the order of the fine structure constant $\alpha \approx 0.0073$. Since the interaction is weak, the electron has a minimal effect on the initial state of the target nucleus. This also allows the interaction to be treated within the framework of first-order perturbation theory (Born Approximation). On the other hand, a hadronic probe such as a proton or pion would interact with the nucleus via the strong force. The coupling constant of the strong force is $\alpha_s \approx 1$, significantly larger than the fine structure constant. This suggests that the interaction of a hadronic probe with the nucleus is surface dominated. Also, this large interaction strength could have an immeasurable effect on the nuclear system under consideration in this dissertation.

Photon scattering is another possibility. However, real photons can only probe excited nuclear states. A nuclear state with excitation energy ω can only be accessed by a photon carrying three-momentum $|\vec{q}| = \omega$. However, the energy transfer of a virtual photon obeys no such restriction. Also, the relatively large mean-free path of a virtual photon allows the probe to explore more of the target volume[15]. This is relevant as it is a virtual photon that mediates the interaction between the electron and the nucleus. The components of the four-momentum transfer q carried by the virtual photon can be varied independently, as long as the relation

$$|\vec{q}|^2 - \omega^2 > 0 \tag{2.1}$$

holds. Thus, we can conclude that the electron is the nuclear probe best suited for the nuclear physics we are studying.

In order to be an effective nuclear probe, the electron must possess sufficiently high energy (momentum) that its (reduced) de Broglie wavelength $\lambda = \hbar/|\vec{k}|$ is on the order of the spatial extension of the nucleus. An empirical formula for the radius of a nucleus of mass number A is

$$R = r_0 A^{1/3} \tag{2.2}$$

where $r_0 \approx 1.5 \times 10^{-13}$ cm. Although this expression is a good fit to the experimental data, there is some evidence that r_0 has some weak dependence on A . The value of r_0 given here is best for medium-weight nuclei, but may be smaller for nuclei with larger mass number[16]. This relationship also holds for the virtual photon mediating the interaction. In this case, the (reduced) de Broglie wavelength is written as

$$\lambda = \frac{2\pi}{|\vec{q}|}. \quad (2.3)$$

Strengthening the relationship between the de Broglie wavelength and the nuclear radius to $\lambda < R$, we can obtain a lower limit on the required three-momentum transfer. Thus, in order to effectively probe a nucleus of mass number A , the three-momentum transferred to the target nucleus from the electron must obey the following relationship,

$$|\vec{q}| > \frac{2\pi}{r_0 A^{1/3}}. \quad (2.4)$$

For the lightest target nuclei used in the experiment, ^{12}C , the relationship becomes $|\vec{q}| \gtrsim 360$ MeV, a condition that is surpassed by all kinematic settings used in this experiment.

3 Electron Scattering Theory

The use of an electron as a probe to study the nucleus is known as *electron scattering*. In an electron scattering experiment, electrons are accelerated towards some target of interest. The incident electron interacts with the target and scatters away. Besides the scattered electron, the composition of the final state after the interaction depends on the incident energy of the electron probe.

At low incident energies, the electron sees the nucleus as a single object, and scatters away, leaving the nucleus intact and in its ground state. This is known as an *elastic scattering* process. At higher energies, the electron can excite the target nucleus into a higher energy state. The excited nucleus then returns to the ground state by emitting secondary particles, a process known as *inelastic scattering*. At extremely high energies, the electron can scatter off of the individual quarks within the nucleon. This is known as *deep inelastic scattering*. At intermediate energy transfers is a process called *quasi-elastic scattering*. In a quasi-elastic scattering process, a nucleus A is transformed into some other nucleus B (or some other nuclear system, either

bound or unbound) through ejection of a single nucleon N . Symbolically, this reaction is written as

$$e + A \rightarrow e' + N + B. \quad (3.1)$$

Not all final state particles are detected in scattering experiments. The remaining nuclear system B is rarely detected, and is left as a *spectator* to the scattering. If only the scattered electron e' is detected, the reaction is referred to as *inclusive*, and is written as (e, e') . This is because all possible final states of the ejected nucleon N must be included when calculating the scattering cross section. When both the final state electron and the ejected nucleon are detected, the scattering is called *exclusive*, and is written compactly as $A(e, e'N)B$, and is often shortened further to just $(e, e'N)$. The scattering is called *exclusive* because if the final hadronic state is known, then all other possible states are excluded when calculating the cross section. When the ejected nucleon and scattered electron are detected at the same time, the process is known as *coincidence scattering*.

The $(e, e'p)$ scattering reaction is a powerful tool in experimental nuclear physics. Coincidence $(e, e'p)$ scattering experiments have shed light on a variety of topics in nuclear physics including short range correlations in nuclei, meson electro-production, and the structure of the nucleon and nucleus.

3.1 Scattering Kinematics

A schematic diagram of $(e, e'N)$ scattering is shown in Fig. 6. An electron e with four-momentum $k = (E_0, \vec{k})$ is incident on a nuclear target of mass number A . After the interaction, a single nucleon N is knocked out of the nucleus, and scatters away with four-momentum $P'_N = (E'_N, \vec{P}'_N)$, leaving the residual nucleus in some state B , possibly unbound and/or excited. The scattered electron e' leaves with four-momentum $k' = (E', \vec{k}')$ at an angle θ with respect to $\hat{\mathbf{k}}$. This angle is referred to as the *scattering angle*. The electron three-momentum vectors \vec{k} and \vec{k}' define the *scattering plane*. Similarly, the three-momentum transfer \vec{q} and nucleon momentum vector \vec{P}'_N define the *reaction plane*. The angle between the two planes is ϕ_{Nq} .

The electron transfers four-momentum $q = (\omega, \vec{q})$ to the target through the exchange of a single virtual photon γ^* . Conservation of four-momentum at the electron vertex gives $q = k - k'$, and hence $\omega = E_0 - E'$ and $\vec{q} = \vec{k} - \vec{k}'$. The four-momentum of a virtual photon does not square to zero, and is defined as $q^\mu q_\mu = -Q^2$. This quantity is known as *Q-squared* and

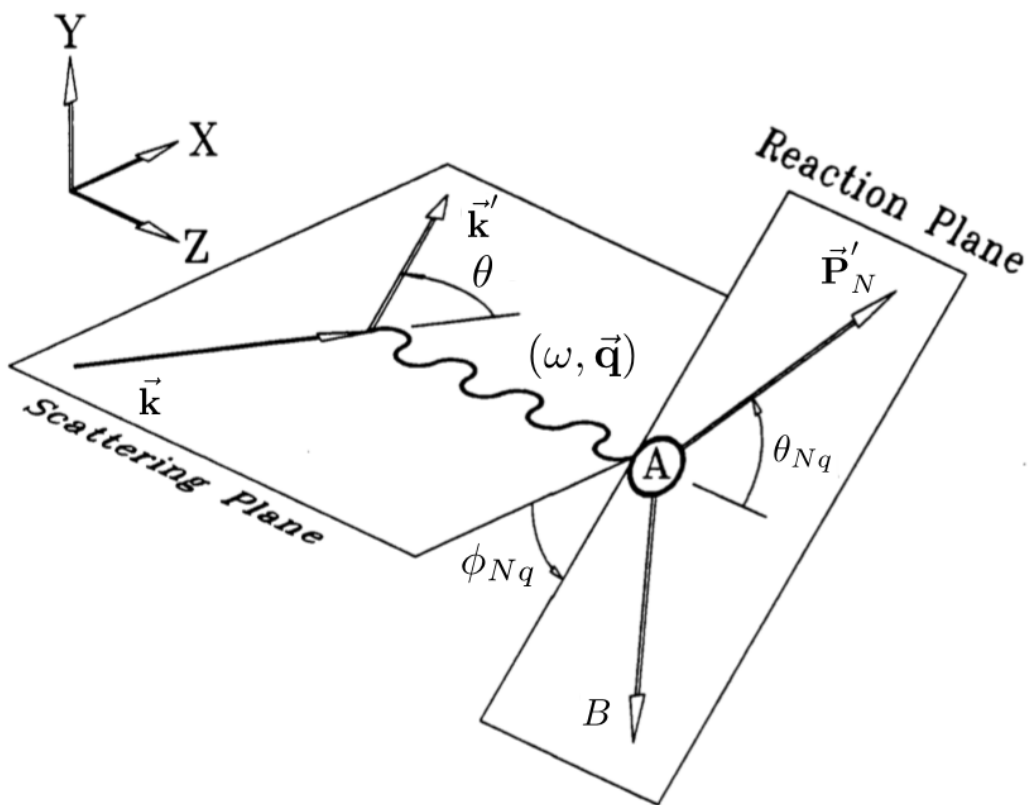


Figure 6: Diagram depicting the kinematics for the $A(e, e'N)B$ reaction in the Born Approximation. Figure modified from Ref. [17].

is important as it describes the scattering kinematics of the electron probe. Carrying out the calculation in the highly-relativistic limit ($m_e \approx 0$) gives

$$Q^2 = 4E_0E' \sin^2 \frac{\theta}{2}. \quad (3.2)$$

The invariant mass of the undetected final hadronic state is defined as $W^2 = (P + q)^2$, and is given as

$$W^2 = M^2 + 2M\omega - Q^2. \quad (3.3)$$

Thus far, no assumption has been made about the type of nucleon ejected from the nucleus. However, from an experimental perspective, the knocked out nucleon that is detected is usually the proton, as detecting the neutron is exceedingly difficult. Thus, further analysis will consider the case of an ejected proton, or an $(e, e'p)$ reaction.

3.2 Derivation of the Cross Sections

A Feynman diagram of $(e, e'p)$ scattering in the single-photon-exchange Born Approximation is shown in Fig. 7. The interaction vertex, which is represented in Fig. 7 by a large black circle, will be modeled by some electro-nuclear processes, and are detailed in the following sections.

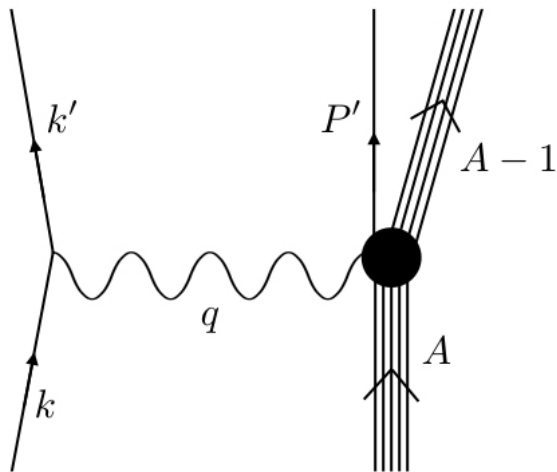


Figure 7: Feynman diagram for single-photon-exchange $(e, e'p)$ scattering.

A general form of the scattering amplitude \mathcal{M} for the reaction can be obtained by using the Feynman rules of quantum electrodynamics (QED).

Let $u^s(k)$ and $U^r(P)$ denote the four-component Dirac spinors for the electron and proton with spin indices s and r , respectively. These spinors are solutions of the free Dirac equations $(\not{k} - m)u^s(k) = 0$ and $(\not{P} - M)U^r(P) = 0$. Applying the Feynman rules to the diagram of Fig. 7 gives

$$i\mathcal{M} = \bar{u}^{s'}(k')(-ie\gamma^\mu)u^s(k)\frac{-ig_{\mu\nu}}{q^2 + i\epsilon}\bar{U}^{r'}(P')(ie\hat{J}^\nu(0))U^r(P). \quad (3.4)$$

Suppressing the arguments and spin indices of the Dirac spinors for notational convenience, the amplitude is written as

$$\mathcal{M} = -\frac{e^2}{q^2}[\bar{u}'\gamma^\mu u]\left[\bar{U}'\hat{J}_\mu(0)U\right]. \quad (3.5)$$

The first bracketed quantity is the leptonic electromagnetic current j^μ , and the second is the hadronic current J^μ .

As neither the electron beam nor the nuclear target are polarized, the scattering amplitude must be averaged over the initial spin states and then summed over the final spin states. The summations are carried out as

$$\langle|\mathcal{M}|^2\rangle = \frac{1}{2}\sum_s\frac{1}{2}\sum_r\sum_{s'r'}|\mathcal{M}|^2. \quad (3.6)$$

Writing the spin-averaged amplitude explicitly in terms of the current four-vectors gives

$$\langle|\mathcal{M}|^2\rangle = \frac{e^4}{q^4}\left(\frac{1}{2}\sum_{ss'}j^\mu j^{\nu*}\right)\left(\frac{1}{2}\sum_{rr'}J_\mu J_\nu^*\right). \quad (3.7)$$

The two parenthetical sums are given explicit definitions. The first sum,

$$L^{\mu\nu} = \frac{1}{2}\sum_{ss'}j^\mu j^{\nu*} \quad (3.8)$$

is known as the *leptonic tensor*, and is a function only of the leptonic four-momenta k and k' . An explicit expression for $L^{\mu\nu}$ can be calculated using the summation identity known as Casimir's Trick, yielding

$$L^{\mu\nu} = 2[k^\mu k'^\nu + k^\nu k'^\mu - g^{\mu\nu}(k \cdot k')] \quad (3.9)$$

in the ultra-relativistic electron approximation. It is straight forward to verify that the leptonic current is conserved by showing that $q_\mu L^{\mu\nu} = L_{\mu\nu} q^\nu = 0$.

The second sum,

$$w_{\mu\nu} = \frac{1}{2}\sum_{rr'}J_\mu J_\nu^*, \quad (3.10)$$

defined as $w_{\mu\nu}$ for notational convenience, is a tensor that characterizes the hadronic response to the scattering. This tensor is a function only of the hadronic four-momenta, P and P' .

Combining everything so far, the spin-averaged amplitude can be written as

$$\langle |\mathcal{M}|^2 \rangle = \frac{e^4}{Q^4} L^{\mu\nu} w_{\mu\nu}. \quad (3.11)$$

This expression is used to calculate the differential cross section.

For two particles in the final state, the differential of the cross section is given by[18]

$$d\sigma = \frac{d^3\vec{\mathbf{k}}'}{(2\pi)^3 2E'} \frac{d^3\vec{\mathbf{P}}'}{(2\pi)^3 2E_{p'}} \frac{\langle |\mathcal{M}|^2 \rangle}{\Phi} (2\pi)^4 \delta^4(k + P - k' - P'). \quad (3.12)$$

The term Φ is the invariant flux of particles, which is calculated as

$$\Phi = 4\sqrt{(P \cdot k)^2 - M^2 m^2} \approx 4P \cdot k = 4ME_0. \quad (3.13)$$

The differential cross section itself is obtained by integrating Eq. 3.12 over any un-observed four-momenta, and then dividing through by the differentials of the remaining observed quantities. Thus, at this point in the calculation, it is necessary to specify which particles are observed in the final state.

Since the scattered electron is the only particle detected in an inclusive reaction, the unobserved proton four-momentum P' must be integrated out of Eq. 3.12 to obtain the cross section. It is customary express the cross section in terms of the fine structure constant, which is related to the electron charge through $e^2 = 4\pi\alpha$. Assuming the electron is highly relativistic ($E \approx |\vec{\mathbf{k}}|$), the electron momentum differential can be written in terms of the energy as

$$d^3\vec{\mathbf{k}}' = |\vec{\mathbf{k}}|^2 d|\vec{\mathbf{k}}| d\Omega' \approx E'^2 dE' d\Omega'. \quad (3.14)$$

Plugging this expression into Eq. 3.12, dividing through by the differentials dE' and $d\Omega$, and integrating over the proton momentum gives the differential cross section per energy and per solid-angle as

$$\frac{d^3\sigma}{d\Omega' dE'} = \frac{\alpha^2}{Q^4} \frac{E'}{E_0} L^{\mu\nu} \left[\frac{1}{2M} \int \frac{d^3\vec{\mathbf{P}}'}{(2\pi)^3 2E_{p'}} w_{\mu\nu}(P, P') (2\pi)^3 \delta^4(k + P - k' - P') \right]. \quad (3.15)$$

The term in square brackets is identified as the hadronic target response tensor. Written explicitly in terms of the nucleon current, the response tensor

is given by

$$W_{\mu\nu} = \frac{1}{8M} \int \frac{d^3\vec{\mathbf{P}}'}{E_{p'}} \left(\sum_{rr'} J_\mu J_\nu^* \right) \delta^4(q + P - P'). \quad (3.16)$$

Making this substitution in Eq. 3.15 gives the general expression for the differential cross section for inclusive electron-nucleus scattering as

$$\frac{d^3\sigma}{d\Omega' dE'} = \frac{\alpha^2}{Q^4} \frac{E'}{E_0} L^{\mu\nu} W_{\mu\nu}. \quad (3.17)$$

As both final state particles are observed in exclusive scattering, no integral is performed on Eq. 3.12 to obtain the cross section. The momentum differential of the final state proton is given by

$$d^3\vec{\mathbf{P}}' = |\vec{\mathbf{P}}'|^2 d|\vec{\mathbf{P}}'| d\Omega_{p'} = |\vec{\mathbf{P}}'| E_{p'} dE_{p'} d\Omega_{p'}, \quad (3.18)$$

where the mass-shell equation was used to eliminate the momentum differential in favor of the proton energy and its differential.

The exclusive differential cross section is obtained by substituting the differentials and spin-averaged amplitude into Eq. 3.12 and dividing through by all energy and solid-angle differentials, giving

$$\begin{aligned} \frac{d^6\sigma}{d\Omega' dE' d\Omega_{p'} dE_{p'}} &= \frac{\alpha^2}{Q^4} \frac{E'}{E_0} |\vec{\mathbf{P}}'| E_{p'} L^{\mu\nu} \\ &\times \left[\frac{1}{4ME_{p'}} w_{\mu\nu} \delta^4(k + P - k' - P') \right]. \end{aligned} \quad (3.19)$$

Again, the remaining term in the square brackets is identified as the hadronic target response tensor $W_{\mu\nu}$, written explicitly in terms of the hadronic currents as

$$W_{\mu\nu} = \frac{1}{8ME_{p'}} \left(\sum_{rr'} J_\mu J_\nu^* \right) \delta^4(q + P - P'). \quad (3.20)$$

The properties of the response tensor are further explored in §3.3. Thus, the general expression for the exclusive differential cross section is

$$\frac{d^6\sigma}{d\Omega' dE' d\Omega_{p'} dE_{p'}} = \frac{\alpha^2}{Q^4} \frac{E'}{E_0} |\vec{\mathbf{P}}'| E_{p'} L^{\mu\nu} W_{\mu\nu}. \quad (3.21)$$

The exclusive cross section is said to be *six-fold* differential, as the cross section is given per-differential in six variables. The inclusive cross section can be obtained from the exclusive cross section by integrating over the proton variables as

$$\frac{d^3\sigma}{d\Omega' dE'} = \iint dE_{p'} d^3\vec{\mathbf{P}}' \left(\frac{d^6\sigma}{d\Omega' dE' d\Omega_{p'} dE_{p'}} \right) \delta^4(q + P - P'). \quad (3.22)$$

3.3 The Hadronic Target Response Tensor

While the expressions of Eq. 3.16 and Eq. 3.20 for the target response tensors are perfectly valid, the mathematical properties of tensors combined with fundamental principles of physics can be used to obtain more informative expressions for the target response tensor. Assume that the hadronic spinors are normalized to their energy as $U^{r\dagger}(P)U^{r'}(P) = 2E_p\delta^{rr'}$. Then, the single particle states are written as $|\vec{\mathbf{P}}, r\rangle = \sqrt{2E_p}\hat{a}_p^{r\dagger}|0\rangle$, where $\hat{a}_p^{r\dagger}$ creates a hadronic state from the vacuum $|0\rangle$ with four-momentum p and spin r . The hadronic current $J_\mu = \bar{U}'\hat{J}_\mu(0)U$ can then be written in terms of the matrix elements of the nuclear current operator $\langle\vec{\mathbf{P}}', r'|\hat{J}_\mu(0)|\vec{\mathbf{P}}, r\rangle$ as

$$J_\mu = 2\sqrt{ME_p}\langle\vec{\mathbf{P}}', r'|\hat{J}_\mu(0)|\vec{\mathbf{P}}, r\rangle \quad (3.23)$$

and hence the exclusive response tensor becomes

$$W_{\mu\nu} = \frac{1}{2}\sum_{rr'}\langle\vec{\mathbf{P}}', r'|\hat{J}_\mu(0)|\vec{\mathbf{P}}, r\rangle\langle\vec{\mathbf{P}}, r|\hat{J}_\nu(0)|\vec{\mathbf{P}}', r'\rangle\delta^4(q+P-P'). \quad (3.24)$$

Since the nuclear current operators are Hermitian, so is the response tensor. That is,

$$W_{\mu\nu} = W_{\mu\nu}^\dagger = W_{\nu\mu}^*. \quad (3.25)$$

This means that Eq. 3.24 can be re-written as

$$W_{\mu\nu} = \frac{1}{2}\sum_{rr'}\langle\vec{\mathbf{P}}, r|\hat{J}_\nu(0)|\vec{\mathbf{P}}', r'\rangle\langle\vec{\mathbf{P}}', r'|\hat{J}_\mu(0)|\vec{\mathbf{P}}, r\rangle\delta^4(q+P-P'). \quad (3.26)$$

Using the properties of translation invariance of the nuclear current operator, the matrix elements evaluated at the vertex ($x=0$) can be related to those evaluated at some other four-position x by

$$\langle\vec{\mathbf{P}}, r|\hat{J}_\nu(x)|\vec{\mathbf{P}}', r'\rangle = e^{i(P-P')\cdot x}\langle\vec{\mathbf{P}}, r|\hat{J}_\nu(0)|\vec{\mathbf{P}}', r'\rangle. \quad (3.27)$$

Integrating this expression over x and using the Fourier transform definition of the Dirac delta function gives

$$\int\frac{d^4x}{(2\pi)^4}e^{iq\cdot x}\langle\vec{\mathbf{P}}, r|\hat{J}_\nu(x)|\vec{\mathbf{P}}', r'\rangle = \langle\vec{\mathbf{P}}, r|\hat{J}_\nu(0)|\vec{\mathbf{P}}', r'\rangle\delta^4(q+P-P'). \quad (3.28)$$

Substituting this identity into the expression for the response tensor, and using the completeness of the final proton states gives

$$W_{\mu\nu} = \frac{1}{2}\sum_r\int\frac{d^4x}{(2\pi)^4}e^{iq\cdot x}\langle\vec{\mathbf{P}}, r|\hat{J}_\nu(x)\hat{J}_\mu(0)|\vec{\mathbf{P}}, r\rangle. \quad (3.29)$$

This expression can be further manipulated into one that is commonly found in the literature. Consider a kinematical situation that would produce an analogous expression to Eq. 3.29, however, with the nuclear current operators switched in the matrix element:

$$\frac{1}{2} \sum_r \int \frac{d^4x}{(2\pi)^4} e^{iq \cdot x} \langle \vec{\mathbf{P}}, r | \hat{J}_\mu(0) \hat{J}_\nu(x) | \vec{\mathbf{P}}, r \rangle. \quad (3.30)$$

Reverse engineering the steps that led to Eq. 3.29 implies that the switched matrix element in Eq. 3.30 originated from an expression of the form

$$\frac{1}{2} \sum_{rr'} \langle \vec{\mathbf{P}}', r' | \hat{J}_\nu(0) | \vec{\mathbf{P}}, r \rangle \langle \vec{\mathbf{P}}, r | \hat{J}_\mu(0) | \vec{\mathbf{P}}', r' \rangle \delta^4(q + P' - P). \quad (3.31)$$

The kinematics implied by this expression, $q = P - P'$, are unphysical, essentially representing the nucleus decaying by emitting a photon. This means that the switched matrix element vanishes, as does its integral in Eq. 3.30. Thus, Eq. 3.30 can be subtracted from Eq. 3.29 without changing its value. Carrying out this subtraction gives a new expression for the exclusive target response tensor in terms of the commutator of the nuclear current operators as

$$W_{\mu\nu} = \frac{1}{2} \sum_r \int \frac{d^4x}{(2\pi)^4} e^{iq \cdot x} \langle \vec{\mathbf{P}}, r | [\hat{J}_\nu(x), \hat{J}_\mu(0)] | \vec{\mathbf{P}}, r \rangle. \quad (3.32)$$

The target response tensor for inclusive scattering is a function of two four-vectors, P and q , as P' is integrated out of Eq. 3.16. The most general tensor $W^{\mu\nu}(q, P)$ that can be formed from two linearly-independent four-vectors has five terms, two corresponding to the self-contractions, two terms of symmetric and anti-symmetric combinations of mixed-contractions, and a term proportional to the metric tensor. That is,

$$\begin{aligned} W^{\mu\nu}(q, P) = & -W_1 g^{\mu\nu} + \frac{W_2}{M^2} P^\mu P^\nu + \frac{W_3}{M^2} q^\mu q^\nu \\ & + \frac{W_4}{M^2} (P^\mu q^\nu + P^\nu q^\mu) + \frac{W_5}{M^2} (P^\mu q^\nu - P^\nu q^\mu) \end{aligned} \quad (3.33)$$

where the coefficients W_i are dimensionless functions of the independent Lorentz scalars q^2 and $P \cdot q$. In the lab frame, $P \cdot q = M\omega$, and by definition $q^2 = -Q^2$. Thus, the coefficients are actually functions of Q^2 and ω , $W_i = W_i(Q^2, \omega)$.

The physical principles of relativistic invariance, gauge invariance, and the conservation of current and parity restrict the possible terms in the expansion of $W^{\mu\nu}(q, P)$ in terms of its arguments. The conservation of current,

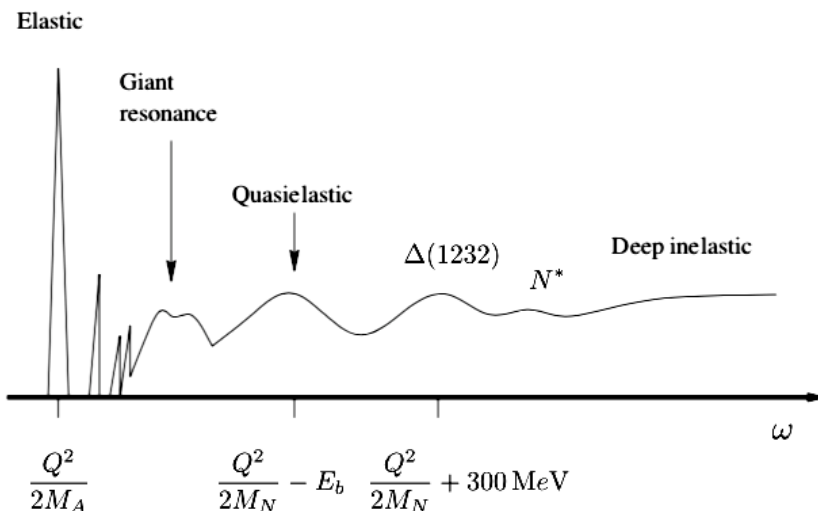


Figure 8: Depiction of a general (e, e') differential cross section spectrum versus energy loss ω , at constant three-momentum transfer $|\vec{q}|$. Figure modified from Ref. [19].

expressed in terms of the hadronic current as $\partial_\mu J^\mu = 0$, translates to the response tensor as

$$q^\mu W_{\mu\nu} = W^{\mu\nu} q_\nu = 0. \quad (3.34)$$

In addition, it is known that the response tensor is Hermitian (see Eq. 3.25). Applying these properties to Eq. 3.33 reduces the number of independent coefficients in the expansion of $W^{\mu\nu}$ to just two, $W_1(Q^2, \omega)$ and $W_2(Q^2, \omega)$. This gives the general expression for the inclusive scattering response tensor as

$$W^{\mu\nu} = W_1 \left(-g^{\mu\nu} + \frac{q^\mu q^\nu}{q^2} \right) + \frac{W_2}{M^2} \left(P^\mu - q^\mu \frac{P \cdot q}{q^2} \right) \left(P^\nu - q^\nu \frac{P \cdot q}{q^2} \right). \quad (3.35)$$

3.4 The (e, e') Cross Section

A diagram showing the general features of the inclusive cross section as a function of energy loss is shown in Fig. 8. There are several peaks corresponding to different physical processes. The first peak in the discrete part of the spectrum corresponds to elastic scattering from a free nucleus at rest. For a nucleus of mass number A and corresponding mass M_A , the elastic peak is located at $\omega_E = Q^2/2M_A$. The following sharp discrete peaks correspond to scattering from low-lying excited states of the nucleus.

The first peaks in the continuous part of the spectrum are the giant multipole resonances. These peaks correspond to collective out-of-phase oscillations of the neutrons and protons within the nucleus. The next peak corresponds to quasi-elastic (QE) single-nucleon knockout reactions, in which the electron transfers enough energy to the nucleus to overcome its binding energy $E_b < 0$ and remove it from the nucleus. If the nucleon (mass M_N) were unbound, the peak would be located at $\omega = Q^2/2M_N$ as in elastic scattering. Accounting for the binding energy shifts the quasi-elastic peak to higher energy transfers[20]

$$\omega_{QE} = \frac{Q^2}{2M_N} - E_b \quad (3.36)$$

(since the binding energy is assumed to be implicitly negative, this is indeed a shift to higher energy transfers). The quantity $Q^2/2M$ can be calculated in terms of the initial electron energy, the target nucleon mass, and the scattering angle as

$$\frac{Q^2}{2M} = \frac{\frac{2E_0^2}{M} \sin^2 \frac{\theta}{2}}{1 + \frac{2E_0}{M} \sin^2 \frac{\theta}{2}}. \quad (3.37)$$

Nucleons are not at rest inside the nucleus. The target nucleon could be moving towards or away from the direction of the three-momentum transfer vector \vec{q} . This *Fermi motion* of the nucleons results in doppler broadening of the quasi-elastic peak. Additionally, the width of the quasi-elastic peak provides an indirect measurement of the average momentum of nucleons in nuclei, and can be used to determine nuclear Fermi momenta[21].

The next peak in the spectrum corresponds to production of the Δ -baryon. The Δ is short-lived, quickly decaying into a nucleon and pion through the process

$$\gamma^* + N \rightarrow \Delta \rightarrow N' + \pi. \quad (3.38)$$

The trough between the quasi-elastic and Δ -production peaks is known as the *dip region*. Effects not included in the Born Approximation, such as multiple photon exchange events, meson exchange currents and pion electroproduction, make a significant contribution to the cross section in this region. Higher energy transfers enter the realm of deep inelastic scattering (DIS). This region of the energy transfer spectrum includes higher nucleon resonances, as well as scattering off individual quarks within the target nucleons.

The range of energy transfers considered in E12-14-012 covers the quasi-elastic and Δ -production peaks. The dominant processes contributing to the inclusive cross section in this region of ω , QE scattering, Δ -production, and

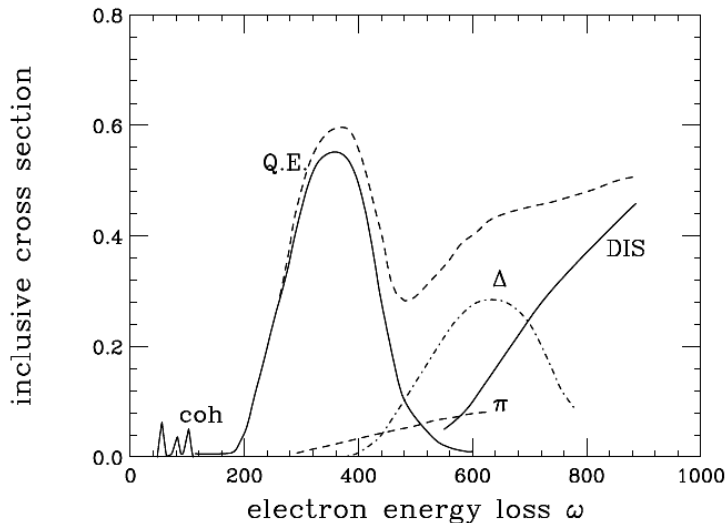


Figure 9: Diagrammatic representation of the processes that contribute to the strength of the inclusive cross section: quasi-elastic knock-out (solid line), Δ -production (dash-dot line), π -production (dashed line), and deep inelastic contributions (solid line, $\omega \gtrsim 600$)[21].

π -production are shown in Fig. 9.

3.5 The $(e, e'p)$ Cross Section

3.5.1 Plane Wave Impulse Approximation

To further analyze the $(e, e'p)$ reaction, additional assumptions about the scattering process and interaction vertex [22] can be made to ease the theoretical analysis. The first assumption is that the virtual photon scatters from a single bound nucleon. In this case, the nuclear current operator becomes a sum over the single-nucleon currents,

$$\hat{J}_\mu = \sum_i \hat{J}_\mu^i, \quad (3.39)$$

and the scattering amplitude for the whole nucleus becomes a sum of single-nucleon scattering events, as shown in Fig. 10. Second, distortion effects from final state interactions (FSI) between the ejected nucleon and the residual nuclear system are considered negligible and are ignored. The next assumption is that the ejected nucleon is detected in coincidence with the scattered electron. Finally, it is assumed that the nucleus is described by an indepen-

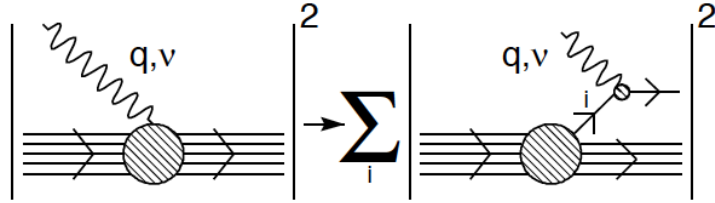


Figure 10: Diagrammatic depiction of assumption (b) of PWIA: the electron-nucleus scattering amplitude is approximated as the sum of individual electron-nucleon scattering events[21].

dent particle model in which the nucleons move in a mean-field potential, free from any nucleon-nucleon correlations.

These assumptions, along with the Born Approximation, are known as the *Plane Wave Impulse Approximation* (PWIA). In summary, the essential approximations of PWIA are:

- (a) A single photon is exchanged between the electron and nucleus (Born Approximation),
- (b) The scattering occurs from a single bound nucleon,
- (c) FSI between the ejected nucleon and recoiling $(A - 1)$ nuclear system is ignored,
- (d) The nucleus is described within the independent particle model,
- (e) Coincidence detection of the scattered electron and knocked-out nucleon.

3.5.2 $(e, e'p)$ Kinematics and PWIA Cross Section

The Feynman diagram for $(e, e'p)$ scattering in PWIA is shown in Fig. 11. The interaction vertex is modified to reflect assumption (b) of PWIA. The target nucleus, assumed to be at rest at the time of interaction, has four-momentum $P_A = (M_A, \vec{0})$. The individual struck proton has four-momentum $P = (E, \vec{P})$. After the scattering, the recoiling $(A - 1)^*$ nuclear system, denoted with the subscript X , leaves with four-momentum $P_X = (E_X, \vec{P}_X)$. The leptonic four-momenta are as given in §3.1, and the ejected proton leaves with $P' = (E_{p'}, \vec{P}')$. Conservation of four-momentum at the $e\gamma^*$ vertex gives the four-momentum transfer as $q = k - k'$. Similarly, $q = P' - P$ is obtained at the γ^*p vertex.

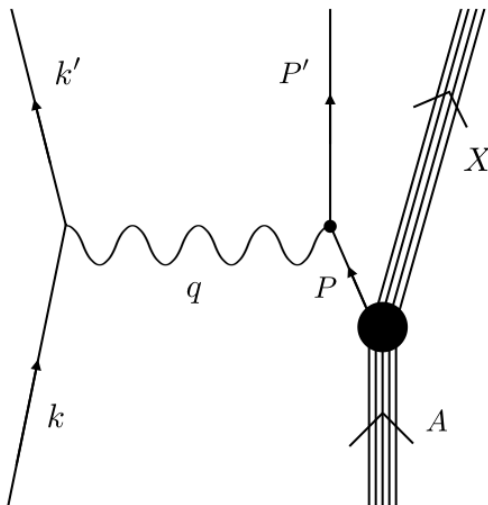


Figure 11: Feynman diagram of $A(e, e'p)X$ scattering in the plane wave impulse approximation.

The energy and three-momentum of the final nuclear state are computed as

$$E_X = \omega - E_{p'} + M_A, \quad (3.40)$$

and

$$\vec{\mathbf{P}}_X = \vec{\mathbf{q}} - \vec{\mathbf{P}}'. \quad (3.41)$$

Expressing $\vec{\mathbf{q}}$ in terms of the proton momentum gives the relationship between the struck proton and recoiling nuclear system as

$$\vec{\mathbf{P}}_X = -\vec{\mathbf{P}}. \quad (3.42)$$

Energy conservation at the γ^*p vertex immediately yields an expression for the bound proton energy as $E = E_{p'} - \omega$. The initial momentum of the bound proton is referred to as the *missing momentum*, and is defined as the difference between the detected proton momentum and the momentum transferred from the scattering process,

$$\vec{\mathbf{p}}_{miss} = \vec{\mathbf{P}}' - \vec{\mathbf{q}}. \quad (3.43)$$

The energies of the final state proton and nuclear system are given by the regular relativistic expressions $E_{p'} = \sqrt{|\vec{\mathbf{P}}'|^2 + M_p^2}$ and $E_X = \sqrt{|\vec{\mathbf{p}}_{miss}|^2 + M_X^2}$, respectively. The *missing energy* is defined as

$$E_{miss} = \omega - E_{p'} - E_X. \quad (3.44)$$

There are other, equivalent, definitions for the missing energy. For example, if the threshold separation energy of the proton is given by

$$E_{thr} = M + M_X - M_A, \quad (3.45)$$

then an equivalent expression for the missing energy is

$$E_{miss} = E_{thr} + E_x, \quad (3.46)$$

where E_x is the excitation energy of the residual nucleus.

The derivation of the exclusive differential cross section in the impulse approximation is beyond the scope of this dissertation. However, a derivation of the PWIA cross section from first principles can be found in Ref. [22]. The result of the calculation gives the PWIA ($e, e'p$) cross section as

$$\frac{d^6\sigma}{d\Omega'dE'd\Omega_{p'}dE_{p'}} = |\vec{\mathbf{P}}'|_{E_{p'}} \left(\frac{d\sigma_p}{d\Omega_e} \right) S(\vec{\mathbf{p}}_m, E_m), \quad (3.47)$$

where $d\sigma_p/d\Omega_e$ is the (off-shell) elastic electron-proton differential cross section. The function $S(\vec{\mathbf{p}}, E)$ is known as the *spectral function*, and is a function of missing momentum and missing energy. The spectral function contains information on the energy and momentum distribution of the nucleons in the nuclear ground state. The spectral function is addressed in much greater detail in §3.5.4.

The first two factors in Eq. 3.47 are often grouped into a kinematical factor $K = |\vec{\mathbf{P}}'|_{E_{p'}}$, which depends only on the final state proton. This notation allows Eq. 3.47 to be recast in a generalized form as

$$\frac{d^6\sigma}{d\Omega'dE'd\Omega'_NdE'_N} = K \cdot \sigma_{eN} \cdot S(\vec{\mathbf{p}}, E). \quad (3.48)$$

The general PWIA cross section neatly factors into three pieces: the kinematical factor, the off-shell electron-nucleon cross section, and the spectral function. The differential cross section for general lepton-nucleus ($\ell, \ell'N$) scattering in the impulse approximation can be written in the form of Eq. 3.48, where σ_{eN} is replaced by the appropriate elastic lepton-nucleus cross section $\sigma_{\ell N}$.

3.5.3 Distorted Wave Impulse Approximation

In general, *final state interactions* (FSI) between the ejected nucleon and the recoiling nuclear system are not negligible. The distorting effects of FSI

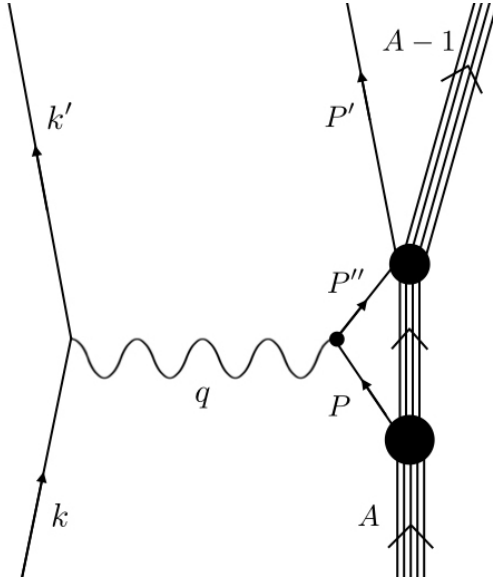


Figure 12: Feynman diagram depicting final state interactions between the knocked-out proton and recoiling nuclear $(A - 1)^*$ system.

invalidate the relationship of Eq. 3.42 between the recoil momentum of the residual nuclear system and the initial proton momentum[22]. Under these circumstances, the plane wave impulse approximation no longer provides an adequate description of nuclear dynamics.

The diagram in Fig. 13 is of the *Complete Distorted Wave Born Approximation* (CDWBA), accounting for all possible interactions before and after the main scattering event. The asymptotic initial state is a plane wave eigenstate of the asymptotically free Hamiltonian $\hat{\mathcal{H}}_i$. The Hamiltonian h_i accounts for electron-nucleus interactions before the main scattering event has occurred. The electromagnetic interaction between the electron and nucleus is given by the interaction Hamiltonian \mathcal{H}_I . Any final state interactions between the scattered electron and recoiling nuclear system are given by h_f . Final state interactions between the knocked-out nucleon and the recoiling nuclear system are accounted for through the distorting optical potential \tilde{V} . It is assumed that \tilde{V} does not appreciably alter the outgoing momenta so that the electron-nucleus interaction can still be evaluated using the asymptotic kinematics[22].

The distorting optical potential is a complex function decomposed into real and imaginary parts as $\tilde{V} = U \pm iW$ (see §6.2). The effect of the real part of the optical potential is to move strength to lower ω 's, while the imaginary part acts to broaden the quasi-elastic peak[23]. The effects of FSI and the optical potential on the electron-nucleus cross section is shown in Fig. 14.

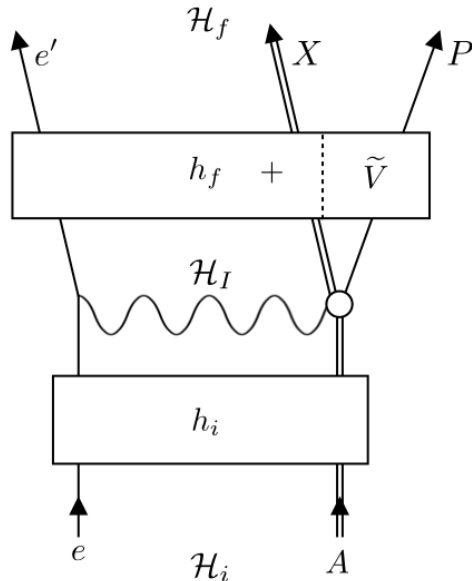


Figure 13: Diagram of the CDWBA, depicting all interactions before and after the main scattering event. Figure modified from Ref. [22].

The dotted line represents the inclusive cross section without FSI, while the dashed line includes the imaginary part of the distorting optical potential. The full FSI corrected cross section is the solid line.

Inclusion of the distorting potential and other higher-order effects (such as contributions from meson exchange currents) in the impulse approximation results in a cross section that cannot be factorized in an analogous way to that of PWIA. However, under a certain set of assumptions and approximations known as the *Distorted Wave Impulse Approximation* (DWIA), a factorized form of the cross section can be obtained. As in the PWIA case, the derivation of the DWIA cross section is beyond the scope of this dissertation, but a detailed derivation can be found in Ref. [22]. The result of the calculation gives the DWIA ($e, e'p$) differential cross section as

$$\frac{d^6\sigma}{d\Omega'dE'd\Omega_p dE_p} = K \left(\frac{d\sigma_p}{d\Omega_e} \right) S_D(\vec{\mathbf{p}}_m, \vec{\mathbf{p}}', E_m). \quad (3.49)$$

The result is analogous to the PWIA result, except the spectral function gains dependence on the momentum of the final state hadron. The DWIA spectral function is referred to as the *distorted spectral function*, and is given by[22]

$$S_D(\vec{\mathbf{p}}, \vec{\mathbf{p}}', E) = \int d^3\vec{\mathbf{p}} |\chi^{(-)*}(\vec{\mathbf{p}}_r, \vec{\mathbf{p}}_r)| S(\vec{\mathbf{p}}, E), \quad (3.50)$$

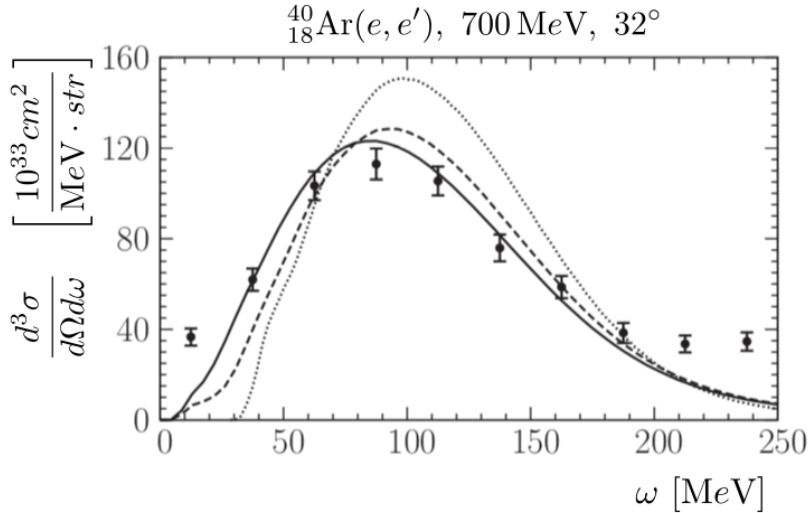


Figure 14: Plot showing the effects of the distorting optical potential on the inclusive cross section: the dotted line represents the cross section without FSI, the dashed line with the imaginary part of the potential applied, and the solid line with full FSI corrections applied[23]. The data (circles) represent the existing LNF Ar(e, e') data.

where $\chi^{(-)}(\vec{\mathbf{p}}', \vec{\mathbf{p}}'')$ is the momentum space wavefunction of the distorted final hadronic state. The distorted wavefunction $\chi^{(-)}$ in Eq. 3.50 is a function of the *relative momentum* of the outgoing proton and residual nucleus in the final and intermediate state, as defined and described in Ref. [22].

In the E12-14-012 exclusive data analysis, final state interactions were modeled by a phenomenological optical potential, which was obtained using a global fit to over 200 data sets using elastic proton-nucleus scattering over a broad range of nuclei, from helium to lead, in an energy range up to 1,040 MeV[24] (see §6.2).

3.5.4 The Spectral Function

The nucleon spectral function $S_N(\vec{\mathbf{p}}, E)$ gives the probability of finding a nucleon N with momentum $\vec{\mathbf{p}}$ and separation energy (missing energy) E in the ground state of the target nucleus. The total spectral function for a nucleus of mass number A is the sum over the individual nucleon spectral functions,

$$S(\vec{\mathbf{p}}, E) = \sum_{i=1}^A S_i(\vec{\mathbf{p}}, E). \quad (3.51)$$

There are two common normalization conventions for the nucleon spectral functions. The primary convention normalizes the spectral functions as

$$\iint dE d^3\vec{\mathbf{p}} S_p(\vec{\mathbf{p}}, E) = \frac{Z}{A} \quad (3.52a)$$

$$\iint dE d^3\vec{\mathbf{p}} S_n(\vec{\mathbf{p}}, E) = \frac{A - Z}{A} \quad (3.52b)$$

for protons and neutrons, respectively. In this convention, the total spectral function for the nucleus integrates to unity. Another common normalization convention normalizes S_p to Z and S_n to $A - Z$, respectively. In this case, the total spectral function is normalized to the mass number A .

Integrating the spectral function over the missing energy gives the nucleon momentum distribution,

$$n_N(\vec{\mathbf{p}}) = \int dE S_N(\vec{\mathbf{p}}, E). \quad (3.53)$$

Similarly, integrating over the momentum gives the energy distribution

$$S_N(E) = \int d^3\vec{\mathbf{p}} S_N(\vec{\mathbf{p}}, E). \quad (3.54)$$

In the *Independent Particle Shell Model* (IPSM), a single particle state with quantum numbers $\alpha = \{n, l, j\}$ is described by a wavefunction $\psi_\alpha(\vec{\mathbf{x}})$ with energy E_α . The momentum space wavefunction is given by the Fourier transform

$$\phi_\alpha(\vec{\mathbf{p}}) = \int d^3\vec{\mathbf{x}} e^{i\vec{\mathbf{p}}\cdot\vec{\mathbf{x}}} \psi_\alpha(\vec{\mathbf{x}}). \quad (3.55)$$

Both sets of momentum- and configuration-space wavefunctions form a complete orthonormal set of functions, and can serve as a basis for expansion of the spectral function. The IPSM spectral function can be expanded as

$$S(\vec{\mathbf{p}}, E) = \sum_{\alpha} |\phi_\alpha(\vec{\mathbf{p}})|^2 \delta(E - E_\alpha), \quad (3.56)$$

where the sum is carried out over all occupied states α .

Energy states in the IPSM are sharply localized, and are accurately described by Dirac delta functions. However, the Fermi-motion of the nucleons and nucleon-nucleon correlations broaden the energy peaks in the PWIA spectral function. Consequently, the (energy) width of the shell model state α can no longer be accurately described by a delta function. The delta function is replaced with a general function $F_\alpha(E - E_\alpha)$ that accurately describes

the width of each state α . Thus, the more general PWIA spectral function is written as[8]

$$S(\vec{\mathbf{p}}, E) = \sum_{\alpha} Z_{\alpha} |\phi_{\alpha}(\vec{\mathbf{p}})|^2 F_{\alpha}(E - E_{\alpha}) \quad (3.57)$$

where $Z_{\alpha} < 1$ are the spectroscopic factors.

A majority of the bound nucleons, approximately 70% – 80%, can be described in the shell model as moving in a mean field (MF) potential due to the surrounding nucleons. The remaining nucleons interact and experience correlations. Considering this, it is natural to decompose the spectral function into a mean field part and a correlated part. Therefore, the full spectral function for a nucleon N is the sum of these two parts,

$$S_N(\vec{\mathbf{p}}, E) = S_N^{MF}(\vec{\mathbf{p}}, E) + S_N^{corr}(\vec{\mathbf{p}}, E) \quad (3.58)$$

The MF and correlated nucleon spectral functions are normalized to the fraction of nucleons that can be described by the relevant spectral function. That is,

$$\iint dE d^3\vec{\mathbf{p}} S_N^{MF}(\vec{\mathbf{p}}, E) = N_N^{MF} \quad (3.59)$$

for the mean field part, and

$$\iint dE d^3\vec{\mathbf{p}} S_N^{corr}(\vec{\mathbf{p}}, E) = N_N^{corr} \quad (3.60)$$

for the correlated part, where $N_N^{MF} + N_N^{corr} = Z$ for protons and $A - Z$ for neutrons. Integrating over the energy produces the corresponding mean field and correlated momentum distributions, $n_N^{MF}(\vec{\mathbf{p}})$ and $n_N^{corr}(\vec{\mathbf{p}})$.

The mean field spectral function is essentially a generalization of the IPSM spectral function. In the absence of nucleon-nucleon correlations, the mean field spectral function collapses to that of the IPSM. That is, all spectroscopic factors become unity, and the function F_{α} describing the level width reduces to the Dirac δ -function. Assuming that each state α contributes equally allows the following substitution to be made in the mean field spectral function[23],

$$Z_{\alpha} |\phi_{\alpha}(\vec{\mathbf{p}})|^2 \rightarrow n_N^{MF}(\vec{\mathbf{p}}). \quad (3.61)$$

The mean field momentum distribution can now be taken out of the summation over α in Eq. 3.57, leaving the following expression for the mean field spectral function,

$$S_N^{MF}(\vec{\mathbf{p}}, E) = n_N^{MF}(\vec{\mathbf{p}}) \sum_{\alpha} F_{\alpha}(E_{\alpha} - E). \quad (3.62)$$

The function $F_\alpha(E_\alpha - E)$ is often assumed to be Gaussian, but it can also be obtained via empirical fit to data.

There are multiple methods used to obtain a theoretical expression for the correlated part of the spectral function. Realistic models of the correlated spectral function have been obtained by Ref. [21] from the *local density approximation* (LDA) in uniform nuclear matter[24]. These LDA models use experimental ($e, e'p$) data to refine how the shell model structure is considered theoretically.

Other theoretical models have been developed by considering a single high-momentum correlated nucleon-nucleon pair, moving in a field of low momentum nucleons (see Ref. [25]). Following the analysis of Ref. [25] and Ref. [23], an analytical expression for the correlated spectral function is

$$S_N^{corr}(\vec{\mathbf{p}}, E) = n_N^{corr}(\vec{\mathbf{p}}) \frac{2M}{|\vec{\mathbf{p}}|} \sqrt{\gamma\pi} \left[e^{-\gamma|\vec{\mathbf{p}}_{min}|^2} - e^{-\gamma|\vec{\mathbf{p}}_{max}|^2} \right]. \quad (3.63)$$

Definitions of the constant γ and the vector-magnitudes $|\vec{\mathbf{p}}_{min}|$ and $|\vec{\mathbf{p}}_{max}|$ can be found in §B.5, and the references cited previously. The energy dependence of Eq. 3.63 is contained in the argument of the exponential function.

It is important to be able to obtain a model of the spectral function from theoretical calculations to use in the analysis of the experimental data. It is apparent from Eq. 3.62 and Eq. 3.63 that determination of the mean-field and correlated spectral functions can be reduced to modeling the mean-field and correlated momentum distributions and the shapes of the shell-model states.

Theoretical models of the spectral function are often weighted by the square of the momentum, $S'(\vec{\mathbf{p}}, E) = |\vec{\mathbf{p}}|^2 S(\vec{\mathbf{p}}, E)$. This is useful in many situations as the spectral function often appears under an integral with the square of the momentum from the Jacobian. It also allows the energy and momentum distributions to be modeled by line-shapes that vanish as E_{miss} and $|\vec{\mathbf{p}}_{miss}|$ approach zero.

The weighted missing momentum distributions for argon and titanium used in the E12-14-012 analysis are shown in Fig. 15. The momentum distributions were compared, using different wave functions ϕ_α to calculate the spectral function, and found little difference between them. Comparison between the weighted missing momentum distributions for argon and titanium also shows little difference between them, which suggests that nuclear effects in argon and titanium are similar[24].

The models of the argon and titanium mean-field spectral functions used in the E12-14-012 analysis contain contributions from the $1s_{1/2}$, $1p_{3/2}$, $1p_{1/2}$,

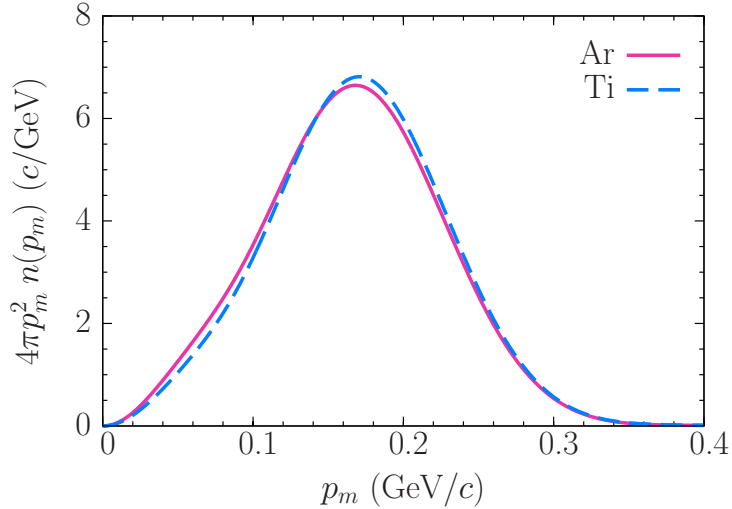


Figure 15: Weighted proton missing momentum distributions for argon and titanium used in the E12-14-012 analysis[24].

$1d_{5/2}$, $2s_{1/2}$, and $1d_{3/2}$ shells. The titanium model contains an additional contribution from the $1f_{7/2}$ shell. Each shell α is described by the Gaussian distribution

$$F_\alpha(E - E_\alpha) = \frac{1}{\sqrt{2\pi}\sigma_\alpha} e^{-\frac{(E-E_\alpha)^2}{2\sigma_\alpha^2}} \quad (3.64)$$

where σ_α is a parameter that describes the width of the shell. The parametrization of the missing energy distributions of the argon and titanium shell-model states used in Eq. 3.64 are shown in Tab. 1. Plots of the missing energy distributions, showing the contributions from each shell, are shown in Fig. 16. Later in the analysis, other line-shapes were considered to more accurately model the width of certain shells. For example, the Maxwell-Boltzmann distribution function, given by

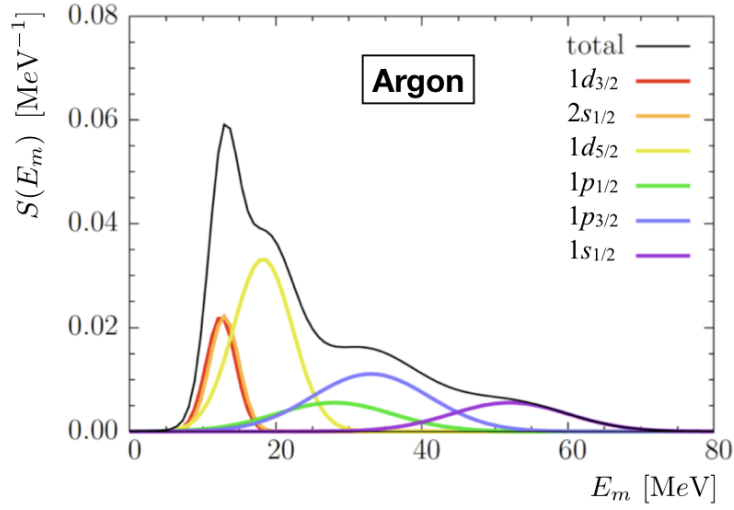
$$F_\alpha(E - E_\alpha) = \frac{4}{\sqrt{\pi}\sigma_\alpha} \left(\frac{E - E_\alpha + \sigma_\alpha}{\sigma_\alpha} \right)^2 e^{-\left(\frac{E-E_\alpha+\sigma_\alpha}{\sigma_\alpha}\right)^2} \quad (3.65)$$

with the normalization convention of

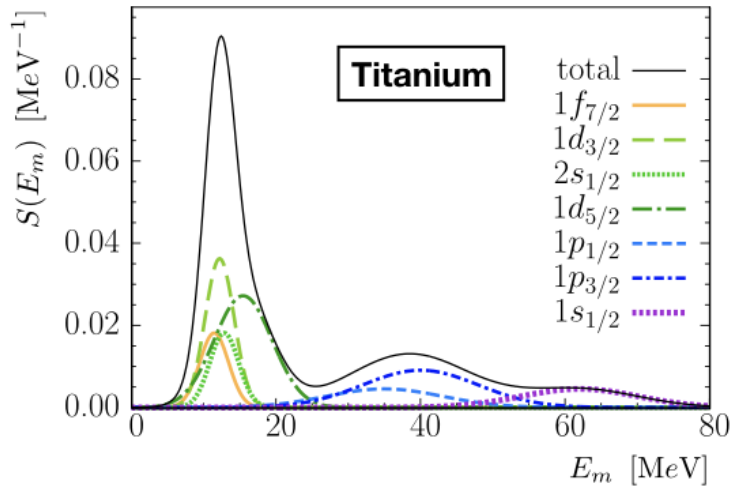
$$\int_{E_\alpha - \sigma_\alpha}^{\infty} dE F_\alpha(E - E_\alpha) = 1. \quad (3.66)$$

was used to parameterize the $1d_{3/2}$, $2s_{1/2}$, and $1d_{5/2}$ shells.

For the numerical and experimental analysis, the missing momentum and missing energy are discretized into a phase space grid, with pieces of size Δp_i



(a)



(b)

Figure 16: Proton missing energy distributions showing individual shell contributions for (a) argon and (b) titanium. Figures modified from Ref. [24].

α	E_α	σ_α	E_{low}^α	E_{high}^α
argon				
$1d_{3/2}$	12.53	2	8	14
$2s_{1/2}$	12.93	2	8	14
$1d_{5/2}$	18.23	4	14	20
$1p_{1/2}$	28.0	8	20	45
$1p_{3/2}$	33.0	8	20	45
$1s_{1/2}$	52.0	8	45	70
titanium				
$1f_{7/2}$	11.45	2	8	14
$2s_{1/2}$	12.21	2	14	30
$1d_{3/2}$	12.84	2	14	30
$1d_{5/2}$	15.46	4	14	30
$1p_{1/2}$	35.0	8	30	54
$1p_{3/2}$	40.0	8	30	54
$1s_{1/2}$	62.0	8	53	80

Table 1: Parametrization of the missing energy distributions of the shell-model states in argon and titanium used in Eq. 3.64. All energies are in units of MeV[24].

and ΔE_j respectively. The model spectral functions must also be discretized on this grid, and are normalized to unity by

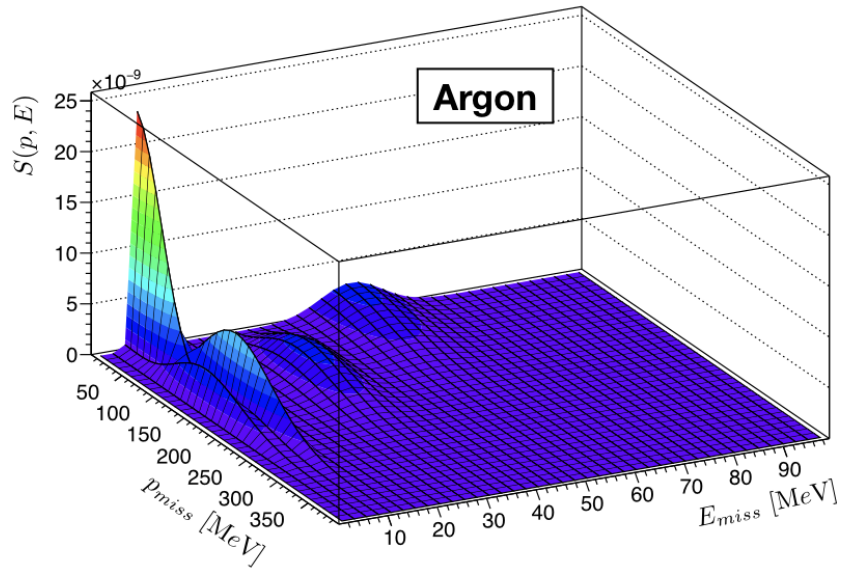
$$4\pi \sum_{ij} [p_i^2 S(p_i, E_j)] \Delta p_i \Delta E_j = 1. \quad (3.67)$$

The discrete spectral functions for argon and titanium used in the E12-14-012 analysis are plotted in Fig. 17, along with their weighted counter-parts in Fig. 18.

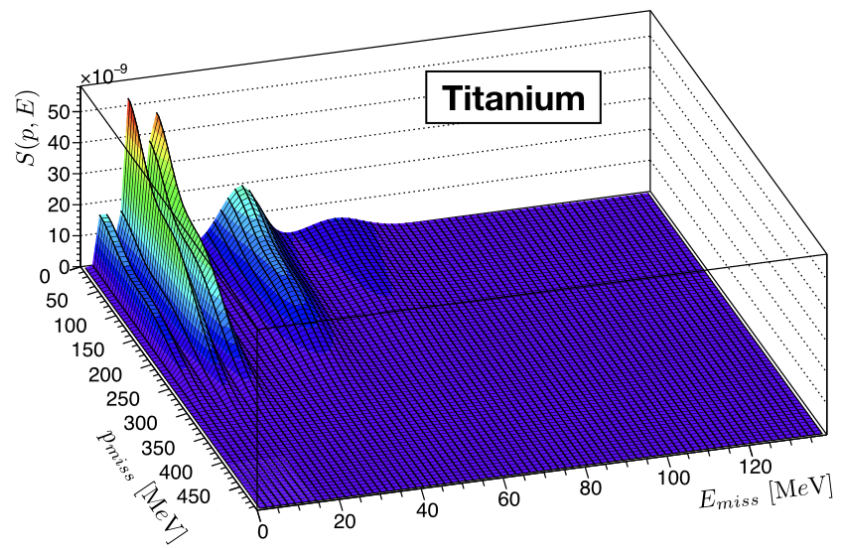
3.6 Scaling in (e, e') Cross Sections

Scaling is a phenomenon of inclusive scattering that connects inclusive data corresponding to different kinematics and different targets. The phenomenon of scaling was first observed in inclusive deep inelastic electron scattering experiments. These experiments showed that the structure functions present in the cross section to become functions of a single variable

$$x_B = \frac{Q^2}{2M\omega} \quad (3.68)$$

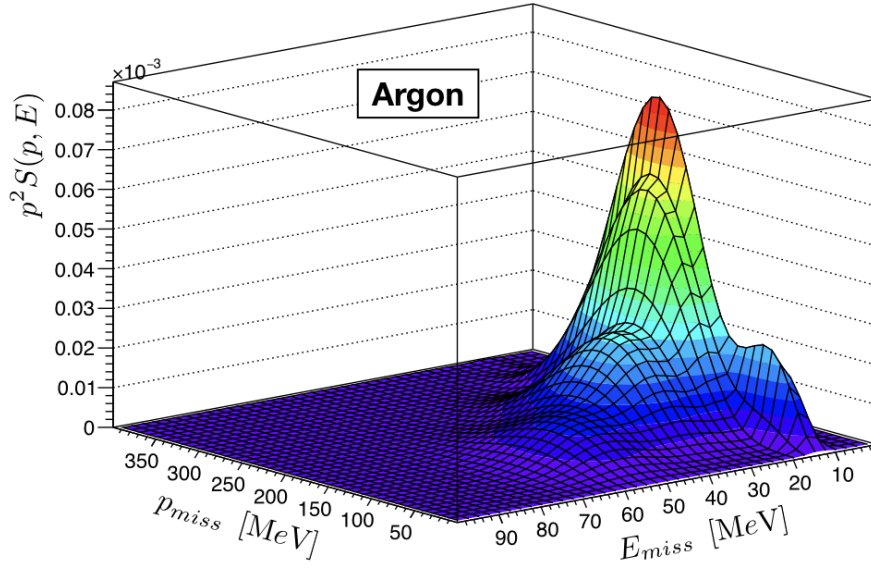


(a)

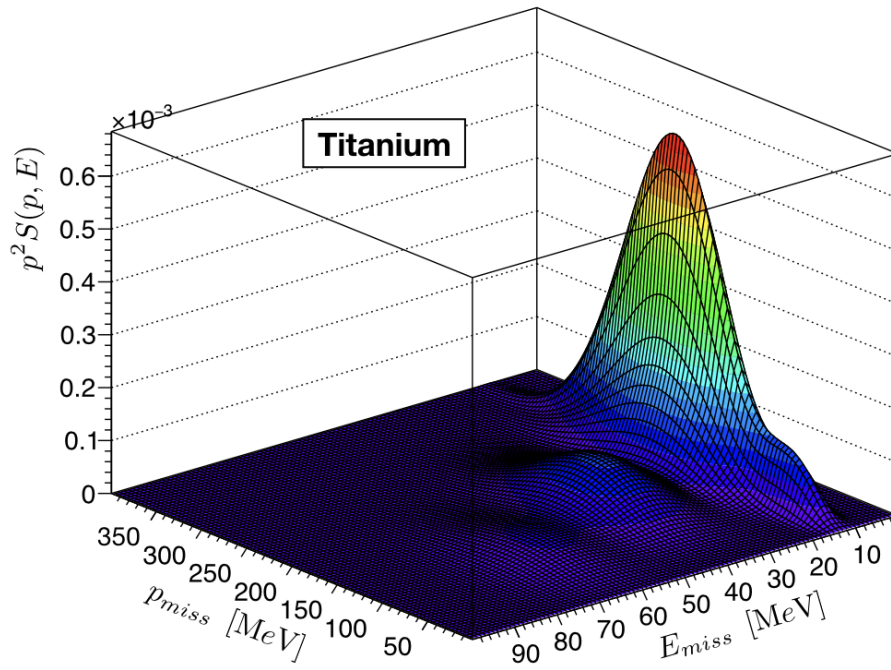


(b)

Figure 17: Surface plots of the (a) argon and (b) titanium model spectral functions used in the E12-14-012 analysis.



(a)



(b)

Figure 18: Surface plots of the weighted model spectral function for (a) argon and (b) titanium used in the E12-14-012 analysis.

known as *Bjorken-x*. Recall that in deep inelastic scattering, the particle probe scatters off of the individual bound quarks. In this case, x_B can be interpreted physically as the fraction of the nucleon four-momentum carried by the struck quark.

Bjorken scaling manifests in the general structure functions $W_{1,2}(Q^2, \omega)$ of the inclusive differential cross section. If the tensor contraction $L^{\mu\nu}W_{\mu\nu}$ of Eq. 3.17 is carried out using Eq. 3.9 for the leptonic tensor and Eq. 3.35 for the response tensor, then the cross section can be written as

$$\frac{d^3\sigma}{d\Omega'dE'} = \frac{4\alpha^2}{Q^4} E'^2 \cos^2 \frac{\theta}{2} \left[W_2(Q^2, \omega) + 2W_1(Q^2, \omega) \tan^2 \frac{\theta}{2} \right]. \quad (3.69)$$

The term outside of the square-brackets is the Mott cross section (Eq. B.8).

If Q^2 and ω are taken to infinity in such a way that their ratio is constant, the structure functions display the following behavior[26],

$$\lim_{Q^2, \omega \rightarrow \infty} \omega W_2(Q^2, \omega) \longrightarrow F_2(x_B), \quad (3.70a)$$

$$\lim_{Q^2, \omega \rightarrow \infty} MW_1(Q^2, \omega) \longrightarrow F_1(x_B). \quad (3.70b)$$

In this kinematic regime, the structure functions become functions of the *ratio* of Q^2 and ω . Scaling of the structure functions in x_B is interpreted as a signature that deep inelastic scattering processes are the dominant ones[27].

The phenomenon of scaling is also present in the cross sections for inclusive quasi-elastic electron-nucleus scattering. Inclusive cross sections generally are functions of two independent variables ω and $|\vec{\mathbf{q}}|$. However, for energy transfers in the region of quasi-elastic scattering, the inclusive cross sections have been shown both experimentally and theoretically to depend (approximately) on a single variable $y = y(\omega, |\vec{\mathbf{q}}|)$, known as the *scaling variable*. In this context, the reduction to dependence on a single variable y is called *y-scaling*, or *scaling of the first kind*.

The scaling variable can be calculated from the energy-balance equation for quasi-elastic scattering from a bound nucleon of mass M and momentum $\vec{\mathbf{p}}$. Energy conservation gives

$$\omega = \sqrt{(\vec{\mathbf{p}} + \vec{\mathbf{q}})^2 + M^2} - M + E + E_{rec}, \quad (3.71)$$

where E is the removal energy and $E_{rec} = \vec{\mathbf{p}}^2/2M_{A-1}$ is the energy of the recoiling nucleus. The nucleon momentum can be split into components parallel and perpendicular to the three-momentum transfer as $\vec{\mathbf{p}} = \vec{\mathbf{p}}_{\parallel} + \vec{\mathbf{p}}_{\perp}$. It is possible to take $\omega, |\vec{\mathbf{q}}| \rightarrow \infty$ in such a way that the removal and recoil energy terms in Eq. 3.71, as well as the square of the perpendicular momentum

component, can all be ignored[21]. Eliminating these terms in the energy conservation equation gives

$$|\vec{\mathbf{p}}_{\parallel}|^2 + 2|\vec{\mathbf{q}}| \cdot |\vec{\mathbf{p}}_{\parallel}| + (|\vec{\mathbf{q}}|^2 - \omega^2 - 2M\omega) = 0, \quad (3.72)$$

a quadratic equation in $|\vec{\mathbf{p}}_{\parallel}|$, with solution

$$|\vec{\mathbf{p}}_{\parallel}| = \sqrt{\omega^2 + 2M\omega} - |\vec{\mathbf{q}}|. \quad (3.73)$$

This means that the parallel momentum component becomes a function of the energy and momentum transfers only, $|\vec{\mathbf{p}}_{\parallel}| = y(\vec{\mathbf{q}}, \omega)$, and that ω and $|\vec{\mathbf{q}}|$ are no longer independent variables[21]. They are related by the parallel component of the nucleon momentum, denoted y , and hence defined as

$$y(\vec{\mathbf{q}}, \omega) = \frac{\vec{\mathbf{p}} \cdot \vec{\mathbf{q}}}{|\vec{\mathbf{q}}|}. \quad (3.74)$$

Under the appropriate conditions, the quasi-elastic cross sections can be written as a product of the elementary electron-nucleon cross section σ_{eN} , a kinematic factor, and a function $F(y)$ [28]. This function $F(y)$ is known as the *scaling function*. Scaling of the inclusive cross sections occurs for $y < 0$. The presence of y -scaling is a signature that the primary reaction mechanism is quasi-elastic single nucleon knockout, as other processes such as Δ -production will not scale in y [29]. The scaling function is derived in PWIA in §3.6.1.

If the typical momentum scale of the nucleus under consideration is incorporated into the definition of the scaling variable, and the response is also scaled by this momentum, then the data is seen to exhibit a new type of scaling behavior[30]. Taking the typical momentum scale to be the nuclear *Fermi momentum* p_F ; if the new scaling variable and function are defined as

$$\psi = \frac{y}{p_F} \quad (3.75a)$$

$$F(\psi) = p_F \cdot F(y/p_F), \quad (3.75b)$$

then a naive version of a phenomenon called *scaling of the second kind*, or ψ -*scaling*, is obtained. If the data exhibits scaling in both y and ψ , the scaling is called *superscaling*. Superscaling can be used to interpolate between existing data on $F(y)$ to theoretically predict the scaling function for nuclei not investigated experimentally[21]. Scaling of the second kind is further discussed in §3.6.2.

3.6.1 y -Scaling in PWIA

The concept of y -scaling of inclusive cross sections was introduced previously in §3.6. The derivation of the scaling function is computationally tedious, but will be outlined in the following. A full detailed derivation of the scaling function, including definitions of terms not defined in this dissertation, can be found in Refs. [28, 31].

The scaling function can also be extracted from an exclusive cross section in the impulse approximation by integrating over the proton four-momentum. For a nucleus of mass number A , the inclusive cross section can be written as a sum over the individual PWIA nucleon cross sections as[28]

$$\frac{d^3\sigma}{d\Omega' dE'} = \sum_{i=1}^A \iint d^3\vec{\mathbf{p}} dE \sigma_{ei} S_i(\vec{\mathbf{p}}, E) \times \delta\left(\omega + M_A - \sqrt{M^2 + |\vec{\mathbf{p}} + \vec{\mathbf{q}}|^2} - \sqrt{M^{*2} + |\vec{\mathbf{p}}|^2}\right). \quad (3.76)$$

The derivation of the scaling function requires many approximations and assumptions. First, assume that the spectral function is isospin independent, that is, independent of nucleon type. Thus, the substitution $S_i(\vec{\mathbf{p}}, E) \rightarrow S(\vec{\mathbf{p}}, E)$ can be made in Eq. 3.76.

It is useful to define an energy parameter $\mathcal{E}(\vec{\mathbf{p}})$ which characterizes the degree of excitation of the $(A - 1)$ nuclear system. This parameter is defined in Eq. B.11 as the difference between the excited-state and ground-state energies. The energy of the struck nucleon, defined in Eq. B.12, can be written as a function of this energy parameter, $E = E(\vec{\mathbf{p}}, \mathcal{E})$. Define a new quantity Ω that simplifies the argument of the delta function in Eq. 3.76 to $\omega - \Omega$. Visual inspection of the definition of Ω in Eq. B.13 reveals that it is a function of \mathcal{E} , $\vec{\mathbf{p}}$, $\vec{\mathbf{q}}$, and $\cos\theta_{pq}$, where θ_{pq} is the angle between the vectors.

With these new definitions, it is possible to make the change of variables $E \rightarrow \mathcal{E}$ and $\theta_{pq} \rightarrow \cos\theta_{pq}$, and carry out the angular integrals in Eq. 3.76. The only ϕ_{pq} dependence is found in the single-nucleon cross sections σ_{ei} , so the azimuthal integral is absorbed into the quantity

$$\bar{\sigma}_{ei} = \frac{1}{2\pi} \int_0^{2\pi} d\phi_{pq} \sigma_{ei}. \quad (3.77)$$

The dependence on the polar angle θ_{pq} in Eq. 3.76 is contained in the argument of the delta function. The θ_{pq} -integration is carried out using Eq. A.3 and the change of variables $\cos\theta_{pq} \rightarrow \Omega(\vec{\mathbf{p}}, \vec{\mathbf{q}}, \cos\theta_{pq}, \mathcal{E})$. After the angular integrations are carried out, the inclusive cross section is written as

$$\frac{d^3\sigma}{d\Omega' dE'} = 2\pi \sum_{i=1}^A \int_{-y}^Y d\vec{\mathbf{p}} |\vec{\mathbf{p}}|^2 \int_0^{\mathcal{E}_M} d\mathcal{E} \bar{\sigma}_{ei} S(\vec{\mathbf{p}}, \mathcal{E}) \left| \frac{\partial\Omega}{\partial \cos\theta_{pq}} \right|_{(\Omega=\omega)}^{-1}. \quad (3.78)$$

Explicit expressions for the limits of integration over $|\vec{\mathbf{p}}|$ and \mathcal{E} can be found in §B.4, and derivations of the same in Ref. [28]. Calculation of the term $|\partial\Omega/\partial\cos\theta_{pq}|^{-1}$ absorbs one factor of $|\vec{\mathbf{p}}|$ in Eq. 3.78, and is replaced by a kinematical factor K (see Eq. B.15).

The assumption of iso-spin independence allows the spectral function to be taken outside of the summation in Eq. 3.78, giving

$$\frac{d^3\sigma}{d\Omega'dE'} = 2\pi \int_{-y}^Y d\vec{\mathbf{p}} |\vec{\mathbf{p}}| \int_0^{\mathcal{E}_M} d\mathcal{E} S(\vec{\mathbf{p}}, \mathcal{E}) \tilde{\sigma}_e(\vec{\mathbf{q}}, y; |\vec{\mathbf{p}}|, \mathcal{E}), \quad (3.79)$$

for the inclusive cross section. The kinematical factor and summation in Eq. 3.78 have been absorbed into the term $\tilde{\sigma}_e$, defined as

$$\tilde{\sigma}_e(\vec{\mathbf{q}}, y; |\vec{\mathbf{p}}|, \mathcal{E}) = K \sum_{i=1}^A \bar{\sigma}_{ei}(\vec{\mathbf{q}}, y; |\vec{\mathbf{p}}|, \mathcal{E}). \quad (3.80)$$

The next major approximation is that

$$\tilde{\sigma}_e(\vec{\mathbf{q}}, y; |\vec{\mathbf{p}}|, \mathcal{E}) \approx \tilde{\sigma}_e(\vec{\mathbf{q}}, y; |\vec{\mathbf{p}}| = -y, \mathcal{E} = 0). \quad (3.81)$$

That is, $\tilde{\sigma}_e$ at arbitrary $|\vec{\mathbf{p}}|$ and \mathcal{E} does not differ appreciably from itself evaluated at the specific kinematics $|\vec{\mathbf{p}}| = -y$ and $\mathcal{E} = 0$. In other words, $\tilde{\sigma}_e$ is assumed to be constant with respect to $|\vec{\mathbf{p}}|$ and \mathcal{E} , and can hence be taken outside of the integral in Eq. 3.79. This approximation is justified in Ref. [28].

After this last approximation, the inclusive cross section is written as

$$\frac{d^3\sigma}{d\Omega'dE'} = \tilde{\sigma}_e(\vec{\mathbf{q}}, y; |\vec{\mathbf{p}}| = -y, \mathcal{E} = 0) \cdot F(\vec{\mathbf{q}}, y), \quad (3.82)$$

where the function $F(\vec{\mathbf{q}}, y)$ is defined as

$$F(\vec{\mathbf{q}}, y) = 2\pi \int_{-y}^Y d\vec{\mathbf{p}} |\vec{\mathbf{p}}| \left(\int_0^{\mathcal{E}_M} d\mathcal{E} S(\vec{\mathbf{p}}, \mathcal{E}) \right). \quad (3.83)$$

For sufficiently large $|\vec{\mathbf{q}}|$, the function $F(\vec{\mathbf{q}}, y)$ has been shown to reduce to a function of y only. The upper limit $Y = Y(\vec{\mathbf{q}}, \omega)$, defined in Eq. B.16b, increases quickly as a function of increasing $|\vec{\mathbf{q}}|$ for fixed y . Thus, the approximation $Y \rightarrow \infty$ can be made, and is valid even for large but finite values of $|\vec{\mathbf{q}}|$ [28].

When evaluated for $|\vec{\mathbf{q}}| \rightarrow \infty$, and $Y \rightarrow \infty$, the function is known as the *scaling function*, and is defined as

$$F(y) \equiv F(\infty, y). \quad (3.84)$$

The scaling function is determined by the target spectral function, and is mostly independent of kinematics[32].

If the upper limit of integration \mathcal{E}_M in Eq. 3.83 is taken to infinity, the \mathcal{E} -integral over the spectral function becomes

$$n(\vec{\mathbf{p}}) = \int_0^\infty d\mathcal{E} S(\vec{\mathbf{p}}, \mathcal{E}), \quad (3.85)$$

the momentum distribution, and $F(y)$ becomes $f(y)$, the probability to find a nucleon with parallel-momentum component $|\vec{\mathbf{p}}_{\parallel}| = y$ in the nucleus[28]

$$f(y) = 2\pi \int_{|y|}^\infty d\vec{\mathbf{p}} |\vec{\mathbf{p}}| n(\vec{\mathbf{p}}), \quad (3.86)$$

also known as the *longitudinal momentum distribution*. Conversely, the full momentum distribution can be obtained from the longitudinal distribution via differentiation as

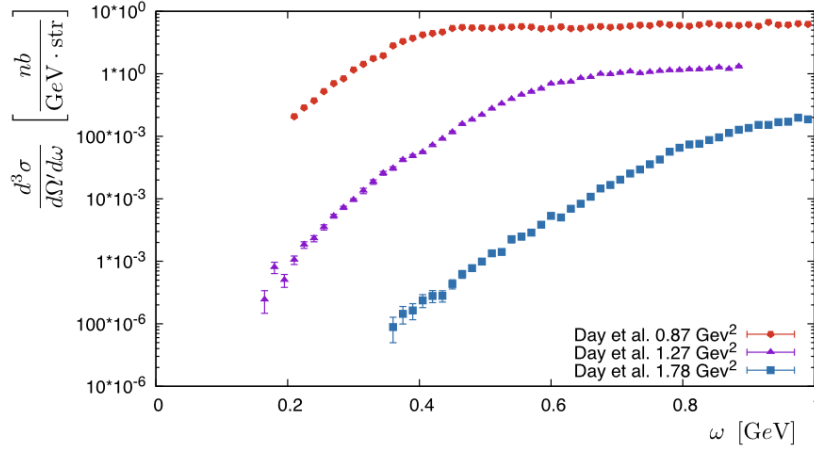
$$n(\vec{\mathbf{p}}) = \frac{1}{2\pi y} \frac{df(y)}{dy}. \quad (3.87)$$

The longitudinal momentum distribution $f(y)$ can be obtained from the scaling function $F(y)$ through $f(y) = F(y) + B(y)$, where $B(y)$ is the *binding correction*, defined in Ref. [33] in terms of the correlated part of the spectral function.

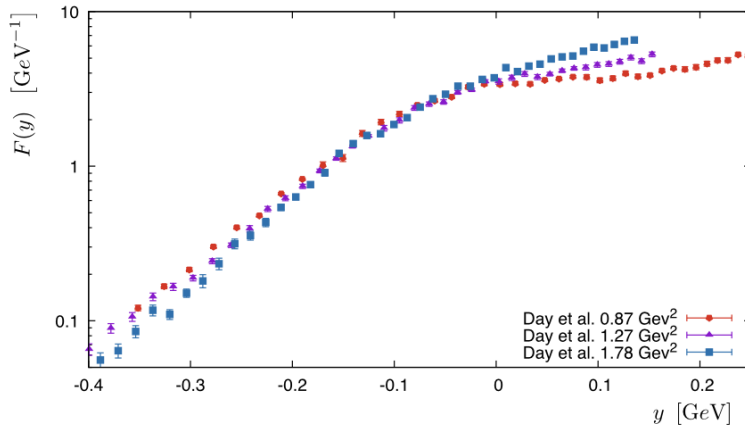
The true power of y -scaling can be seen by examining the plots in Fig. 19. Inclusive cross sections for aluminum at three values of Q^2 are shown in Fig. 19a. At their most extreme, the cross sections differ by over four orders of magnitude. However, once the y -scaling analysis is applied to the cross sections, the data collapse onto nearly a single line, as shown in Fig. 19b. The scaling function can be used to predict the quasi-elastic response of a nucleus by interpolating between existing data collected at specific values of Q^2 . As discussed in §3.6, the data (mostly) scale for $y < 0$, but the presence of non-quasi-elastic processes breaks the scaling for $y > 0$.

3.6.2 ψ -Scaling in RFG

The phenomenon of scaling has been analyzed theoretically in the *Relativistic Fermi Gas* (RFG) approximation[35]. Analysis of inclusive electron-nucleus scattering in the RFG model avoids the complications of describing the off-shell dynamics of the struck nucleon inherent in PWIA, while keeping the description of the scattering fully relativistic.



(a)



(b)

Figure 19: Plots of (a) the inclusive cross sections, and (b) the y -scaling functions for aluminum from D. Day *et al.*[34], showing the effect of scaling on the cross section. Data covering nearly five orders of magnitude collapse onto nearly a single line.

In the approximation that the ground state momentum distribution is given by a Heaviside step-function (Θ -function), the inclusive differential cross section can be written as[35]

$$\frac{d^3\sigma}{d\Omega'dE'} = \frac{\mathcal{N}}{4M\kappa}\sigma_M X(\theta, \tau, \psi, \eta_F)F(\psi), \quad (3.88)$$

where \mathcal{N} is the number of particles ($\mathcal{N} = Z$ for protons, and $\mathcal{N} = A - Z$ for neutrons), and σ_M is the familiar Mott cross section (Eq. B.8). The analysis is done in terms of the dimensionless kinematic variables, $\lambda = \omega/2M$, $\kappa = |\vec{q}|/2M$, and $\tau = Q^2/4M^2 = \kappa^2 - \lambda^2$. The dimensionless *Fermi momentum* and *Fermi energy* are respectively defined as $\eta_F = p_F/M$ and $\varepsilon_F = \sqrt{1 + \eta_F^2}$, respectively. The function $X(\theta, \tau, \psi, \eta_F)$ is defined in Ref. [35]. The remaining function $F(\psi)$ is the scaling function, which depends only on the dimensionless scaling variable ψ .

In the (non-Pauli blocked) kinematic regime such that $\kappa > \eta_F$ ($|\vec{q}| > 2p_F$), the dimensionless scaling variable is defined by[35]

$$\psi = \sqrt{\frac{\gamma_- - 1}{\varepsilon_F - 1}} \quad (3.89)$$

where $\gamma_- = \kappa\sqrt{1 + \tau^{-1}} - \lambda$. In the step-function approximation, the RFG scaling function is given by

$$F(\psi) = \frac{3}{4}(1 - \psi^2)\Theta(1 - \psi^2), \quad (3.90)$$

which is independent of p_F up to first order[36].

To bridge the gap between the PWIA and RFG descriptions, Donnelly and Sick in Ref. [36] have defined a scaling function in the RFG, inspired by the PWIA scaling function defined in Eq. 3.82. The new scaling function is defined as

$$F(\kappa, \psi) = \frac{d^3\sigma/d\Omega d\omega}{\sigma_M [v_L G_L(\kappa, \lambda) + v_T G_T(\kappa, \lambda)]} \quad (3.91)$$

where $v_{L,T}$ are the *lepton kinematical factors* and $G_{L,T}$ are the longitudinal and transverse (on-shell) *single-nucleon responses*, as defined in Ref. [36]. In this case, the dimensionless scaling variable ψ is written as

$$\psi = \frac{1}{\sqrt{\varepsilon_F - 1}} \frac{\lambda - \tau}{\sqrt{(1 + \lambda)\tau + \kappa\sqrt{\tau(1 + \tau)}}}, \quad (3.92)$$

which is equivalent to the expression of Eq. 3.89[37]. As in the PWIA analysis (Eq. 3.84), the *scaling function of the second kind* is defined by Eq. 3.91 in the limit that $\kappa \rightarrow \infty$,

$$F(\psi) \equiv F(\infty, \psi). \quad (3.93)$$

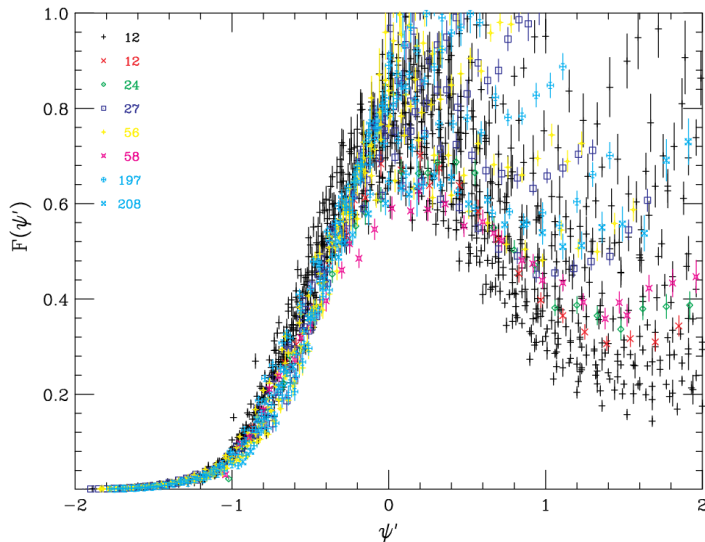


Figure 20: Plot of the scaling function of the second kind $F(\psi')$ for several nuclei ($A \geq 12$) extracted from experimental data[38].

If the energy transfer is shifted by an empirically determined amount E_s , and the following substitutions $\omega \rightarrow \omega' = \omega - E_s$, $\lambda \rightarrow \lambda'$, $\tau \rightarrow \tau'$ are made in Eq. 3.92, then a new scaling variable ψ' is defined. The scaling in ψ' is nearly identical to the scaling in the naive variable defined in Eq. 3.75a, and in some conditions they can be used interchangeably[38]. A plot of the scaling function of the second kind $F(\psi')$ extracted from experimental data for $A \geq 12$ is shown in Fig. 20[38]. Scaling is observed in the region $\psi' < 0$, but is violated for $\psi' > 0$.

3.7 Radiative Corrections

The treatment of radiative corrections to the cross sections is a crucial part of the theoretical analysis of electron scattering. There are multiple kinds of radiation effects that must be accounted for. Some of these effects arise from fundamental physics, and others are caused by the experimental apparatus and target material used. Many authors have published comprehensive theoretical treatments of radiative corrections to electron-nucleon scattering, some of which can be found in Refs. [39, 40, 41, 42, 43, 44].

All charged particles emit electromagnetic radiation when subject to acceleration. This radiation, called *bremsstrahlung*, is one of the radiative processes that must be accounted for when calculating the cross section.

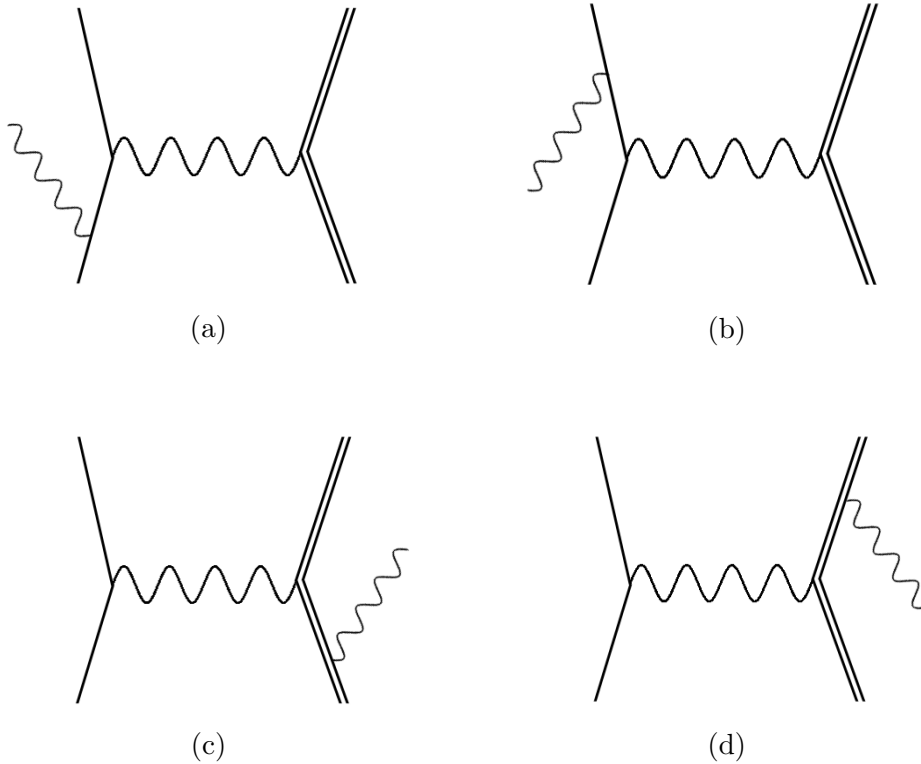


Figure 21: Feynman diagrams depicting bremsstrahlung (external wavy line) from the electron (a) before and (b) after the scattering. Also included are diagrams of hadronic bremsstrahlung (c) before and (d) after the scattering.

Bremsstrahlung can be emitted before and after the main scattering process by both leptonic and hadronic particles. Diagrams depicting these processes are shown in Fig. 21. The small mass of the electron makes it susceptible to accelerations, emitting bremsstrahlung radiation in the process. However, in some circumstances, bremsstrahlung from the heavier hadronic particles can be ignored.

Other radiative effects arise from $\mathcal{O}(\alpha)$ corrections to the cross section. These higher order diagrams include one-loop contributions to the fermion and photon propagators, known as self-energy corrections. The leptonic and hadronic self-energy diagrams are shown in Fig. 22. The virtual photon self-energy diagram, also known as the vacuum polarization, is shown in Fig. 24b. Also included are one-loop corrections to the interaction vertices, known as vertex corrections. The vertex correction diagrams are shown in Fig. 23. The last of the one-loop level corrections are the two-photon exchange diagrams,

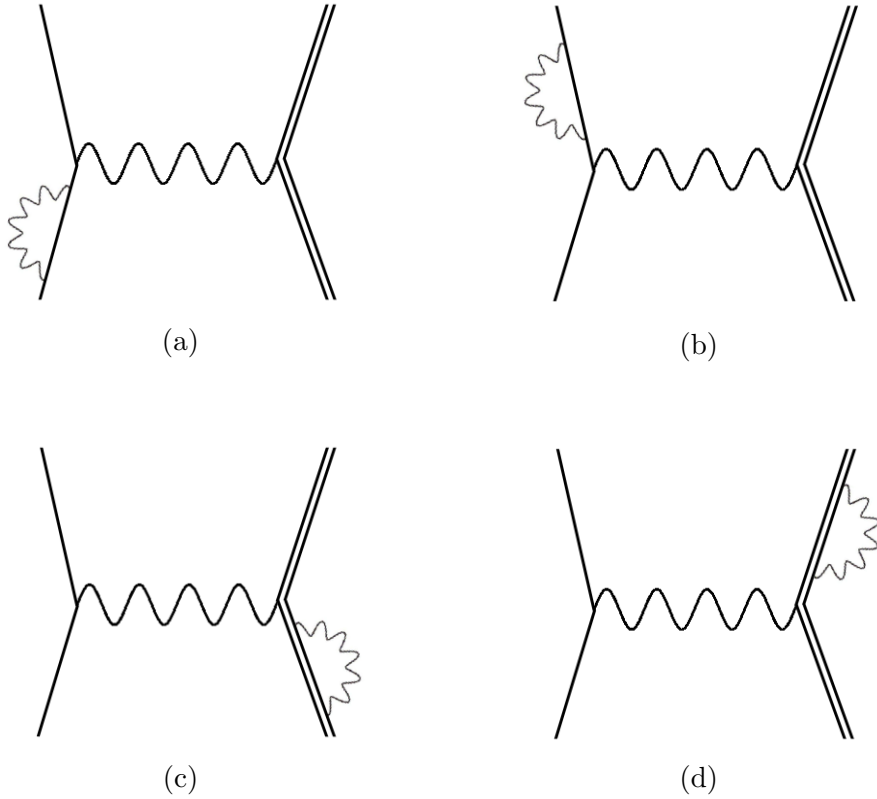


Figure 22: Feynman diagrams of the leptonic and hadronic self-energy correction. Diagrams (a) and (b) show the correction to the leptonic propagators (single-line). Diagrams (c) and (d) show the correction to the hadronic propagators (double line). Virtual photon propagators are represented by wavy lines.

one of which is shown in Fig. 24a.

Not all of these corrections are applied in this analysis. As the Born Approximation has been explicitly assumed throughout, the two-photon exchange corrections will be ignored. It is also assumed that hadronic bremsstrahlung and vertex corrections are negligible.

The $\mathcal{O}(\alpha)$ radiative corrections are incorporated into the Born cross section by a multiplicative factor of $(1 + \delta_S)$, where δ_S is the *Schwinger correction* defined in Eq. B.25. The Schwinger correction can be decomposed into individual components as $\delta_S = \delta_{\text{vac}} + \delta_{\text{ver}} + \delta_{\text{inf}} + \dots$, where δ_{vac} and δ_{ver} are the contributions from the vacuum polarization and vertex correction diagrams.

While the Schwinger correction is a straight-forward, albeit difficult, calculation in quantum electrodynamics, the most challenging part is determining the correction that should be applied due to the bremsstrahlung emitted

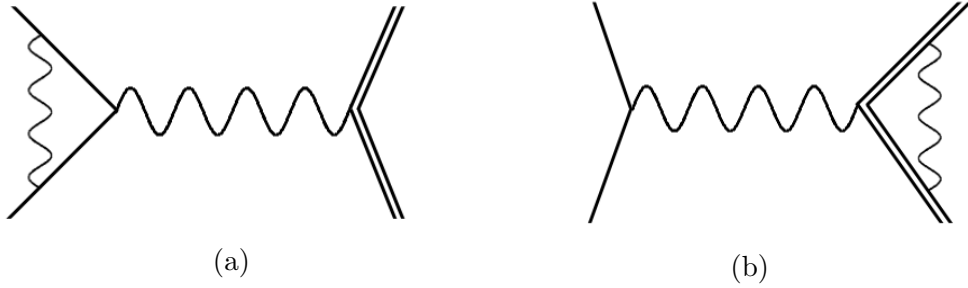


Figure 23: Feynman diagrams of the (a) leptonic and (b) hadronic vertex corrections. Wavy lines represent virtual photon propagators, while the solid single- and double-lines represent leptonic and hadronic propagators.

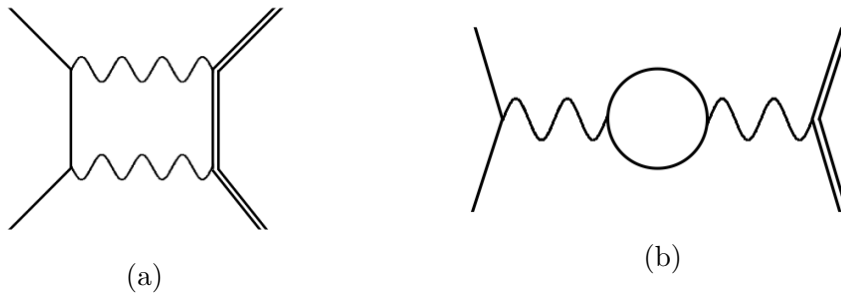


Figure 24: Additional one-loop correction diagrams depicting (a) the two photon exchange correction and (b) the vacuum polarization correction. Leptonic and hadronic propagators are represented by single and double lines respectively, while virtual photon propagators are represented by wavy lines.

by the electron as a result of its interaction with the target material. The effect of energy losses in the target material is to add a *radiative tail* to the cross section. These radiative tails are calculated using *peaking approximations*. The *energy peaking approximation* assumes that the infinite number of low energy photons emitted can be approximated by the emission of one high-energy photon. The *angular peaking approximation* assumes that this photon is emitted along either $\hat{\mathbf{k}}$ or $\hat{\mathbf{k}}'$, the direction of the initial or scattered electron.

The electron bremsstrahlung is characterized based on when the radiation was emitted during the scattering process. Bremsstrahlung emitted as the electron passes through the target medium *before* and *after* the scattering is called *external bremsstrahlung*. The bremsstrahlung emitted during the actual interaction (collision) is called *internal bremsstrahlung*. The effect of the internal bremsstrahlung can be approximated by two external radiators, one before and one after the scattering, each of thickness[42]

$$t_{i,f} = \frac{\alpha}{b\pi} \left(\log \frac{Q^2}{m^2} - 1 \right), \quad (3.94)$$

where $b = 4/3 + a$ is a number defined in §B.6. Let t_b and t_a be the thickness of the target, in units of radiation lengths X_0 [g/cm^2], traversed by the electron before and after the scattering. If these quantities obey the inequalities $t_b, t_a \gg t_b \cdot t_a$, the electron can be assumed to radiate in either t_b or t_a , but not both[39].

As the electron passes through the target material, it loses energy due to ionization of the medium and the external bremsstrahlung; a process called *straggling*. The probability of the electron losing energy Δ through straggling effects over a path of length t radiation lengths is given by a probability distribution $F(\Delta, t)$ called the *straggling function*, or the *energy loss distribution function*.

Let $v_i = v_i(E, E_1, t)$, for $i \in \{b, a\}$, be an equivalent radiator describing the hard-photon bremsstrahlung processes. Furthermore, let $w(E, E_1)$ be the probability of the electron to lose energy $E - E_1$ per unit-radiation length by emitting a single photon[41]. Then, the straggling function for $\Delta = E - E_1$ and $t = t_i$ is given by

$$F_i(E, E_1, t_i) = \frac{v_i}{E - E_1} + t_i w(E, E_1). \quad (3.95)$$

Expressions for the radiators $v_{b,a}$ and ionization probability $w(E, E_1)$ can be found in Ref. [41]. The quantity $t \neq t_i$ in the argument of v_i is an equivalent radiator, defined in Eq. B.26.

Combining all of the corrections discussed above, the experimentally measured cross section $d^3\sigma_{exp}/d\Omega'dE'$ is written in terms of the non-radiative, or corrected cross section $d^3\sigma/d\Omega'dE'$ as

$$\begin{aligned}
\frac{d^3\sigma_{exp}}{d\Omega'dE'}(E, E', \theta) &= \frac{d^3\sigma_{el,rad}}{d\Omega'dE'}(E, E', \theta) \\
&+ \frac{d^3\sigma}{d\Omega'dE'}(E, E', \theta) \left(\frac{\Delta E}{E}\right)^{\frac{t}{2}+bt_b} \left(\frac{\Delta E'}{E'}\right)^{\frac{t}{2}+bt_a} \frac{1 + \delta(Q^2)}{\Gamma(1 + bt_b + bt_a)} \\
&+ \int_{E_{min}}^{E-\Delta E} dE_1 \left[\left(\frac{v_b}{E-E_1} + t_b w(E, E_1)\right) \frac{d^3\sigma}{d\Omega'dE'}(E_1, E', \theta) \right. \\
&\quad \left. \times \left(\frac{k_1}{E}\right)^{\frac{t}{2}+bt_b} \left(\frac{k'_1}{E'}\right)^{\frac{t}{2}+bt_a} \frac{1 + \delta(Q_1^2)}{\Gamma(1 + bt_b + bt_a)} \right] \\
&+ \int_{E'+\Delta E'}^{E'_{max}} dE'_1 \left[\left(\frac{v_a}{E'_1-E'} + t_a w(E'_1, E')\right) \frac{d^3\sigma}{d\Omega'dE'}(E, E'_1, \theta) \right. \\
&\quad \left. \times \left(\frac{k_1}{E}\right)^{\frac{t}{2}+bt_b} \left(\frac{k'_1}{E'}\right)^{\frac{t}{2}+bt_a} \frac{1 + \delta(Q_1'^2)}{\Gamma(1 + bt_b + bt_a)} \right].
\end{aligned} \tag{3.96}$$

Equation 3.96 is quite complicated, and explaining every term in detail is beyond the scope of this dissertation. Definitions and mathematical expressions of quantities in Eq. 3.96 not referenced herein can be found in Ref. [41]. The first term, $d^3\sigma_{el,rad}/d\Omega'dE'$, represents the contribution to the measured cross section from elastic scattering from discrete states. The integrals in the third and fourth terms represent the energy lost by the electron through straggling effects before and after the interaction, respectively.

The non-radiative cross section must be extracted from the expression for the experimentally measured cross section. The process begins by solving

Eq. 3.96 for the corrected non-radiative cross section as

$$\begin{aligned}
\frac{d^3\sigma}{d\Omega'dE'}(E, E', \theta) &= \left[\left(\frac{\Delta E}{E} \right)^{\frac{t}{2}+bt_b} \left(\frac{\Delta E'}{E'} \right)^{\frac{t}{2}+bt_a} \frac{1 + \delta(Q^2)}{\Gamma(1 + bt_b + bt_a)} \right]^{-1} \\
&\times \left[\frac{d^3\sigma_{exp}}{d\Omega'dE'}(E, E', \theta) - \frac{d^3\sigma_{el,rad}}{d\Omega'dE'}(E, E', \theta) \right. \\
&\quad - \int_{E_{min}}^{E-\Delta E} dE_1 \left[\left(\frac{v_b}{E - E_1} + t_b w(E, E_1) \right) \frac{d^3\sigma}{d\Omega'dE'}(E_1, E', \theta) \right. \\
&\quad \quad \left. \times \left(\frac{k_1}{E} \right)^{\frac{t}{2}+bt_b} \left(\frac{k'_1}{E'} \right)^{\frac{t}{2}+bt_a} \frac{1 + \delta(Q_1^2)}{\Gamma(1 + bt_b + bt_a)} \right] \\
&\quad \left. - \int_{E'+\Delta E'}^{E'_{max}} dE'_1 \left[\left(\frac{v_a}{E'_1 - E'} + t_a w(E'_1, E') \right) \frac{d^3\sigma}{d\Omega'dE'}(E, E'_1, \theta) \right. \right. \\
&\quad \quad \left. \left. \times \left(\frac{k_1}{E} \right)^{\frac{t}{2}+bt_b} \left(\frac{k'_1}{E'} \right)^{\frac{t}{2}+bt_a} \frac{1 + \delta(Q_1'^2)}{\Gamma(1 + bt_b + bt_a)} \right] \right]. \tag{3.97}
\end{aligned}$$

The result is an integral equation for the corrected cross section, which can only be solved numerically. The numerical method for extracting the non-radiative cross section from Eq. 3.97 is known as *unfolding*, and is described in detail in Ref. [42].

The code used to calculate the radiative corrections in the E12-14-012 analysis was based on the method of Ref. [44]. There are some differences from the mathematical analysis of Ref. [41], as different approximations and notation conventions were employed. In the method of Ref. [44], the unfolding procedure is carried out on the *effective non-radiative cross section*, which is defined as

$$\sigma_{\text{eff}}(E, E') = F(Q^2, T)\sigma(E - \Delta, E' + \Delta'). \tag{3.98}$$

The Δ in the argument of the corrected cross section is the most probable energy loss of the incident particle due to ionization after passing through a material of thickness $T/2$ radiation lengths. This modification to the electron energies, characterized by the substitution $E_0 \rightarrow E - \Delta$ and $E' \rightarrow E' + \Delta'$, is also applied to Q^2 in Eq. 3.98, and shall be assumed implicitly for the remainder of this section.

The function modifying the non-radiative cross section in Eq. 3.98 is

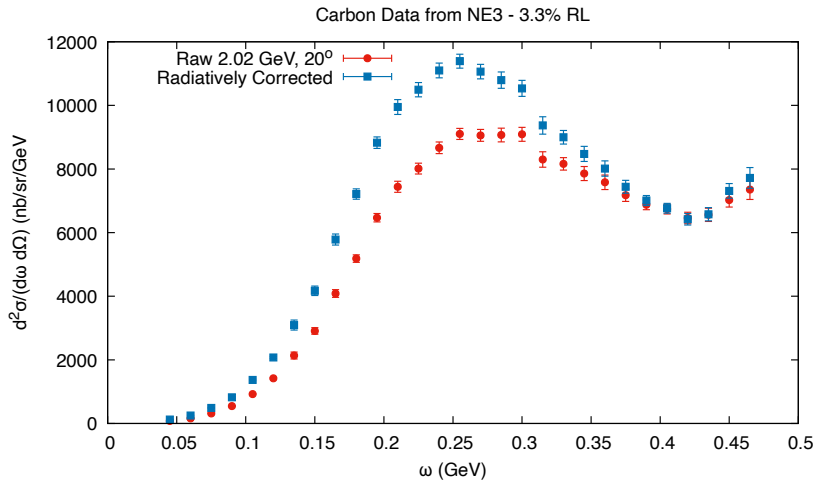


Figure 25: SLAC NE3 carbon data showing the effects of radiative corrections[34]. The red points are raw carbon cross section data, and the blue points have the radiative corrections applied. It should be noted that these plots represent an intermediate stage of the data analysis, and do not have all corrections applied.

given by[44]

$$\begin{aligned}
 F(Q^2, T) = & (1 + \gamma bT) + \frac{2\alpha}{\pi} \left[\frac{13}{12} \log \frac{Q^2}{m^2} - \frac{14}{9} \right] \\
 & + \frac{\alpha}{\pi} \left[\frac{\pi^2}{6} - \text{Li}_2 \left(\cos^2 \frac{\theta}{2} \right) \right] - \frac{2\alpha}{\pi} \log^2 \left(\frac{E}{E'} \right), \quad (3.99)
 \end{aligned}$$

where $\gamma \approx 0.57721$ is the Euler-Mascheroni constant (see Eq. A.8), and $\text{Li}_2(x)$ is the *dilogarithm function* (see §A.2). The first parenthetical term in Eq. 3.99 is the first-order Taylor series expansion of $\Gamma(1 + bT)^{-1}$. The second term is the sum of the vacuum polarization and vertex corrections, $\delta_{\text{vac}} + \delta_{\text{ver}} = \delta$. This is the same δ that appears in the Schwinger correction term of Eq. 3.96. The third term, along with the term just described, are parts of the high-electron-energy Schwinger correction (see Eq. B.25). The last term is a correction factor for the peaking-approximation.

An electron of initial energy E_0 will arrive at the interaction vertex with an energy $E < E_0$ due to losses from bremsstrahlung and other radiative processes. Similarly, the scattered electron that leaves the interaction vertex with energy E' will arrive at the detector with an energy $E < E'$, again due to losses from bremsstrahlung and other radiative processes. The goal of the

radiative corrections is to account for these processes, as well as those in Fig. 21, Fig. 22, Fig. 23, and Fig. 24, and hence obtain the Born cross section from the radiated cross section.

The effect of radiative corrections on experimental data is shown in Fig. 25. The figure shows raw cross section data (red points) from the SLAC experiment NE3[34]; electron scattering from carbon at 2.02 GeV and 20°. The blue data points show the cross section with the radiative corrections applied. When applied to a histogram, the correction moves events out of lower E' bins and back into the E' bin the event would have been in, if not for radiative losses. An examination of the correction on a bin-by-bin basis shows that the magnitude of the correction is largely driven by the size of the cross section in adjacent bins. The correction is small for small ω (large E'), as there is barely any strength in the neighboring bins to be moved. The correction is largest for ω 's in the vicinity of the quasi-elastic peak, as this is where the cross section is largest.

3.8 Off-Shell Corrections

Nucleons bound inside a nucleus are off of their mass-shell. That is, the energy of the bound nucleon is *not* given by the relativistic energy equation, $E \neq \sqrt{|\vec{\mathbf{p}}|^2 + M^2}$. There have been many theoretical attempts to account for the off-shell kinematics of the bound nucleon on the cross section, a number of which can be found in Ref. [45]. However, the most employed off-shell extrapolations to the Rosenbluth cross section were developed by T. deForest in Ref. [45].

The extrapolation to off-shell kinematics comes through the calculation of the nucleon current $J^\mu = \langle \vec{\mathbf{p}}' | \hat{J}^\mu(q) | \vec{\mathbf{p}} \rangle$. For an on-shell nucleon, the current is given by

$$J^\mu = \bar{U}(\vec{\mathbf{p}}') \left[\gamma^\mu F_1(q^2) + \sigma^{\mu\nu} q_\nu \frac{i}{2M} F_2(q^2) \right] U(\vec{\mathbf{p}}). \quad (3.100)$$

The functions $F_1(q^2)$ and $F_2(q^2)$ are the Dirac and Pauli form factors with the normalization conventions $F_1(0) = 1$ and $F_2(0) = \kappa$, where κ is the anomalous magnetic moment of the nucleon. The Gordon Identity of quantum electrodynamics can be used to eliminate the dependence of the nuclear current operator on $\sigma^{\mu\nu} q_\nu$, where $\sigma^{\mu\nu} = \frac{i}{2}[\gamma^\mu, \gamma^\nu]$, in favor of the total momentum $(p + p')^\mu$ as

$$J^\mu = \bar{U}(\vec{\mathbf{p}}') \left[\gamma^\mu (F_1(q^2) + F_2(q^2)) - (p + p')^\mu \frac{1}{2M} F_2(q^2) \right] U(\vec{\mathbf{p}}). \quad (3.101)$$

After extrapolating to off-shell kinematics, either of these two expressions for the nuclear current can be used in Eq. 3.10 to calculate the off-shell hadronic response tensor $W_{\mu\nu}^{\text{off}}$. The off-shell electron-nucleon cross section is calculated from Eq. 3.17 with the off-shell response tensor just defined. Carrying out the tensor contraction $L^{\mu\nu}W_{\mu\nu}^{\text{off}}$, assuming full angular dependence, gives[45]

$$\begin{aligned} \sigma_{eN} = \sigma_M \left[\frac{Q^4}{|\vec{\mathbf{q}}|^4} W_C + \frac{Q^2}{|\vec{\mathbf{q}}|^2} \sqrt{\frac{Q^2}{|\vec{\mathbf{q}}|^2} + \tan^2 \frac{\theta}{2}} \cos \phi_{Nq} W_I \right. \\ \left. + \left(\frac{Q^2}{2|\vec{\mathbf{q}}|^2} + \tan^2 \frac{\theta}{2} \right) W_T + \left(\frac{Q^2}{|\vec{\mathbf{q}}|^2} \cos^2 \phi_{Nq} + \tan^2 \frac{\theta}{2} \right) W_S \right], \end{aligned} \quad (3.102)$$

where σ_M is the Mott cross section, defined in Eq. B.8. The structure functions in Eq. 3.102 depend on J^μ , and any difference in calculating J^μ will be reflected in the W terms only.

Applying the off-shell extrapolation technique to the nucleon current of Eq. 3.101 gives the following expressions for the structure functions[45],

$$W_C = \frac{1}{4\bar{E}E'_N} \left[(\bar{E} + E'_N)^2 \left(F_1^2 + \frac{\bar{Q}^2}{4M^2} F_2^2 \right) - |\vec{\mathbf{q}}|^2 (F_1 + F_2)^2 \right] \quad (3.103a)$$

$$W_T = \frac{\bar{Q}^2}{2\bar{E}E'_N} (F_1 + F_2)^2 \quad (3.103b)$$

$$W_S = \frac{|\vec{\mathbf{p}}'|^2 \sin^2 \theta_{Nq}}{\bar{E}E'_N} \left(F_1^2 + \frac{\bar{Q}^2}{4M^2} F_2^2 \right) \quad (3.103c)$$

$$W_I = -\frac{|\vec{\mathbf{p}}'| \sin \theta_{Nq}}{\bar{E}E'_N} (\bar{E} + E'_N) \left(F_1^2 + \frac{\bar{Q}^2}{4M^2} F_2^2 \right). \quad (3.103d)$$

It should be noted that these structure functions were derived in the old relativistic framework, where four-vectors exist in a Euclidean space-time with an imaginary time-like component. This convention also applies to the structure functions of Eq. 3.104. In Eq. 3.103 for the structure functions, θ_{Nq} is the angle between the momentum vectors $\vec{\mathbf{p}}'$ and $\vec{\mathbf{q}}$ (see §3.1). The quantity $\bar{E} = \sqrt{|\vec{\mathbf{p}}|^2 + M^2}$ is the effective energy of the initial proton. The modified momentum transfer is given by $\bar{q} = (\vec{\mathbf{q}}, i\bar{\omega})$, where $\bar{\omega} = E'_N - \bar{E}$. Substituting the results of 3.103 in the expression for σ_{eN} is referred to as CC1, and the associated cross section is denoted σ_{CC1} .

The result of the off-shell extrapolation using Eq. 3.100 for the nuclear current is considerably more complicated, giving

$$\begin{aligned}
W_C = \frac{1}{\bar{E}E'_N} & \left[\left(\bar{E}E'_N + \frac{1}{2} (\bar{\mathbf{p}} \cdot \mathbf{p}' + M^2) \right) F_1^2 - \frac{1}{2} |\bar{\mathbf{q}}|^2 F_1 F_2 \right. \\
& - \left(((\bar{\mathbf{p}} \cdot \mathbf{q})E'_N + (\mathbf{p}' \cdot \mathbf{q})\bar{E}) \omega - \bar{E}E'_N Q^2 \right. \\
& \left. \left. + (\bar{\mathbf{p}} \cdot \mathbf{q})(\mathbf{p}' \cdot \mathbf{q}) - \frac{1}{2} (\bar{\mathbf{p}} \cdot \mathbf{p}' - M^2) |\bar{\mathbf{q}}|^2 \right) \frac{1}{4M^2} F_2^2 \right] \quad (3.104a)
\end{aligned}$$

$$\begin{aligned}
W_T = \frac{1}{\bar{E}E'_N} & \left[- (\bar{\mathbf{p}} \cdot \mathbf{p}' + M^2) F_1^2 + (\bar{\mathbf{q}} \cdot \mathbf{q}) F_1 F_2 \right. \\
& \left. + (2(\bar{\mathbf{p}} \cdot \mathbf{q})(\mathbf{p}' \cdot \mathbf{q}) - (\bar{\mathbf{p}} \cdot \mathbf{p}' - M^2) Q^2) \frac{1}{4M^2} F_2^2 \right] \quad (3.104b)
\end{aligned}$$

$$W_S = \frac{|\bar{\mathbf{p}}'|^2 \sin^2 \theta_{Nq}}{\bar{E}E'_N} \left[F_1^2 + \frac{Q^2}{4M^2} F_2^2 \right] \quad (3.104c)$$

$$\begin{aligned}
W_I = \frac{|\bar{\mathbf{p}}'| \sin \theta_{Nq}}{\bar{E}E'_N} & \left[- (\bar{E} + E'_N) F_1^2 \right. \\
& \left. + (\omega(\bar{\mathbf{p}} + \mathbf{p}') \cdot \mathbf{q} - (\bar{E} + E'_N) Q^2) \frac{1}{4M^2} F_2^2 \right] \quad (3.104d)
\end{aligned}$$

for the generalized structure functions. Substituting the results of Eq. 3.104 in the expression for σ_{eN} is referred to as CC2, and is denoted σ_{CC2} . In the E12-14-012 analysis, both CC1 and CC2 were used to calculate DWIA cross sections and reduced cross sections.

4 E12-14-012 Experimental Setup

4.1 CEBAF Accelerator and Beam

The *Continuous Electron Beam Accelerator Facility* (CEBAF) is the electron accelerator at Jefferson Lab. An illustration of the accelerator, post 12 GeV upgrade, is shown in Fig. 26. The accelerator loop consists of two parallel linear accelerators (LINAC) connected by several magnetic arcs that guide the electrons around the loop. Electrons are injected into the accelerator ring, and begin circling the loop, gaining 2.2 GeV of energy during each lap

Parameter	Past @ 6 GeV	Present @ 12 GeV
Horizontal emittance ϵ_x	2.9×10^{-7} mrad	9×10^{-6} mrad
Vertical emittance ϵ_y	2.9×10^{-7} mrad	1.9×10^{-6} mrad
Energy Spread $\delta p/p$	1×10^{-4}	2×10^{-4}

Table 2: Key parameters of CEBAF beam quality, before and after the 12 GeV upgrade[46].

of the accelerator ring[46]. The electron beam is virtually continuous, as the electrons are bunched into groups with nano-second separation. The resulting high energy electron beam can be delivered simultaneously to the four experimental halls, Hall A, B, C, and D. The typical size of the beam is on the order of tenths of a millimeter, or smaller[47]. Table 2 shows the important parameters of the CEBAF beam pre- and post-12 GeV upgrade.

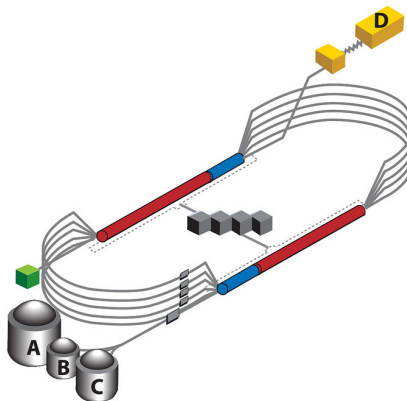


Figure 26: The CEBAF accelerator at JLab, post 12 GeV upgrade[48]. Electrons are introduced into the accelerator ring at the injector (green box), and are further accelerated by the LINAC's (red and blue cylinders) before being diverted to the experimental halls (A, B, C, and D).

4.2 Experimental Hall A

The spectrometers in Hall A are ideal for studying nucleon spin structure and nucleon and few-body form factors at high momentum transfer at small inter-nucleon separations. As a result, experimental Hall A has hosted several previous $(e, e'p)$ scattering experiments, summarized in Table 3.

E-89-003	Study of the Quasi-elastic $(e, e'p)$ reaction in ^{16}O at High Recoil Momentum[49]
E-89-044	Selected Studies of the ^3He and ^4He Nuclei through Electrodisintegration at High Momentum Transfer[50]
E-94-004	In-Plane Separations and High Momentum Structure in $d(e, e'p)n$ [51]
E-97-111	Systematic Probe of Short-Range Correlations via the Reaction $^4\text{He}(e, e'p)^4\text{He}$ [52]
E-00-102	Testing the limits of the Single Particle Model in ^{16}O $(e, e'p)$ [53]
E-03-104	Probing the Limits of the Standard Model of Nuclear Physics with the $^4\text{He}(\bar{e}, e'\bar{p})^3\text{He}$ Reaction[54]
E-06-007	Impulse Approximation limitations to the $(e, e'p)$ on ^{208}Pb , Identifying Correlations and Relativistic Effects in the Nuclear Medium[55]

Table 3: List of previous $(e, e'p)$ experiments in Hall A[1].

A diagram showing the layout of Hall A is shown in Fig. 27. The hall houses two high resolution spectrometers, which rotate about the scattering chamber at the center of the hall. The spectrometers are labeled left and right, reckoned with respect to the direction of the beamline. The highest beam energy available in Hall A is approximately 11.5 GeV, despite the capability of CEBAF to produce electron beams at 12 GeV. The beam is rastered over an $2 \times 2 \text{ mm}^2$ area on the target to avoid burn damage to the target cell and minimize density changes from heat deposition. The effects of target heating are discussed further in §4.3.3.

4.3 Targets

Data was collected from multiple targets during the E12-14-012 experimental run. The main physics targets are the argon gas cell and titanium slab. Additional targets included a aluminum dummy target and a carbon multi-foil target. The target nuclei and thicknesses (in g/cm^2) are listed in Tab. 4, along with associated radiation lengths and percentages. The targets are arranged on a *target ladder*, which can be operated remotely to select which target is exposed to the electron beam. A photograph of the target ladder, with the argon target cell mounted, is shown in Fig. 30.

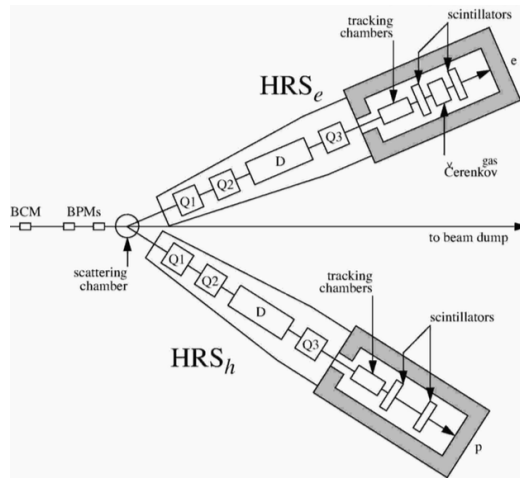


Figure 27: Top-down view of the high-resolution spectrometer arms in Hall A[56]. Located upstream (left) of the scattering chamber are the beam position monitors (BPM) and beam current monitors (BCM), part of the beam-line monitoring equipment.

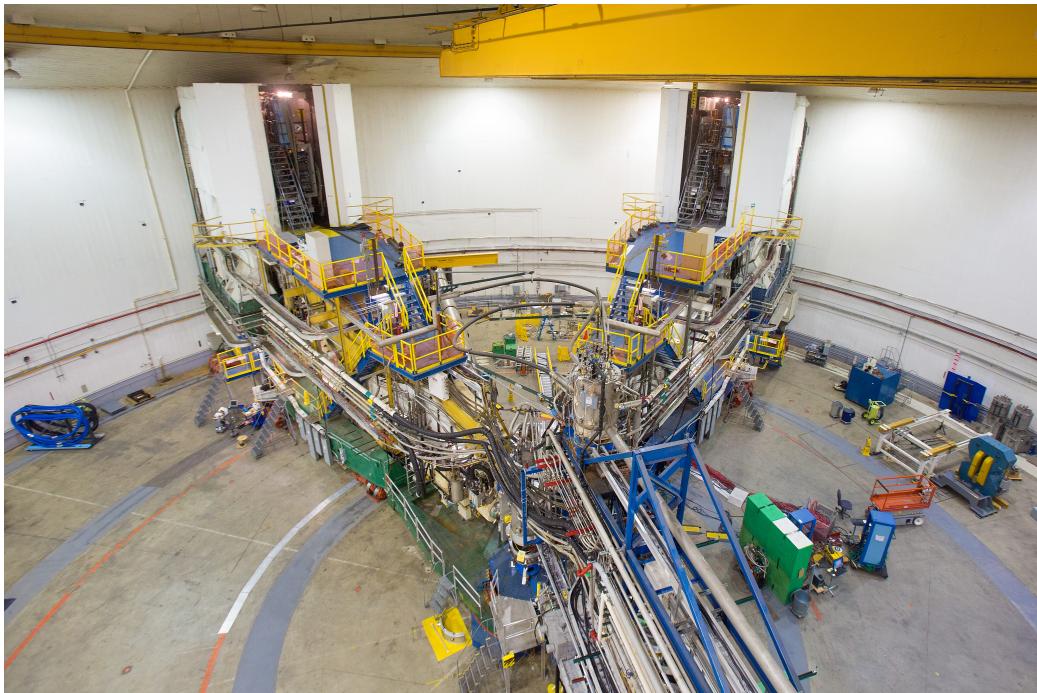


Figure 28: Photograph of Hall A showing the beamline structure (bottom) and the LHRS (left) and RHRS (right) spectrometers[57].

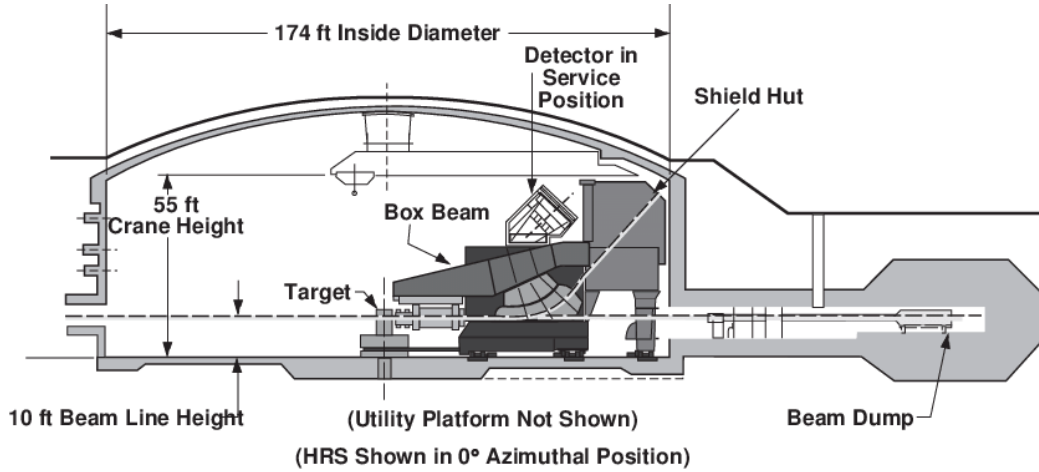


Figure 29: Cross-sectional schematic of Hall A showing the orientation of the beamline (dotted line) and the spectrometer with respect to the hall center[58].

Nucleus	X_0 [g/cm^2]	thickness [g/cm^2]	% X_0
^{12}C	42.70	0.167 ± 0.001	0.4%
^{27}Al	14.01	0.889 ± 0.002	3.7%
^{40}Ar (gas)	19.55	1.455 ± 0.005	7.4%
^{48}Ti	16.16	0.729 ± 0.001	4.5%

Table 4: Table comparing target thicknesses (in g/cm^2) and radiation lengths X_0 . Radiation lengths obtained from Ref. [59].



Figure 30: Photograph of the Hall A target ladder used in E12-14-012, showing the argon gas cell (top), the aluminum dummy target (middle), and the carbon optics target (bottom)[10]. The beam (arrow) enters from the far right, and exits the target tube at the left of the photograph.

4.3.1 Argon Target Cell

The gaseous argon used as the nuclear target is sealed within a target cell. The target cell used in E12-14-012, shown in Fig. 31 as a computer generated image, was originally developed to contain gaseous ^3H for a different experiment. The argon is kept in a 25cm aluminum tube, closed at both ends with thick aluminum caps.

The electron beam passes through the target along its length. This means that the beam encounters the aluminum cell end caps before encountering the argon gas itself. In order to account for the scattering events from the target cell cap, an aluminum *dummy target* was designed to simulate the effect of the target end caps. The dummy target consists of two ^{27}Al slabs 25 cm apart. The slabs were made of the aluminum alloy Al 7075, with an areal density, or thickness, of $0.889 \pm 0.002 \text{ g/cm}^2$ to match the radiation length of the argon target.

A histogram of the reconstructed coordinate y_{tg}^e from the inclusive data for the 25 cm dummy target (blue), superimposed over the argon target data (red), is shown in Fig. 32. This data shows that the effect of the target end caps is negligible for $|y_{tg}^e| \leq 0.1 \text{ m}$. The vertical lines in Fig. 32 represent outdated cuts on the data.

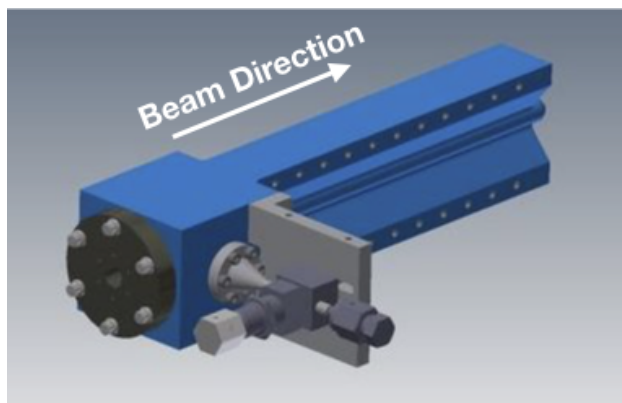


Figure 31: Computer generated image of the argon gas cell[60]. The beam (arrow) enters the cell from the left, and exits on the top right.

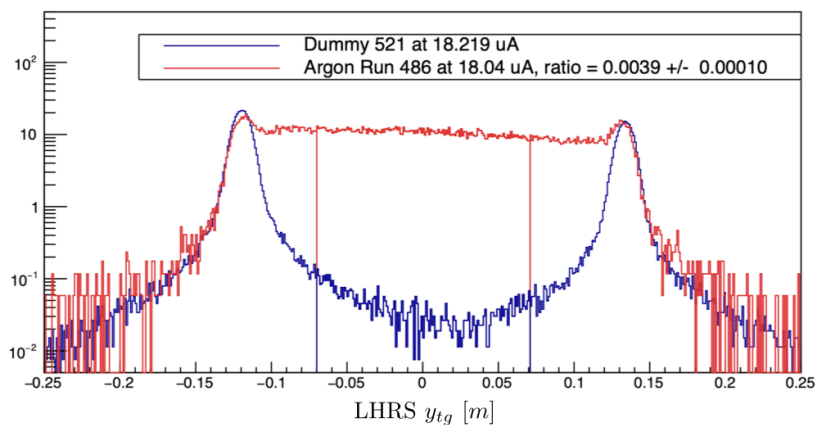


Figure 32: Overlay of argon (blue) and aluminum dummy (red) y_{tg}^c histograms[61]. The vertical lines represent suggested cuts on the histograms.

4.3.2 Titanium Target

The titanium target was a rectangular slab of ^{48}Ti of natural isotope composition with a thickness of $0.729 \pm 0.001 \text{ g/cm}^2$ [62].

4.3.3 Target Density Study

It is known that heat transfer from the electron beam to the nuclear target is a non-negligible effect, and must be considered in the analysis of the experimental data. Rastering of the electron beam over a set area minimizes the risk of damaging the target from overheating, but does not eliminate the heat transfer. Changes in target temperature result in changes to the target density and hence, interaction rates (yield). To determine the effect of the electron beam on the yield Y , data was collected on both argon and titanium targets as the beam current I was varied from $3 \mu\text{A}$ to $18 \mu\text{A}$. The yield is normalized to unity at the lowest value of the current.

Figure 33 shows the argon yield decreasing as the beam current increases. Fitting a quadratic function to the yield data gives the *density correction factor* as[63]

$$B(I) = (5.5 \times 10^{-4}) \cdot I^2 + (-0.02372) \cdot I + 1.07385. \quad (4.1)$$

A linear fit to the data was also tried, but the quadratic function resulted in the lowest χ^2 -per-degrees-of-freedom. When the target is gaseous or liquid, the density variation due to beam heating is called *target boiling*.

A similar study was conducted to determine the effect of the electron beam on the solid titanium and carbon targets. Then beam current was varied in the same way, and the results for titanium are shown in Fig. 34. The data clearly shows that the effect of heating on the solid target is negligible, the yield being consistent with unity within uncertainty. Thus, the density correction factor is unity for all currents, $B(I) = 1$.

4.3.4 Carbon Target

The carbon target was a foil of ^{12}C of natural isotope composition with a thickness of $0.167 \pm 0.001 \text{ g/cm}^2$ [62].

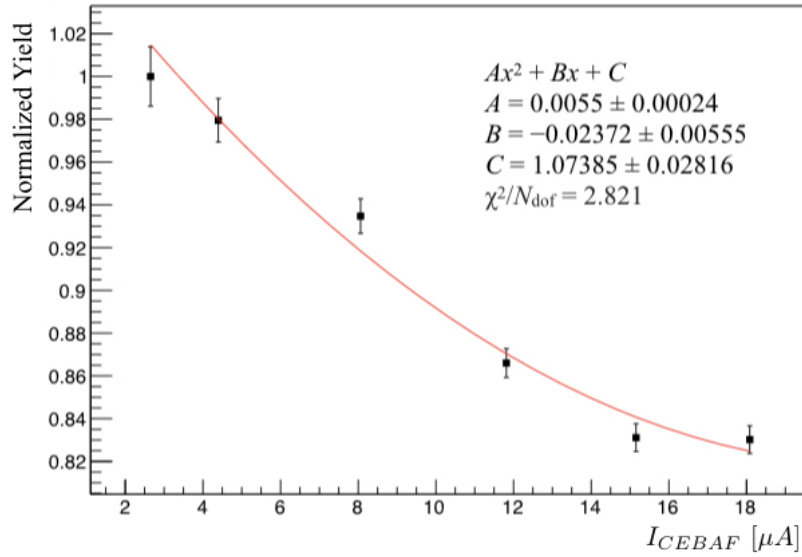


Figure 33: Normalized yield versus CEBAF beam current from the argon target boiling study[63].

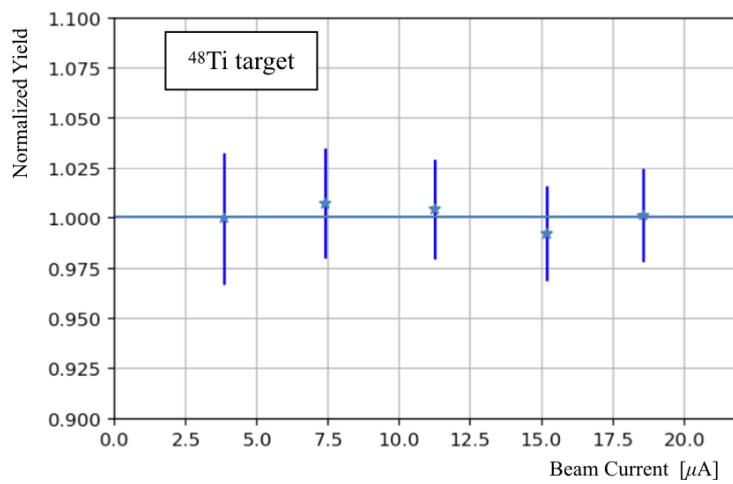


Figure 34: Normalized yield versus CEBAF beam current from the titanium target density study[64].

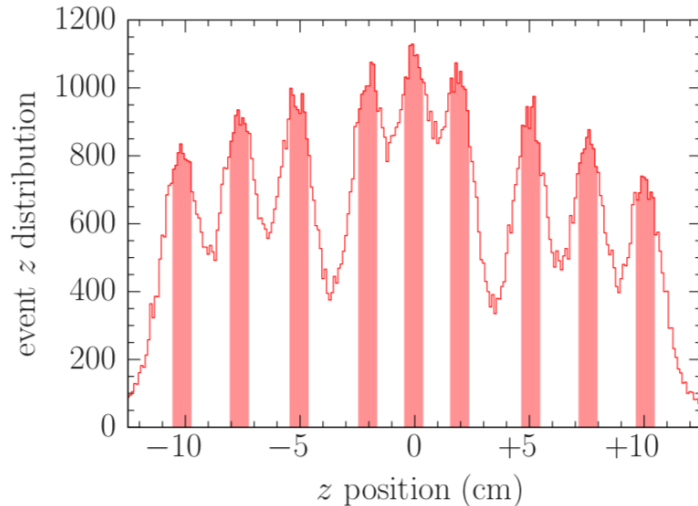


Figure 35: Histogram of the z_{tg}^e distribution from the carbon optics target[65]. The shape of the distribution is defined by the acceptance of the spectrometer.

4.3.5 Optics Target

The *optics target* consists of a series of nine carbon foils. The carbon slabs are located symmetrically about the TCS z -axis origin (see §4.5.5) at $z_{tg} = 0$ cm, ± 2 cm, ± 5 cm, ± 7.5 cm, and ± 10 cm[65]. A histogram of the optics target z_{tg}^e distribution is shown in Fig. 35.

4.4 Experimental Kinematics

The experiment E12-14-012 took data at five kinematic settings, shown in Table 5. Exclusive scattering data was collected for the argon and titanium targets at all five kinematics settings. Inclusive scattering data on argon, titanium, carbon, and aluminum targets was collected at kinematic setting 5 only. The LHRS central momentum was varied from 2.160 GeV to 1.317 GeV over nine production runs, known as the momentum delta scan. Inclusive scattering data was collected for each target at each of the nine momentum settings. The momentum settings of the delta scan are shown in Table 6. In total, E12-14-012 took approximately nine days of data. A table summarizing the data collected is presented in Table 7.

All data was collected in a momentum configuration such that $\vec{p} \parallel \vec{q}$, known as *parallel kinematics*. Data collected in previous $(e, e'p)$ experiments

	E_e MeV	$E_{e'}$ MeV	θ_e deg	P_p MeV/c	θ_p deg	$ \vec{q} $ MeV/c	$ \vec{p}_m $ MeV/c	x_B
kin1 (Ar)	2222	1777	21.5	915	-50.0	857.5	50.0	0.66
kin1 (Ti)	2222	1799	21.5	915	-50.0	857.5	57.7	0.70
kin2	2222	1716	20.0	1030	-44.0	846.1	183.9	0.48
kin3	2222	1799	17.5	915	-47.0	740.9	174.1	0.47
kin4	2222	1799	15.5	915	-44.5	658.5	229.7	0.37
kin5	2222	1716	15.5	1030	-39.0	730.3	299.7	0.29

Table 5: Kinematic settings used in the E12-14-012 experiment. The quantities E_e and $E_{e'}$ are the initial (beam) and final (scattered) electron energies, and θ_e is the scattering angle. The proton momentum and scattering angle are P_p and θ_p , respectively. The vectors \vec{q} and \vec{p}_m are the three-momentum transfer and missing momentum, and x_B is the Bjorken scaling variable.

Target	$^{12}_6\text{C}$	$^{48}_{22}\text{Ti}$	$^{40}_{18}\text{Ar}$	$^{27}_{13}\text{Al}$	P_0 [GeV]
Run#	730	728	725	?	2.160
	731	732	734	726	2.030
	739	737	735	733	1.909
	740	741	743	736	1.797
	747	746	744	742	1.686
	748	749	751	745	1.585
	755	754	752	750	1.490
	756	757	759	753	1.401
	763	762	760	758	1.317

Table 6: Momentum delta-scan run numbers and corresponding spectrometer central momentum.

suggests that the effects of final state interactions on the ejected nucleon can be greatly reduced by measuring the cross section in parallel kinematics[1]. A diagram showing the relative orientation of the momentum vectors in parallel kinematics is shown in Fig. 36.

4.5 Coordinate Systems

4.5.1 Hall Coordinate System

The *Hall Coordinate System* (HCS) is a right-handed system of coordinates with its origin located at the center of the hall. A diagram of the HCS is

Kin 1			Kin 3		
Target Type	Hours	Events (k)	Target Type	Hours	Events (k)
Ar	29.6	43955	Ar	13.5	73176
Ti	12.5	12755	Ti	8.6	28423
Dummy	0.75	955	Dummy	0.6	2948
Kin 2			Kin 4		
Target Type	Hours	Events (k)	Target Type	Hours	Events (k)
Ar	32.1	62981	Ar	30.9	158682
Ti	18.7	21486	Ti	23.8	113130
Dummy	4.3	5075	Dummy	7.2	38591
Optics	1.15	1245	Optics	0.9	4883
C	2.0	2318	C	3.6	21922
Kin 5			Kin 5 - Inclusive		
Target Type	Hours	Events (k)	Target Type	Minutes	Events (k)
Ar	12.6	45338	Ar	57	2928
Ti	1.5	61	Ti	50	2993
Dummy	5.9	16286	Dummy	56	3235
Optics	2.9	160	C	115	3957

Table 7: Summary of the scattering data collected by the E12-14-012 experiment.

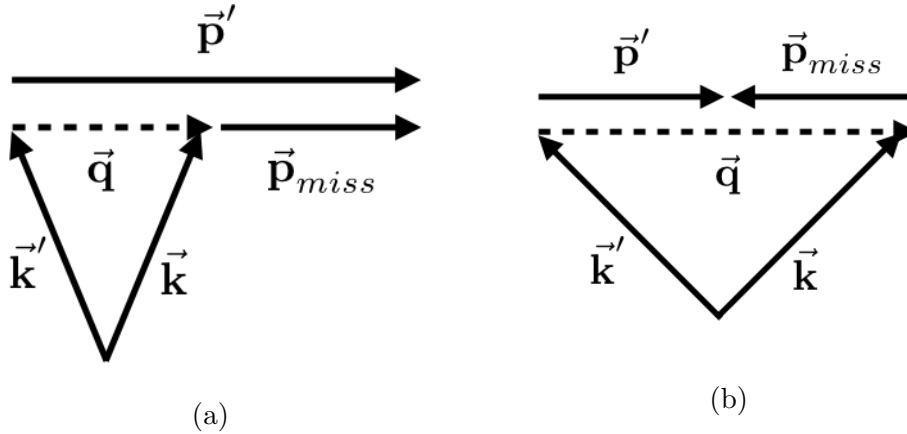


Figure 36: Vector diagrams depicting (a) parallel kinematics ($|\vec{q}| < |\vec{p}'|$) and (b) anti-parallel kinematics ($|\vec{q}| \geq |\vec{p}'|$).

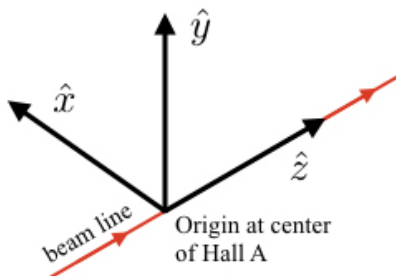


Figure 37: Diagram of the Hall Coordinate System.

shown in Fig. 37. The positive z -axis points along the beam line, and the y -axis points vertically upwards. The x -axis is parallel to the floor, its direction determined by the right hand rule, $\hat{\mathbf{x}} = \hat{\mathbf{y}} \times \hat{\mathbf{z}}$.

4.5.2 Detector Coordinate System

The *Detector Coordinate System* (DCS) is a right-handed coordinate system with variables reconstructed from the four individual VDC wire planes. The origin of the DCS is defined as the intersection of wire 184 in the U1 plane, and the projection of the same wire in the V1 plane onto the U1 plane. The $\hat{\mathbf{z}}$ -axis points vertically upward from the VDC plane, with the $\hat{\mathbf{x}}$ -axis pointing along the long symmetry axis of the lower VDC plane. A depiction of the DCS is shown in Fig. 38.

Consider the particle trajectory intersecting the the wire planes in Fig. 47. The particle intersects the lower VDC at (u_1, v_1) and the upper VDC at (u_2, v_2) . The U and V layers of each VDC are separated by a distance d_1 . The distance between the the U1 and U2 planes (and V1 and V2) planes is d_2 . Define two angles η_1 and η_2 such that the particle trajectory in Fig. 47 forms the hypotenuse of a right triangle with the distance d_2 the adjacent side with respect to the angles. Then, the tangents of the angles are defined in terms of the intersection points as

$$\tan \eta_1 = \frac{u_2 - u_1}{d_2} \quad (4.2a)$$

$$\tan \eta_2 = \frac{v_2 - v_1}{d_2}. \quad (4.2b)$$

The DCS variables are written in terms of these angles as

$$\theta_{det} = \frac{1}{\sqrt{2}}(\tan \eta_1 + \tan \eta_2) \quad (4.3a)$$

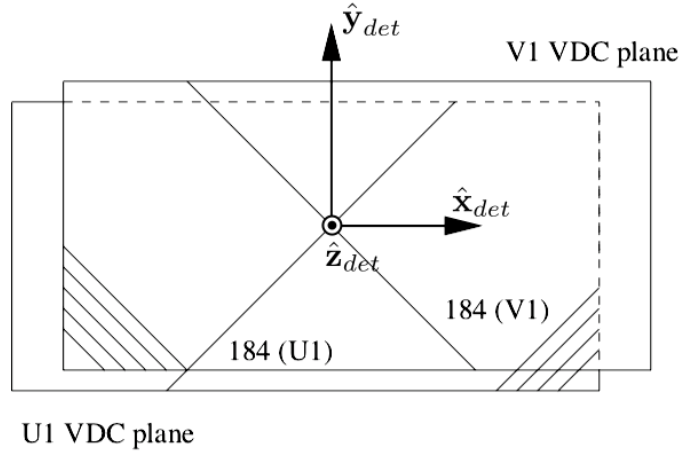


Figure 38: Diagram of the Detector Coordinate System. Figure modified from Ref. [66].

$$\phi_{det} = \frac{1}{\sqrt{2}}(\tan \eta_2 - \tan \eta_1) \quad (4.3b)$$

$$x_{det} = \frac{1}{\sqrt{2}}(u_1 + v_1 - d_1 \tan \eta_2) \quad (4.3c)$$

$$y_{det} = \frac{1}{\sqrt{2}}(v_1 - u_1 - d_1 \tan \eta_2). \quad (4.3d)$$

4.5.3 Transport Coordinate System

The *Transport Coordinate System* (TRCS), shown in Fig. 39, is obtained from the DCS by a $\rho_0 = -45^\circ$ rotation around the \hat{y}_{det} -axis. The TRCS variables are given by[66]

$$\theta_{tra} = \frac{\theta_{det} + \tan \rho_0}{1 - \theta_{det} \tan \rho_0} \quad (4.4a)$$

$$\phi_{tra} = \frac{\phi_{det}}{\cos \rho_0 - \theta_{det} \sin \rho_0} \quad (4.4b)$$

$$x_{tra} = x_{det}(1 + \theta_{tra} \tan \rho_0) \cos \rho_0 \quad (4.4c)$$

$$y_{tra} = y_{det} + x_{det} \phi_{tra} \sin \rho_0 \quad (4.4d)$$

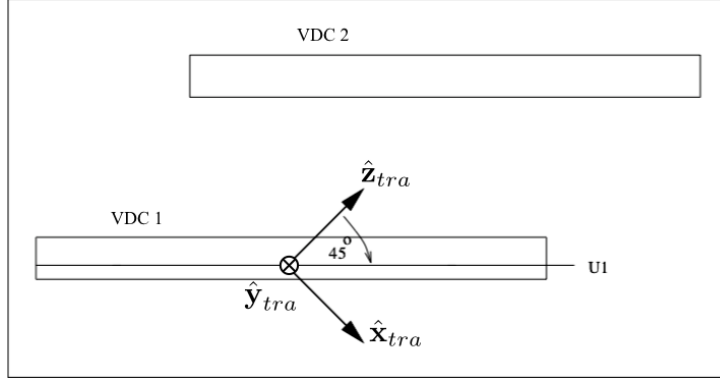


Figure 39: Diagram of the Transport Coordinate System. Figure modified from Ref. [66].

4.5.4 Focal Plane Coordinate System

The *Focal Plane Coordinate System* (FPCS), shown in Fig. 40, is a locally rotating coordinate system obtained by rotating the DCS through an angle ρ around the \hat{y}_{det} -axis. The FPCS is similar to the transport coordinate system, defined in §4.5.3, and the focal plane variables are defined in terms of the DCS variables and the TRCS rotation angle ρ_0 . The angle $\rho = \rho(x_{fp})$, defined in Eq. 4.5b, is the angle between the \hat{z} -axis of the the DCS and the \hat{z} -axis of the FPCS. The rotation angle is a function of position on the focal plane, as shown in Fig. 40. The FPCS \hat{z} -axis lies along the *local central ray*, the trajectory such that $\theta_{tg} = \phi_{tg} = 0$ [66]. The FPCS variables are then written as

$$x_{fp} = x_{tra} \quad (4.5a)$$

$$\tan \rho = \sum_i t_{i000} x_{fp}^i \quad (4.5b)$$

$$y_{fp} = y_{tra} - \sum_i y_{i000} x_{fp}^i \quad (4.5c)$$

$$\theta_{fp} = \frac{x_{det} + \tan \rho}{1 - \theta_{det} \tan \rho} \quad (4.5d)$$

$$\phi_{fp} = \frac{\phi_{det} - \sum_i p_{i000} x_{fp}^i}{\cos \rho_0 - \theta_{det} \sin \rho_0}. \quad (4.5e)$$

The polynomial coefficients t_{i000} , y_{i000} , and p_{i000} in Eqs. 4.5 are numbers determined during the HRS optics calibration that account for any spectrometer offsets.

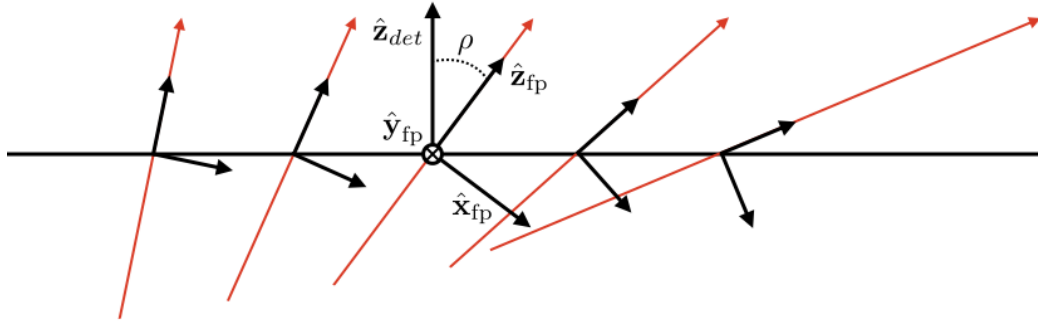


Figure 40: Diagram of the rotating focal plane coordinate system. The red lines represent local central rays that define the \hat{z} -axis of the FPCS.

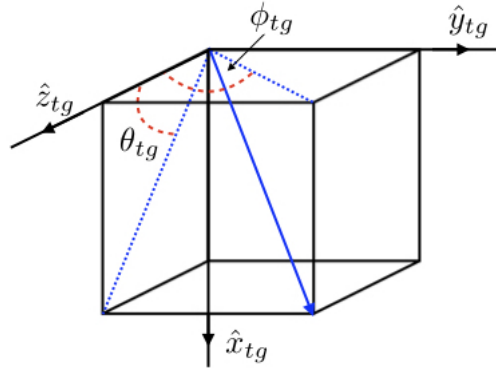


Figure 41: Diagram of the Target Coordinate System. The blue arrow is a vector representing the possible trajectory of a particle. The in-plane (ϕ_{tg}) and out-of-plane (θ_{tg}) angles are marked by dotted red lines.

4.5.5 Target Coordinate System

The *Target Coordinate System* (TCS), shown in Fig. 41, is a right handed coordinate system specific to each of the spectrometers. The z -axis is oriented along the central axis of the spectrometer, and the x -axis points vertically downwards. The direction of the y -axis is determined by $\hat{y}_{tg} = \hat{z}_{tg} \times \hat{x}_{tg}$. Ideally, the TCS has the same origin as the HCS, but usually deviates from this position in both x and y . The relationship between the HCS and TCS is shown in Fig. 42. In this diagram, θ_0 is the spectrometer central angle and L is the distance from the sieve to the TCS origin. The TCS origin is offset from the HCS origin in both x and y directions by D_x and D_y . The angle θ_0 is also the angle between the HCS and TCS z -unit vectors.

Consider a particle with trajectory defined by the blue vector in Fig. 41.

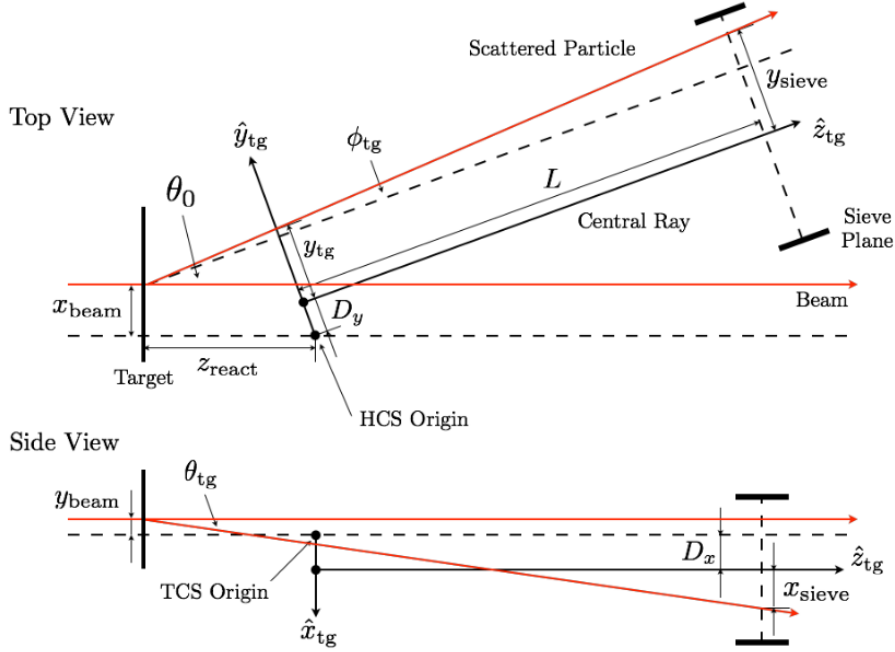


Figure 42: Top and side views of the Target Coordinate System[67].

A box can be drawn around this vector to project its components onto the target coordinate system. Since the TCS is aligned along the central axis of the HRS, the deviation of the particles momentum p from the HRS central momentum P_0 is given in the TCS as dp_{tg} . This deviation is given by

$$dp_{tg} = \frac{p - P_0}{P_0}. \quad (4.6)$$

It is also written as $\delta p/p$ and called the *momentum fraction*. Solving for the particle momentum gives

$$p = P_0(1 + dp_{tg}). \quad (4.7)$$

Consider the plane defined by the \hat{z}_{tg} and \hat{y}_{tg} TCS unit vectors. There are two angles measured with respect to this plane that define the angular position of the scattered particle vector in the TCS. The angle formed between the z -axis and the projection of the scattered particle vector onto the zy -plane is the in-plane angle ϕ_{tg} . The angle formed by the scattered particle vector and the zy -plane is the out-of-plane angle θ_{tg} . These angles are usually defined by their tangents in the small-angle approximation,

$$\tan \theta_{tg} = \frac{\Delta x}{\Delta z} \approx \theta_{tg} \quad (4.8)$$

$$\tan \phi_{tg} = \frac{\Delta y}{\Delta z} \approx \phi_{tg}. \quad (4.9)$$

The kinematic variables in the target coordinate system are reconstructed from the focal plane coordinates. The transformation from the focal plane system to the target coordinate system is implemented in ESPACE (see §7.1) as a fifth order polynomial in x_{fp} , given by the equations

$$y_{tg} = \sum_{jkl} \sum_{i=1}^5 Y_{jkl}^i x_{fp}^i \theta_{fp}^j y_{fp}^k \phi_{fp}^l \quad (4.10a)$$

$$\theta_{tg} = \sum_{jkl} \sum_{i=1}^5 T_{jkl}^i x_{fp}^i \theta_{fp}^j y_{fp}^k \phi_{fp}^l \quad (4.10b)$$

$$\phi_{tg} = \sum_{jkl} \sum_{i=1}^5 P_{jkl}^i x_{fp}^i \theta_{fp}^j y_{fp}^k \phi_{fp}^l \quad (4.10c)$$

$$\delta_{tg} = \sum_{jkl} \sum_{i=1}^5 D_{jkl}^i x_{fp}^i \theta_{fp}^j y_{fp}^k \phi_{fp}^l, \quad (4.10d)$$

where the superscripts i, j, k, l represent powers of the focal plane variables. The coefficients Y_{jkl}^i are read in from an ESPACE database.

5 Hall A High Resolution Spectrometers

Jefferson Lab's Hall A contains two High Resolution Spectrometers (HRS). The spectrometers are attached to two movable *arms* that are able to rotate about the hall center. With respect to the beam line, the arms are labeled left and right. The Left HRS (LHRS) measures negatively charged particles, and is also called the *electron arm*. Positively charged particles are measured in the Right HRS (RHRS), known as the *hadron arm*. The left and right spectrometers, shown in Fig. 44, have similar detectors and configurations. Each spectrometer has a VDC for particle tracking, two scintillator planes for triggers, and a Cherenkov detector and dual layer lead-glass calorimeter for particle identification.

A diagram detailing the magnetic transport system of the HRS is given in Fig. 43. Each HRS has three superconducting quadrupole magnets and one dipole magnet in a QQDQ configuration. The quadrupole (Q) magnets focus the scattered particles as the dipole (D) bends their trajectories through 45° into the HRS detector stack.

Configuration	QQD _n Q vertical bend
Bending angle	45°
Optical length	12.4 m
Momentum range	0.3 - 4.0 GeV/c
Momentum acceptance	-4.5 % < $\delta p/p$ < + 4.5 %
Momentum resolution	1×10^{-4}
Dispersion at the focus (D)	12.4 m
Radial linear magnification (M)	-2.5
D/M	5.0
Angular range	
LHRS	12.5 – 150°
RHRS	12.5 – 130°
Angular acceptance	
Horizontal	±30 mrad
Vertical	±60 mrad
Angular resolution	
Horizontal	0.5 mrad
Vertical	1.0 mrad
Solid angle at $\delta p/p = 0, y_0 = 0$	6 msr
Transverse length acceptance	±5 cm
Transverse position resolution	1 mm

Table 8: Main design characteristics of the Hall A high resolution spectrometers[58].

5.1 Scintillators

A scintillator is a particle detector that operates on the physical principle of scintillation. An incoming particle will deposit energy into the material as it passes through it. This absorbed energy is then re-emitted as light. This process of energy absorption and light emission is called scintillation.

Each HRS has space for two scintillator planes. The configuration for E12-14-012 included one scintillator with segmented paddles, labelled $S2$, and one non-segmented scintillator, labeled $S0$. The inclusion of a non-segmented scintillation plane allows for high hadron trigger efficiency[68]. The $S2$ scintillator is made of sixteen plastic scintillating bars forced together under pressure. Each bar is made of a special scintillating plastic material that allows for very fast timing[68]. Each scintillating bar is viewed on both ends by a *photomultiplier tube* (PMT). The $S0$ scintillator plane consists of a single plastic paddle, which is viewed on each side by three PMTs. The signals from these PMTs are used to form the data acquisition triggers.

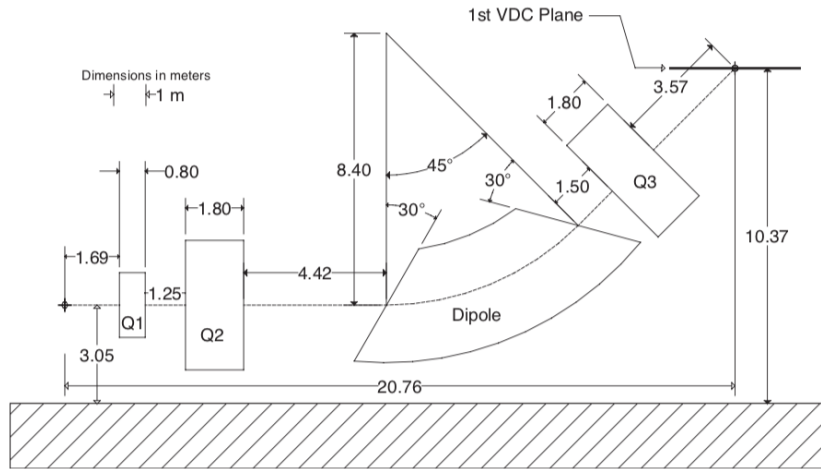


Figure 43: Diagram detailing the QQDQ magnetic transport system that guides charged particles into the spectrometers[58].

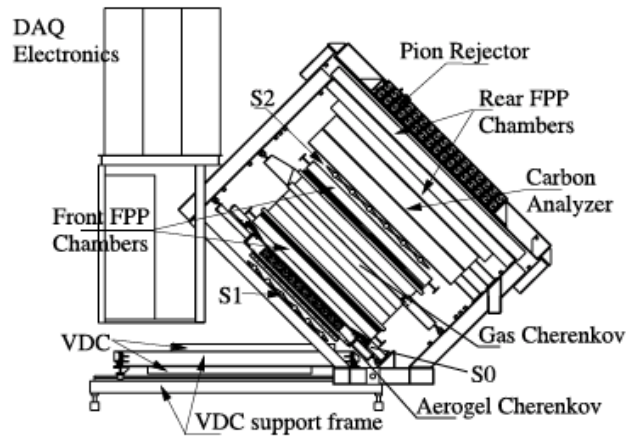
There is an additional segmented scintillator, $S1$, which was not used in this experiment.

5.2 Vertical Drift Chambers

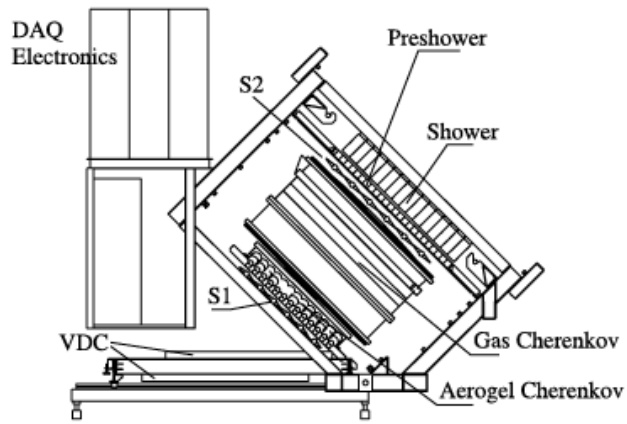
A Vertical Drift Chamber (VDC), sometimes called a wire chamber, is a device that reconstructs the trajectory of particles that pass through it. The Hall A VDCs consist of two wire planes, an upper and lower layer, separated by 335 mm. The lower VDC layer is positioned to coincide as closely as possible with the HRS focal plane. The second VDC plane, located above the first, allows increased precision in reconstructing particle trajectories. The ideal particle trajectory will carry it through the VDC layers at an angle of 45° , as shown in Fig. 46.

Each VDC plane has two layers of sense wires, referred to as the U and V planes, separated by 26 mm. The U sense wires are orthogonal to the V sense wires. Furthermore, the entire VDC detector is sealed within a gas chamber. The configuration of the U and V planes for each VDC layer is shown in Fig. 47.

A particle traveling through the VDC ionizes the gas as it passes through. The freed electrons are then attracted to the sense wires, creating a signal. These signals are collected and used to calculate the distance traveled by the electron to the wire. The tracking algorithm fits a line to the drift distances, thus determining the location and angle at which the particle passes through the plane. In all, the particle traverses four sense-wire planes. This multiple



(a)



(b)

Figure 44: Schematic diagrams of the detector packages of the (a) electron arm (left arm) and (b) proton arm (right arm) of the High-Resolution Spectrometers[58].

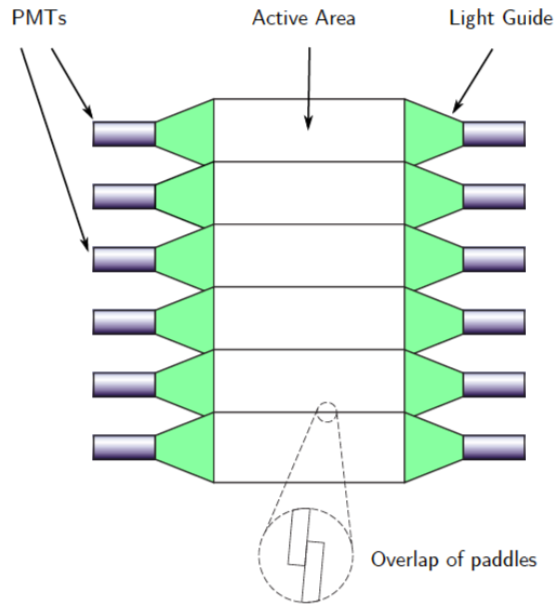


Figure 45: Drawing of a portion of the scintillator paddles[10]. Each overlapping plastic paddle is viewed by two PMTs.

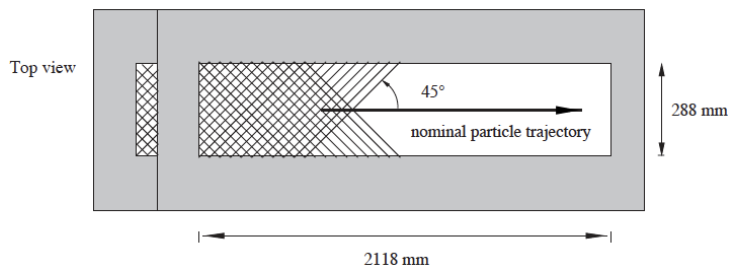


Figure 46: Diagram showing the relative orientation of the VDC wire planes with respect to the nominal particle trajectory[58].

wire-plane configuration allows for tracking efficiencies of virtually 100%[56].

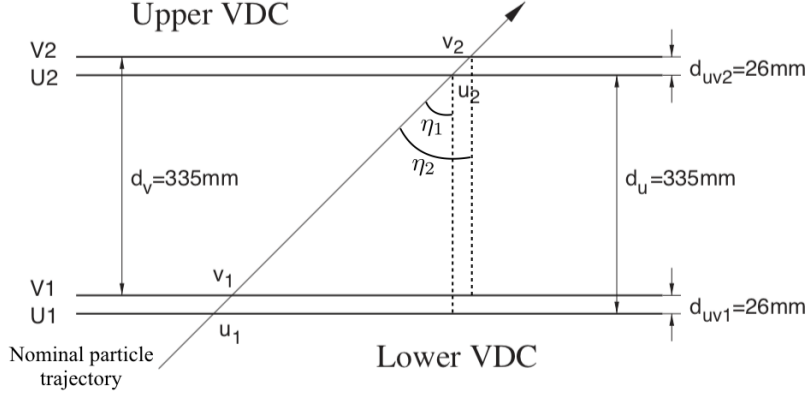


Figure 47: Schematic diagram of the upper and lower VDC wire planes with a nominal particle trajectory[58]. The separation of the wire planes are re-defined as $d_1 = d_{uv1} = d_{uv2}$ and $d_2 = d_u = d_v$.

5.3 Gas Cherenkov Detector

A Cherenkov detector is a device that separates particles based on the principle of Cherenkov radiation. Cherenkov radiation is emitted by a particle propagating in a dielectric medium when it moves faster than the phase-velocity of light in that medium. The particle velocity threshold at which Cherenkov radiation is emitted depends on the medium used. For a dielectric medium with index of refraction n , the energy threshold for emission of Cherenkov radiation is

$$E_{th} = \gamma_{th} mc^2 = \frac{n}{\sqrt{n^2 - 1}} mc^2. \quad (5.1)$$

This corresponds to propagation speeds $\beta > \frac{1}{n}$ [6]. Once past the energy threshold, the particle starts emitting Cherenkov radiation at an angle given by

$$\theta = \cos^{-1} \frac{1}{n\beta}. \quad (5.2)$$

The LHRS Cherenkov detector chamber is filled with CO_2 gas at atmospheric pressure. This medium gives an energy threshold for Cherenkov radiation from electrons at 17.04 MeV and pions at 4.7 GeV. Electrons emit Cherenkov radiation at $\theta = 1.72^\circ$. Each spectrometer also has an aerogel Cherenkov detector, but neither are used in this experiment.

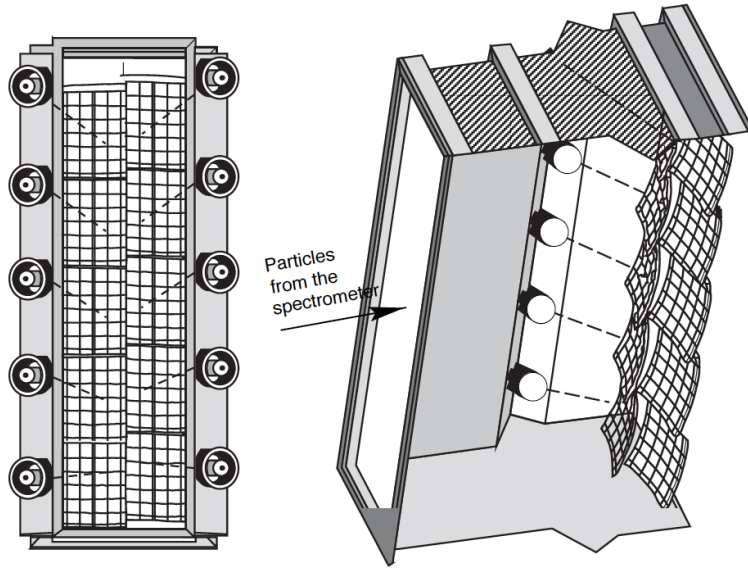


Figure 48: Computer rendered model of the Hall A CO_2 gas Cherenkov detector, showing the ten spherical mirrors and PMTs[69].

The detection chamber is equipped with ten spherical mirrors arranged in two columns of five mirrors. Each mirror is viewed by a corresponding PMT to collect the Cherenkov light produced in the chamber. The signals from the PMTs are combined and used to form part of the data acquisition triggers.

5.3.1 Cherenkov PMT Calibration

To ensure that the combined signal from the Cherenkov detector can be interpreted correctly, the photomultiplier tubes must be calibrated. The calibration ensures that each of the ten PMTs are measuring the Cherenkov radiation with the same scale. A histogram of the uncalibrated (raw) ADC spectrum from one of the PMT's is shown in Fig. 49a. Three peaks are readily visible, two of them being important for the calibration process. The first, sharp peak is known as the *pedestal*, and the second peak is the single-photoelectron peak (SPEP). The third, broad peak is the double-photoelectron peak.

The calibration procedure is as follows. First, the location of the pedestal is determined by fitting the raw PMT ADC spectrum with an appropriate lineshape. This information is then entered into a database which contains the location of the pedestal for each PMT, and the run is replayed in the

analyzer. Next, the location of the single-photoelectron peak, M_{SPEP} , is determined by another fit to the pedestal-subtracted PMT ADC spectrum, shown in Fig. 49b. Then, calculate the gain factor $C = M_{SPEP}/100$, update the appropriate database, and replay the run. The result is the fully calibrated PMT ADC spectrum, shown in Fig. 49c; the pedestal is centered at 0, and the single-photoelectron peak is centered at 100. When calibrated, the ADC channel of the PMT is equal to 100 times the number of photo-electrons $N_{\gamma e}$ produced within the PMT, or

$$N_{\gamma e} = \frac{\text{PMT ADC channel}}{100}. \quad (5.3)$$

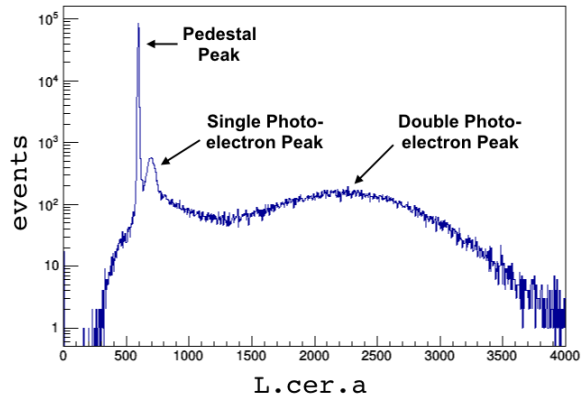
This process is repeated for each of the ten PMT's used, and is summarized in the following list:

1. Align the pedestal peak to 0 ADC channel,
2. Determine the location (center) of the single-photoelectron peak,
3. Calculate the gain factor $C = 100/M_{SPEP}$,
4. Align single photoelectron peak to 100 ADC channel.

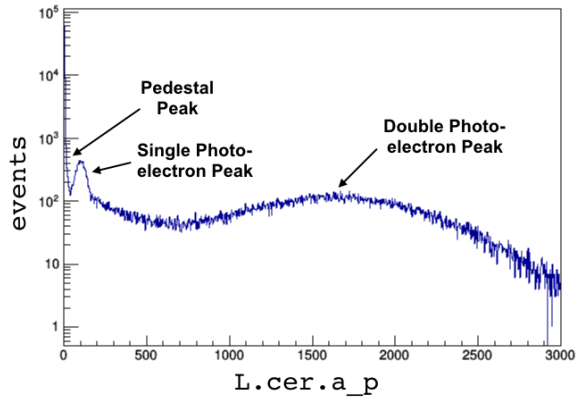
5.4 Lead Glass Calorimeters

An electromagnetic calorimeter is a detector designed to absorb the energy of a particle that passes through it. A high energy particle entering the device will emit a cascade of secondary particles, called a *shower*. For this reason, electromagnetic calorimeters are often referred to as *shower detectors*. Most (if not all) of the energy produced in the shower is absorbed by the detector, allowing a good determination of the original particles energy and identity.

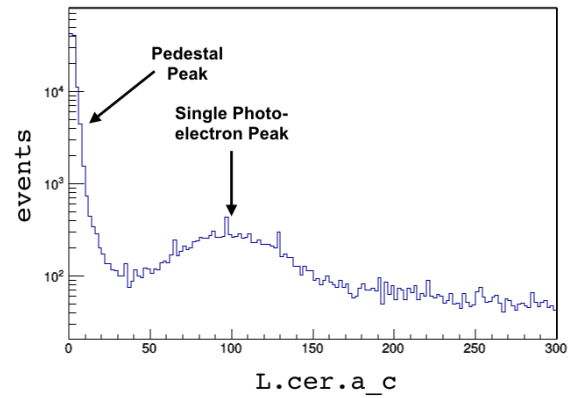
Each of the HRS spectrometers are fitted with a two-layer lead glass calorimeter, each layer containing multiple individual lead glass blocks (see Fig. 50). The only differences between the LHRS and RHRS calorimeters are the number of lead glass blocks used in each layer, and the orientation of the blocks in the second layer. The calorimeters are split into two sections to decrease the likelihood of pions triggering the DAQ electronics. Due to the difference in mean-free path-length between electrons and pions, the electron is more likely to shower in the first layer of the calorimeter than the pion. The probability of mistakenly identifying a pion as an electron can be greatly reduced by requiring a coincidence signal between the first and second layers in the DAQ triggers[70].



(a)



(b)



(c)

Figure 49: LHRS Cherenkov PMT ADC spectra, (a) raw, (b) pedestal-subtracted, and (c) fully calibrated.

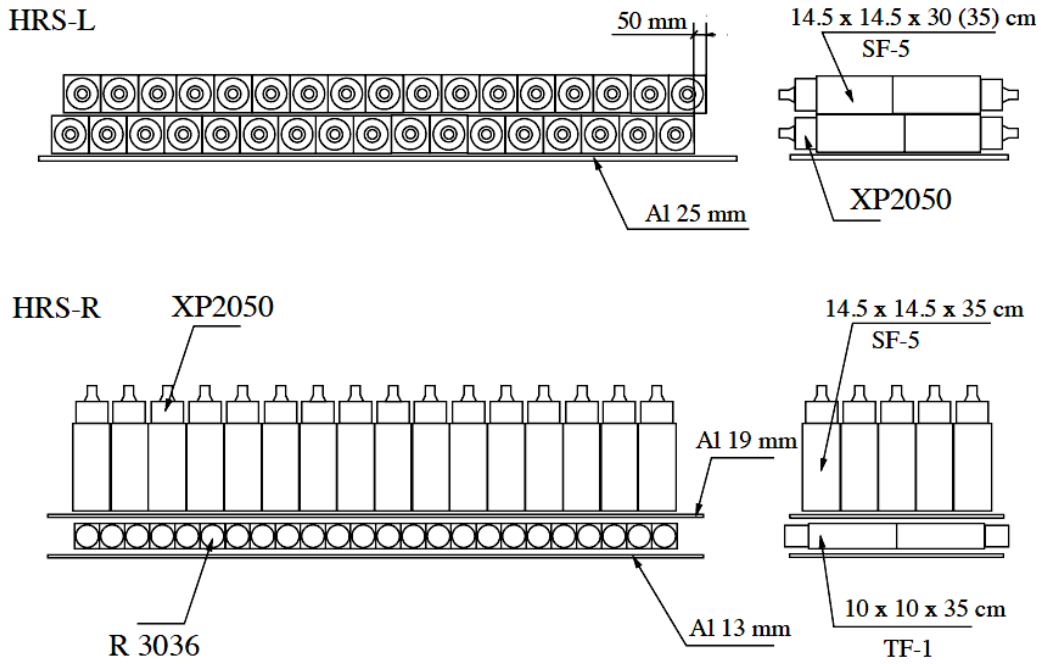


Figure 50: Diagrams of the LHRs (top) and RHRS (bottom) lead glass calorimeters[58].

Both layers of the LHRs calorimeter contain 34 lead glass blocks oriented perpendicularly to the incident particle trajectory. The lead glass blocks rest on a 25mm thick layer of aluminum which blocks extraneous low energy particles from entering the calorimeter. The first layer is often referred to as the *pre-radiator*, with the second layer called the *total absorber*. The LHRs calorimeter is referred to as a *pion rejector*, due to the central role it plays in the particle identification process, identifying and excluding contaminating pions from the data.

The first row of the RHRS calorimeter, or the *pre-shower* detector, consists of 48 lead glass blocks oriented perpendicularly to the incident particle trajectory. The second layer, or the *shower* detector, consists of 75 blocks oriented parallel to the trajectory of the incident particle. The top and bottom layer of blocks are supported by a 13mm and 19mm sheet of aluminum.

5.4.1 Calorimeter Calibration

The lead-glass calorimeter must be calibrated to ensure proper energy measurement of the detected particles. When an incident particle of energy E'

showers in the calorimeter, it deposits energy into multiple lead glass blocks in each layer. The group of lead-glass blocks in each layer in which energy is deposited is called a *cluster*. If the particle shower deposits energy E_i into the i^{th} lead-glass block of the cluster M , then the total energy deposited into the calorimeter is given by the sum of the energy deposited in each layer as

$$E_{tot} = \sum_{i \in M_1} E_i + \sum_{j \in M_2} E_j. \quad (5.4)$$

The cluster of lead-glass blocks in layer-one and layer-two are denoted in Eq. 5.4 as M_1 and M_2 , respectively.

The purpose of the calibration procedure is to relate the ADC signal amplitude from each lead-glass block to the energy deposition in that block. That is, to obtain a set of coefficients C_i such that the energy deposited in the i^{th} block is given by

$$E_i = C_i(ADC_i - Ped_i), \quad (5.5)$$

where ADC_i is the raw signal amplitude and Ped_i is the signal pedestal. After the calibration procedure, the total energy deposited in the calorimeter (Eq. 5.4) will be equal to the incident particle energy $E_{tot} = E'$. The calibration coefficients are determined by minimizing the χ^2 functional of Eq. 5.6. The calibration procedure should be carried out by fitting the χ^2 to a clean sample of elastic electron-proton scattering data[71].

$$\chi^2 = \sum_{n=1}^N \left[\sum_{i \in M_1^n} C_i(ADC_i^n - Ped_i) + \sum_{j \in M_2^n} C_j(ADC_j^n - Ped_j) - E'_n \right]^2 \quad (5.6)$$

5.5 Triggers

A trigger is a signal that initiates the data acquisition software to record an event of interest in the presence of background events[6]. The six triggers used are defined by the following logic statements,

$$T1 = (S0 \wedge S2)_L \wedge (GC \vee PR)_L \wedge (S0 \wedge S2)_R \quad (5.7a)$$

$$T2 = (S0 \vee S2)_L \wedge (GC \vee PR)_L \wedge (S0 \wedge S2)_R \wedge \neg(PS_e)_R \quad (5.7b)$$

$$T3 = (S0 \wedge S2)_L \wedge (GC \vee PR)_L \quad (5.7c)$$

$$T4 = (S0 \wedge S2)_R \quad (5.7d)$$

$$T5 = (S0 \vee S2)_L \wedge (GC \vee PR)_L \quad (5.7e)$$

$$T6 = (S0 \wedge S2)_R \wedge \neg(PS_e)_R. \quad (5.7f)$$

All but one of the triggers are formed in a multi-step process. The first step requires a signal from both scintillator planes, eliminating potentially contaminated events (cosmics) from being considered by the data acquisition electronics. The second step incorporates signals from the particle identification detectors, which determine whether or not the event is recorded.

Triggers $T3$ through $T6$ are single arm triggers, and apply only to the HRS arm indicated. Triggers $T1$ and $T2$ require signals from both HRS arms to activate, and are formed from the singles triggers as $T1 = T3 \wedge T4$ and $T2 = T5 \wedge T6$. The singles production trigger $T3$ and efficiency trigger $T5$ are activated to record an inclusive scattering event. A coincidence event is recorded when the coincidence triggers $T1$ and $T2$ are fired. Schematic diagrams detailing the logic of the singles and coincidence triggers are given in Fig. 51 and Fig. 52.

The time between the firing of a trigger and the subsequent recording of that event must be accounted for in the analysis. Even though this time is extremely short, there is the chance that many events will be missed while the electronics are busy. The percentage of time when the DAQ is busy and unable to record events is called the *dead time* (DT). Conversely, the percentage of time that the DAQ is ready to record an event is called the *live time* (LT). One can be derived from the other through the relationship

$$LT + DT = 1. \quad (5.8)$$

The live time actually consists of two components, known as the *computer live time* (CLT) and the *electronic live time* (ELT), and is the product of the two, $LT = CLT \cdot ELT$. The computer and electronic live times have associated dead times, which are defined by the equations $CLT + CDT = 1$ and $ELT + EDT = 1$. The computer dead time arises due to the inability of the DAQ to record an event while it is already recording another event[72]. The electronic dead time, which is only significant at high rates, arises due to the overlap of two signals. It reflects the ability of the DAQ to discriminate between two signals when the rates are high.

Single Arm Triggers in Each Spectrometer

R. Michaels (Aug 2003)

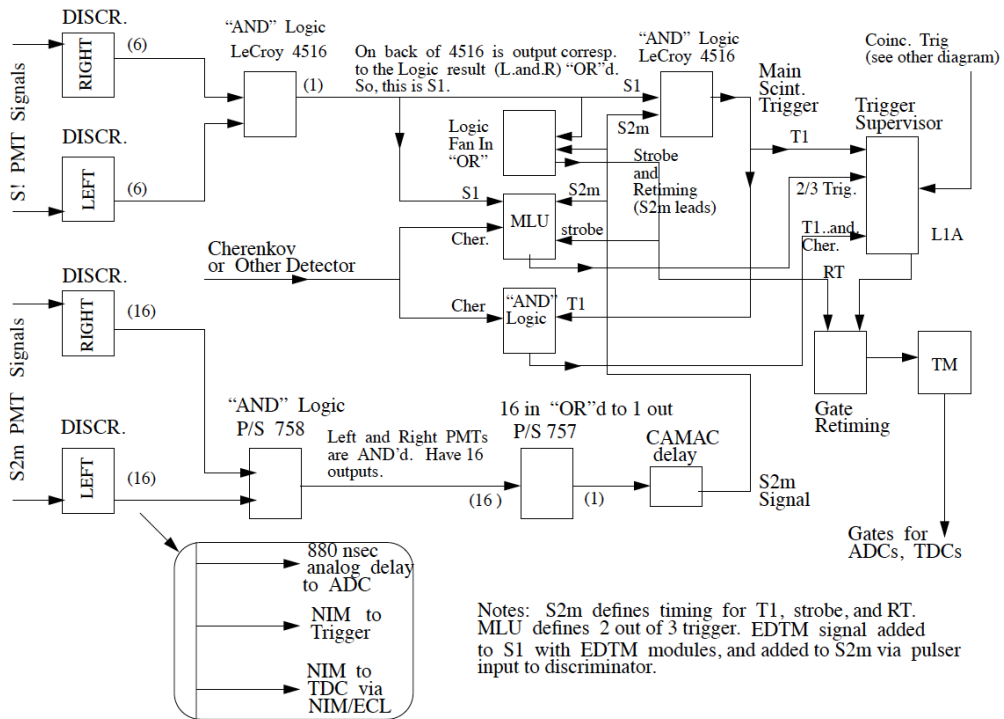


Figure 51: Diagram of the LHRS singles trigger logic[68].

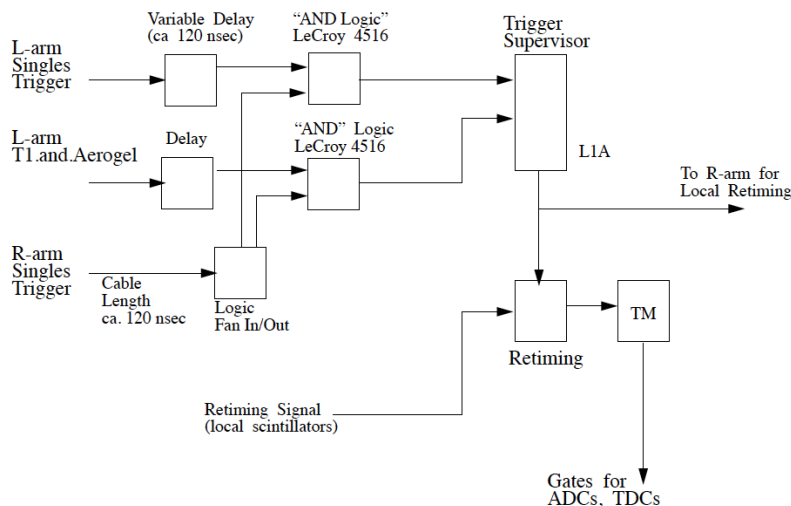


Figure 52: Diagram of the HRS coincidence trigger logic[68].

6 Modeling the Physics and the HRS

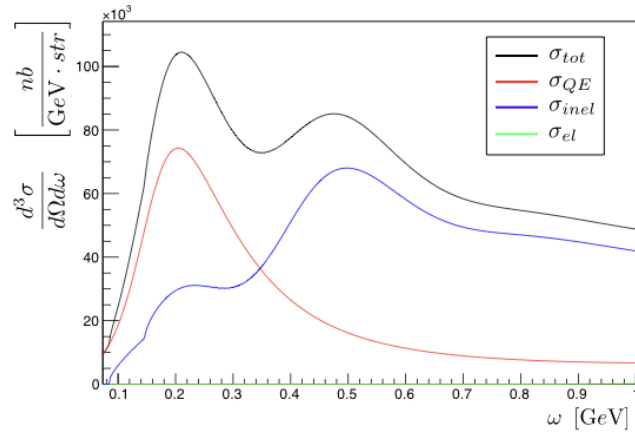
6.1 The Inclusive Cross Section Model

The model code (`externals_all_new.f`) calculates the inclusive differential cross section in the Born Approximation as the sum of quasi-elastic, inelastic, and elastic components,

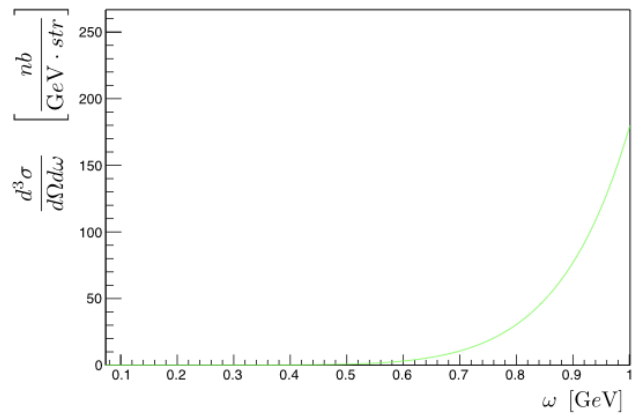
$$\sigma_{born} = \sigma_{QE} + \sigma_{inel} + \sigma_{el}. \quad (6.1)$$

The plots of Fig. 53 show the components of the model cross section for titanium at Kin5 (inclusive). The red line is the quasi-elastic component σ_{QE} . The blue line is the inelastic component σ_{inel} , which contains contributions from multiple particle resonances and meson exchange currents. The green line, also shown separately in Fig. 53b, is the elastic component σ_{el} . Although included in the calculation, the contribution of σ_{el} to the total inclusive cross section is negligible compared to the quasi-elastic and inelastic components. The cross sections per-nucleon for argon, titanium, and carbon are plotted in Fig. 54.

The code computes the quasi-elastic cross section based on the y -scaling analysis of Ciofi degli Atti *et al.* in Ref. [33]. The cross section is calculated



(a)



(b)

Figure 53: Plots of (a) the components of the titanium inclusive (Kin5) cross section model, and (b) a closer look at the elastic component σ_{el} .

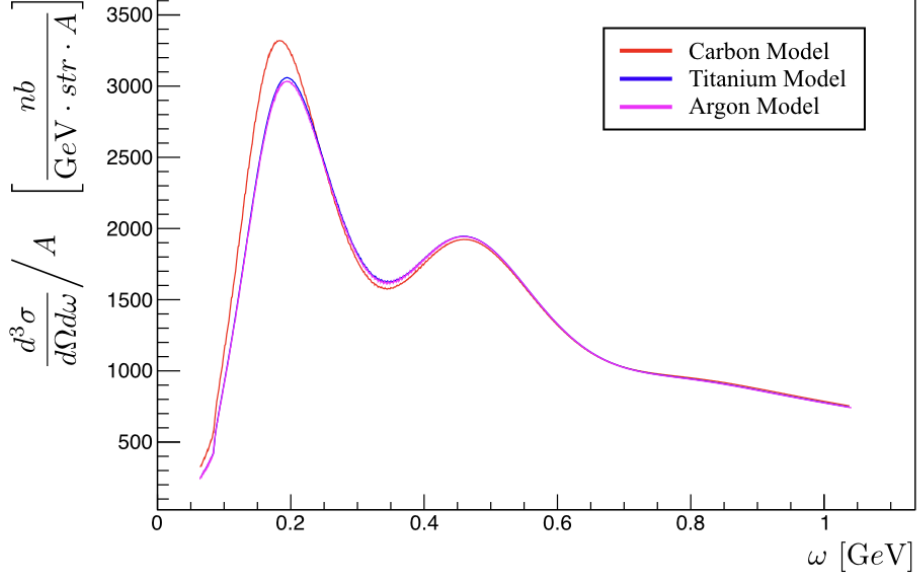


Figure 54: Plots of the inclusive differential cross sections-per-nucleon calculated from the model for carbon, titanium, and argon.

from

$$\sigma_{QE} = \sigma_M f_{rec}^{-1} \left(W_2^{QE} + 2W_1^{QE} \tan^2 \frac{\theta}{2} \right) \frac{\partial y}{\partial E'} f(y), \quad (6.2)$$

where σ_M is the Mott cross section defined in Eq. B.8, and f_{rec}^{-1} is the *recoil factor*, given by

$$f_{rec}^{-1} = \frac{M}{M + E_0(1 - \cos \theta)}. \quad (6.3)$$

The quasi-elastic structure functions in the third term are calculated from

$$W_1^{QE} = P_1(\tilde{Q}) \tau (ZG_{Mp}^2 + (A - Z)G_{Mn}^2) \quad (6.4a)$$

$$W_2^{QE} = \frac{P_2(\tilde{Q}) (ZG_{Ep}^2 + (A - Z)G_{En}^2) + W_1}{1 + \tau} \quad (6.4b)$$

where $\tau = Q^2/(4M^2)$. The nucleon electromagnetic form factors $G_{Ep,n}(Q^2)$ and $G_{Mp,n}(Q^2)$ are obtained from an empirical fit to world elastic scattering data[73]. The $P_{1,2}(\tilde{Q})$ are *Pauli suppression factors*, as defined in Ref. [74]. It was discovered that P_2 is incorrectly defined in the code, as the expression is missing a factor of $(4p_F)^{-1}$. However, as $4p_F \approx 1$ GeV, the effect of the error is minimal. Additionally, there seems to be a discrepancy between the

definitions of the variable \tilde{Q} (related to, but not equal to $\sqrt{Q^2}$) defined in the code, and that defined in Ref. [74].

The term $\frac{\partial y}{\partial E'}$ arises from a change of variables in the derivation of the scaling function. The derivative is calculated as

$$\frac{\partial y}{\partial E'} = \left[1 + \frac{(|\vec{\mathbf{q}}| + y)}{E_{p'}} \cdot \frac{E' - E_0 \cos \theta}{|\vec{\mathbf{q}}|} \right] / \left[\frac{y}{E_{A-1}} + \frac{(|\vec{\mathbf{q}}| + y)}{E_{p'}} \right], \quad (6.5)$$

where the energy terms are given by

$$E_{p'} = \sqrt{M_p^2 + (|\vec{\mathbf{q}}| + y)^2}, \quad (6.6a)$$

$$E_{A-1} = \sqrt{M_{A-1}^2 + y^2}. \quad (6.6b)$$

The scaling variable y is itself defined in the code as the solution to the quadratic equation $Ay^2 + By + C = 0$, where the coefficients are given by

$$A = 4|\vec{\mathbf{q}}|^2 - 4(E_0 - E' + M_A)^2 \quad (6.7a)$$

$$B = -4|\vec{\mathbf{q}}| [M_{A-1}^2 - M_p^2 - |\vec{\mathbf{q}}|^2 + (E_0 - E' + M_A)^2] \quad (6.7b)$$

$$C = (E_0 - E' + M_A)^4 + (M_{A-1}^2 - M_p^2 - |\vec{\mathbf{q}}|^2)^2 - 2(E_0 - E' + M_A)^2 (M_p^2 + |\vec{\mathbf{q}}|^2 + M_{A-1}^2) \quad (6.7c)$$

The function $f(y)$ in Eq. 6.2 is the longitudinal momentum distribution, as defined in Eq. 3.86. Ciofi degli Atti *et al.* in Ref. [33] parameterize the longitudinal momentum distribution as

$$f(y) = \frac{C_1 e^{-a^2 y^2}}{\alpha^2 + y^2} + C_2 e^{-b|y|} \quad (6.8)$$

with the parameters given in Tab. 9. Some of the parameters have been updated to better fit recent experimental data, with the original value given in parenthesis.

The inelastic cross section is computed within the code from

$$\sigma_{inel} = \sigma_M \left(W_2^{inel} + 2W_1^{inel} \tan^2 \frac{\theta}{2} \right), \quad (6.9)$$

with the inelastic structure functions given by

$$W_1^{inel}(\omega, Q^2) = \frac{F_1^{inel}}{M} \quad (6.10a)$$

Nucleus	C_1 [GeV]	α [GeV]	a [GeV $^{-1}$]	C_2 [GeV $^{-1}$]	b [GeV $^{-1}$]
$A = 2$	0.018	0.045	5.6 (6.1)	0.25	8.0 (6.0)
$A = 3$	0.041	0.083	6.1 (7.1)	0.396 (0.33)	8.0 (6.0)
$A = 4$	0.1272 (0.106)	0.167	5.8 (6.8)	0.78 (0.65)	8.0 (6.0)
$4 < A \leq 30$	0.083	0.166	5.1	0.684 (0.57)	8.0 (6.0)
$A \geq 30$	0.058	0.138	4.6	0.806 (0.62)	8.0 (6.0)

Table 9: Parameters for the longitudinal momentum distribution $f(y)$ used in the code. Parenthetical numbers correspond to the original parameterization of Eq. 6.8 in Ref. [33].

$$W_2^{inel}(\omega, Q^2) = \frac{F_2^{inel}}{\omega}. \quad (6.10b)$$

The structure functions are calculated from the inelastic form factors $F_{1,2}^{inel}$, which themselves are obtained from empirical fits to experimental inelastic scattering data.

The nucleon form factors $F_{1,2}^{p,n}$, split into longitudinal and transverse components, are themselves extracted from empirical fits to inelastic cross sections in the resonance region. These cross sections consist of contributions from particle resonances and a non-resonant background,

$$\sigma_{inel} = \sigma_{inel}^R + \sigma_{inel}^{NR}. \quad (6.11)$$

The (transverse) resonances and background contributions are parameterized according to Ref. [75] (see Ref. [76] for the longitudinal contributions).

Seven resonances in four resonance regions are considered. The first resonance is from the $P_{33}(1232)$ state, the $\Delta(1232)$ resonance discussed in §3.4. The second resonance region consists of two states, $S_{11}(1535)$ and $D_{13}(1520)$. The third region has resonances from the $S_{15}(1650)$ and $F_{15}(1680)$ states. A fourth resonance region was included with the $P_{11}(1440)$ Roper resonance and an additional wide resonance at $\sqrt{W^2} \approx 1.9$ GeV with angular momentum $\ell = 3$. Three decay modes, π , $\pi\pi$, and η , were considered for each resonance. The inelastic resonance cross section is calculated as the sum of these seven contributions,

$$\begin{aligned} \sigma_{inel}^R = & \sigma_{P_{33}(1232)} + \sigma_{S_{11}(1535)} + \sigma_{D_{13}(1520)} + \sigma_{S_{15}(1650)} \\ & + \sigma_{F_{15}(1680)} + \sigma_{P_{11}(1440)} + \sigma_{\ell=3} \end{aligned} \quad (6.12)$$

This holds for both transverse and longitudinal resonance cross sections, $\sigma_{inel}^{R,T}$, and $\sigma_{inel}^{R,L}$. The parameterizations and fits to the non-resonant background σ_{inel}^{NR} are discussed in Refs. [75, 76].

The longitudinal and transverse nucleon form factors are extracted from Eq. 6.11 through

$$F_1^{p,n} = \frac{\sigma_{p,n}^T |W^2 - M_p^2|}{8\pi^2 \alpha (\hbar c)^2}. \quad (6.13a)$$

$$F_L^{p,n} = \frac{\sigma_{p,n}^L 2x |W^2 - M_p^2|}{8\pi^2 \alpha (\hbar c)^2}. \quad (6.13b)$$

$$F_2^{p,n} = \frac{2x F_1^{p,n} + F_L^{p,n}}{(1 + 4x^2 M^2 / Q^2)} \quad (6.13c)$$

The contributions from meson exchange currents in the dip region, $F_{1,2}^{dip}$, are obtained from an empirical fit to data. Unfortunately, the code does not reference the source or data used in the fit, but assumes the contribution is purely transverse. The code assumes a rather complex parameterization for F_1^{dip} , and then calculates the second form factor as

$$F_2^{dip} = \frac{2x F_1^{dip}}{1 + \frac{4x^2 M^2}{Q^2}}. \quad (6.14)$$

The single-nucleon form factors and the dip-region contribution are combined to give the total inelastic form factors as

$$F_1 = A F_1^p + (A - Z) F_1^n + F_1^{dip} \quad (6.15a)$$

$$F_2 = A F_2^p + (A - Z) F_2^n + F_2^{dip}. \quad (6.15b)$$

Finally, the elastic contribution to the Born cross section is calculated in the model code from the general form

$$\sigma_{el} = \sigma_M f_{rec}^{-1} \left(W_2^{el} + 2W_1^{el} \tan^2 \frac{\theta}{2} \right), \quad (6.16)$$

with the elastic structure functions given by

$$W_1^{el}(\omega, Q^2) = 0 \quad (6.17a)$$

$$W_2^{el}(\omega, Q^2) = Z^2 F(Q^2)^2. \quad (6.17b)$$

Equation 6.17a is implemented in the code for nuclei with $A > 3$. The elastic form factor $F(Q^2)$ in Eq. 6.17b is obtained from a Fourier-Bessel series expansion of the nuclear charge density distribution (see Ref. [77]).

6.1.1 Calculating the Cross Section

For each run in the inclusive delta scan, a discrete phase space grid in the scattering angle θ_e and final electron energy E' is generated (see Fig. 55). The grid code calculates important kinematic values over a discrete range of possible scattering angles $[\theta_e^{min}, \theta_e^{max}]$ and possible final electron energy values $[E'_{min}, E'_{max}]$. The range of possible E' values is designed to cover the momentum range of the delta scan, and the range of angles must include the experimental scattering angle.

For each scattering angle, Q^2 and W^2 are calculated and organized into a table. This table then serves as the input for the model code that calculates the inclusive cross section according to Eq. 6.1 for each point (E'_i, θ_i) on the grid.

The cross section $\sigma(E', \theta)$ for an arbitrary point, where $E'_i < E' < E'_{i+1}$ and $\theta_j < \theta < \theta_{j+1}$, is calculated by bilinear interpolation across the phase space grid (see Fig. 55). The result of this calculation is

$$\begin{aligned} \sigma(E', \theta) = & \left(\frac{\theta_{i+1} - \theta}{\theta_{i+1} - \theta_i} \right) \left(\frac{E'_{j+1} - E'}{E'_{j+1} - E'_j} \right) \sigma_{born}(E'_j, \theta_i) \\ & + \left(\frac{\theta_{i+1} - \theta}{\theta_{i+1} - \theta_i} \right) \left(\frac{E' - E'_j}{E'_{j+1} - E'_j} \right) \sigma_{born}(E'_{j+1}, \theta_i) \\ & + \left(\frac{\theta - \theta_i}{\theta_{i+1} - \theta_i} \right) \left(\frac{E'_{j+1} - E'}{E'_{j+1} - E'_j} \right) \sigma_{born}(E'_j, \theta_{i+1}) \\ & + \left(\frac{\theta - \theta_i}{\theta_{i+1} - \theta_i} \right) \left(\frac{E' - E'_j}{E'_{j+1} - E'_j} \right) \sigma_{born}(E'_{j+1}, \theta_{i+1}) \end{aligned} \quad (6.18)$$

where the $\sigma_{born}(E'_j, \theta_i)$ are given in Tab. 10.

After the Born and radiated cross sections are calculated, a secondary code calculates the *radiative correction factor*, R_{corr} , defined as the ratio of σ_{rad} , the radiated cross section, to σ_{born} , the Born cross section:

$$R_{corr} = \frac{\sigma_{rad}}{\sigma_{born}}. \quad (6.19)$$

This factor can be used to estimate the magnitude of the systematic uncertainty from the radiative corrections (see §10.2.1). The Born cross section and the correction factor, as discrete functions of final electron energy E' , are collected into a table, organized by increasing scattering angle. The layout of the table is shown in Tab. 10.

The actual calculation in Eq. 6.18 is carried out in an external code (`rc_mod.f`). This code also applies the bilinear interpolation to the radiative

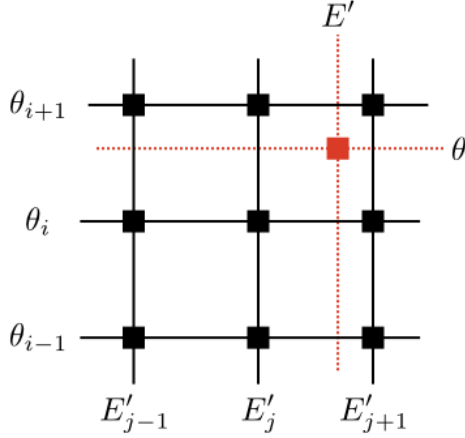


Figure 55: Discretization of the (E', θ) phase-space. The model calculates the inclusive cross section for each point on the grid. The cross section for a general set of coordinates (E', θ) , indicated by the red box, is given by bilinear interpolation across the phase space grid.

correction factor of Eq. 6.19. This interpolation code is called within another code which is discussed in §6.1.2.

6.1.2 Corrections to the Cross Section

There is an additional code (`recon_mc.f`) that applies multiple correction factors to the inclusive cross section calculated previously in §6.1 and §6.1.1.

The first correction factor is given as

$$f = \frac{L \cdot \Phi_{MC} \cdot B(I)}{N_{MC} \cdot PS} \cdot CLT \cdot ELT \cdot \varepsilon_{VDC} \cdot \varepsilon_{trig} \cdot \varepsilon_{cer} \cdot \varepsilon_{cal}, \quad (6.20)$$

where PS is the DAQ pre-scale factor and N_{MC} is the number of generated MC events. The ε 's are the detector efficiencies (see §8), and CLT and ELT are the computer and electronic livetimes (see §5.5). The function $B(I)$ is the target density correction factor defined in §4.3.3.

The quantity L is the integrated luminosity, and is calculated as

$$L = \frac{(\rho l) \cdot N_A}{M} \cdot \frac{Q_{avg}^{BCM}}{e} \quad (6.21)$$

where $Q_{avg}^{BCM} = (Q_1^{BCM} + Q_2^{BCM})/2$ is the average charge measured by both beam current monitors, and M is the molar mass of the target. The dimen-

A	Z	E_0	E'	θ_e	σ	R_{corr}
\vdots	\vdots	\vdots	E'_{min}	\vdots	\vdots	\vdots
A	Z	E_0	\vdots	θ_e^{min}	σ_{born}	$\frac{\sigma_{rad}}{\sigma_{born}}$
\vdots	\vdots	\vdots	E'_{max}	\vdots	\vdots	\vdots
\vdots	\vdots	\vdots	\vdots	\vdots	\vdots	\vdots
\vdots	\vdots	\vdots	E'_{min}	\vdots	\vdots	\vdots
A	Z	E_0	\vdots	θ_e^{max}	σ_{born}	$\frac{\sigma_{rad}}{\sigma_{born}}$
\vdots	\vdots	\vdots	E'_{max}	\vdots	\vdots	\vdots

Table 10: Layout of the inclusive Born cross section table from the inclusive model. The last column R_{corr} is the radiative correction factor.

sions of the integrated luminosity should be expressed in inverse nano-barns (nb^{-1}).

The quantity Φ_{MC} is a monte-carlo phase space factor, given by

$$\Phi_{MC} = \Delta\theta \Delta\phi \Delta p, \quad (6.22)$$

with units of $\text{rad}^2 \text{MeV}$. The Δ 's in Eq. 6.22 represent the ranges of the variables considered in the monte-carlo simulation.

The phase space factor just defined in Eq. 6.22 needs an additional correction factor. The MC generates events in the *spectrometer angles*, *not* in the *physics angles* θ and ϕ . Thus, to transfer to the physics angles, each event requires a Jacobian to account for the mapping between the solid angle on the unit sphere and the MC phase-space volume[78]. The Jacobian J is defined as

$$J = \cos^{-3}(\Delta\theta), \quad (6.23)$$

where $\Delta\theta = \theta - \theta_c$ is the difference between the event angle and the spectrometer central angle θ_c . The event angle θ is defined as

$$\theta = \cos^{-1}(\cos(\theta_c + \theta_{MC}) \cos(\phi_{MC})), \quad (6.24)$$

where, θ_{MC} and ϕ_{MC} are the angles generated by the MC for the corresponding event.

Another correction factor Δ_{cor} is defined as a fifth-order polynomial in dp_{MC} . This quantity is an optical correction factor for the LHRS most likely taken from a fit to data, however, no comment on its origin is made in the code.

This code reads in the contents of the NTUPLE (or Tree, see §C.1) generated from the single arm MC (see §6.3.1), and re-writes them to a new NTUPLE. The inclusive cross sections calculated from Eq. 6.18 are also written to the new NTUPLE with the following corrections

$$\sigma \cdot \frac{\Delta_{cor}}{\cos^3(\Delta\theta)} \quad (6.25a)$$

$$\sigma \cdot \frac{\Delta_{cor}}{\cos^3(\Delta\theta)} \cdot \frac{f}{R_{corr}} \quad (6.25b)$$

In Eq. 6.25b, R_{corr} is the ratio defined previously (in Eq. 6.19), interpolated according to Eq. 6.18.

6.2 Phenomenological Modeling of Final State Interactions

The effects of final state interactions are determined by comparing the reduced cross section in PWIA to that in DWIA. The *reduced cross section* is defined as

$$\sigma_{red} = \frac{\sigma_{exp}}{K \cdot \sigma_{ep}} \quad (6.26)$$

where σ_{exp} is the experimentally measured cross section, K is a kinematic factor and σ_{ep} is the off-shell electron-proton cross section. DWIA incorporates FSI through use of a distorting optical potential $\tilde{V}(r)$, the effects of which on the cross section were discussed in §3.5.3.

The optical potentials are derived using the scalar-vector model of Dirac phenomenology[79]. The potential is described as the sum of a *scalar optical potential* $\tilde{V}_s(r)$ and a *vector optical potential* $\tilde{V}_v(r)$, which are both of the form $\tilde{V}(r) = U(r) + iW(r)$. The real and imaginary parts of \tilde{V} are further decomposed into the product of a strength factor and a lineshape/geometry function. Phenomenologically, the scalar and vector potentials are modeled as

$$\tilde{V}_s(r; E, A) = U_s(E, A)f_s(r; E, A) + iW_s(E, A)g_s(r; E, A) \quad (6.27a)$$

$$\tilde{V}_v(r; E, A) = U_v(E, A)f_v(r; E, A) + iW_v(E, A)g_v(r; E, A). \quad (6.27b)$$

With this notation, the full expression for the distorting optical potential is given by

$$\begin{aligned} \tilde{V}(r; E, A) = & U_v(E, A)f_v(r; E, A) + U_s(E, A)f_s(r; E, A) \\ & + i[W_v(E, A)g_v(r; E, A) + W_s(E, A)g_s(r; E, A)]. \end{aligned} \quad (6.28)$$

The *strengths* $U_{s,v}(E, A)$ and $W_{s,v}(E, A)$ are parametrized in terms of the proton center-of-mass energy E and the target mass number A . The functions $f_{s,v}(r; E, A)$ and $g_{s,v}(r; E, A)$, referred to as *geometries*, are parametric functions in E and A of the radial coordinate r that describe the shape of the potential.

The geometries are often modeled by Woods-Saxon functions of the form $f(x) = (1 + e^x)^{-1}$. However, the authors in Refs. [80, 79] developed a new geometry given in terms of the hyperbolic cosine, which showed an improved fit to experimental data compared to Woods-Saxon geometries. Mathematical expressions for the parameterizations of the strengths and geometries in Eqs. 6.27 can be found in Refs. [80, 79].

The E12-14-012 analysis used three different phenomenological models for the distorting optical potential. The first model, referred to as the *democratic optical potential* (DEM), was obtained from fits to 204 sets of elastic proton-nucleus scattering data on 33 nuclear targets from ^4He to ^{208}Pb (excluding argon) at energies from 20 – 1040 MeV[80]. The remaining two optical potentials used come from energy-dependent and A -dependent (EDAD) fits to elastic proton scattering data from 5 nuclear targets (again, excluding argon) in the same energy range[79]. The potentials derived from these fits are referred to as EDAD1 and EDAD3. The democratic optical potential was the primary one utilized in the E12-14-012 analysis, while EDAD1 and EDAD3 were used to determine the effect of choice of \tilde{V} on the cross sections and to calculate systematic uncertainty due to the FSI correction.

As the phenomenological optical potentials were obtained from data that did *not* include argon, their ability to accurately describe the scattering response from argon was initially called into question. The DEM, EDAD1, and EDAD3 optical potentials were tested against experimental $^{40}\text{Ar}(p, p')$ data collected by Ref. [81] at the Los Alamos Meson Physics Facility (LAMPF). As seen in Fig. 56, the (p, p') cross sections calculated using the DEM, EDAD1, and EDAD3 optical potentials are nearly identical, and are a decent fit to the experimental data. Although the dynamics of (p, p') scattering differ from those of (e, e') scattering, the goodness-of-fit of all three optical potentials to the LAMPF argon data suggests that they will be more than adequate to describe the electron-scattering dynamics.

The reduced cross sections in PWIA (blue) and DWIA (red) for $1d_{3/2}$ proton knockout from argon are plotted in Fig. 57 and Fig. 58. These reduced cross sections were obtained using the relativistic $(e, e'p)$ model of Ref. [82]. The vertical dotted lines in Fig. 57 show the shift in the peak of missing momentum, due to the real part of the optical potential. The shift Δ is calculated as the difference in missing momentum between the peaks of the DWIA and PWIA reduced cross sections. Figure 58 shows the reduction

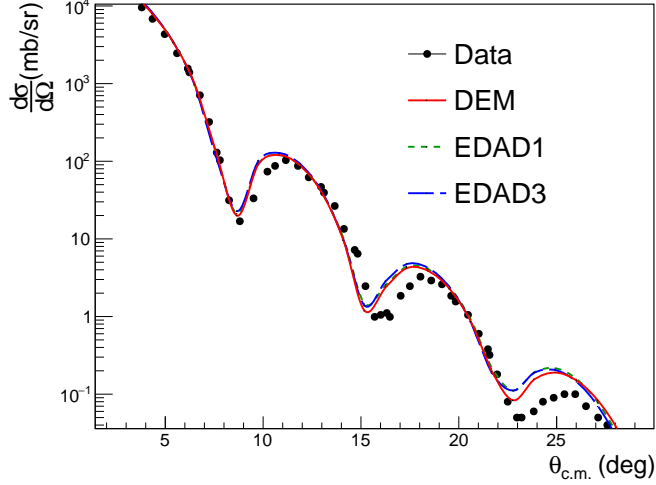


Figure 56: Differential cross section for $^{40}\text{Ar}(p, p')$ scattering at 0.8 GeV versus scattering angle[24]. The cross sections calculated using the DEM (red line), EDAD1 (green line), and EDAD2 (blue line) are compared to the LAMPF data (black dots).

of σ_{red} due to the imaginary part of the optical potential. This reduction in strength is described by the ratio of the peaks of the DWIA to PWIA reduced cross sections, $\frac{\sigma_{DWIA}}{\sigma_{PWIA}}$. The DWIA-to-PWIA ratio is calculated between the dotted lines for $|\vec{p}'| > |\vec{q}|$, and between the solid lines for $|\vec{p}'| < |\vec{q}|$. The shifts and DWIA-to-PWIA ratios are calculated for each shell, for both positive and negative missing momentum.

The FSI correction is applied to the SIMC result by the following process. Let $H_X^{\text{SIMC}}(m, L, U)$ be a m -bin histogram on the interval $[L, U] \subset \mathbb{R}$ of the SIMC quantity X , which in this case is the missing momentum. The FSI correction is applied to H_X^{SIMC} on an event by event basis. For each event i , the missing momentum and energy are calculated. The shift Δ and ratio $\frac{\sigma_{DWIA}}{\sigma_{PWIA}}$ are then read in from a database of values. The missing momentum of event i is corrected by the shift to form the new missing momentum $P_{miss}^i = P_{miss}^i + \Delta$. Next, the new missing momentum is used to re-calculate the missing energy E'_{miss} . The new missing momentum and energy are then weighted by the cross section ratio $\frac{\sigma_{DWIA}}{\sigma_{PWIA}}$. Some of the shifts and ratios calculated for the three optical potential fits in the region $p_{miss} > 0$ are listed in Tab. 11.

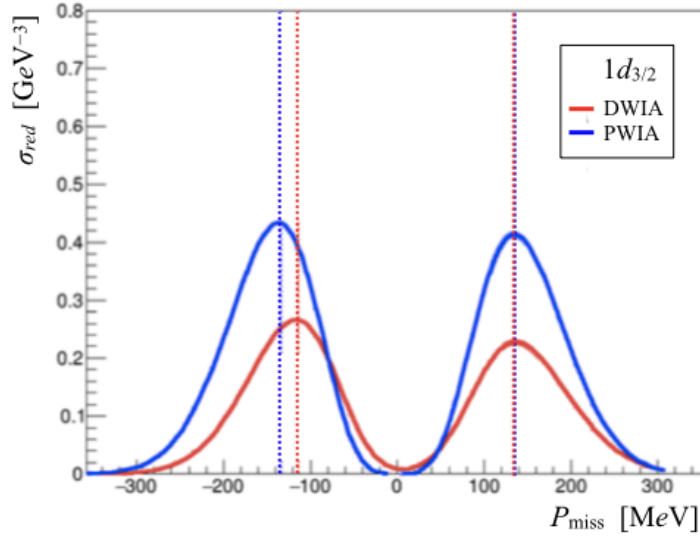


Figure 57: Plots of PWIA (blue) and DWIA (red) reduced cross sections for $1d_{3/2}$ proton knockout from argon. The missing momentum shift Δ is calculated between the red and blue vertical dotted lines.

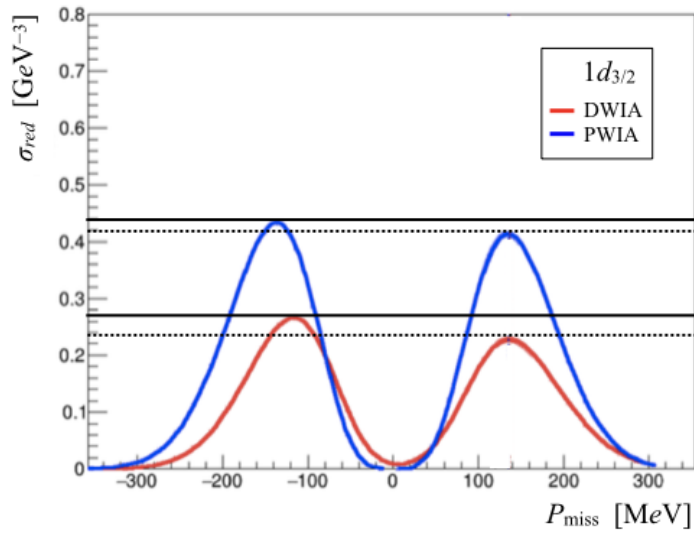


Figure 58: Plots of PWIA (blue) and DWIA (red) reduced cross sections for $1d_{3/2}$ proton knockout from argon. The ratio is calculated between the dotted (solid) lines for parallel (anti-parallel) kinematics.

Shell	Shift Δ [MeV]			$\sigma_{DWIA}/\sigma_{PWIA}$		
	EDAD1	EDAD3	DEM	EDAD1	EDAD3	DEM
$1d_{3/2}$	1.5	-2.0	1.5	0.58	0.57	0.58
$2s_{1/2}$	8.0	7.0	8.0	0.78	0.78	0.78
$1d_{5/2}$	-2.0	-6.5	-3.0	0.57	0.57	0.58
$1p_{1/2}$	12.5	9.0	12.5	0.43	0.39	0.42
$1p_{3/2}$	9.5	5.0	9.0	0.47	0.44	0.46
$1s_{1/2}$	13.0	10.0	13.0	0.42	0.38	0.41

Table 11: Missing momentum shifts and DWIA to PWIA reduced cross section ratios calculated from the three optical potential fits for $p_m > 0$ [24].

6.3 The HRS Monte-Carlo Model

Monte-Carlo (MC) simulation has become a vital aspect in the analysis of scattering experiments, as the experimental data must be compared to a theoretical prediction to extract the physics[6]. For E12-14-012, the theoretical prediction relies on an accurate simulation of the Hall A spectrometers. A uniform distribution of particles is randomly generated by a monte-carlo simulation, and then “sent through” the spectrometer. The HRS’s are a combination of several detectors, each of which have an effect on a particle as it passes through. Thus, any accurate model of the HRS must reflect the detector acceptance and response into the analysis of the data. The random nature of monte-carlo simulation makes it a perfect tool for the analysis of our experimental data[6].

6.3.1 Single Arm Monte-Carlo

The single arm monte-carlo code (`mc_hrs_single.f`) generates simulations of electron scattering events in the left arm of the HRS. A monte-carlo event is created by generating the point (x, y, z) (in units of cm) within the target. The beam width x and beam height y are chosen from truncated Gaussian distributions, while the interaction point z is chosen uniformly. Next, the code generates (θ, ϕ, dp) , the corresponding scattering angles and fractional momentum, from independent uniform distributions. The code then calculates the initial momentum p_i and initial energy E_i of this event from the generated dp .

The effects of energy loss are calculated before and after the scattering, taking into account the particles passage through the target, aluminum, air,

and mylar material.

$$E_{loss}^{total} = E_{loss}^{targ} + E_{loss}^{Al} + E_{loss}^{air} + E_{loss}^{mylar} \quad (6.29)$$

The total energy loss is subtracted from the initial energy to give the energy of the particle-event before it reaches the spectrometer as $E_s = E_i - E_{loss}^{total}$.

The code then checks whether the generated event would successfully pass through the LHRS. The transport through the spectrometer is handled by an external code (`mc_hrs1.f`) which consists of a series of logic tests on the acceptance variables. If the MC-event passes the test, the reaction vertex z is reconstructed from the (θ, ϕ, dp) , y_{tar} , and spectrometer offsets. The reconstructed vertex points z_{tar}^{recon} , y_{tar}^{recon} , and the original (θ, ϕ, dp) , are then written into an NTUPLE, along with other important quantities, such as the focal plane coordinates, energy and momentum, and energy loss.

6.3.2 SIMC

The JLab monte-carlo code known as SIMC[83] was used to analyze the exclusive data. The code is able to handle several different types of coincidence scattering scenarios. Besides $(e, e'p)$, SIMC is also capable of simulating $(e, e'\pi^\pm)$ and $(e, e'K^\pm)$ for several different nuclei. SIMC generates specific events over a limited phase space that matches the HRS acceptance. Further physical processes that may produce background events are not simulated in SIMC. Final state interactions between the knocked out nucleon and recoiling nuclear system are not accounted for in SIMC[84].

A weight must be applied to each SIMC event to accurately model the data. The weighting factor applied to the histograms is `Weight·Normfac`/ N_{MC} , where N_{MC} is the number of generated monte-carlo events, and `Weight` and `Normfac` are histograms generated by SIMC. The quantity `Weight`, shown in Fig. 59 for argon Kin2, is calculated for each SIMC event by combining weights from the model spectral function, the off-shell electron-proton cross section, and Coulomb corrections. The normalization factor `Normfac` is a constant that depends on the target and beam luminosity[85].

6.3.3 Comparing Data to Monte-Carlo Simulation

A significant portion of the data analysis consists of comparing the experimental data to monte-carlo simulation. This is an important step in the analysis process, for accurate monte-carlo simulation is crucial to extracting physics from experimental data, as mentioned in §6.3.

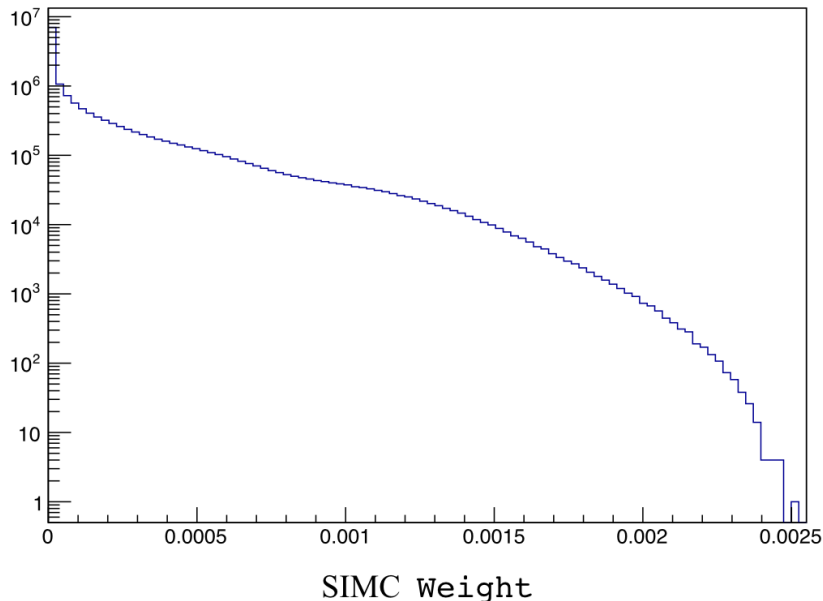


Figure 59: Histogram of the SIMC quantity `Weight`, generated with 15 million MC events for argon Kin2.

First, the kinematic acceptance variables in the target coordinate system $(\theta_{tg}, \phi_{tg}, dp_{tg}, z_{tg}, y_{tg})$ were compared to the monte-carlo simulation result to ensure that the code was accurately simulating the transport through the spectrometer. These comparisons partially informed the placement of the acceptance cuts on the HRS acceptance variables.

Also of importance to the analysis is the data-to-MC ratio. A histogram of this ratio reveals how well the monte-carlo simulation models the acceptance of the spectrometers. For the kinematic variables mentioned previously, an approximately constant data-to-MC ratio means that the monte-carlo model accurately models the HRS acceptance. Cuts are applied to the variable histograms to exclude regions where the experimental data and monte-carlo disagree.

After the acceptance cuts and other selection cuts are determined, the analysis continued to more important quantities. Of crucial importance to the analysis was the comparison of the experimental missing energy and missing momentum spectra to the monte-carlo simulation based on the model spectral function. The missing momentum, written explicitly in terms of the kinematic variables, is

$$P_{miss} = P' - \sqrt{k'^2 \sin^2 \theta_e - (E_0 - k' \cos \theta_e)^2}. \quad (6.30)$$

Region:	Ar	Ti
I	$0 \leq E_{miss} \leq 27$	$0 \leq E_{miss} \leq 30$
II	$27 \leq E_{miss} \leq 44$	$30 \leq E_{miss} \leq 54$
III	$44 \leq E_{miss} \leq 70$	$54 \leq E_{miss} \leq 90$

Table 12: Definitions of the shell-cuts (regions) applied to the missing energy spectrum. All energy units are MeV.

This is then used to calculate the missing energy as

$$E_{miss} = \omega - \sqrt{M_p^2 + P'^2} - \sqrt{M_{A-1}^2 + P_{miss}^2} + M_A. \quad (6.31)$$

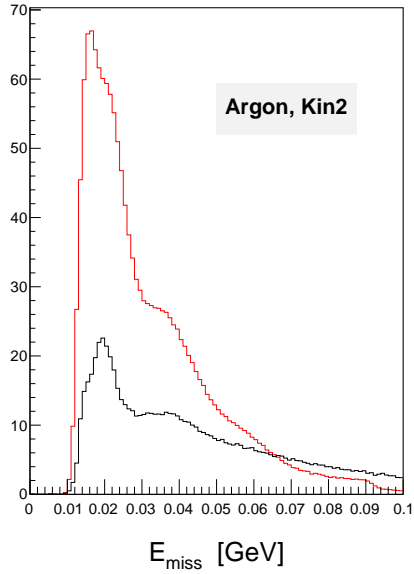
For titanium, the masses used in Eq. 6.31 are $M_A = 45.07$ MeV and $M_{A-1} = 44.13$ MeV; for argon, they are $M_A = 37.558$ MeV and $M_{A-1} = 36.62$ MeV. Histograms of Eq. 6.30 and Eq. 6.31 with SIMC result are shown in Figs. 60 and Figs. 61, respectively.

The missing energy spectrum was split into three regions to better analyze the contribution from each individual shell. These *shell cuts* are defined in Tab. 12, and histograms of the missing energy spectra with the shell-cut regions highlighted for argon and titanium at Kin2 are shown in Fig. 62. For titanium, region I highlights contributions from the $1f_{7/2}$, $1d_{3/2}$, $2s_{1/2}$, and $1d_{5/2}$ shells. Region II includes contributions from the $1p_{1/2}$ and $1p_{3/2}$ shells, and region III isolates the contribution from the $1s_{1/2}$ shell. The same applies for argon, without any contribution from a $1f_{7/2}$ shell in region I.

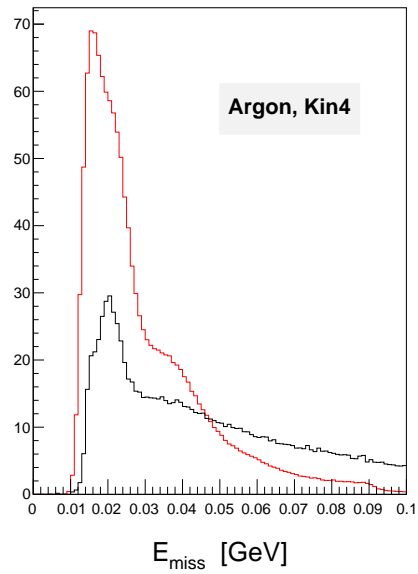
The shape of the missing energy distribution $S(E_m)$ for titanium in Fig. 16b allows for clean separation of the regions with the shell-cuts described in Tab. 12. However, this is not the case for the argon missing energy distribution (Fig. 16a). For example, the $1p_{1/2}$ and $1p_{3/2}$ shells in argon still have a significant contribution in region I ($E_m < 27$ MeV). Contributions from these states also bleed into region III, with the $1s_{1/2}$ shell also contributing strength in region II.

Histograms of the missing momenta corresponding to each region, with the SIMC result for comparison, are shown in Figs. 63 and Figs. 64 for argon Kin2 and Kin4, respectively. The same plots for titanium are given in Figs. 65 for Kin2 and Figs. 66 for Kin4.

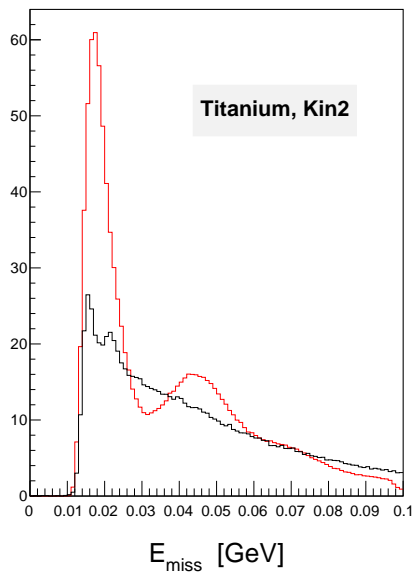
It is clear from inspection of these histograms that the monte-carlo simulation does not accurately re-produce the experimental yield. SIMC over estimates the yield for all simulated kinematical settings and targets. However, this was to be expected, as SIMC does not account for final state interactions, with the exception of the nuclear transparency.



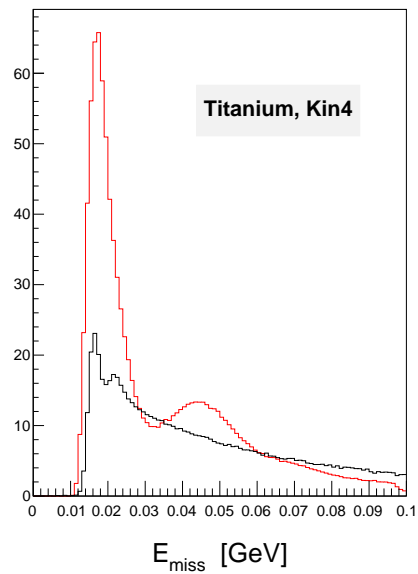
(a)



(b)

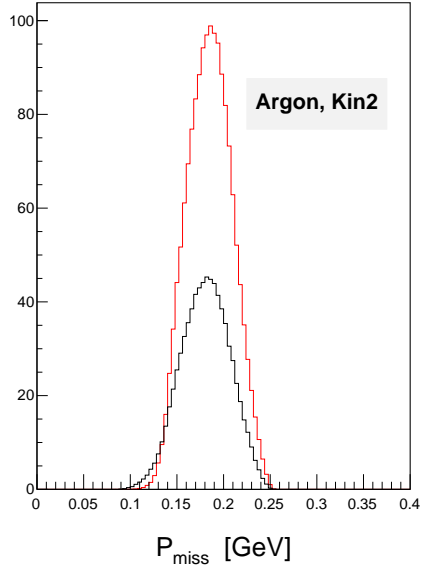


(c)

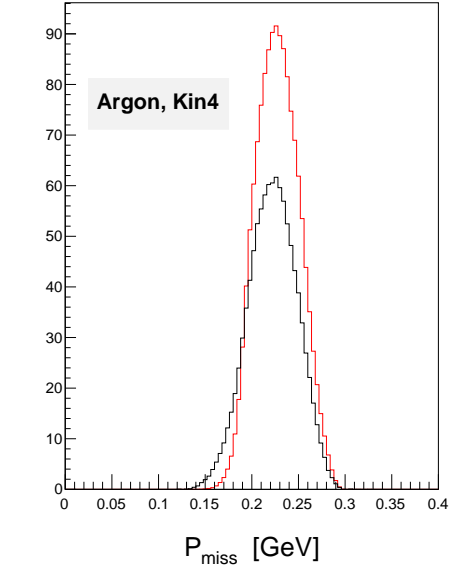


(d)

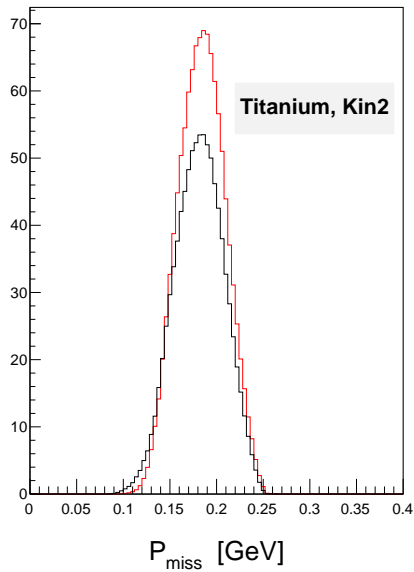
Figure 60: Histograms of the missing energy spectra for argon (a) Kin2, (b) Kin4, and titanium (c) Kin2 and (d) Kin4. The black line represents the data, while the red line represents the SIMC prediction (without FSI corrections).



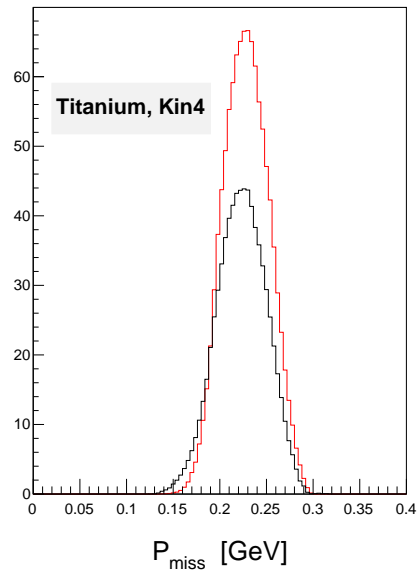
(a)



(b)



(c)



(d)

Figure 61: Histograms of the missing momentum spectra for argon (a) Kin2, (b) Kin4, and titanium (c) Kin2 and (d) Kin4. The black line represents the data, while the red line represents the SIMC prediction (without FSI corrections).

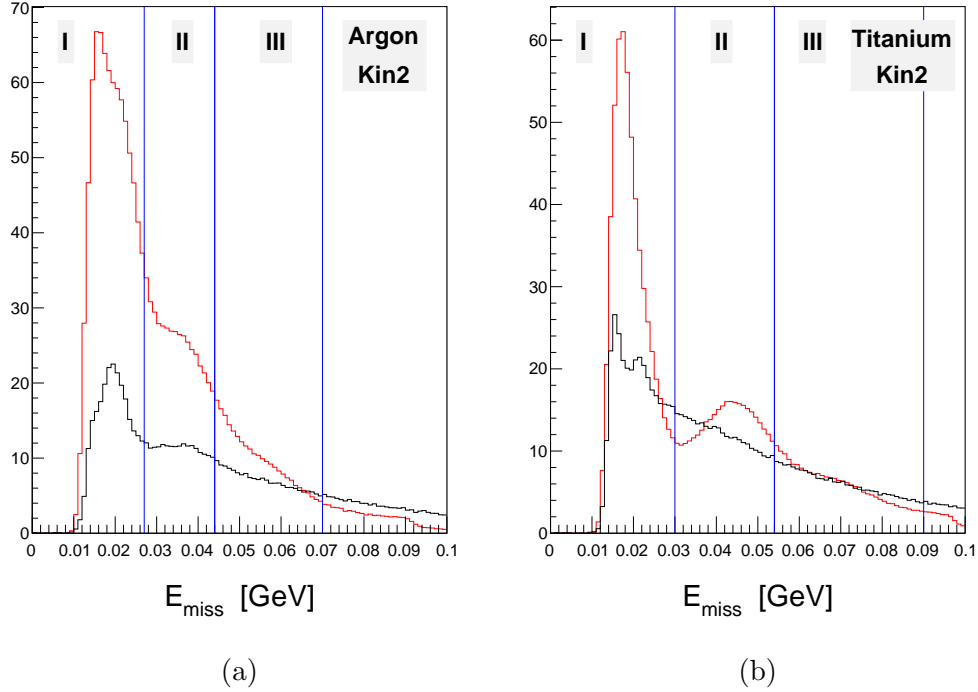


Figure 62: Histograms of the missing energy spectra (black line) and SIMC prediction (red line, no FSI) for (a) argon and (b) titanium at Kin2, showing the three shell cut regions defined in Tab. 12.

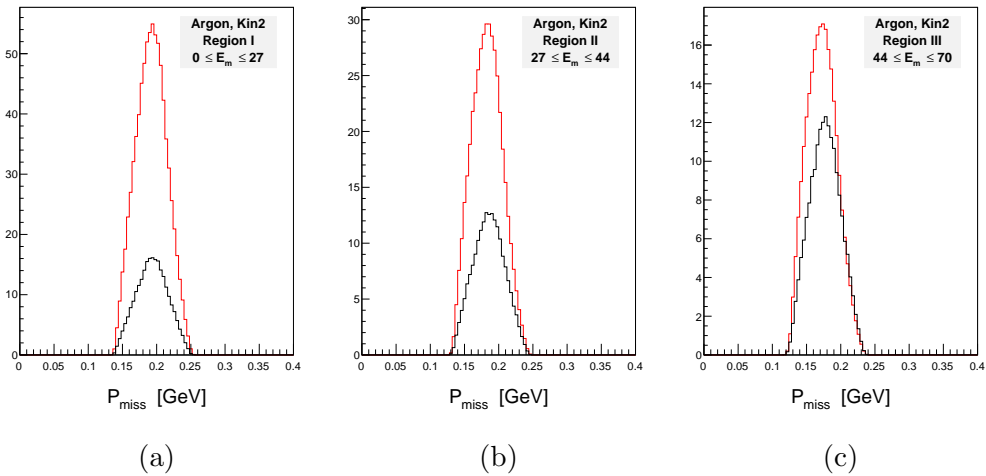


Figure 63: Histograms of the missing momentum for argon Kin2 with (a) region I, (b) region II, and (c) region III E_{miss} shell cuts applied.

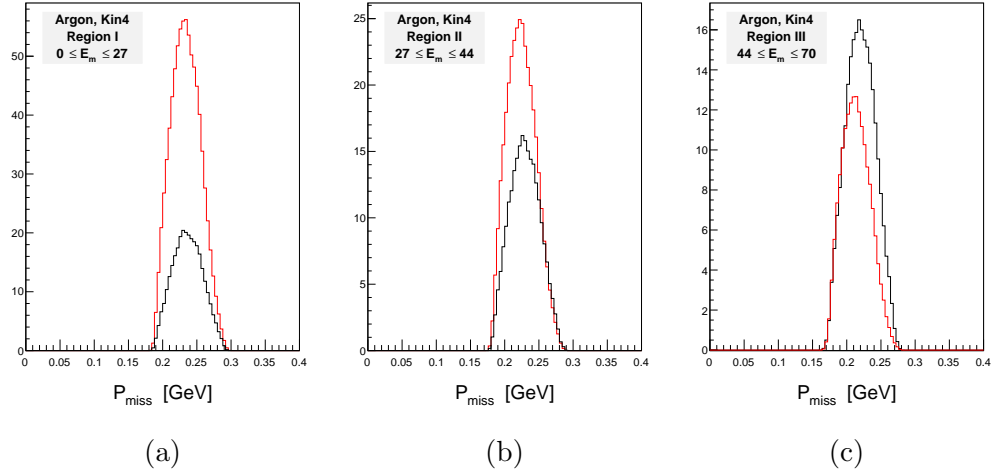


Figure 64: Histograms of the missing momentum for argon Kin4 with (a) region I, (b) region II, and (c) region III E_{miss} shell cuts applied.

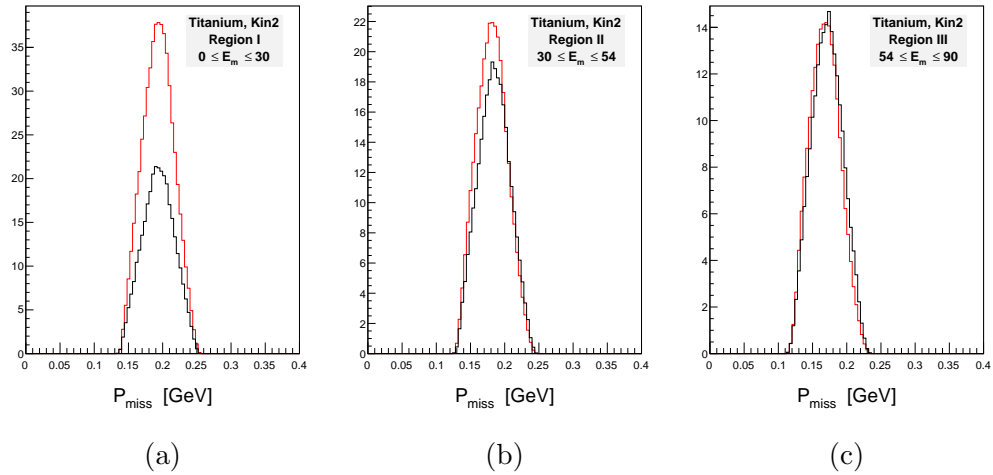


Figure 65: Missing momentum histograms for titanium Kin2 with (a) region I, (b) region II, and (c) region III E_{miss} shell cuts applied.

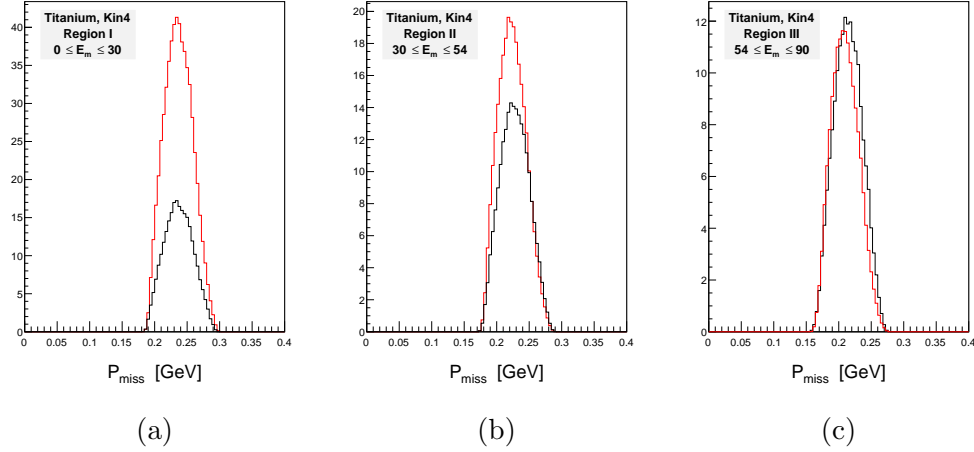


Figure 66: Histograms of the missing momentum for titanium Kin4 with (a) region I, (b) region II, and (c) region III E_{miss} shell cuts applied.

7 E12-14-012 Data Analysis

7.1 Data Acquisition

Raw event data from the Hall A spectrometers is collected using the CEBAF On-line Data Acquisition System (CODA). To collect data, CODA is started, and allowed to run for a variable length of time, usually one hour. The data collected during this time are aggregated into a single file, called a *run*, and assigned a number, the *run number*. The data from each run is analyzed and processed into histograms by the Event Scanning Program for Hall A Collaboration Experiments (ESPACE) software[58]. This process is referred to as *replaying* the CODA run. After replaying, the data is accessed using the ROOT analysis software developed at CERN. The data acquisition system as a whole is often referred to as the DAQ.

Periodically during the data collection, several CODA runs were collected without any electron beam on the target. These runs, known as *cosmics*, are used to collect environmental background events caused by cosmic radiation that reaches the Earth's surface. Cosmic runs are used in the spectrometer calibration process. CODA runs used to collect actual physics data are referred to as *production* runs.

7.2 Event Selection Criterion

When several CODA runs are combined into one data set, all events are included. In order to isolate the physics events of interest, *cuts* are applied to the data set to remove the unwanted events. A *cut* is defined as a logic statement or series of logic statements that are applied to the data set under consideration. The following subsections detail the cuts applied to the data and monte-carlo simulation histograms.

7.2.1 Acceptance Cuts

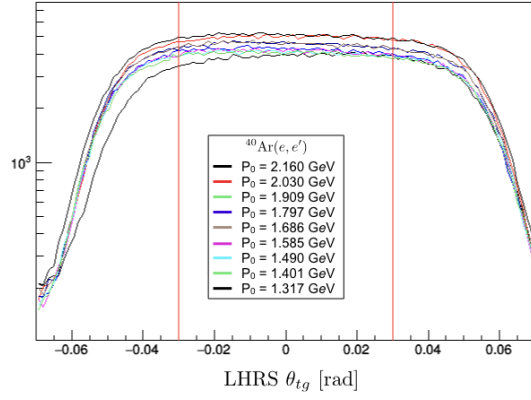
Acceptance cuts are applied to the data to exclude events on or near the edge of the spectrometer acceptance. Particles near the edge of the acceptance may have experienced additional interactions while traveling through the spectrometer, such as scattering off the wall of the beam enclosure; an interaction that alters the particle's momentum.

The acceptance cuts are applied to the spatial variables in the target coordinate system (see §4.5.5) such as θ_{tg} , ϕ_{tg} , and the fractional HRS momentum dp_{tg} . The plots of Figs. 68 - 67 show the acceptance histograms for argon and titanium for each of the nine central momentum settings of the inclusive delta scan. The bounds of the acceptance cuts are determined by visual inspection of the histograms, as well as by examining plots of detector efficiency as a function of the acceptance variables. The efficiency plots are relatively flat, but fall dramatically on the edge of the acceptance, which helps determine the cut bounds.

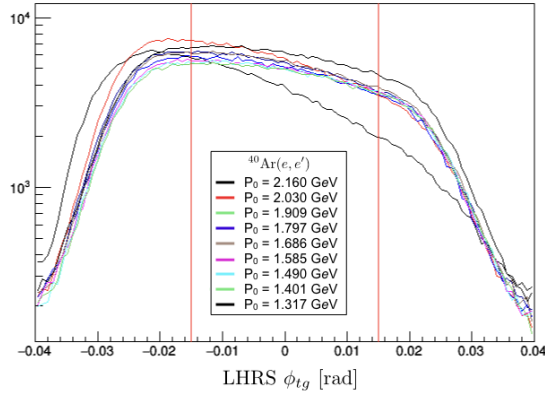
Cuts on the spatial extension of the target are also considered among the acceptance cuts. Figure 69 shows histograms of z_{tg}^e , the length of the argon target reconstructed from the LHRS VDC. The two peaks at either end are events from the aluminum end caps of the argon gas target cell. These events are removed by cutting z_{tg}^e within the flat region of the spectrum. Figure 70 shows y_{tg}^e for the carbon foil target delta scan. A Gaussian distribution of the form

$$Ae^{-\frac{(x-\mu)^2}{2\sigma^2}} \quad (7.1)$$

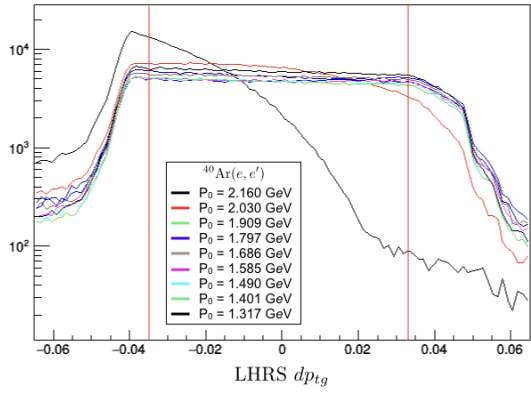
is fit to the peak of y_{tg}^e , from which the *amplitude* A , *mean* μ (peak location), and *standard deviation* σ (peak spread) are determined. The cut on y_{tg}^e keeps events within five standard deviations from the peak center. The acceptance cuts applied to the data from the inclusive delta scan are summarized in Table 13.



(a)

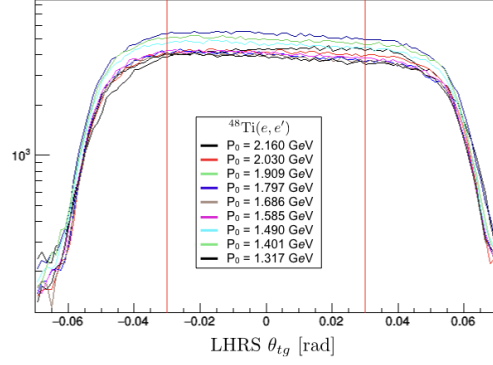


(b)

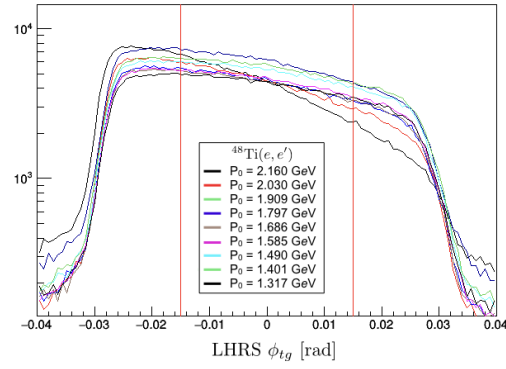


(c)

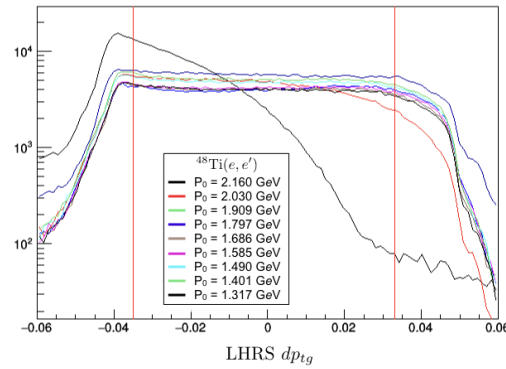
Figure 67: Histograms of the LHRs acceptance variables (a) θ_{tg}^e , (b) ϕ_{tg}^e and (c) dp_{tg}^e from the argon inclusive delta scan. The vertical red lines represent cuts applied to the histograms.



(a)



(b)



(c)

Figure 68: Histograms of the LHRs acceptance variables (a) θ_{tg}^e , (b) ϕ_{tg}^e and (c) dp_{tg}^e from the titanium inclusive delta scan. The vertical red lines represent cuts applied to the histograms.

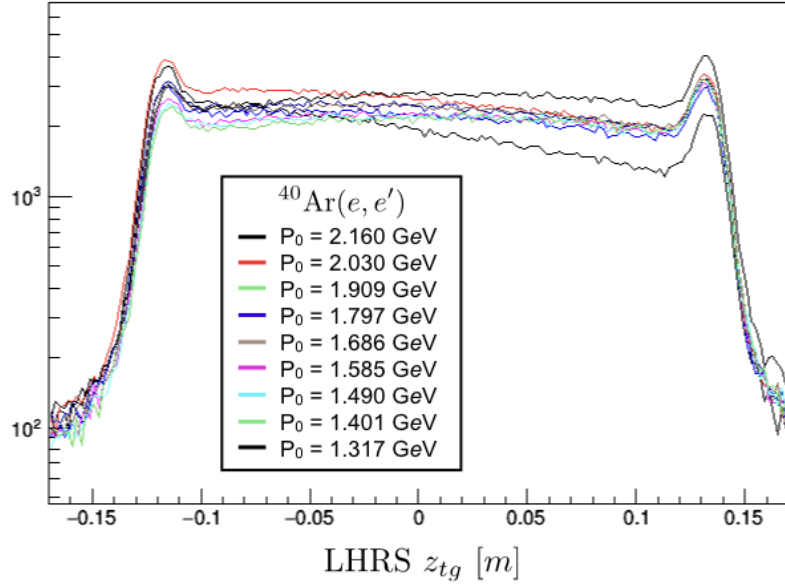


Figure 69: Histogram of the argon target vertex- z distribution z_{tg}^e from the inclusive delta scan.

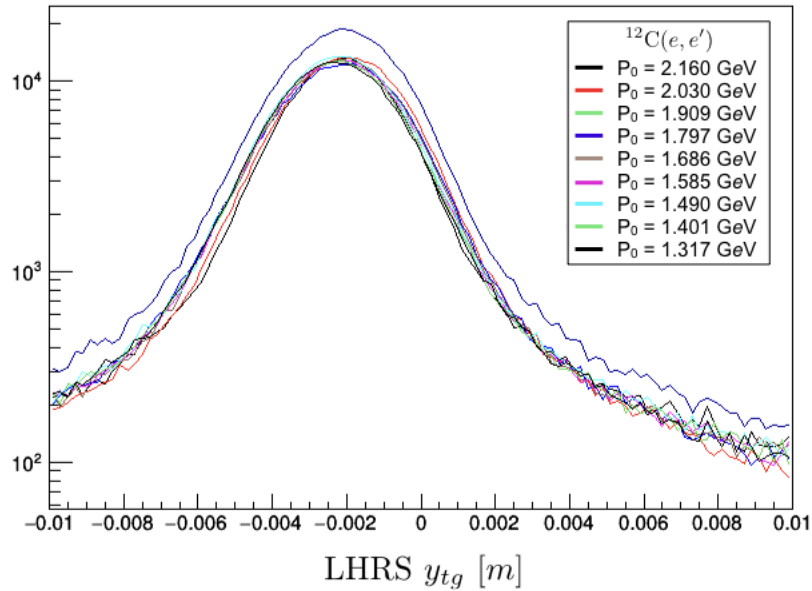


Figure 70: Histogram of carbon y_{tg}^e from the inclusive delta scan.

Target	Kinematic Variable	Cut
$^{12}_6\text{C}$	dp_{tg}^e	$[-0.038, 0.033]$
	θ_{tg}^e [rad]	$[-0.03, 0.03]$
	ϕ_{tg}^e [rad]	$[-0.015, 0.015]$
	$ y_{tg}^e - y_{\text{peak}}^e $ [m]	$\leq 5\sigma_{\text{peak}}$
$^{48}_{22}\text{Ti}$	dp_{tg}^e	$[-0.035, 0.033]$
	θ_{tg}^e [rad]	$[-0.03, 0.03]$
	ϕ_{tg}^e [rad]	$[-0.015, 0.015]$
	$ y_{tg}^e - y_{\text{peak}}^e $ [m]	$\leq 5\sigma_{\text{peak}}$
$^{40}_{18}\text{Ar}$	dp_{tg}^e	$[-0.035, 0.033]$
	θ_{tg}^e [rad]	$[-0.03, 0.03]$
	ϕ_{tg}^e [rad]	$[-0.015, 0.015]$
	z_{tg}^e [m]	$[-0.075, 0.05]$

Table 13: Acceptance cuts used in the inclusive data analysis.

7.2.2 Beam Trip Cut

The electron beam often cuts out suddenly, and then ramps up again to full current after a variable length of time. This sudden loss of beam is known as a *beam trip*. It is known that heat transfer from the electron beam to the target has a measurable effect on its density; a phenomenon discussed in detail in §4.3.3. Multiple beam trips with subsequent periods of cooling and reheating lead to fluctuations in target density, and hence reaction rates. Events affected by these density fluctuations can be removed by applying a cut on the beam current. For each run, the beam current histogram is fit with a Gaussian distribution (Eq. 7.1), and a $\pm 4\sigma$ cut is made around the average beam current,

$$|I_{\text{beam}} - I_{\text{avg}}| \leq 4\sigma \quad (7.2)$$

7.3 Particle Identification

Not all particles detected in the spectrometers are guaranteed to have originated from a genuine $A(e, e')X$ or $A(e, e'p)X$ event. Different types of particles leave distinct signals in the spectrometers, which usually manifest as a peak in the spectrum of a histogrammed quantity. The process of identifying which particles correspond to a certain HRS signal is called *particle identification*, often shortened to PID.

The particle identification procedures are different for the left and right arms of the HRS. Electron events in the LHRS are identified by analysis of the

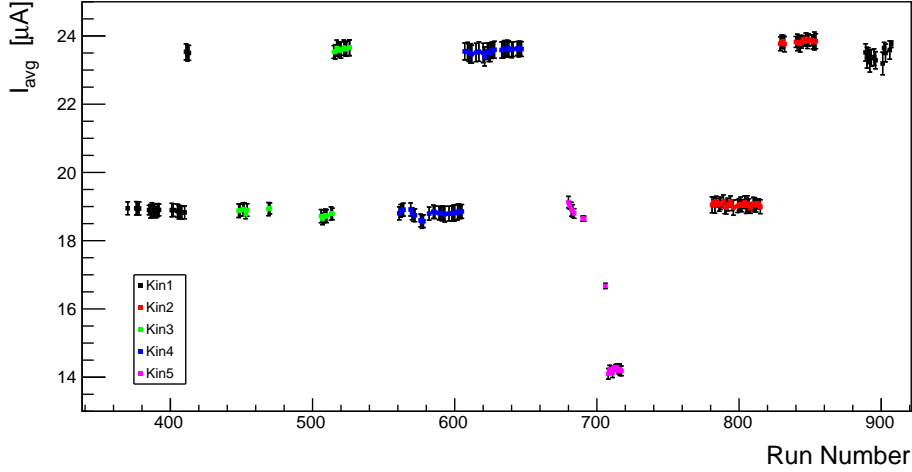


Figure 71: Plot of the CEBAF electron beam current versus run number.

Cherenkov and calorimeter signals. In the ultra-relativistic approximation, which is valid for the energies considered in E12-14-012, the electron mass is negligible, and the relativistic energy-momentum relation reduces to $E = p$. Identically, this means that their ratio is unity, $E/p = 1$. A histogram of the E/p spectrum obtained from the LHRS calorimeter will show a peak centered at unity, which corresponds to electron events. Any additional peaks in the E/p spectrum correspond to different particles, and can be excluded from the data with a cut.

Particles detected in the RHRS are identified through speed and time-of-flight analysis. The speed ($\beta = v/c \rightarrow v$ in natural units where $c = 1$) of the particles can be calculated from their mass and momentum. A particle of mass m moving at a relativistic speed v has momentum $p = \gamma m v$, and energy $E = \gamma m c^2$. Taking their ratio gives a new expression for β ,

$$\frac{p}{E} = \frac{\gamma m v}{\gamma m c^2} = \frac{\beta}{c} \rightarrow \beta \quad (7.3)$$

in natural units. This expression can be written in terms of the momentum p and mass m only as

$$\beta = \frac{p}{\sqrt{p^2 + m^2}}. \quad (7.4)$$

The reconstructed particle speed is recorded in the data histogram `R.tr.beta`, which is denoted as β_{HRS}^R . Similarly, the reconstructed momentum is histogrammed in `R.tr.p`, denoted as p_{HRS}^R . Taking the difference of β_{HRS}^R and

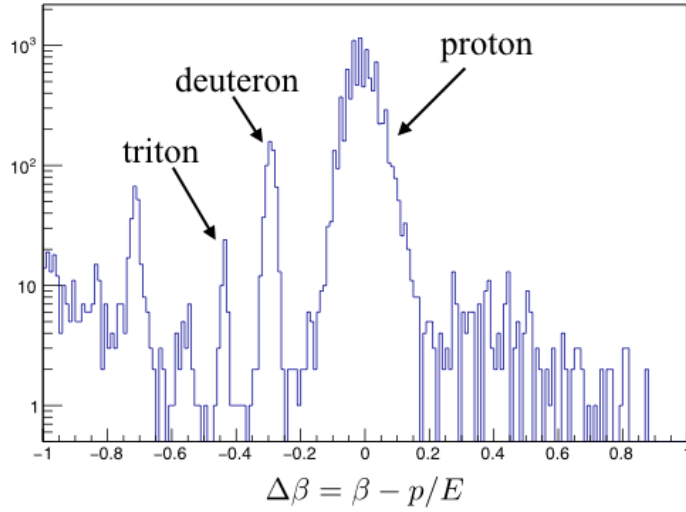


Figure 72: Histogram of $\Delta\beta(m)$ evaluated at the proton mass, showing peaks corresponding to protons, deuterons, and tritons.

Eq. 7.4 gives

$$\Delta\beta(m) = \beta_{HRS}^R - \frac{p_{HRS}^R}{\sqrt{(p_{HRS}^R)^2 + m^2}} \quad (7.5)$$

When evaluated at a specific particle mass m , a histogram of $\Delta\beta(m)$ will have a peak centered at zero if that particle appeared in the spectrometer. Peaks to the left of the origin represent heavier particles, while peaks to the right of the origin correspond to less massive particles.

A histogram of $\Delta\beta(m)$ evaluated at the proton mass $m = 938.272 \text{ MeV}/c^2$ is shown in Fig. 72. The distribution has a large peak centered at the origin, which is identified as the proton signal. The remaining peaks represent particles of mass $m = 1875.6 \text{ MeV}/c^2$ and $m = 2808.921 \text{ MeV}/c^2$, corresponding to deuterons and tritons, respectively.

7.3.1 Coincidence Time

Simultaneous events detected in the left and right HRS, which originated from the same scattering event at the target, are designated as *coincidental* if they activate the coincidence trigger T1 the left and right scintillators S0 within a specific window of time. The timing spectra of the LHRS and RHRS S0 scintillator are stored in the histograms `L.s0.time` and `R.s0.time`, respectively. The coincidence time distribution Δt_{coinc} is defined by the dif-

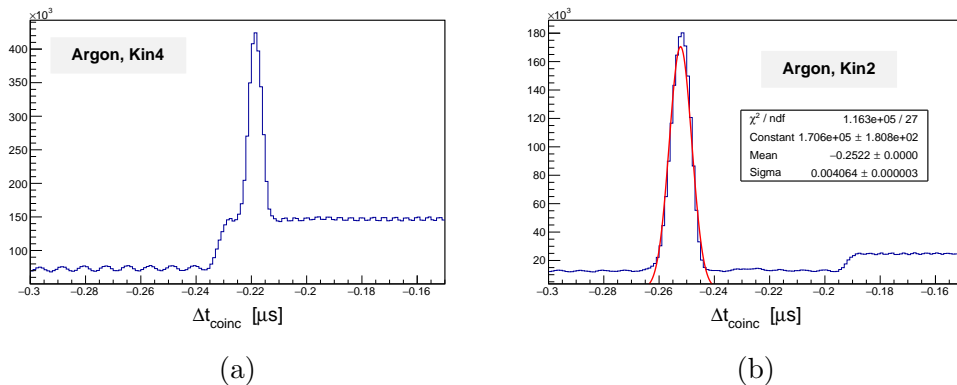


Figure 73: Histograms of the coincidence time spectra for (a) argon at Kin4 with the trigger timing issue evident, and (b) the same at Kin2 (no trigger issue), with a representative Gaussian fit used to calculate the location and spread of the coincidence time peak.

ference in timing spectra

$$\Delta t_{coinc} = \text{L.s0.time} - \text{R.s0.time}. \quad (7.6)$$

A typical Δt_{coinc} distribution consists of a peak sitting on a relatively flat and constant background. When fit with a Gaussian distribution (Eq. 7.1) as shown in Fig. 73b, the location of the peak $\mu = t_{coinc}$ is known as the *coincidence time*. Events apart from the coincidence time peak are *background events*. These background events are removed by making a tight $\pm 2\sigma$ cut around the coincidence time peak

$$|\Delta t_{coinc} - t_{peak}| \leq 2\sigma. \quad (7.7)$$

If the resolution of the coincidence time spectrum is increased, an oscillatory structure is revealed in the background. The background oscillations in Δt_{coinc} are known to be a reflection of the nano-second timing structure of the CEBAF electron beam, as seen in Fig. 74 for argon Kin5.

A problem with the coincidence trigger timing was discovered during the initial stages of the experiment, while data was being collected at Kin4. The problem was fixed for data collected at subsequent kinematic settings. Histograms of Δt_{coinc} for argon at Kin2 and Kin4 are shown in Fig. 73. The trigger problem manifests as a drop in the background level at $\Delta t_{coinc} \approx -0.23 \mu\text{s}$, almost immediately to the left of the coincidence time peak in Fig. 73a. The same problem exists for the Kin4 titanium data. A coincidence time spectrum with the trigger timing problem resolved is given in

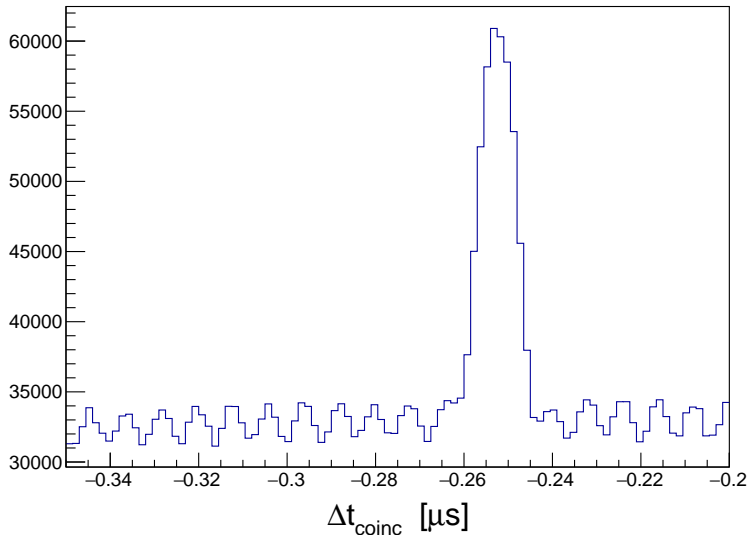


Figure 74: Increased resolution histogram of Δt_{coinc} for argon Kin5, showing the discrete nature of the CEBAF electron beam.

Fig. 73b, showing the coincidence time peak sitting on top of a relatively flat background. This timing issue with the Kin4 data also affects the calculation of the coincidence time cut efficiency, which is described in §8.5.

7.3.2 DR.t1 Cut

In addition to the cut on the coincidence time spectrum, an additional cut is made on the trigger quantity DR.t1. Histograms of the DR.t1 spectra for Ti Kin4 and Ar Kin5 are shown in Fig. 75 and 76 respectively. Figures 75a-76a show the DR.t1 histograms with the trigger cut

$$T_1 \wedge \neg(T_2 \vee T_3 \vee T_4 \vee T_5 \vee T_6) \quad (7.8)$$

applied to filter only T_1 events. The features of the *pure* DR.t1 spectra include multiple peaks sitting on a relatively constant background. Applying the particle identification and coincidence time cuts will reveal which peak(s) corresponds to actual physical events, and which are background events.

Figures 75b-76b show the DR.t1 histograms with these cuts applied. The PID and coincidence time cuts remove virtually all the background events, leaving behind a single peak corresponding to the actual physical events. A cut can be made on DR.t1 around the peak to further isolate these events.

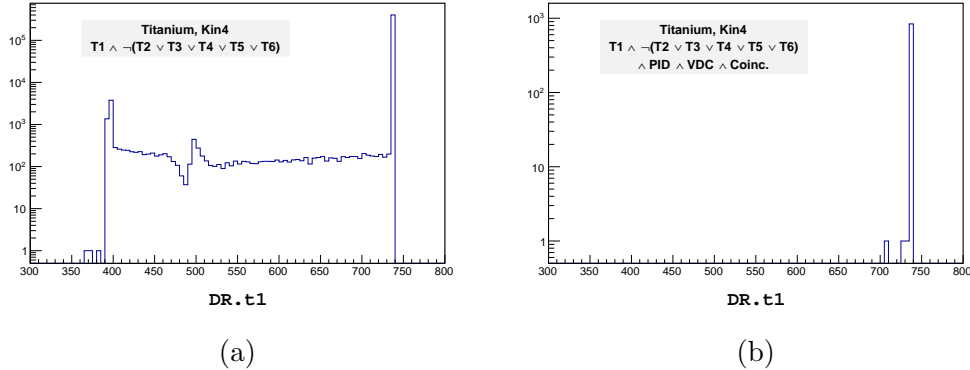


Figure 75: Histograms of (a) the pure `DR.t1` spectrum and (b) the same with PID, VDC, and coincidence-time cuts applied, for titanium Kin4 (with trigger timing issue).

For example, the cut for Ar Kin5 would be

$$600 \leq \text{DR.t1} \leq 700. \quad (7.9)$$

The `DR.t1` cut is utilized in the calculation of the coincidence time cut efficiency (see §8.5) and in the selection of background events (see §7.5.3).

7.4 Weighting the Data

To extract the correct physics from the experimental data, one must account for the effects of the HRS spectrometers on the particles detected within them. For each run i , the data histograms must be weighted by

$$W^i = \frac{1}{(LT \cdot \varepsilon_{T1} \varepsilon_{cer} \varepsilon_{calo} \varepsilon_{beta} \varepsilon_{coinc} \varepsilon_{VDC}^R)^i \cdot B(I) \cdot \varepsilon_{VDC}^L(dp_{tg}^e)}. \quad (7.10)$$

The ε 's are the detector efficiencies (see §8) and LT the livetime correction. The factor $B(I)$ is a correction to account for the change in density of the target material due to heating from the electron beam (see §4.3.3).

After applying the weight, the data is then normalized to the total charge collected during all the runs used. The same weight and charge normalization is also applied to the background histograms.

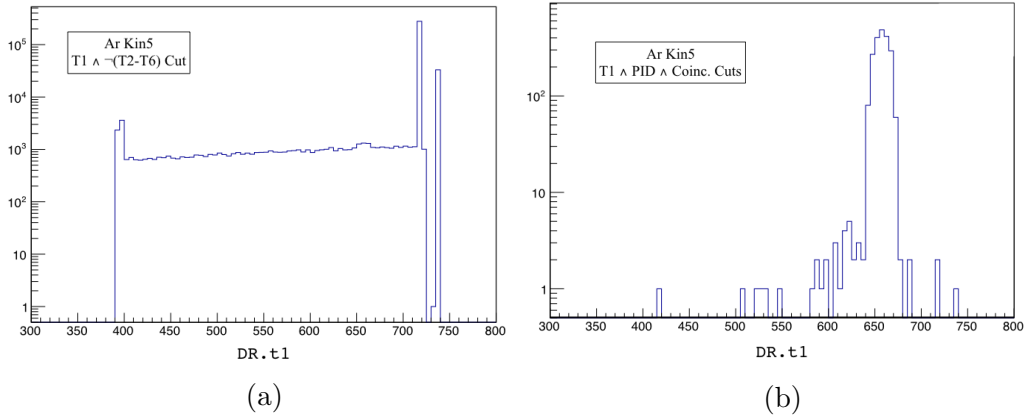


Figure 76: Histograms of (a) the pure DR. τ_1 spectrum and (b) the same with PID and coincidence-time cuts applied, for argon Kin5 (no trigger timing issue).

7.5 Analysis of the Background

7.5.1 Charge Symmetric Background

Another source of background are electron events referred to as the *charge-symmetric background*. These electron events emerge along with a positron from a variety of secondary reactions. They are referred to as charge-symmetric as positrons are produced in equal amounts in these reactions. For instance, consider the photons radiated from the electron as it travels through the spectrometer. If one of these photons transforms into an electron positron pair $\gamma \rightarrow e^+e^-$, that electron can be detected in the LHRS. Another source of charge-symmetric electron events is the neutral pion decay $\pi^0 \rightarrow 2\gamma \rightarrow e^+e^-$. These pions can be produced by scattering events with the spectrometer apparatus.

To determine the background from these events, one can reverse the polarity of the LHRS magnets to detect positrons instead. Since there are an equal amount of electrons produced, the positron yield can be used to remove the charge-symmetric electrons. However, no such study was conducted during the data collection phase of E12-14-012. Instead, a computer program was used to calculate the positron yield Y_{e^+} , and compare it to the regular electron yield Y_{e^-} . The yield correction factor, defined as $(Y_{e^-} - Y_{e^+})/Y_{e^-}$ and shown in Fig. 77, is essentially unity throughout the entire range of energy loss. This implies that $Y_{e^+} \approx 0$, and that the effects of the charge symmetric background on the cross section are negligible.

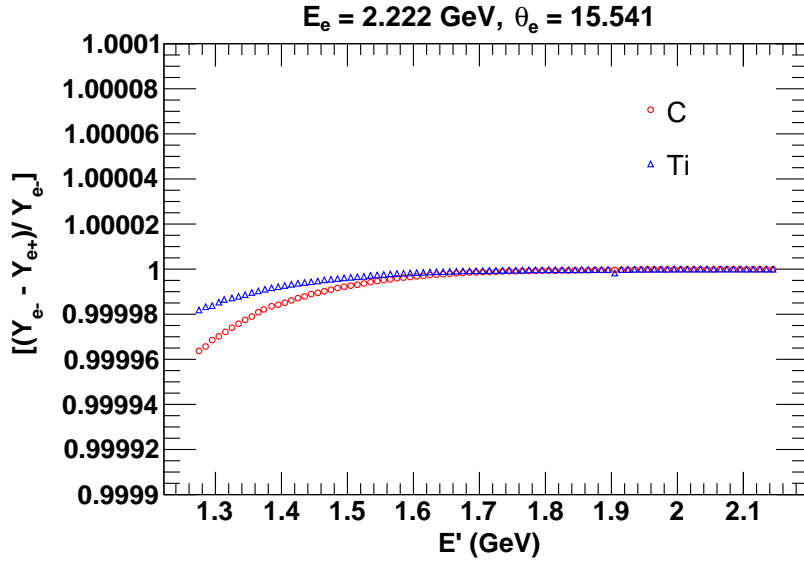


Figure 77: Carbon and titanium yield correction factor for the charge symmetric background correction.

7.5.2 Pion Contamination

Pions can be created through intermediate Δ -excitation process such as $\gamma^* + N \rightarrow \Delta \rightarrow N' + \pi$. There are four types of Δ baryons, Δ^{++} , Δ^+ , Δ^0 , Δ^- . These deltas will decay into a nucleon and pion combination determined by conservation of charge. Possible decay channels of the Δ are

$$\Delta^{++} \rightarrow p + \pi^+ \quad (7.11a)$$

$$\Delta^+ \rightarrow n + \pi^+ \quad (7.11b)$$

$$\Delta^+ \rightarrow p + \pi^0 \quad (7.11c)$$

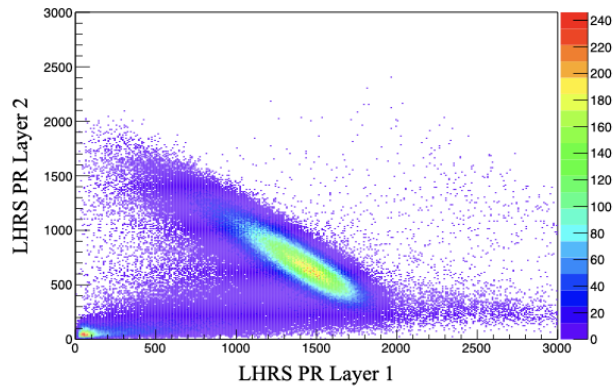
$$\Delta^0 \rightarrow n + \pi^0 \quad (7.11d)$$

$$\Delta^0 \rightarrow p + \pi^- \quad (7.11e)$$

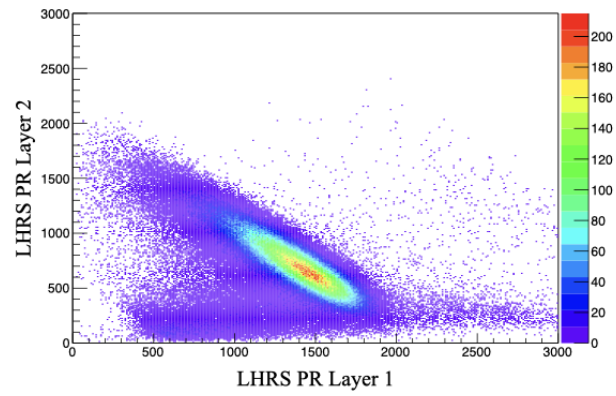
$$\Delta^- \rightarrow n + \pi^- \quad (7.11f)$$

The products of these reactions could contaminate the data with unwanted events and accidental coincidences. Pions that don't decay may also make it through the spectrometer. These events will form a distinct peak in the LHRS calorimeter spectrum.

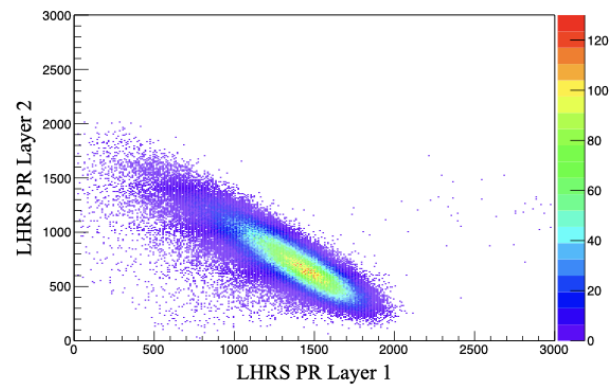
The peak near the origin of the plot of Fig. 78a are pion events. Applying the PID cuts to the data removes these events, as seen in Fig. 78b.



(a)



(b)



(c)

Figure 78: Scatter plots of the LHRs calorimeter data with (a) no cuts applied, (b) with the calorimeter and Cherenkov PID cuts applied, and (c) with all cuts applied.

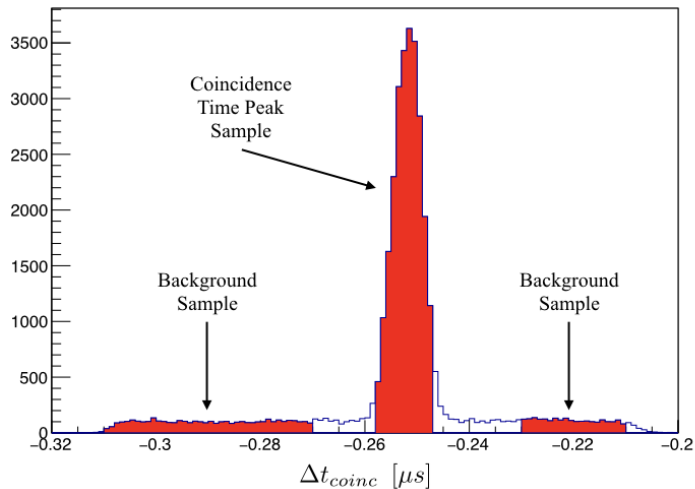


Figure 79: Histogram of a sample coincidence time spectrum showing the background sample and coincidence peak selection cuts, highlighted in red.

Applying the remaining acceptance cuts cleans up the rest of the data. The clean sample of good electron events is shown in Fig. 78.

7.5.3 Background Subtraction

Not all events that fall within the coincidence trigger timing window are true electron-proton coincidence events. Consider the histogram of the coincidence time spectrum in Fig. 79, and assume that the background events are uniformly distributed across Δt_{coinc} . Under this assumption, these background events will also appear within the bounds of the coincidence time cut (defined in Eq. 7.7). These imitation events are known as *accidental coincidences*, or *accidentals*, and they must be subtracted from the coincidence events.

Referring to Fig. 79, denote the length (width) of the coincidence time window as W_{peak} . The highlighted time intervals to the left and right of the coincidence time peak represent a sample of the background events. If W_{BG}^L and W_{BG}^R are the lengths of these time intervals respectively, then the total length of the background time-interval is their sum, $W_{BG} = W_{BG}^L + W_{BG}^R$. Applying a cut to the data that requires events to fall within the background interval, known as the *anti-coincidence cut*, separates the background events from the true coincidence events.

The sample of background events and the properties of a uniform distribution can be used to determine the number of accidentals that lie within

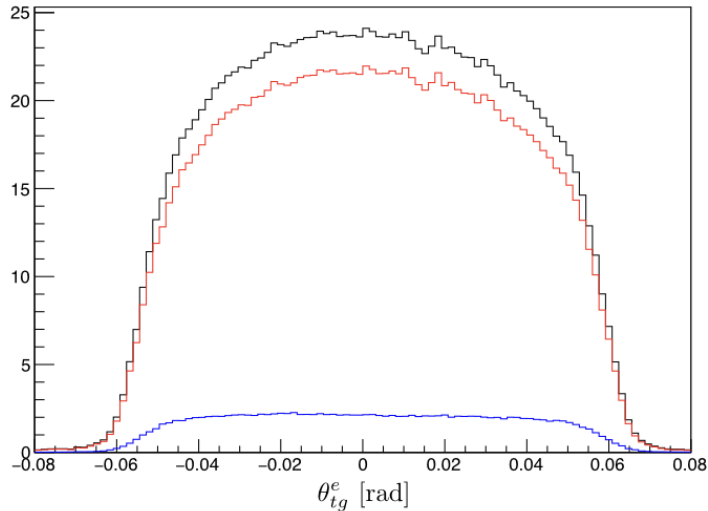


Figure 80: Histogram of θ_{tg}^e (black), associated background events (blue), and θ_{tg}^e with the background-subtracted (red).

the coincidence time peak. Assuming a uniform distribution, the number of background events N_{BG} in any time interval of length W in the coincidence time spectrum is constant. In other words, the number density of background events N_{BG}/W is constant. Applying this property to the events that fall within the time intervals W_{peak} and W_{BG} gives $N_{BG}/W_{BG} = N_{peak}^{BG}/W_{peak}$, or

$$N_{peak}^{BG} = \frac{N_{BG} \cdot W_{peak}}{W_{BG}}. \quad (7.12)$$

The histograms in Fig. 80 show the steps in the subtraction process for LHRs θ_{tg} . The black line is the weighted and charge-normalized θ_{tg}^e data histogram before any subtraction. The blue line is the background events, also weighted and normalized by the accumulated charge. The red line represents the data with the background subtracted.

8 Detector Efficiency Calculations

Each detector in the spectrometer has an efficiency associated with how well it operates. The detector efficiency ε is defined as the ratio of the number of events that satisfy a specific criterion N_{pass} to the total number of event triggers accepted N_{total} ,

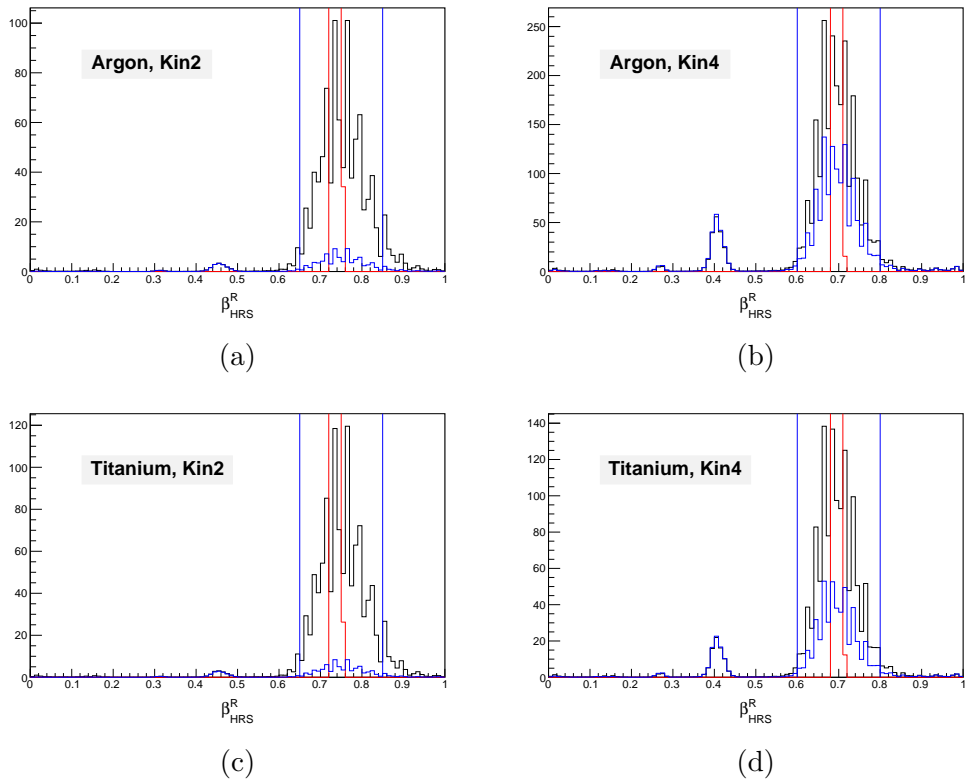


Figure 81: Histograms of β_{HRS}^R distributions for (a) argon at Kin2, (b) argon at Kin4, (c) titanium at Kin2, and (d) titanium at Kin4. The black line represents the (weighted) data before background subtraction, the blue line represents the (weighted) background noise, and the red line is the SIMC prediction.

$$\varepsilon = \frac{N_{pass}}{N_{total}}. \quad (8.1)$$

The selection criteria are imposed by applying a series of cuts on the data. Certain cuts are used in calculating both N_{pass} and N_{total} . These common cuts, denoted \mathfrak{B} , are called *base cuts*. In addition to the base cut, N_{pass} has additional cuts applied to it, referred to as *selection cuts*. The selection cuts are denoted as \mathfrak{S} where appropriate. The base cuts refine the sample of events to be considered, while the selection cuts choose events from this sample that pass the selection criterion. In this notation, the number of events that pass an arbitrary cut \mathfrak{C} is denoted by $N(\mathfrak{C})$.

8.1 Scintillator/Trigger Efficiency

The scintillator/trigger efficiency is a measure of the ability of the HRS DAQ to respond to relevant physics events. Despite being calculated differently, the scintillator efficiency and trigger efficiency represent the same thing, as the triggers are formed by signals from the scintillators. The two triggers for single-event data collection are the *main trigger* $T3$, and the *efficiency trigger* $T5$. The coincidence-event selection trigger is $T1$, and its associated efficiency trigger is $T2$. The coincidence trigger $T1$ is discussed further in §7.3.1. These triggers are defined by the logic statements of Eq. 5.7.

The DAQ efficiency for the inclusive data is calculated through cuts on the timing spectra of the scintillator planes S2 and S0. The timing spectra for S2 are the 15-element arrays L.s2.1t and L.s2.rt. The cut on the j^{th} element is defined as

$$\mathfrak{S}_{S2}^j = (\text{L.s2.1t}[j] \geq 100) \wedge (\text{L.s2.rt}[j] \geq 100). \quad (8.2)$$

Thus, the total cut applied to the S2 scintillator is the logical *and* of these statements,

$$\mathfrak{S}_{S2} = \bigwedge_{j=1}^{15} \mathfrak{S}_{S2}^j \quad (8.3)$$

Similarly, the cut applied to the S0 scintillator plane is

$$\mathfrak{S}_{S0} = (\text{L.s0.1t} \geq 100) \wedge (\text{L.s0.rt} \geq 100). \quad (8.4)$$

These cuts will form the selection cut for the inclusive scintillator efficiency. The base cut includes acceptance, PID, tracking cuts, and a cut on the singles

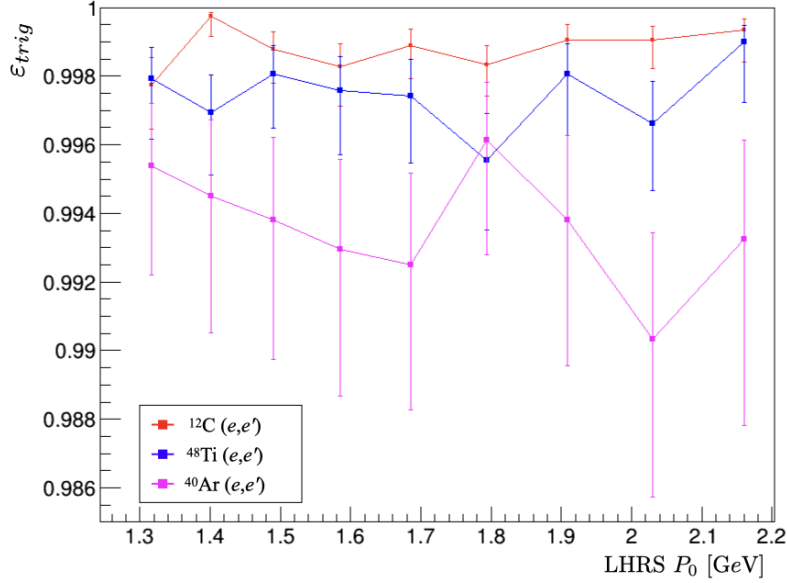


Figure 82: Plot of the scintillator efficiency versus LHRS central momentum from the inclusive delta scan. Note the small scale of the y -axis, indicating the small statistical uncertainty of the efficiency.

efficiency trigger T5, and is given by

$$\mathfrak{B}_{scint} = \text{Acceptance}_L \wedge \text{Target} \wedge \text{PID} \wedge T5 \wedge (N_{tracks}^L = 1). \quad (8.5)$$

Combining the logic statements of Eqs. 8.3, 8.4 and 8.5 gives the definition of the inclusive scintillator efficiency as

$$\epsilon_{scint} = \frac{N(\mathfrak{B}_{scint} \wedge \mathfrak{S}_{S0} \wedge \mathfrak{S}_{S2})}{N(\mathfrak{B}_{scint})}. \quad (8.6)$$

Equation 8.6 as a function of HRS central momentum is plotted in Fig. 82. Note the small scale of the y -axis, indicating that the associated statistical uncertainty is small.

For the exclusive analysis, the DAQ performance is represented by both a scintillator efficiency and a traditional trigger efficiency. The trigger efficiency is defined by cutting directly on the coincidence and efficiency triggers as

$$\epsilon_{trig} = \frac{N(\mathfrak{B}_{trig} \wedge T1)}{N(\mathfrak{B}_{trig} \wedge T2)}, \quad (8.7)$$

where the base cut is given by

$$\mathfrak{B}_{trig} = \text{Acceptance}_L \wedge \text{Acceptance}_R \wedge \text{Target} \wedge \text{Beam}. \quad (8.8)$$

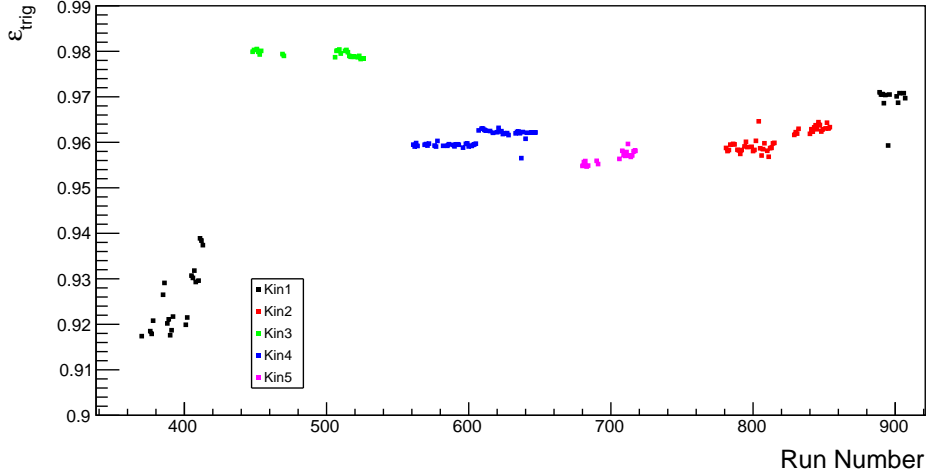


Figure 83: Plot of the T1 trigger/scintillator efficiency versus run number for all kinematic settings.

Ideally, the trigger efficiency would work across all exclusive kinematics. However, due to the coincidence trigger timing error discussed in §7.3.1, Eq. 8.7 gave unphysical results greater than unity when applied to the Kin4 data. Thus, for the Kin4 data, the efficiency is calculated by an expression analogous to that of Eq. 8.6, with the base cut given by

$$\mathfrak{B}_{scint} = \text{Acceptance}_L \wedge \text{Acceptance}_R \wedge \text{Target} \wedge \text{Beam} \wedge T2. \quad (8.9)$$

The trigger and scintillator efficiencies are plotted in Fig. 83 versus run number for all kinematic settings.

8.2 Cherenkov Cut Efficiency

The Cherenkov cut efficiency is based on a cut on the LHRS Cherenkov PMT signal sum (`L.cer.asum_c`). This cut is part of the particle identification (PID) cut, as it selects the events with the best signal from the gas Cherenkov detector. The data histograms `L.pr11.e` and `L.pr12.e` represent the energy deposited in the first and second layers of the LHRS calorimeter, respectively. Their sum gives the total energy deposited in the lead-glass calorimeter.

The efficiency calculation relies on a good sample of electron events, which is obtained by making cuts on the LHRS calorimeter energy variables. The

cuts used to isolate the electron sample are

$$\text{L.tr.p*1000} \cdot 0.97 \leq (\text{L.pr11.e} + \text{L.pr12.e}) \leq \text{L.tr.p*1000} \cdot 1.02 \quad (8.10a)$$

$$400 \leq \text{L.pr12.e} \leq 800. \quad (8.10b)$$

The electron sample cut is represented by the symbol $\mathfrak{C}_{sample}^{cal}$, and forms part of the base cut. The selection cut is made on the PMT sum `L.cer.asum_c`. Thus, the efficiency for a given ADC cut value is

$$\varepsilon_{cer}(\text{ADC}) = \frac{N(T_{main} \wedge \text{Beam} \wedge \mathfrak{C}_{sample}^{cal} \wedge \text{L.cer.asum}_c \geq \text{ADC})}{N(T_{main} \wedge \text{Beam} \wedge \mathfrak{C}_{sample}^{cal})}, \quad (8.11)$$

where T_{main} is the *main* trigger; the singles trigger $T3$ for inclusive data and the coincidence trigger $T1$ for exclusive data.

Figure 84 shows the percent efficiency as a function of the ADC cut value on the Cherenkov sum. Examination of the plots shows the Cherenkov efficiency to be relatively stable for ADC cut values below approximately 400. The efficiency is high in this region, with $\varepsilon_{cer} > 99.8\%$ for all targets. However, the efficiency falls dramatically for cuts on the Cherenkov sum greater than 400. Based on this analysis, the Cherenkov sum ADC was cut at 400 (`L.cer.asum_c` \geq 400).

8.3 Calorimeter Cut Efficiency

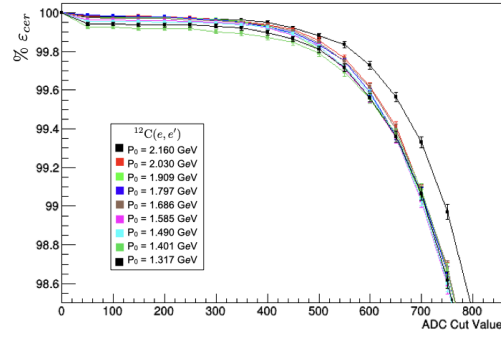
The calorimeter cut is actually a cut on E/p , the ratio of the energy to the momentum of the detected electrons. The electron energy is calculated as the sum of the LHRs calorimeter layer energies, while the momentum is represented by the ideal momentum known as the *golden momentum* (`L.gold.p`). In terms of the data histograms, the electron energy-momentum ratio is given by

$$\frac{E}{p} = \frac{\text{L.pr11.e} + \text{L.pr12.e}}{\text{L.gold.p*1000}} \quad (8.12)$$

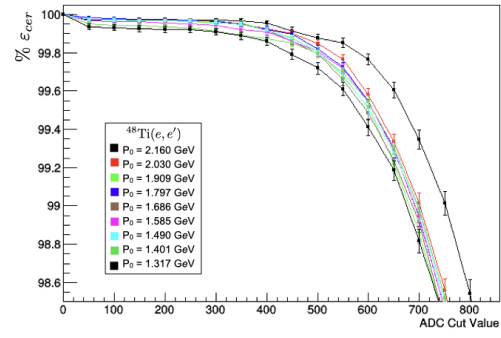
As the electrons have energy large enough to be treated as relativistic massless particles, the ratio should be equal to unity. This phenomenon can be seen in the plots of Fig. 87, which are histograms of Eq. 8.12 from the inclusive scattering data.

The calorimeter cut efficiency is calculated as a function of the E/p cut value ($\#$) by

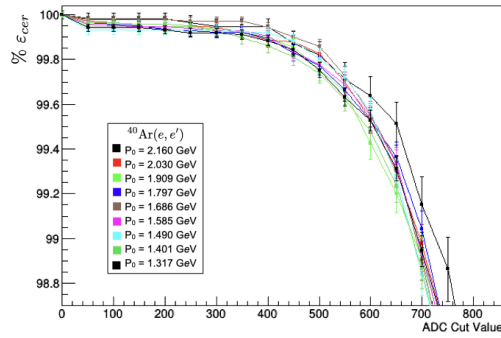
$$\varepsilon_{cal}(\#) = \frac{N(T_{main} \wedge \text{Cherenkov} \wedge \text{Beam} \wedge (E/p \geq \#))}{N(T_{main} \wedge \text{Cherenkov} \wedge \text{Beam})}. \quad (8.13)$$



(a)



(b)



(c)

Figure 84: Plots of the inclusive (Kin5) Cherenkov cut efficiency versus ADC cut value for (a) carbon, (b) titanium, and (c) argon targets.

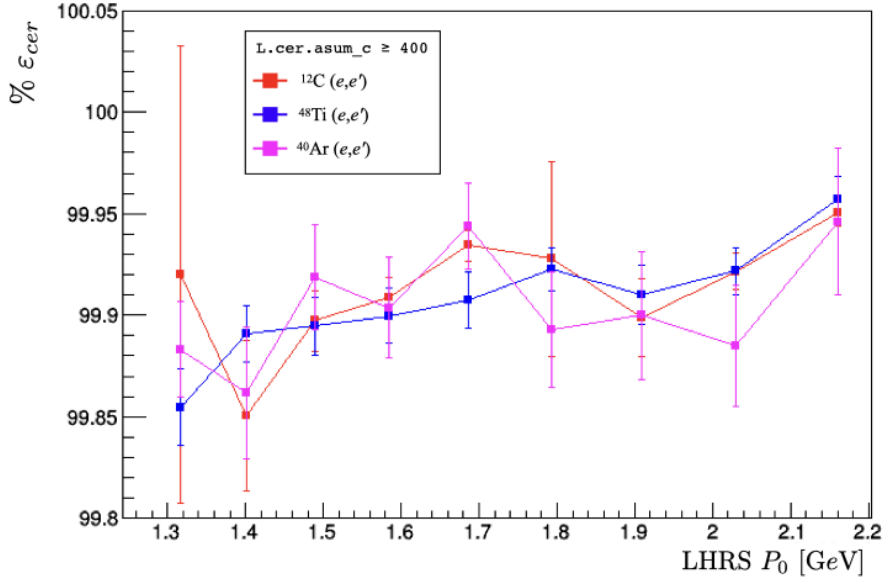


Figure 85: Plot of the Cherenkov cut efficiency versus LHRs central momentum from the inclusive delta scan.

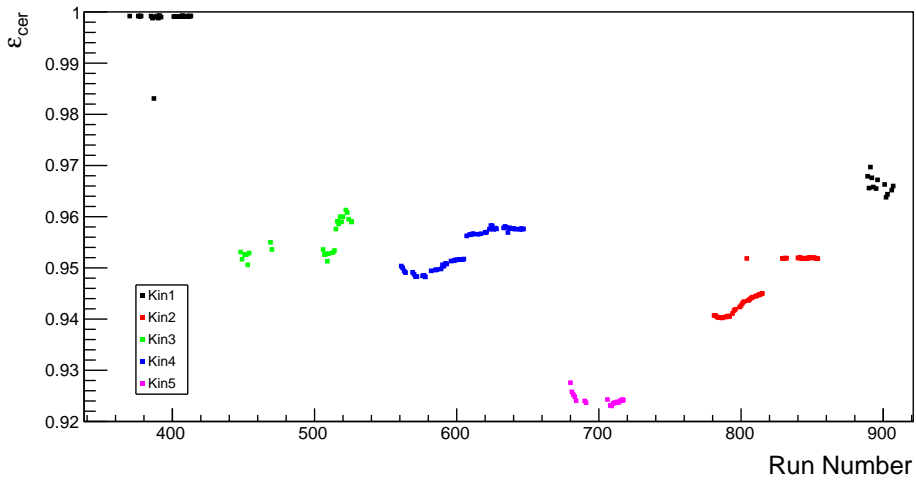
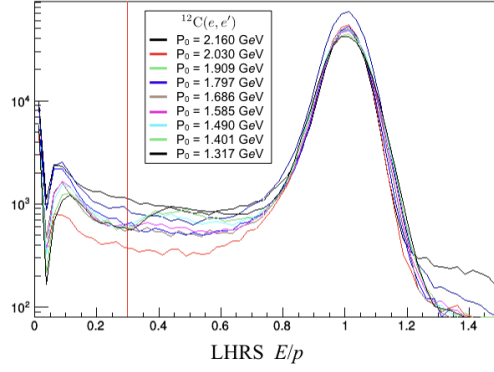
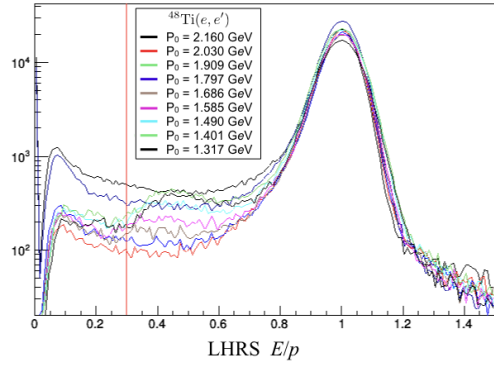


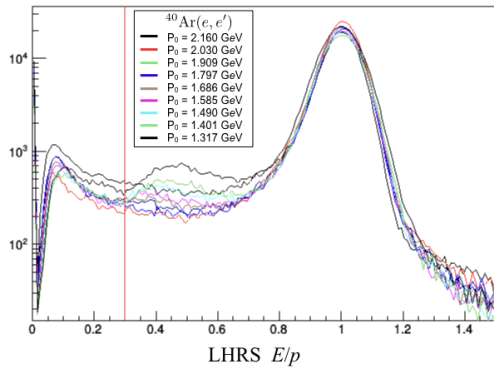
Figure 86: Plot of the Cherenkov cut efficiency versus run number for all kinematic settings.



(a)



(b)



(c)

Figure 87: Histograms of E/p from the (a) carbon, (b) titanium, and (c) argon inclusive delta scans. The red line represents the cut $E/p \geq 0.3$.

The Cherenkov cut is tightened to obtain a cleaner electron sample, doubling the cut on the Cherenkov sum to `L.cer.asum_c` ≥ 800 .

The plots of Fig. 88 show the efficiency versus E/p cut value for the inclusive LHRS momentum delta scan data. The calorimeter efficiency varies greatly between each momentum setting, and begins to drop quickly after $E/p \geq 0.3$. Taking $E/p \geq 0.3$ results in a cut efficiency greater than 93% for all delta scan momentum settings, as seen in Fig. 89.

8.4 VDC/Tracking Efficiency

The VDC efficiency, or tracking efficiency, is a measure of the ability of the VDC's tracking algorithm to accurately reconstruct the trajectory of charged particles that pass through it. The efficiency is defined in two pieces, R_1 and R_2 ; the overall efficiency being their product

$$\varepsilon_{VDC} = R_1 \cdot R_2. \quad (8.14)$$

The VDC is capable of generating multiple possible tracks for a single particle event. The first factor, R_1 , quantifies the ability of the tracking algorithm to reconstruct any number of possible trajectories for a single event. The second factor, R_2 , is the single-track-event efficiency, correcting the first term for events with only a single track reconstructed in the VDC.

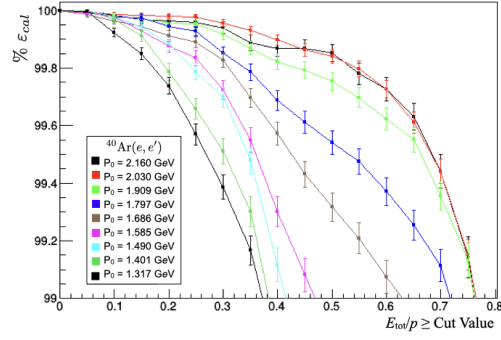
The VDC efficiency for the left and right arms are calculated separately. For the inclusive analysis, only the efficiency of the left arm is needed, as only electron events are considered. For the left arm, the first factor R_1 is given by

$$R_1 = \frac{N(T3 \wedge \text{Cherenkov} \wedge E/p \wedge N_{tracks}^L > 0)}{N(T3 \wedge \text{Cherenkov} \wedge E/p)}. \quad (8.15)$$

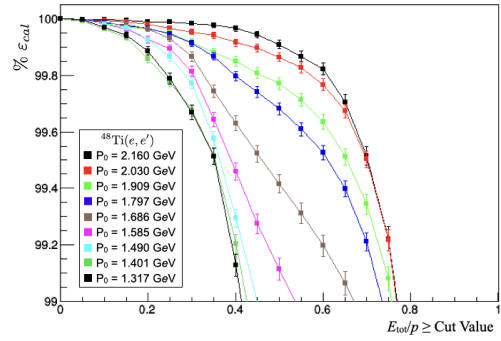
There is a slight change to the definition of E/p when calculating the VDC efficiency. In Eq. 8.12, the golden momentum in the denominator is replaced with the HRS central momentum P_0 . For notational convenience, define the base cut for R_1 as $\mathfrak{B}_{R_1} = (T3 \wedge \text{Cherenkov} \wedge E/p)$. With this definition, the single-track efficiency R_2 is given by

$$R_2 = \frac{N(\mathfrak{B}_{R_1} \wedge \text{Acceptance}_L \wedge \text{Target} \wedge N_{tracks}^L = 1)}{N(\mathfrak{B}_{R_1} \wedge \text{Acceptance}_L \wedge \text{Target})}, \quad (8.16)$$

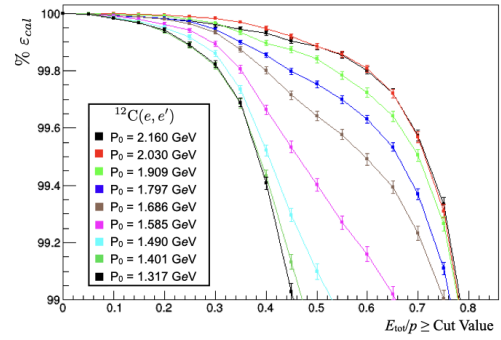
Plots of R_1 and R_2 for the three targets are drawn in Fig. 91. The efficiencies are calculated for each run considered. Similarly, the base cut for R_2 is



(a)



(b)



(c)

Figure 88: Plots of calorimeter cut efficiency versus E/p cut value for the (a) argon, (b) titanium, and (c) carbon inclusive delta scan.

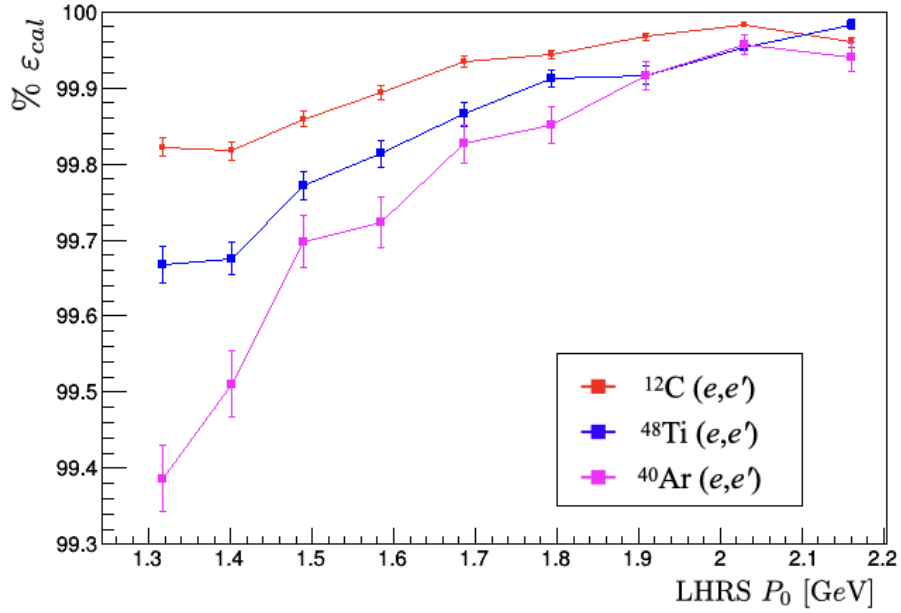


Figure 89: Plot of the calorimeter cut efficiency versus LHRs central momentum for $E/p \geq 0.3$, from the inclusive (Kin5) delta scan.

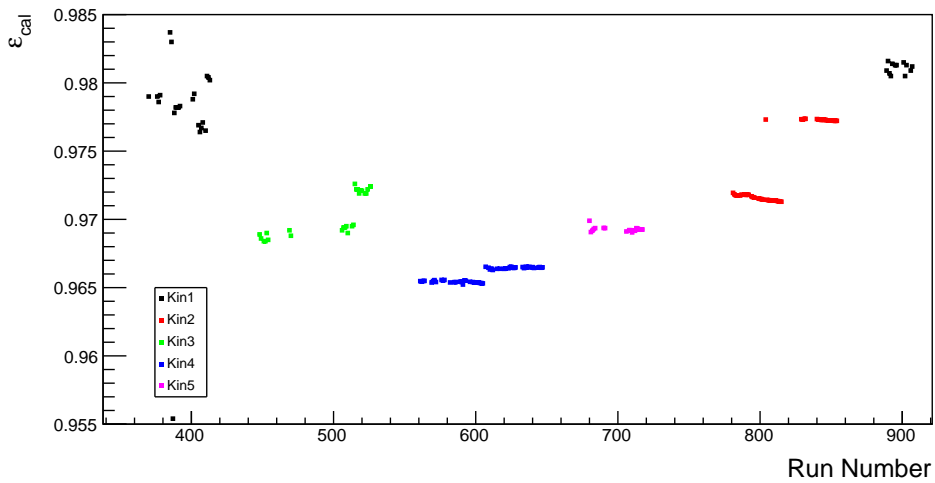


Figure 90: Plot of the calorimeter cut efficiency versus run number for all kinematic settings.

defined as $\mathfrak{B}_{R_2} = (\mathfrak{B}_{R_1} \wedge \text{Acceptance}_L \wedge \text{Target})$. In this compact notation, the total LHRS VDC efficiency is given by

$$\varepsilon_{VDC}^L = \frac{N(\mathfrak{B}_{R_1} \wedge N_{tracks}^L > 0)}{N(\mathfrak{B}_{R_1})} \cdot \frac{N(\mathfrak{B}_{R_2} \wedge N_{tracks}^L = 0)}{N(\mathfrak{B}_{R_2})}. \quad (8.17)$$

The inclusive LHRS VDC efficiency is plotted against the spectrometer central momentum in Fig. 92.

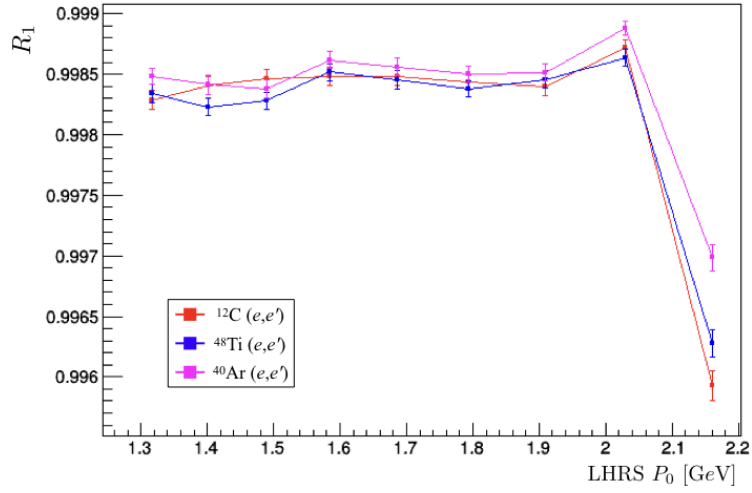
The VDC efficiency for both spectrometer arms is needed for the exclusive analysis. Adapting Eqs. 8.15 and 8.16 to apply to the right arm is straightforward. The single-track event cut is switched to the RHRS VDC variable, and the acceptance cuts are applied to the right arm variables. Since coincidence events are now considered, the cut on the singles event trigger $T3$ is replaced with a cut on the coincidence trigger $T1$. The RHRS VDC efficiency ε_{VDC}^R is plotted in Fig. 93 as a function of run number.

For the exclusive data analysis, it was decided to include electron events across the entire range of the LHRS momentum acceptance. In this case, the left arm VDC efficiency is calculated as a function of dp_{tg}^e to account for the change in efficiency for events on the edge of the momentum acceptance. The LHRS dp_{tg} spectrum was divided into segments, and the tracking efficiency was calculated using Eq. 8.17 for each segment. Usually, the efficiencies are calculated on a run-by-run basis. However, to reduce the effect of low statistics on the efficiency for events on the edge of the acceptance, all runs were combined before the efficiency was calculated. A plot of the efficiencies $\varepsilon_{VDC}^L(dp_{tg}^e)$ for Kin2, Kin4, and Kin5 is shown in Fig. 94. Even with all of the runs combined, the efficiencies at the extremes of dp_{tg}^e still suffer from low statistics, and thus have large statistical uncertainty.

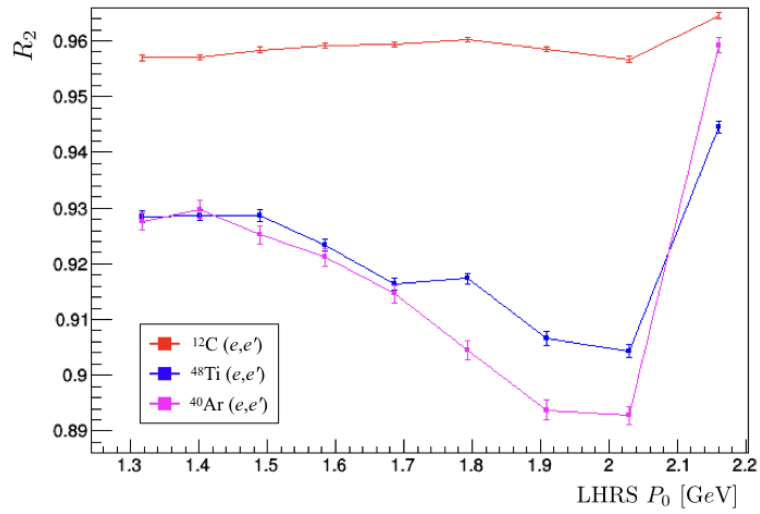
8.5 Coincidence Time Cut Efficiency

The coincidence time cut efficiency accounts for the removal of background events from outside of the coincidence time peak. The peak of the coincidence time spectrum Δt_{coinc} is fitted with a Gaussian distribution (Eq. 7.1), and the mean $\mu = t_{peak}$ and standard-deviation σ are extracted. The selection cut discards any event that falls outside two standard deviations from the mean. The coincidence time cut efficiency is calculated as

$$\varepsilon_{coinc} = \frac{N(\mathfrak{B}_{coinc} \wedge |\Delta t_{coinc} - t_{peak}| \leq 2\sigma)}{N(\mathfrak{B}_{coinc})}, \quad (8.18)$$



(a)



(b)

Figure 91: Plots of (a) the non-zero track-reconstruction efficiency (R_1) and (b) the single-track reconstruction efficiency (R_2) for the VDC, as a function of LHRS central momentum from the inclusive (Kin5) delta scan.

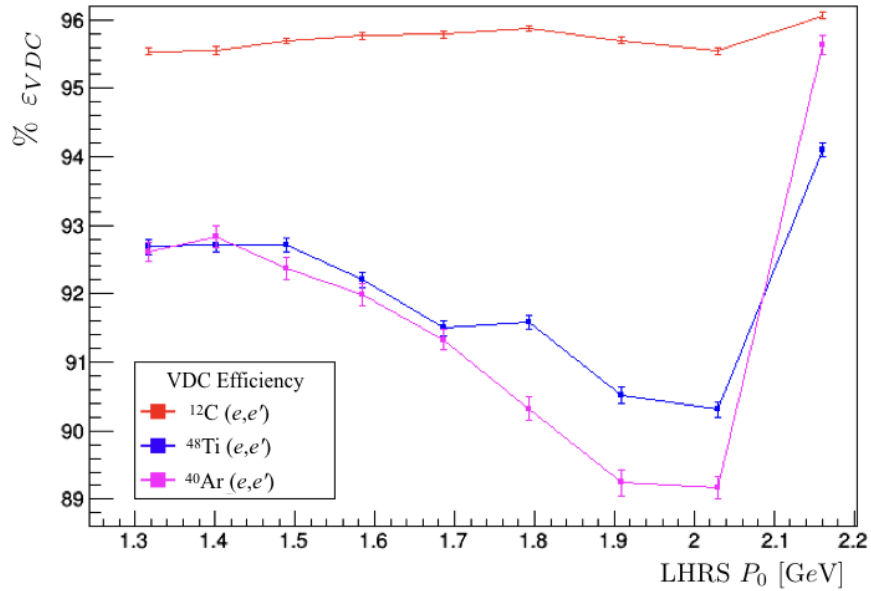


Figure 92: Plot of the LHRs VDC efficiency ($\varepsilon_{VDC} = R_1 \cdot R_2$) versus LHRs detector central momentum from the inclusive (Kin5) delta scan.

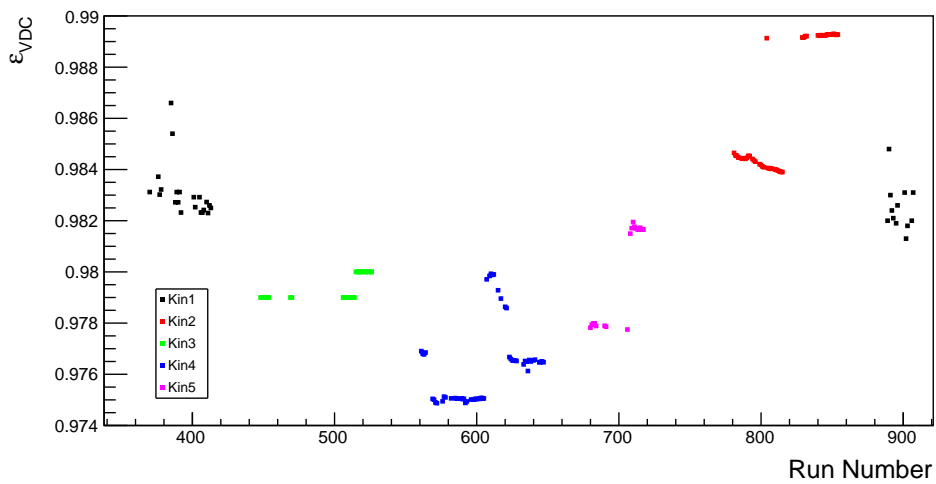


Figure 93: Plot of the RHRS VDC efficiency versus run number for all kinematic settings.

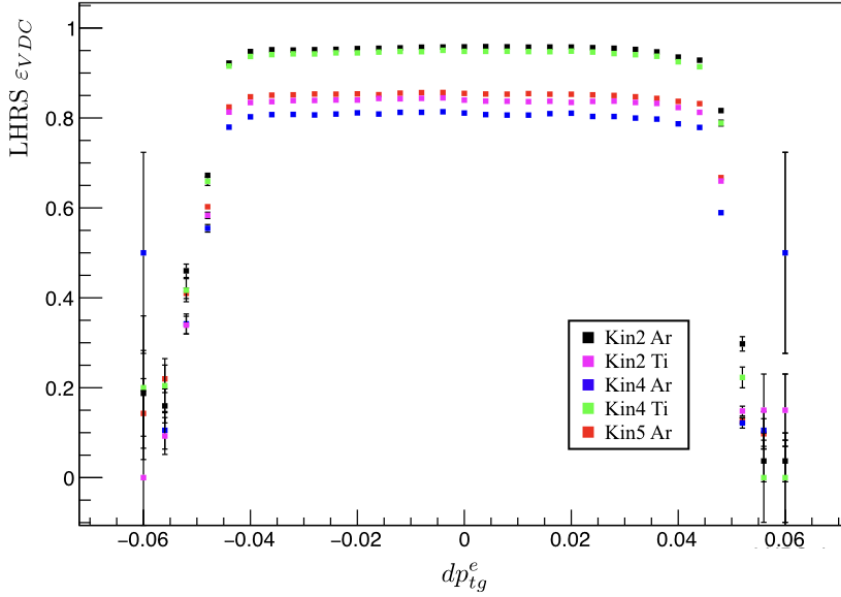


Figure 94: Plot of the LHRS VDC efficiency as a function of the electron fractional momentum dp_{tg}^e .

where the base cut is given by

$$\mathfrak{B}_{coinc} = \text{Acceptance} \wedge (N_{tracks} = 1) \wedge \text{PID} \wedge \text{Beam} \wedge T1 \wedge \text{DR.}\tau 1. \quad (8.19)$$

In this expression, the single-track and acceptance cuts are applied to both spectrometer arms, with the acceptance cut including a cut on z_{tg} . The PID cut includes a tightened cut on β_{HRS}^R for increased sample purity, as well as the LHRS Cherenkov and calorimeter cuts. In addition to the coincidence trigger cut, a cut on the trigger timing spectrum DR. $\tau 1$ is also applied.

A problem occurred when analyzing the coincidence time cut efficiency for Kin4. As mentioned previously in §7.3.1, an error in the coincidence trigger timing was discovered that only affected the data collected at Kin4. The effect is visible in the Δt_{coinc} spectrum for Kin4 (see Fig. 73a) as a sudden downward shift in the background immediately to the left of the coincidence time peak. As a result, efficiencies calculated with Eq. 8.18 assume values greater than unity for Kin4. A remedy for this problem is to change the selection cut to use only the right half of the coincidence time peak. Additionally, a four-sigma cut on Δt_{coinc} was added to the denominator to remove events from the altered part of the spectrum. For Kin4, the new definition of the efficiency is

$$\varepsilon_{coinc} = \frac{N(\mathfrak{B}_{coinc} \wedge (t_{peak} \leq \Delta t_{coinc} \leq t_{peak} + 2\sigma))}{N(\mathfrak{B}_{coinc} \wedge (t_{peak} \leq \Delta t_{coinc} \leq t_{peak} + 4\sigma))}. \quad (8.20)$$

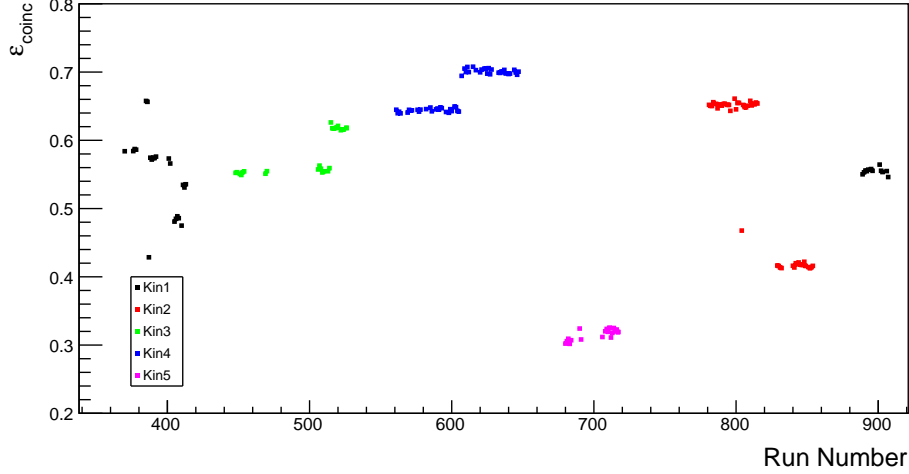


Figure 95: Plot of the coincidence time cut efficiency versus run number.

8.6 Beta Cut Efficiency

Part of the particle identification cuts, the beta cut efficiency accounts for the removal of non-proton coincidence events based on their speed. The selection cut is made on the RHRS β histogram, chosen by visual inspection to isolate the proton peak from other particle peaks. If the lower and upper bounds of the beta cut interval are respectively L and U , then the beta cut efficiency is

$$\epsilon_{\text{beta}} = \frac{N(\mathfrak{B}_{\text{beta}} \wedge \beta_{\text{HRS}}^R \in [L, U])}{N(\mathfrak{B}_{\text{beta}})}. \quad (8.21)$$

The base cut for the beta efficiency is given by

$$\mathfrak{B}_{\text{beta}} = T1 \wedge (N_{\text{tracks}} = 1) \wedge \text{PID} \wedge \text{Acceptance} \wedge \text{Beam} \wedge (|\Delta t_{\text{coinc}} - t_{\text{peak}}| \leq 1\sigma). \quad (8.22)$$

Note that the coincidence time cut interval is tightened to $\pm 1\sigma$ around the peak. This tighter cut ensures only good coincidence events are considered in the efficiency calculation. A plot of the β -cut efficiency is given in Fig. 96.

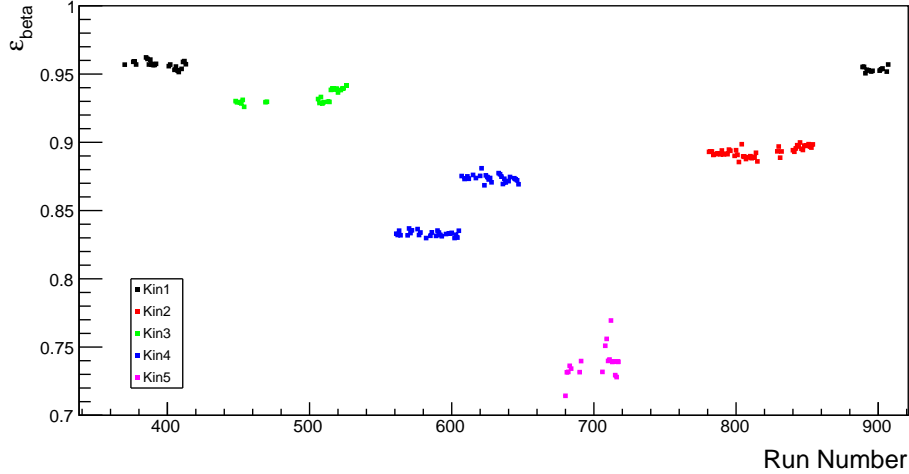


Figure 96: Plot of the RHRs β -cut efficiency versus run number for all kinematic settings.

9 Extracting Cross Sections From Experimental Data

9.1 The Inclusive Cross Section

9.1.1 Acceptance Correction Method

The most straight-forward method to extract the inclusive cross section directly from the data is known as the *acceptance correction method*, or just the *acceptance method*. We begin by writing down an expression for the number of electrons that are detected in the HRS spectrometers. For each bin i , the number of detected electrons N_i^- is given by[86]

$$N_i^- = L \cdot \frac{d^3\sigma}{d\Omega' dE'} \cdot (\Delta E' \Delta\Omega') \cdot \varepsilon_{det} \cdot A(E', \Omega') + N_{BG} \quad (9.1)$$

where L is the (integrated) luminosity, ε_{det} is the total detector efficiency, and $A(E', \Omega')$ is the *acceptance function* for the spectrometer. The term $d^3\sigma/d\Omega' dE'$ is the inclusive differential cross section, introduced with the volume of the phase space, $\Delta E' \Delta\Omega'$. All background events are grouped into the last term N_{BG} . The *yield* is defined as the number of detected events minus the background events, $Y = N_i^- - N_{BG}$. Substitution into Eq. 9.1 gives

$$Y = L \cdot \frac{d^3\sigma}{d\Omega'dE'} \cdot (\Delta E' \Delta \Omega') \cdot \varepsilon_{det} \cdot A(E', \Omega'). \quad (9.2)$$

The yield is a function of the final electron energy and solid angle, so we denote it as $Y(E', \Omega')$. Dividing the yield by the luminosity, phase space, efficiency, and acceptance gives the inclusive differential cross section as

$$\left(\frac{d^3\sigma}{d\Omega'dE'} \right)_{\text{exp}} = \frac{Y(E', \Omega')}{L (\Delta E' \Delta \Omega') \varepsilon_{det} A(E', \Omega')}. \quad (9.3)$$

An acceptance function $A(E', \Omega')$ must be calculated for each target. For an extremely detailed analysis, an array of acceptance functions $A^i(E', \Omega')$ should be generated at multiple points along the length of the target. The partitioning of the target need not be uniform, and should be based on the statistics of the data. In the limit of a large number of sections, the acceptance function becomes an integral over the target length. However, a single matrix was used to represent the target acceptance in this analysis[65].

9.1.2 Yield Ratio Method

The primary method used to obtain the inclusive differential cross section from the experimental data is the *yield ratio method*. This method relies on a monte-carlo model which is designed to calculate the yield, Y_{MC} , based on models of the Hall A spectrometers. The cross section of the yield ratio method is derived from the acceptance method described previously.

Equation 9.2 gives the yield calculated from the experimental data, denoted as Y_{data} . The acceptance method can be applied to the monte-carlo events, resulting in an analogous expression for the monte-carlo yield,

$$Y_{\text{MC}} = L \cdot \left(\frac{d^3\sigma_{\text{model}}}{d\Omega'dE'} \right) \cdot (\Delta E' \Delta \Omega') \cdot \varepsilon_{det} \cdot A_{\text{MC}}(E', \Omega'). \quad (9.4)$$

Dividing Y_{data} by Y_{MC} gives

$$\frac{Y_{\text{data}}}{Y_{\text{MC}}} = \frac{L \cdot \left(\frac{d^3\sigma_{\text{exp}}}{d\Omega'dE'} \right) \cdot (\Delta \Omega' \Delta E') \cdot \varepsilon_{det} \cdot A_{\text{HRS}}(E', \Omega')}{L \cdot \left(\frac{d^3\sigma_{\text{model}}}{d\Omega'dE'} \right) \cdot (\Delta \Omega' \Delta E') \cdot \varepsilon_{det} \cdot A_{\text{MC}}(E', \Omega')}. \quad (9.5)$$

As both acceptance functions are describing the same spectrometer, the MC and HRS acceptance functions are considered equal, $A_{\text{MC}}(E', \Omega') = A_{\text{HRS}}(E', \Omega')$. Thus, nearly everything on the right hand side of Eq. 9.5

cancel, leaving the ratios of the differential cross sections and yields. Solving for the experimental cross section gives the equation of the yield ratio method as

$$\left(\frac{d^3\sigma}{d\Omega'dE'}\right)_{exp} = \frac{Y_{data}}{Y_{MC}} \left(\frac{d^3\sigma}{d\Omega'dE'}\right)_{model}. \quad (9.6)$$

The charge-normalized yields Y_{data} and Y_{MC} are obtained from the data and monte-carlo respectively. The inclusive data is binned into a histogram, from which the yield is calculated discretely for each bin. The yield for the i^{th} bin is calculated as

$$Y^i = \frac{N_S^i \cdot PS}{N_e \cdot LT \cdot \varepsilon}, \quad (9.7)$$

where N_e is the total number of electrons on the target, and N_S^i is the number of scattered electrons[62]. The quantities LT and ε are the LHRS livetime and LHRS efficiency, respectively. The number PS is the DAQ pre-scale, a number that determines what fraction of events are successfully recored, considering the HRS dead time.

9.1.3 Carbon Comparison Method

The final method was conceived as a way to obtain the titanium inclusive differential cross section without an actual model of the titanium cross section. Termed the *carbon comparison method*, it is essentially the yield ratio method, replacing the model cross section in Eq. 9.6 with the experimentally derived carbon inclusive differential cross section. For each bin of the carbon result, the titanium differential cross section at that point is calculated through[62]

$$\left(\frac{d^3\sigma}{d\Omega'dE'}\right)_{Ti}^i = \frac{Y_{Ti}^i}{Y_C^i} \left(\frac{d^3\sigma}{d\Omega'dE'}\right)_C^i \quad (9.8)$$

where Y_C^i is the data yield of carbon for bin i , and Y_{Ti}^i is the same for titanium.

Even though this approximation seems to neglect fundamental differences between the carbon and titanium nucleus, the results match decently well with the titanium cross sections obtained through other methods. This method works so well partially because the C and Ti targets are thin foil targets. This method would not work with the argon cross section, as the argon target is an extended gas target.

9.2 The Exclusive Cross Section

The exclusive differential cross section was extracted from the experimental data using a slightly modified version of the acceptance method described in §9.1.1 for the inclusive cross section. The six-fold exclusive cross section is given by[24]

$$\frac{d^6\sigma}{d\Omega'dE'd\Omega_{p'}dE_{p'}} = \frac{Y(p_m, E_m)}{Q \cdot \rho \cdot B(I) \cdot LT \cdot V_B \cdot C_{rad}}. \quad (9.9)$$

Here, $Y(p_m, E_m)$ is the yield, which has *not* been normalized by the accumulated charge, which is explicitly represented by Q in the denominator. The target density is ρ , which in the case of argon, has been corrected for the nominal density of the argon gas in the target cell[24]. As described in §4.3.3, the function $B(I)$ is the target density correction factor due to heating from the electron beam. The effects of the acceptance and kinematical cuts are described by the term V_B . Finally, the term C_{rad} accounts for the effect of radiative corrections and the bin-centering correction. The terms V_B and C_{rad} are determined by the SIMC spectrometer package.

An alternate method to obtain the exclusive cross section as a 2D histogram in missing momentum and missing energy is discussed in §B.7.

9.2.1 Extraction of the Spectral Function

The spectral function is extracted from the experimentally measured cross section σ_{exp} assuming DWIA. Using Eq. 3.49 to write σ_{exp} in the impulse approximation, the spectral function can be written as

$$S(p, E) = \frac{\sigma_{exp}}{K \cdot \sigma_{eN}^{off}}, \quad (9.10)$$

where σ_{eN}^{off} is the off-shell electron-nucleon cross section. The most common off-shell extrapolations to the Rosenbluth cross sections used are CC1 and CC2, developed by T. de Forest[45] (see §3.8).

10 Uncertainty and Error Analysis

Uncertainty and error affect every experiment conducted, and the experimentalist must carefully account for all sources of error and potential bias in the data. While there is arguably a difference in meaning between the words *uncertainty* and *error*, this dissertation shall use the terms interchangeably.

The measurement of any physical quantity involves a *statistical* uncertainty, as well as an additional *systematic* error. Often, the definition of these two sources of uncertainty in a measurement is not well defined, which can either lead to an understatement, or overstatement of the experimental error[87].

10.1 Statistical Uncertainty

When the statistical characteristics of a population or data-set are inferred from a sample of that data, *sampling error* is introduced to reflect the lack of knowledge of the entire population under consideration. Thus, *statistical uncertainty* is a reflection of the limited size of the data set under consideration. By definition, statistical variations between identical measurements of the same quantity are uncorrelated, and as the number of data points N under consideration increases, the statistical uncertainty decreases as $1/\sqrt{N}$ [87].

Let $H_X(m, l, u)$ be a histogram of a quantity X with m bins on the interval $[l, u]$. The statistical uncertainty associated with the quantity X is calculated on a bin-by-bin basis. If the i^{th} bin of $H_X(m, l, u)$ contains N_{events}^i events, then the relative statistical uncertainty of X associated with this bin is

$$\frac{\sigma_{stat}^i}{|X|} = \frac{1}{\sqrt{N_{events}^i}}. \quad (10.1)$$

The calculation of the statistical error associated with the detector efficiencies forms a large part of the spectrometer analysis. As mentioned in §8, the efficiency associated with a specific cut is calculated on a pass/fail basis with respect to that cut. The events that pass the selection cut are considered *successes*, and the rest are *failures*. This event sorting process is essentially a Bernoulli trial where the probability of success is the efficiency. These repeated calculations are statistically independent Bernoulli trials, and hence the statistics of the binomial distribution applies to the error analysis.

10.1.1 Restricted Binomial Error

Authors such as T. Ullrich and Z. Xu in Ref. [88] have argued that treating statistical errors with a standard binomial distribution is flawed as it does not reproduce expected asymptotic behavior. Let the detector cut efficiency be $\varepsilon = k/n$, where k events out of a total of n events pass the selection cut. In this notation, the standard *binomial distribution* is given by

$$P(\varepsilon) = \binom{n}{k} \varepsilon^k (1 - \varepsilon)^{n-k}. \quad (10.2)$$

It should be noted that $P(\varepsilon)$ makes no assumptions about the efficiency ε . That is, any $\varepsilon \in \mathbb{R}$ is allowed by the standard binomial distribution. However, an efficiency $\varepsilon \in \mathbb{R} \setminus [0, 1]$ is unphysical, and should not be allowed by the probability distribution. The proposed solution is to restrict the binomial distribution to the closed unit interval $[0, 1]$ by multiplying $P(\varepsilon)$ by a piecewise function

$$f(\varepsilon) = \begin{cases} 1 & \text{if } \varepsilon \in [0, 1] \\ 0 & \text{otherwise} \end{cases}. \quad (10.3)$$

The amended distribution $P(\varepsilon)f(\varepsilon)$ must be “renormalized” over the unit interval. Carrying out these calculations gives the new restricted binomial distribution as

$$P(\varepsilon) = \frac{(n+1)!}{k!(n-k)!} \varepsilon^k (1 - \varepsilon)^{n-k}. \quad (10.4)$$

The statistical uncertainty, given by $\sigma_\varepsilon = \pm \sqrt{\text{Var}(\varepsilon)}$, is calculated with this new probability distribution function, yielding

$$\sigma_\varepsilon = \sqrt{\frac{(k+1)(k+2)}{(n+2)(n+3)} - \frac{(k+1)^2}{(n+2)^2}}. \quad (10.5)$$

10.1.2 The Wilson Score Interval

Another method to measure the statistical uncertainty is to use the *Wilson score interval*. The Wilson score interval is a binomial proportion confidence interval for Bernoulli trial events. The interval is defined by the upper (w^+) and lower (w^-) bounds given by

$$w^\pm = \frac{n_S + \frac{z^2}{2}}{n + z^2} \pm \frac{z}{n + z^2} \sqrt{\frac{n_S n_F}{n} + \frac{z^2}{4}}. \quad (10.6)$$

In this expression, n_S is the number of successes and n_F the number of failures. The number z is the $1 - \frac{\alpha}{2}$ quantile of the normal distribution. We choose $z = 1.96$ for a confidence level of 95%. That is, one can be 95% confident that the efficiency is contained in the interval $[w^-, w^+]$. A depiction of the Wilson score interval on a number line is given in Fig. 97.

As the efficiency is not guaranteed to be the center of the interval, the error σ_\pm is asymmetrical around ε . In terms of the bounds, the error is calculated as $\sigma_+ = w^+ - \varepsilon$ and $\sigma_- = \varepsilon - w^-$.

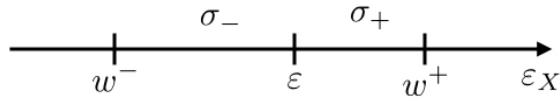


Figure 97: Depiction of the Wilson score interval on a number line.

10.2 Systematic Uncertainty

Systematic uncertainties, often shortened to *systematics*, arise from multiple sources, including the limited precision of the measurement apparatus, and the methods and models used to analyze the experimental data. Thus, identifying and accounting for all the relevant sources of systematic uncertainty in a measurement is a crucial component of the data analysis. As systematics are inherent to the measuring device, repeated measurement of the same quantity does not reduce the associated systematic uncertainty, and the uncertainties from each measurement are usually correlated[87].

Any quantity measured by the HRS that has a cut applied to it has an associated systematic uncertainty. Additionally, measurements used as input for the SIMC have associated systematic uncertainty. The sources of systematic uncertainty considered in the analysis are listed in Tab. 14. There are multiple methods used to calculate the magnitude of the systematics, and not all methods are considered equal or valid by some authors. The methods in the E12-14-012 analysis are described below.

Let $H_X^{data}(m, L, U)$ be a histogram of the measured quantity X divided into m bins on the interval $[L, U]$. Consider a cut on X defined by the interval $[l, u] \subseteq [L, U]$. The associated systematic uncertainty is calculated by varying the cut interval bounds by a small amount δ , then calculating the percent error as a result of that variation. Four varied histograms are generated, one for each of the cut variations

$$[l - \delta, u] \tag{10.7a}$$

$$[l + \delta, u] \tag{10.7b}$$

$$[l, u - \delta] \tag{10.7c}$$

$$[l, u + \delta] \tag{10.7d}$$

The percent error is calculated between each variation histogram and the original histogram, and the contributions from each variation are summed in quadrature. If the variations for the quantity X are labeled X_1 through X_4 , then the contribution to the total systematic uncertainty is given by

$$\sigma_X^{sys} = \sqrt{\sigma_{X_1}^2 + \sigma_{X_2}^2 + \sigma_{X_3}^2 + \sigma_{X_4}^2}. \quad (10.8)$$

Each of the contributions to σ_X^{sys} are calculated on a bin-by-bin basis between the original and varied histograms of X , normalized by the fractional number of SIMC events per-bin.

The method of calculating the contribution of each source to the total systematic uncertainty is as follows. Let $H_X^{\text{SIMC}}(m, L, U)$ be the histogram of the SIMC approximation of the quantity X . Note that the binning of H_X^{SIMC} must be identical to H_X^{data} . If the number of SIMC events in the i^{th} bin is N_{SIMC}^i , then the total number of monte-carlo events in H_X^{SIMC} is given by the sum

$$N_{\text{SIMC}} = \sum_{i=0}^{m-1} N_{\text{SIMC}}^i. \quad (10.9)$$

Similarly, let N_{data}^i be the number of events in the i^{th} bin of the data histogram. For each bin, define the triple ratio C^i as

$$C^i = \frac{N_{\text{data}}^i}{\left(\frac{N_{\text{SIMC}}^i}{N_{\text{SIMC}}}\right)}. \quad (10.10)$$

The triple ratio is essentially the number of data events-per-bin normalized by the ratio of the number of SIMC events-per-bin to the total number of generated monte-carlo events. The variation of the quantity X in the i^{th} bin is calculated as the fractional difference

$$\sigma^i = \frac{C^i - C_0^i}{C_0^i}, \quad (10.11)$$

where C_0^i is the triple ratio for the un-altered variable histogram. The total contribution to the systematics in the i^{th} bin from the experimentally measured quantity X is calculated by using Eq. 10.11 in Eq. 10.8.

The contributions from the SIMC to the systematics are evaluated by varying specific quantities in the SIMC input files, re-running the code, and then comparing these results to the un-altered SIMC file. The variation of the SIMC quantity X in the m^{th} bin is given by the difference ratio

$$\sigma^m = \frac{N_{\text{SIMC}}^m - N_{\text{SIMC}}^{0m}}{N_{\text{SIMC}}^{0m}}, \quad (10.12)$$

where N_{SIMC}^{0m} is the number of SIMC events in the un-altered histogram. The contributions σ^m from each variation are summed in quadrature to determine the contribution from X to the systematic error.

The effect of the variations described in Tab. 14 on the detector efficiencies was investigated. It was discovered that the cut-variations, when applied to β_{RHRS} , altered the beta-cut efficiency enough to affect the calculation of the systematic uncertainty. This is due to the fact that the variations defined in Eq. 10.7b and Eq. 10.7c remove good events from the sample, thus decreasing the calculated efficiency ε_{beta} , as seen in Fig. 98. As the coincidence-time cut-efficiency is sensitive to cuts on β_{RHRS} , ε_{coinc} was also re-calculated for each beta-cut variation (see Fig. 99). Thus, for each variation of the beta-cut interval, the beta-cut and coincidence time cut efficiency were re-calculated and the variation histograms re-weighted before calculating the systematics.

The systematic uncertainties for the inclusive analysis are summarized in Tab. 15. Overall, the total systematic uncertainty calculated from the inclusive data is low, being $< 3\%$ for all targets.

The systematic uncertainties for the argon and titanium exclusive Kin1 data are summarized in Tab. 16. The systematics for argon at the remaining kinematics are summarized in Tab. 17. The exclusive data for the first three kinematic settings enjoy low systematic uncertainty ($\leq 3.32\%$ for Kin3). However, the systematic uncertainty is significantly higher for the other kinematics, reaching as high as 10.23% for Kin4. This jump in the uncertainty is not unexpected, as the systematics at the higher kinematic settings include contributions from the background summed in quadrature with the signal[89].

Some authors and researchers contend that the method of estimating the magnitude of a systematic uncertainty as a shift in magnitude of a quantity as the result of a variation is flawed. P. Sinervo argues that this method is likely to overestimate the uncertainty, as the observed variation in the quantity may be dominated by the statistical uncertainty in the measurement, thus obscuring the systematic bias in the measurement[87]. In other words, a one-standard-deviation variation on a quantity may not fully capture how it changes as a result of said variation, due to low data statistics. These potential statistical variations in data-events between cut variations cannot be overcome by increasing MC statistics[90].

10.2.1 Systematics from Radiative Corrections

To estimate the systematic uncertainty from the choice of model used to calculate the radiative corrections (denoted δ_{rad}^{sys}), an overall scaling factor of $\sqrt{Q^2}/2$ was applied to the model Born cross section (§6.1) on a bin-by-bin

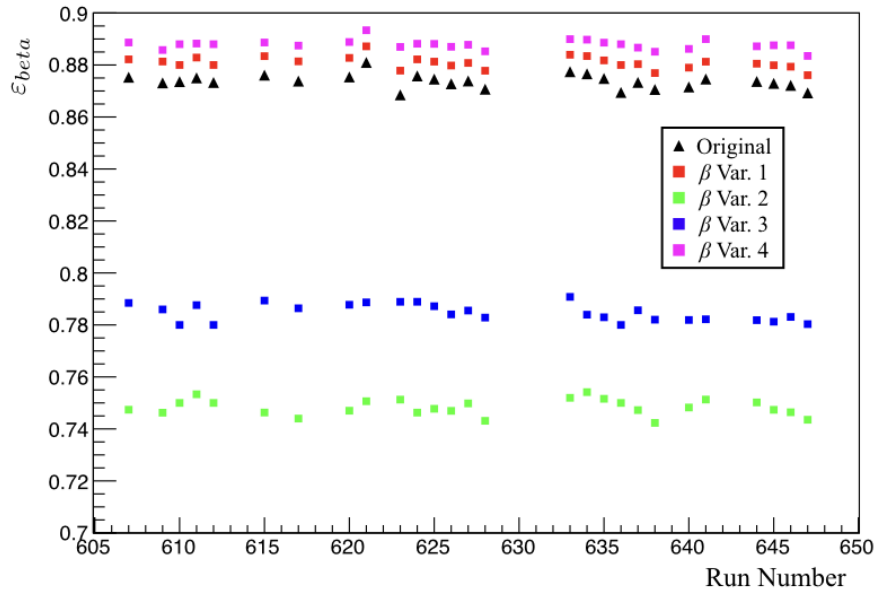


Figure 98: Change in β -cut efficiency for each variation of the cut interval, for Ti Kin4.

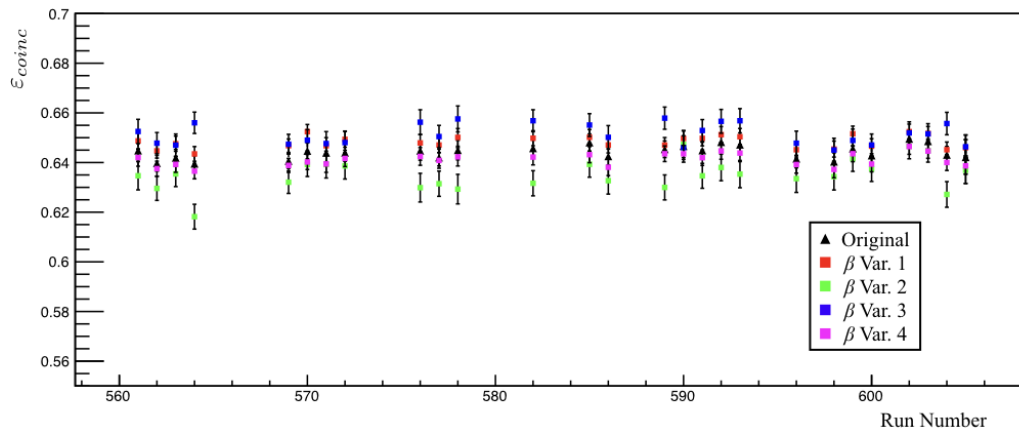


Figure 99: Change in coincidence time cut efficiency for each variation of the RHRS beta cut interval (Argon Kin4).

Source	Quantity	Variation
Data Cuts	θ_{tg}^e	$\theta_{tg}^e + [\pm 0.0002, \pm 0.0002]$ rad
	θ_{tg}^p	$\theta_{tg}^p + [\pm 0.0002, \pm 0.0002]$ rad
	ϕ_{tg}^e	$\phi_{tg}^e + [\pm 0.0002, \pm 0.0002]$ rad
	ϕ_{tg}^p	$\phi_{tg}^p + [\pm 0.0002, \pm 0.0002]$ rad
	dp_{tg}^e	$dp_{tg}^e + [\pm 0.0002, \pm 0.0002]$
	dp_{tg}^p	$dp_{tg}^p + [\pm 0.0002, \pm 0.0002]$
	z_{tg}^e	$z_{tg}^e + [\pm 0.01, \pm 0.01]$ cm
	β	$\beta_{RHRS} + [\pm 0.05, \pm 0.05]$
	Δt_{coinc}	$ \Delta t_{coinc} - t_{peak} \leq 2 \cdot (\sigma \pm 0.3 \text{ ns})$
CEBAF	x_{beam}	$x_{beam} \pm 0.04$ cm
	y_{beam}	$y_{beam} \pm 0.04$ cm
HRS	x_L	$x_L \pm 0.0005$ cm
	y_L	$y_L \pm 0.0005$ cm
	x_R	$x_R \pm 0.0005$ cm
	y_R	$y_R \pm 0.0005$ cm
COSY	Q_1	$Q_1 \pm 1\%$
	Q_2	$Q_2 \pm 1\%$
	Q_3	$Q_3 \pm 1\%$

Table 14: Sources of systematic uncertainty with cut variations used to calculate the contribution to the total systematic uncertainty.

	²⁷ Al	⁴⁰ Ar	¹² C	⁴⁸ Ti
a. Beam energy	0.1%	0.1%	1.40%	1.40%
b. Beam charge	0.3%	0.3%	1.00%	1.00%
c. Beam x offset	1.0%	0.8%	0.66%	0.66%
d. Beam y offset	1.0%	0.9%	0.28%	0.28%
e. HRS x offset	0.8%	1.0%	0.39%	0.39%
f. HRS y offset	0.6%	0.8%	0.43%	0.43%
g. Optics (Q_1, Q_2, Q_3)	1.8%	1.0%	-	-
h. Target thickness/density/length	0.2%	0.7%	0.51%	0.38%
i. Acceptance cut (θ, ϕ, dp, z, y)	1.0%	2.4%	1.43%	1.43%
j. Calorimeter cut	0.02%	0.02%	0.01%	0.01%
k. Cherenkov cut	0.12%	0.07%	0.02%	0.02%
l. Cross section model	0.2%	1.3%	0.2%	-
m. Radiative and Coulomb corr.	1.3%	1.3%	1.3%	-
Total systematic uncertainty	2.7%	3.0%	2.9%	-
Total statistical uncertainty	2.0%	2.0%	1.10%	0.99%

Table 15: Sources and contributions to the systematic uncertainty from the aluminum, argon, carbon, and titanium inclusive data[62, 65].

	Ar	Ti
a. Beam x, y offset	0.63%	0.49%
b. Beam energy	0.10%	0.10%
c. Beam charge	0.30%	0.30%
d. HRS x, y offset	0.83%	0.58%
e. Optics (Q_1, Q_2, Q_3)	0.94%	0.48%
f. Acceptance cut (θ, ϕ, z)	1.16%	1.36%
g. Target thickness/density/length	0.2%	0.2%
h. Calorimeter & Cherenkov cut	0.02%	0.02%
i. Radiative and Coulomb corr.	1.00%	1.00%
j. β cut	0.47%	0.39%
k. Boiling effect	0.70%	-
l. Cross section model	1.00%	1.00%
m. Trigger and coincidence time cut	0.92%	0.78%
Total systematic uncertainty	2.65%	2.35%

Table 16: Sources and contributions to the systematic uncertainty from the argon and titanium Kin1 exclusive data[24].

Argon		Kin2	Kin3	Kin4	Kin5
a.	Beam x, y offset	0.85%	0.69%	0.91%	1.68%
b.	Beam energy	0.10%	0.10%	0.10%	0.10%
c.	Beam charge	0.30%	0.30%	0.30%	0.30%
d.	HRS x, y offset	1.17%	0.78%	1.44%	1.71%
e.	Optics (Q_1, Q_2, Q_3)	0.77%	0.55%	0.90%	1.72%
f.	Acceptance cut (θ, ϕ, z)	1.33%	1.75%	2.19%	7.72%
g.	Target thickness/density/length	0.20%	0.20%	0.20%	0.20%
h.	Calorimeter & Cherenkov cut	0.02%	0.02%	0.02%	0.02%
i.	Radiative and Coulomb corr.	1.00%	1.00%	1.00%	1.00%
j.	β cut	0.55%	0.39%	7.74%	5.87%
k.	Boiling effect	0.70%	0.70%	0.70%	0.70%
l.	Cross section model	1.00%	1.00%	1.00%	1.00%
m.	Trigger and coincidence time cut	0.52%	0.98%	5.55%	2.58%
Total systematic uncertainty		3.24%	3.32%	10.23%	9.01%
Total statistical uncertainty		0.57%	0.64%	0.54%	1.65%

Table 17: Sources and contributions to the systematic uncertainty from the argon exclusive data at Kin2 through Kin5[89]. The systematics for Kin4 and Kin5 include the contribution from the background, summed in quadrature with the contribution from the signal.

basis. Let $\sigma_{born}^i(\sqrt{Q_i^2}/2)$ denote the scaled Born cross section, noting that the parenthesis do not indicate functional dependence. Then, the magnitude of the (completely uncorrelated) systematic error is given by the difference

$$\delta_{rad}^{sys,i} = \frac{\sigma_{born}^i - \sigma_{born}^i(\sqrt{Q_i^2}/2)}{\sigma_{born}^i}. \quad (10.13)$$

It should be noted that there is no physics behind the choice of this scaling factor. Other quantities, such as x_B , have been used to scale the inclusive cross sections to calculate the contribution to the systematic uncertainty[91]. The choice is not crucial, as it is known that radiative corrections are largely independent of cross section model.

10.2.2 Systematics from Final State Interactions

The inclusion of final state interactions introduces four sources of systematic uncertainty, which arise from the

- (a) Choice of off-shell electron-proton cross section used to calculate the reduced cross section,
- (b) Choice of pairing mechanism used to calculate the ground-state wavefunction,
- (c) Choice of phenomenological optical potential model,
- (d) Choice of nucleon form factor parametrization.

To avoid confusion with the notation for the reduced cross section, the symbol δ_i^{sys} will be used to denote the systematic uncertainty from a source i .

The reduced cross section σ_{red} , defined in Eq. 6.26, is calculated in terms of the off-shell electron proton cross section σ_{ep} . The two off-shell extrapolations used, CC1 and CC2, are described in §3.8. The choice of σ_{ep} in the reduced cross section contributes $\delta_{\sigma_{ep}}^{sys}$ to the systematic uncertainty.

In 1958, A. Bohr et al. proposed an analogy between the low-energy spectra of nuclei and the electrons in a superconducting metal[92]. This analogy is based on an empirically observed energy gap between the nuclear ground state and first intrinsic excited state, signifying the presence of attractive forces between the nucleons[92]. These attractive forces lead to a *pairing effect* between the nucleons, just like the electron *Cooper pairs* in a superconducting metal. Indeed, the nuclear pairing can be theoretically described by the Bardeen-Cooper-Schrieffer (BCS) theory[93, 94].

Alternatively, ground state properties of the nucleus can be calculated using self-consistent mean-field theories derived from relativistic energy density functionals[95]. The Dirac-Hartree-Bogoliubov (DHB) model calculates the nuclear ground state wave function by solving the stationary relativistic Hartree-Bogoliubov equations through self-consistent numerical iteration schemes[95].

The theoretical model used to describe the nuclear pairing is known as the *pairing mechanism*. The choice of pairing mechanism (BCS or DHB) used to calculate the nuclear ground-state wave function ψ contributes δ_{ψ}^{sys} to the systematic uncertainty.

Three phenomenological fits were used to model the optical potential \tilde{V} , as described in §6.2. The choice of fit for the optical potential (DEM, EDAD1, or EDAD3) contributes δ_{opt}^{sys} to the systematic uncertainty. As there are three choices for \tilde{V} , the systematic uncertainty is taken as the maximum deviation from the default choice (see Eq. 10.15)[96].

There are many parameterizations used to describe the nucleon electric and magnetic form factors $G_{Ep,n}(Q^2)$ and $G_{Mp,n}(Q^2)$. The choice of form factor parameterization contributes δ_{FF}^{sys} to the systematic uncertainty. However, the choice of form factor has been shown to have a negligible effect on the calculation of the reduced cross section, and hence the contribution to Eq. 10.14 can be ignored ($\delta_{FF}^{sys} \approx 0$)[96].

The contributions listed above are summed in quadrature to give the total contribution to the systematic uncertainty from the FSI correction as

$$\delta_{FSI}^{sys} = \sqrt{\delta_{\sigma_{ep}}^{sys2} + \delta_{\psi}^{sys2} + \delta_{opt}^{sys2} + \delta_{FF}^{sys2}}. \quad (10.14)$$

Each non-zero term in Eq. 10.14 is evaluated by comparing the shifted and scaled reduced cross section calculated from a default set of quantities ($\sigma_{ep}, \psi, \tilde{V}$) to that obtained by altering the choice of the specified quantity.

The reduced cross sections are calculated from missing momentum and missing energy spectra that have been shifted and scaled as described in §6.2. The missing momentum shift Δ and scaling factor $R = \frac{\sigma_{DWIA}}{\sigma_{PWIA}}$ are calculated from the set of quantities ($\sigma_{ep}, \psi, \tilde{V}$). The default quantities are (CC1,BCS,DEM); CC1 for the off-shell cross section, the BCS ground state wave function, and the democratic fit to the optical potential (DEM) .

Let $\sigma_{red}(\Delta, R; \sigma_{ep}, \psi, \tilde{V})$ denote the (shifted and scaled) reduced cross section with shift Δ and scaling factor R calculated from the quantities ($\sigma_{ep}, \psi, \tilde{V}$). Then, $\sigma_{red}^0 = \sigma_{red}(\Delta, R; \text{CC1, BCS, DEM})$ is the cross section evaluated with the default parameters. In this notation, the contribution from a source i to the systematic uncertainty in Eq. 10.14 is calculated as

$$\delta_i^{sys} = \sigma_{red}^i(\Delta, R; \sigma_{ep}, \psi, \tilde{V}) - \sigma_{red}^0. \quad (10.15)$$

10.3 Propagation of Error

Once the error or uncertainty has been calculated, it is important to know how it propagates through a mathematical expression for a given quantity. Consider a function $f(x, y, \dots)$ of at least two variables. The equation for the statistical variance $\text{Var}(f) = \sigma_f^2$ is

$$\sigma_f^2 = \sigma_x^2 \left(\frac{\partial f}{\partial x} \right)^2 + \sigma_y^2 \left(\frac{\partial f}{\partial y} \right)^2 + \dots + 2\sigma_{xy} \left(\frac{\partial f}{\partial x} \right) \left(\frac{\partial f}{\partial y} \right) + \dots \quad (10.16)$$

The quantity $\sigma_{xy} = \text{Cov}(x, y)$ in the mixed partial derivative term is known as the *covariance* of x and y . If the variables x and y are *uncorrelated*, their covariance vanishes.

While Eq. 10.16 applies to any multi-variable function $f(x, y, \dots)$, the only functions with uncertainty considered in this analysis can be factored into (at least) two terms. Assume the function factors into two terms A and B , each with an associated uncertainty σ_A and σ_B . In this case, Eq. 10.16 is used to calculate the relative uncertainty of f as

$$\frac{\sigma_f}{|f|} = \sqrt{\left(\frac{\sigma_A}{A} \right)^2 + \left(\frac{\sigma_B}{B} \right)^2 \pm 2 \frac{\sigma_{AB}}{AB}} \quad (10.17)$$

where the plus sign is used for $f = A \cdot B$ and the minus sign for $f = A/B$. Clearly, ignoring (or mis-calculating) the covariance/correlation term in Eq. 10.17 can lead to an over- or under-estimation of the systematic error. However, in the case of σ_f describing a statistical uncertainty, the correlation term vanishes identically and the equation for the relative uncertainty reduces to

$$\frac{\sigma_f}{|f|} = \sqrt{\left(\frac{\sigma_A}{A} \right)^2 + \left(\frac{\sigma_B}{B} \right)^2}. \quad (10.18)$$

Take, for example, the statistical uncertainty of the VDC efficiency, $\varepsilon_{\text{VDC}} = R_1 \cdot R_2$. Applying Eq. 10.18 gives the relative uncertainty as

$$\frac{\sigma_{\text{VDC}}}{\varepsilon_{\text{VDC}}} = \sqrt{\left(\frac{\sigma_{R_1}}{R_1} \right)^2 + \left(\frac{\sigma_{R_2}}{R_2} \right)^2}. \quad (10.19)$$

A table detailing the contribution of each source to the total systematic uncertainty is given in Table 15. The numbers listed reflect the maximum contribution to the systematics of each source.

10.4 Uncertainty in the Cross Section

The experimentally measured inclusive cross section in the yield ratio method is given as $\sigma_{\text{exp}} = \sigma_{\text{born}} \cdot Y_{\text{ratio}}$, and the statistical uncertainty must be propagated through this equation. To avoid confusion with notation for the cross section, the uncertainty of the cross section will be denoted with δ . The model cross section σ_{born} is treated as a constant, and has no statistical uncertainty associated with it. Thus, the statistical error of the experimental cross section is

$$\delta_{\text{exp}}^{\text{stat}} = \sigma_{\text{exp}} \cdot \frac{\delta_{\text{ratio}}^{\text{stat}}}{Y_{\text{ratio}}}, \quad (10.20)$$

where $\delta_{\text{ratio}}^{\text{stat}}$ is the statistical uncertainty of the yield ratio. To calculate $\delta_{\text{ratio}}^{\text{stat}}$, the uncertainty must be propagated through $Y_{\text{ratio}} = Y_{\text{data}}/Y_{\text{MC}}$. Applying Eq. 10.18 to the yield ratio gives

$$\frac{\delta_{\text{ratio}}^{\text{stat}}}{Y_{\text{ratio}}} = \sqrt{\left(\frac{\delta_{\text{data}}^{\text{stat}}}{Y_{\text{data}}}\right)^2 + \left(\frac{\delta_{\text{MC}}^{\text{stat}}}{Y_{\text{MC}}}\right)^2}, \quad (10.21)$$

where $\delta_{\text{data}}^{\text{stat}}$ and $\delta_{\text{MC}}^{\text{stat}}$ are the statistical errors of the data yield and MC yield, respectively. If enough monte-carlo events are generated, the statistical error from the monte-carlo yield becomes negligible and hence can be ignored. Assuming N_{SIMC} is large enough to take $\delta_{\text{MC}}^{\text{stat}} \rightarrow 0$, the definition of Eq. 10.1 gives the statistical error of the yield ratio as

$$\sigma_{\text{ratio}}^{\text{stat}} = \frac{Y_{\text{ratio}}}{\sqrt{N_{\text{data}}}}. \quad (10.22)$$

Thus, we have the statistical uncertainty of the inclusive cross section as

$$\delta_{\text{exp}}^{\text{stat}} = \sigma_{\text{born}} \cdot \frac{Y_{\text{ratio}}}{\sqrt{N}}. \quad (10.23)$$

There are different conventions for reporting the uncertainty on the cross section. Often, the statistical and systematic errors are listed individually, with the cross section written as

$$\frac{d^3\sigma}{d\Omega d\omega} = \sigma_{\text{exp}} \pm \delta_{\text{exp}} \pm \delta_{\text{exp}}^{\text{sys}}, \quad (10.24)$$

where $\delta_{\text{exp}}^{\text{sys}}$ is the total systematic uncertainty calculated previously. The uncertainties can be added in quadrature to obtain the total uncertainty as

$$\delta_{\text{tot}} = \sqrt{(\delta_{\text{exp}}^{\text{stat}})^2 + (\delta_{\text{exp}}^{\text{sys}})^2}. \quad (10.25)$$

11 E12-14-012 Experimental Results

11.1 Inclusive Cross Sections

The inclusive differential cross sections extracted from the data are presented in this section. All inclusive cross sections were taken at Kin5, with $E_0 = 2.222$ GeV at $\theta = 15.541^\circ$. The results for ^{12}C , ^{48}Ti , ^{40}Ar and ^{27}Al are shown in Figs. 100, 101, 102, and 103, respectively. The carbon, titanium, and argon cross sections were calculated with the yield ratio method, while the aluminum result was calculated with the acceptance correction method.

Overall, the agreement between the data and model cross sections are within expectations. The best agreement with the model comes from the carbon result, especially in the regions where $\omega < 0.15$ GeV and $\omega > 0.6$ GeV. It is also clear that the model over-estimates the cross section in the Δ -production region for all nuclei. However, this discrepancy is expected, as accurately modeling the dip region between the quasi-elastic peak and Δ -production peak is known to be difficult.

The inclusive cross sections for different nuclei can be compared by dividing by the atomic mass number A . The per-nucleon responses of the four target nuclei investigated are plotted in Fig. 104. The normalized cross sections are in exceptional agreement for most of the E' spectrum, except for the dip region and the maximum of the quasi-elastic peak[65]. However, it is clear from inspection of Fig. 104 that the carbon cross section differs greatly from the cross sections of the other nuclei in the dip region and at the quasi-elastic peak. This implies that the ‘‘Doppler broadening’’ of the quasi-elastic peak due to final state interactions is not as pronounced in carbon as it is for the heavier nuclei[65].

Further comparison can be made between the inclusive cross sections by normalizing them to the sum of the single-nucleon cross sections σ_{eN} . The four inclusive cross sections, normalized according to Eq. 11.1, are shown in Fig. 105. However, even with this normalization convention, the carbon result still stands out in the dip region and at the quasi-elastic peak.

$$\frac{d^3\sigma/d\Omega'dE'}{Z\sigma_{ep} + (A - Z)\sigma_{en}} \quad (11.1)$$

11.2 Scaling Functions

In this section, the scaling functions obtained from the inclusive cross sections are presented. The scaling function of the first kind $F(y)$ is extracted from

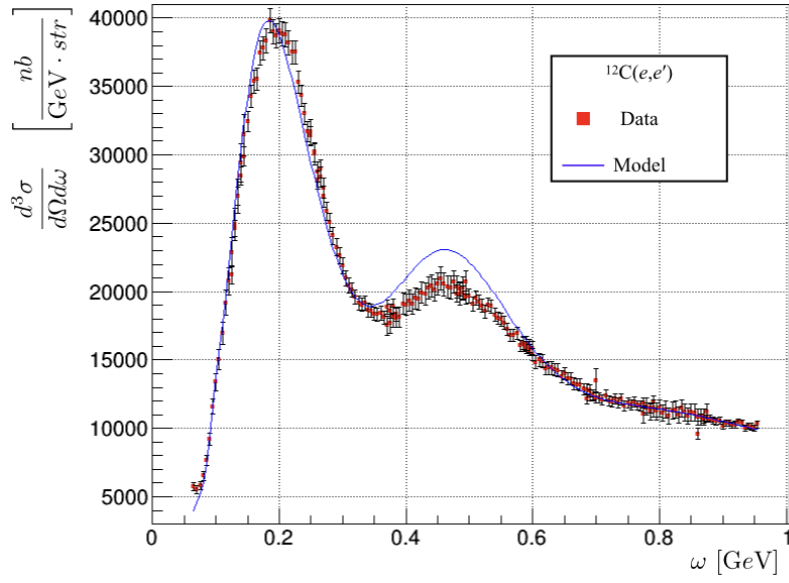


Figure 100: $^{12}\text{C}(e, e')$ differential cross section from the yield ratio method at $E_0 = 2.222$ GeV, $\theta = 15.541^\circ$ (inclusive Kin5).

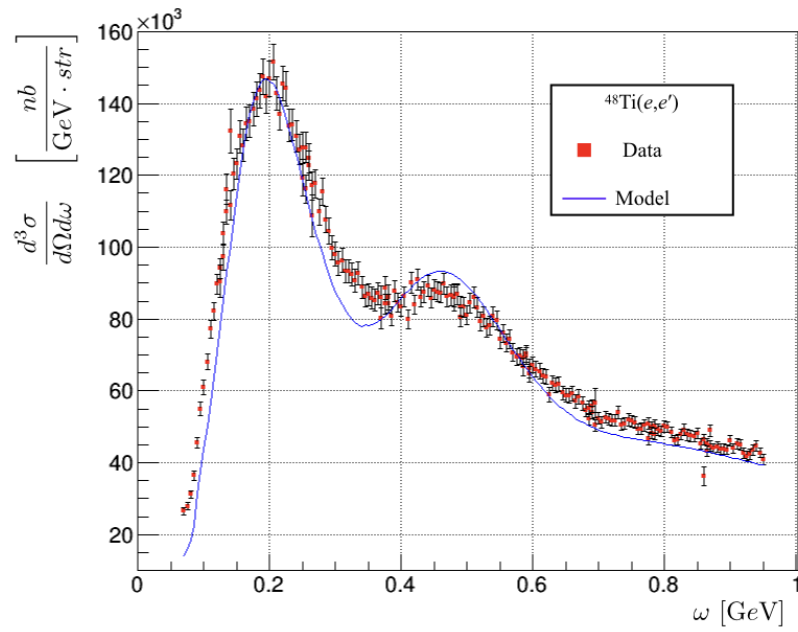


Figure 101: $^{48}\text{Ti}(e, e')$ differential cross section from the yield ratio method at $E_0 = 2.222$ GeV, $\theta = 15.541^\circ$ (inclusive Kin5).

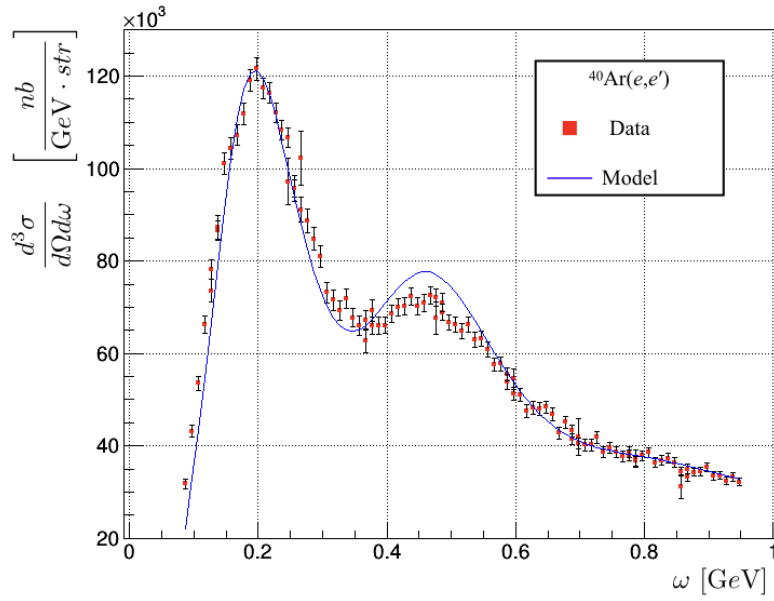


Figure 102: $^{40}\text{Ar}(e, e')$ differential cross section from the yield ratio method at $E_0 = 2.222$ GeV, $\theta = 15.541^\circ$ (inclusive Kin5).

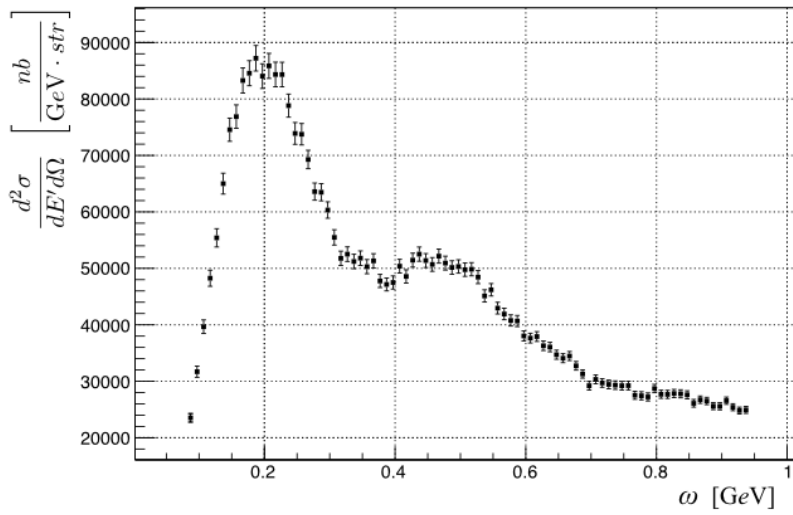


Figure 103: $^{27}\text{Al}(e, e')$ differential cross section from the yield ratio method at $E_0 = 2.222$ GeV, $\theta = 15.541^\circ$ (inclusive Kin5).

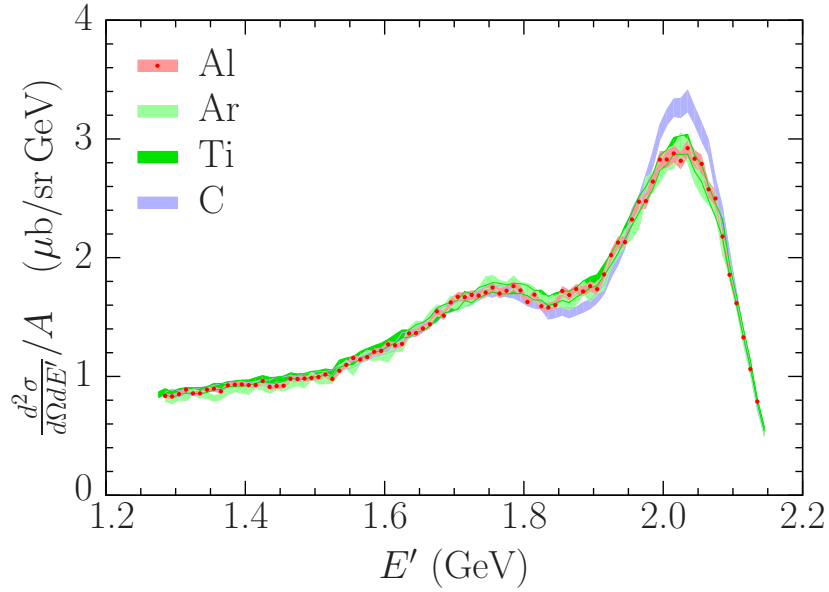


Figure 104: Carbon (blue), titanium (green), argon (light-green), and aluminum (red) inclusive cross sections-per-nucleon at $E_0 = 2.222$ GeV, $\theta = 15.541^\circ$ (inclusive Kin5)[65].

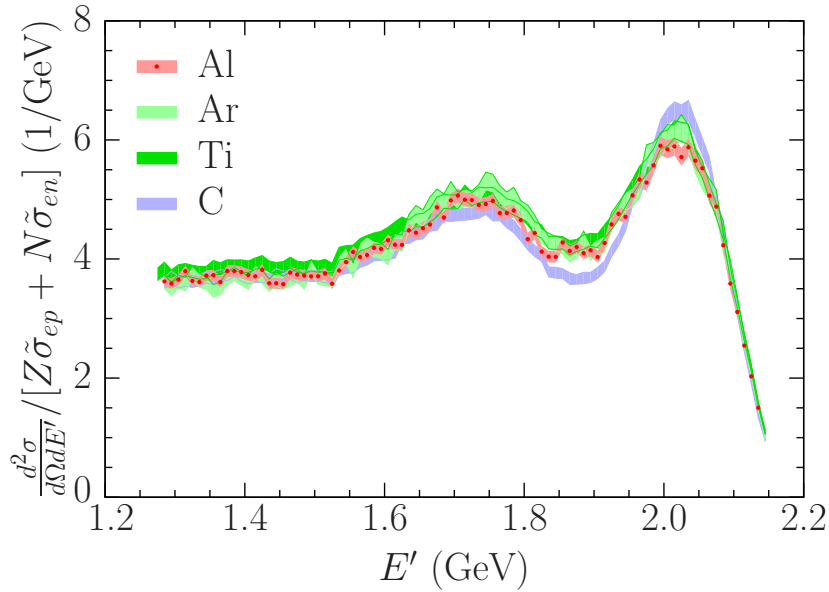


Figure 105: The carbon (blue), titanium (green), argon (light-green), and aluminum (red) inclusive cross sections normalized to the sum of the elementary single-nucleon cross sections (see Eq. 11.1)[65].

the experimental data through[97]

$$F(y) = \frac{\sigma_{exp} \cdot \frac{dE'}{dy}}{Z\sigma_{ep} + (A - Z)\sigma_{en}} \quad (11.2)$$

where σ_{exp} is the experimentally measured inclusive cross section, and the σ_{eN} are the elementary electron-nucleon cross sections (see §3.6.1).

The scaling function of the first kind for carbon is shown in Fig. 106, with the E12-14-012 data represented by magenta diamonds. Also shown for comparison are the scaling functions obtained at various values of Q^2 from the data of R. Sealock *et al.*[98] (circle-exes), J. O'Connell *et al.*[99] (circle-crosses), and D. Day *et al.*[34] (squares, exes, circles). The carbon scaling function is also shown in Fig. 109, extended to include a wide range of positive y values. Figure 107 shows the scaling function for aluminum extracted from the experimental data (magenta diamonds). Similarly, the scaling functions obtained from the data of D. Day *et al.*[34] at $Q^2 = 0.87 \text{ GeV}^2$ (squares), $Q^2 = 1.27 \text{ GeV}^2$ (crosses), and $Q^2 = 1.78 \text{ GeV}^2$ (circles), are shown for comparison purposes.

Scaling of the carbon and aluminum data is clear for $y \in [-0.1, 0] \text{ GeV}$ in the vicinity of the quasi-elastic peak, but begins to break down for $y < -0.1 \text{ GeV}$. However, the deviation from the scaling behavior at large negative y can be attributed to the effects of final state interactions between the ejected nucleon and spectator particles. This can be seen by examining the momentum-transfer dependence of the scaling function at fixed y . The scaling function for $y = -0.2 \text{ GeV}$ is shown in the inset of Fig. 106 for carbon, and in Fig. 107 for aluminum. This functional dependence, decreasing with increasing momentum-transfer, is evidence that the effects of FSI are still significant at the kinematics used in E12-14-012[62, 65].

The scaling functions for argon (red) and titanium (blue) derived from the experimental data are shown in Fig. 109. The scaling function obtained from the LNF argon cross section data (grey) is also shown for comparison purposes. There is significant disagreement between the E12-14-012 argon result and the LNF result; the only agreement existing for the single point at $y \approx -0.17 \text{ GeV}$.

The scaling functions of the second kind obtained from the E12-14-012 inclusive data are shown in Fig. 110[32]. The data show remarkable ψ -scaling behavior near the origin, and in the region $\psi \in [-0.25, 0]$. However, the argon and aluminum data begin to diverge from the other data for $\psi < -0.25$. Alternatively, the carbon and titanium data scale excellently across the entire range of ψ calculated. The ψ -scaling function derived from the LNF argon data (blue circles) is shown in Fig. 111 with the E12-14-012 argon result (red

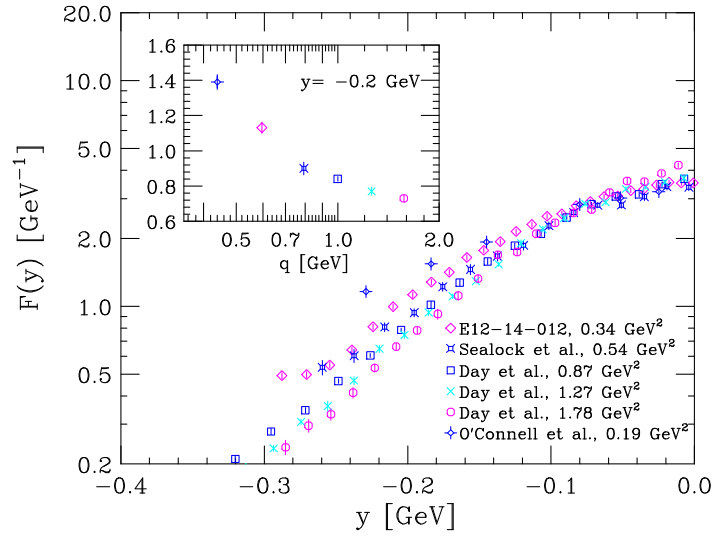


Figure 106: Carbon scaling function derived from E12-14-012 experimental data (diamonds)[62]. Other data points are from R. Sealock *et al.*[98], J. O'Connell *et al.*[99], and D. Day *et al.*[34]. The inset shows the momentum-transfer dependence of the scaling function at $y = -0.2 \text{ GeV}$.

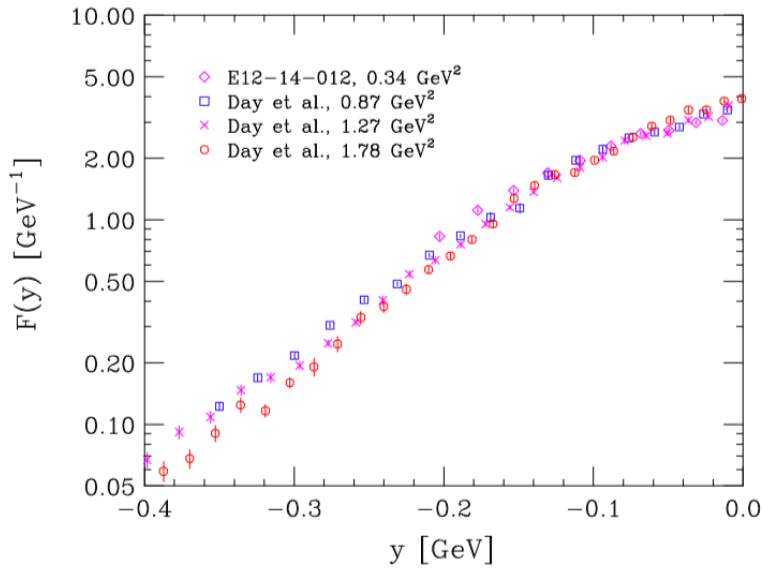


Figure 107: Plot of the y -scaling function extracted from the E12-14-012 inclusive aluminum data (diamonds), compared with previous results from D. Day *et al.* (Ref. [34]) at different values of Q^2 [65].

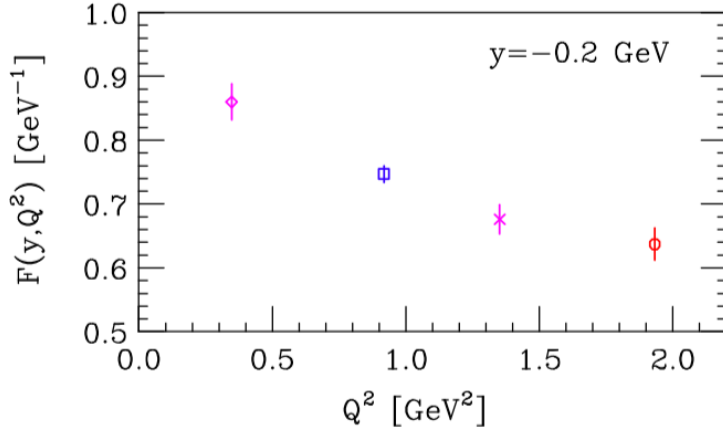


Figure 108: Plot showing the Q^2 dependence of the aluminum scaling function at $y = -0.2$ GeV[65]. The data point at $Q^2 = 0.34$ GeV² (diamond) is from the E12-14-012 inclusive data, while the remaining data points are from D. Day *et al.* in Ref. [34].

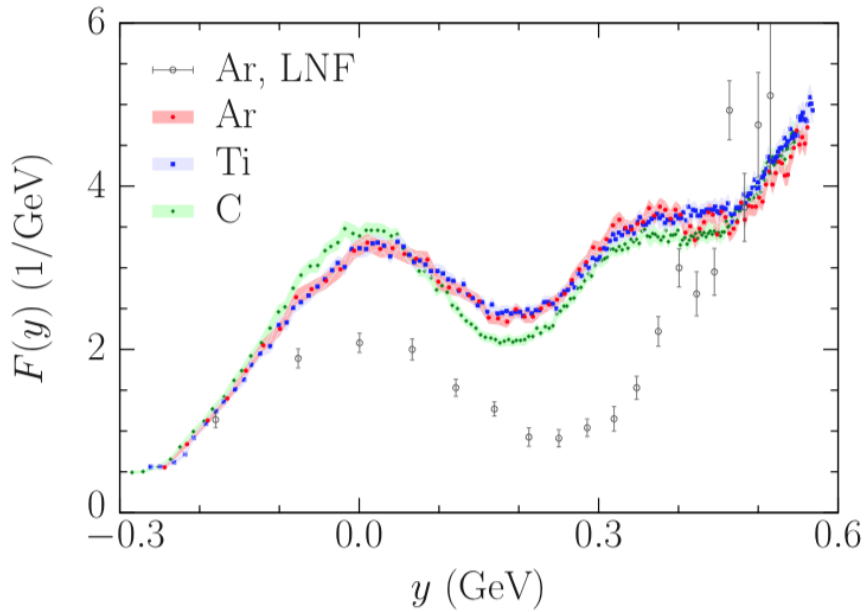


Figure 109: Scaling functions of the first kind obtained from the E12-14-012 inclusive data with the LNF argon result for comparison[32].

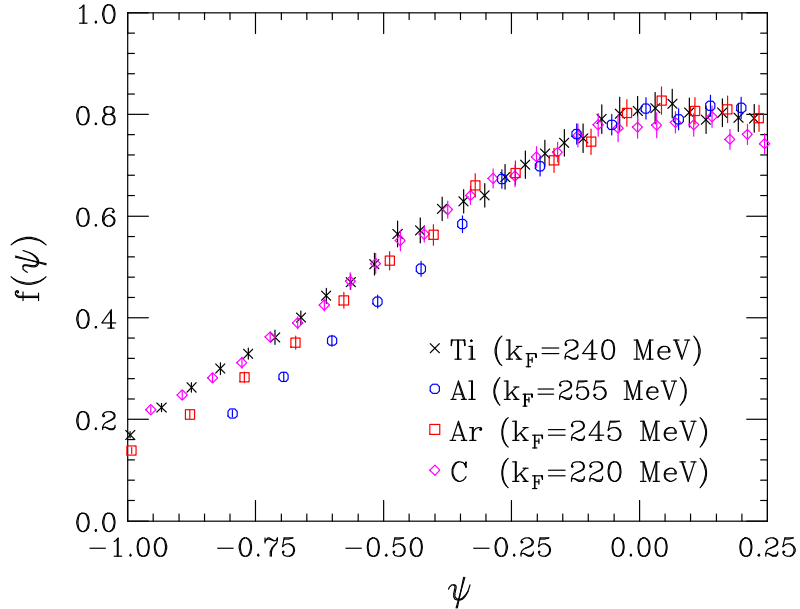


Figure 110: Scaling functions of the second kind obtained from the E12-14-012 inclusive data[32].

squares) for comparison. The LNF data only scale for $\psi > -0.25$ GeV, and requires an unrealistic Fermi momentum of 375 MeV.

11.3 Exclusive Cross Sections

In this section, the six-fold differential $(e, e'p)$ cross sections obtained from the experimental data are presented as functions of the missing energy and missing momentum. Although E12-14-012 took data at five kinematic settings, only the data taken at Kin1 was fully analyzed by the completion of this dissertation. The remaining experimental data at the other four kinematic settings is currently being analyzed, and is expected to be published in the near future.

The measured exclusive cross sections as functions of missing energy at Kin1 are shown in Fig. 112 for argon, and Fig. 113 for titanium. Also shown are the SIMC cross section and the experimental background, which was multiplied by a factor of ten for clarity in the figures. Clearly the SIMC prediction overestimates the data in nearly all cases. However, this result is not surprising as the SIMC does not account for final state interactions,

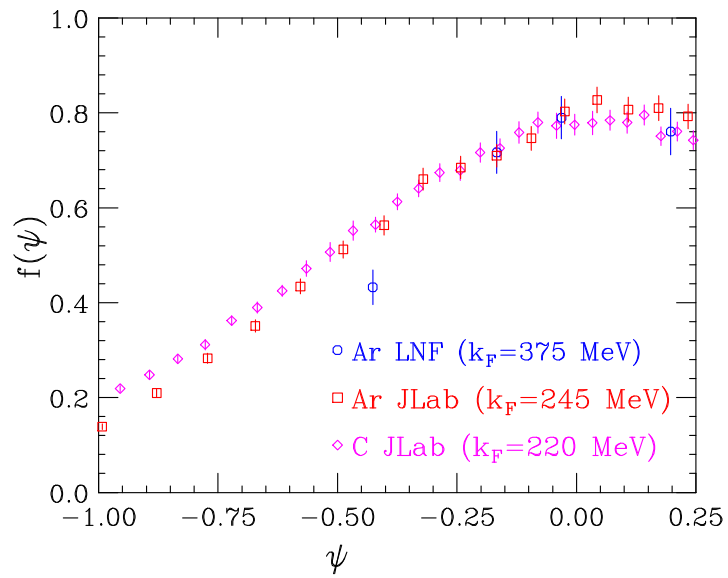


Figure 111: Argon ψ -scaling functions obtained from the E12-14-012 inclusive data and the LNF data (with E12-14-012 carbon data for comparison). Three of the LNF data points scale in ψ , but require an unrealistic Fermi momentum to do so.

save for the nuclear transparency. Also, the model spectral function used by SIMC does not account for NN-correlations, which are important at higher missing energies.

The exclusive cross sections, integrated over the full range of missing energy, are shown as functions of missing momentum in Fig. 114 for argon and Fig. 115 for titanium. Also shown is the SIMC cross section with the FSI correction applied (see §6.2). The FSI correction reduced the SIMC prediction significantly, but there is still significant disagreement with the data.

The cross sections integrated over different ranges of missing energy are shown in Fig. 116 and Fig. 117 for argon and titanium, respectively. These are the same E_{miss} ranges discussed in §6.3.3, and are listed in Tab. 12. Clearly, the best agreement between data and SIMC prediction is in the first region of missing energy ($E_{miss} \in [0, 27]$ MeV and Fig. 116a for argon, $E_{miss} \in [0, 30]$ MeV and Fig. 117a for titanium). However, the SIMC prediction does diverge with the data for increasing missing momentum.

As can be seen from Figs. 116–117, the data and SIMC agreement is not as good for the higher missing energy regions. There is quite a large shift in the SIMC missing momentum for both E_{miss} regions, and a significant difference in magnitude in Region II for titanium (Fig. 117b).

This discrepancy can be explained by the model spectral functions used in the analysis. The missing energies of Regions II and III ($E_{miss} > 27$ MeV) correspond to proton knockout from the $1p_{1/2}$, $1p_{3/2}$, and $1s_{1/2}$ shells. However, the energies and widths of these deeply bound shells were estimated, and not determined from experimental data[24]. The observed shifts in the missing momentum can be explained by underestimating the widths and associated overlaps of the energy distributions of these states[24]. The discrepancies between data and SIMC can also be ascribed to the limitations of the mean-field approximation used in the spectral function model[24].

12 Summary and Conclusions

This dissertation has presented the analysis and results of experiment E12-14-012 at Jefferson Lab. Inclusive cross sections for ^{12}C , ^{48}Ti , ^{40}Ar , and ^{27}Al were measured at $E_0 = 2.222$ GeV and $\theta = 15.541^\circ$. Scaling functions of the first and second kind were also obtained for these nuclei. Exclusive cross sections for ^{40}Ar and ^{48}Ti were also measured at five kinematic settings, listed in Tab. 5.

The inclusive data presented in this dissertation has led to three publi-

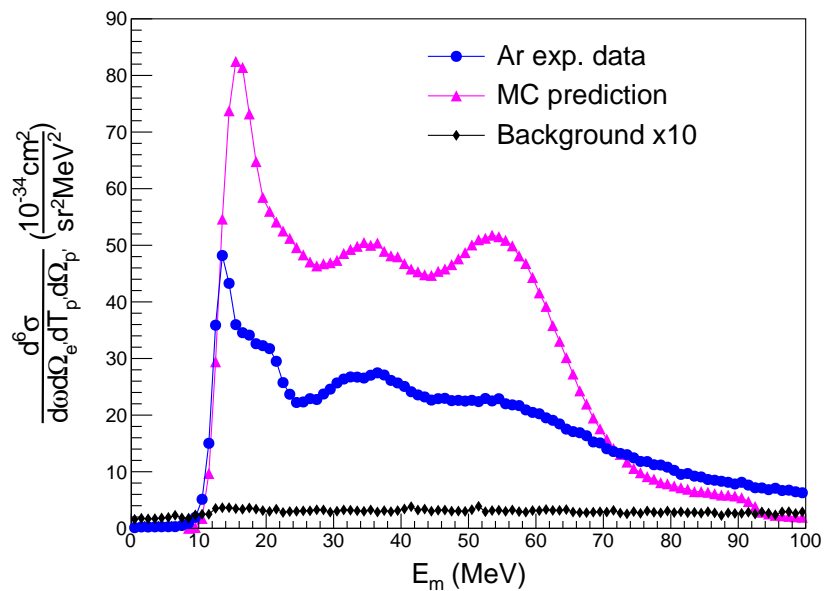


Figure 112: $^{40}\text{Ar}(e, e'p)$ Kin1 differential cross section as a function of missing energy, with SIMC prediction and background ($\times 10$) for comparison[24].

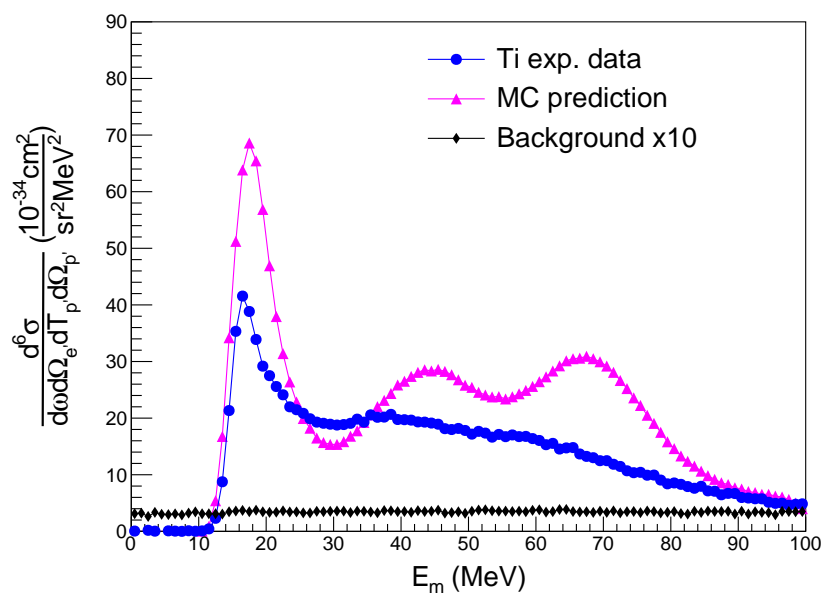


Figure 113: $^{48}\text{Ti}(e, e'p)$ Kin1 differential cross section as a function of missing energy, with SIMC prediction and background ($\times 10$) for comparison[24].

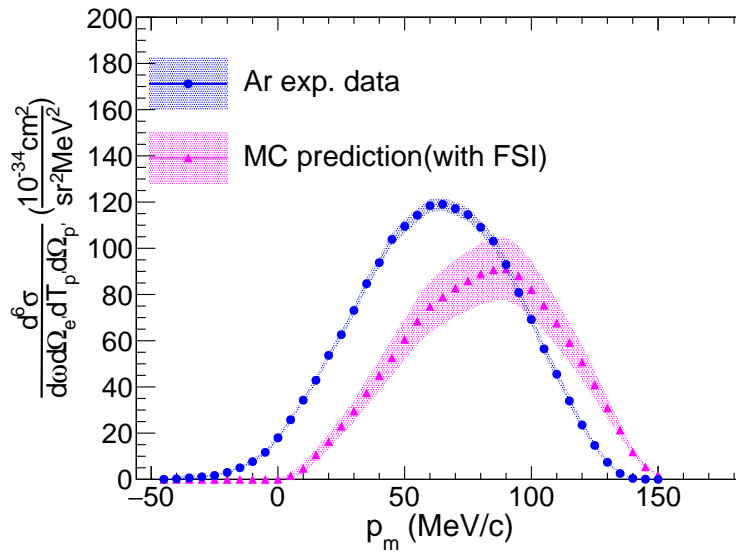


Figure 114: $^{40}\text{Ar}(e, e'p)$ Kin1 differential cross section as a function of missing momentum.

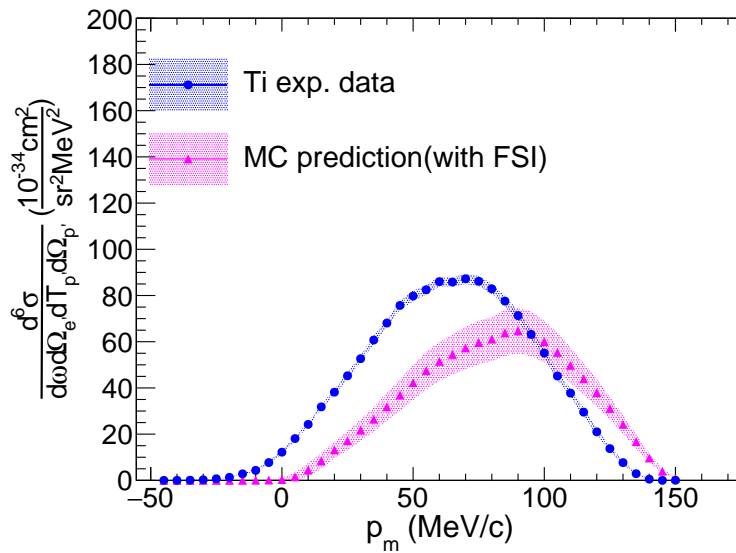
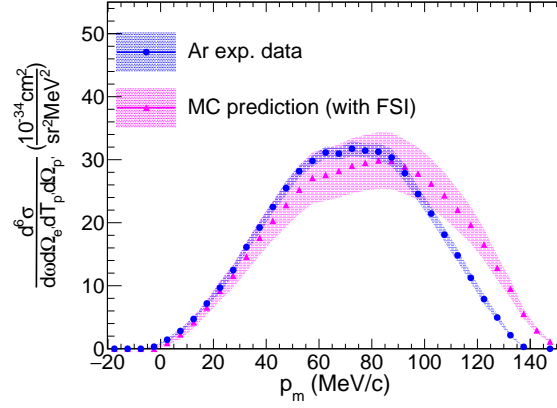
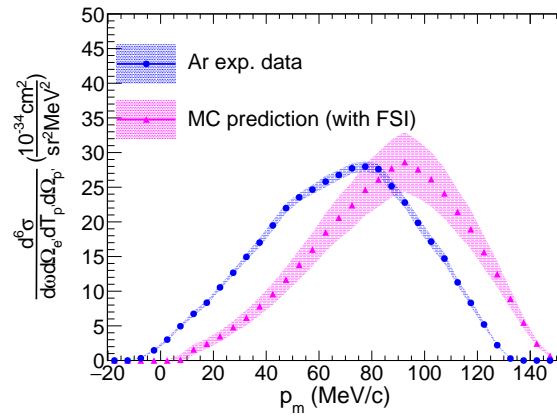


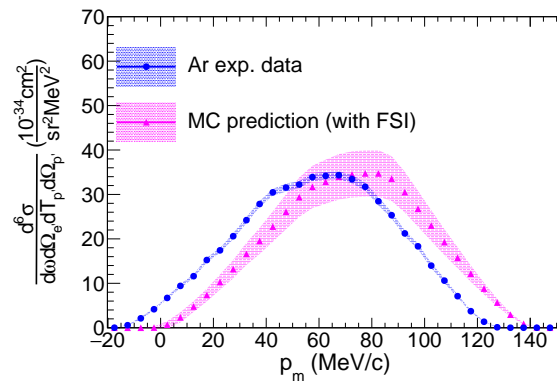
Figure 115: $^{48}\text{Ti}(e, e'p)$ Kin1 differential cross section as a function of missing momentum.



(a) $0 \leq E_{miss} \leq 27$ MeV

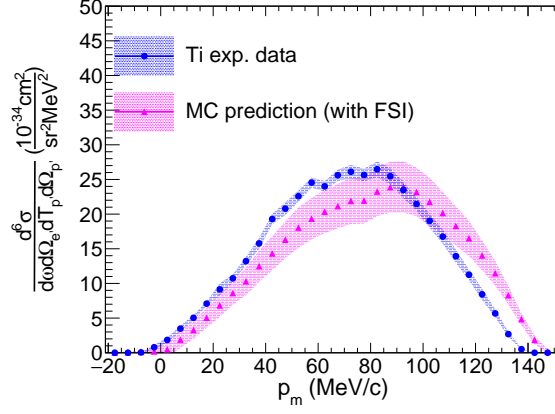


(b) $27 \leq E_{miss} \leq 44$ MeV

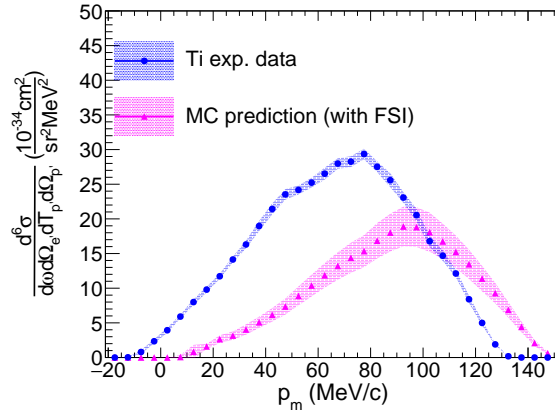


(c) $44 \leq E_{miss} \leq 70$ MeV

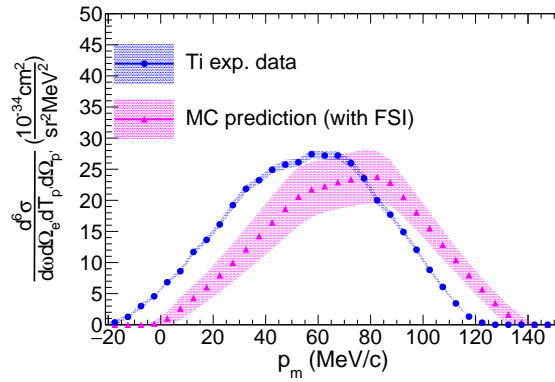
Figure 116: $^{40}\text{Ar}(e, e'p)$ differential cross sections (Kin1) for E_{miss} (a) region I, (b) region II, and (c) region III.



(a) $0 \leq E_{miss} \leq 30$ MeV



(b) $30 \leq E_{miss} \leq 54$ MeV



(c) $54 \leq E_{miss} \leq 90$ MeV

Figure 117: $^{48}\text{Ti}(e, e'p)$ differential cross sections (Kin1) as a function of missing momentum for E_{miss} (a) region I, (b) region II, and (c) region III[24].

cations in Physical Review C (see Refs. [32, 62, 65]), which have garnered nearly sixty combined citations (according to the INSPIRE-HEP archive). The citations show that the (e, e') scattering data collected during the E12-14-012 experiment, and its subsequent analysis, has been well received by the physics community.

The topics of publications that have referenced our papers cover a wide range of nuclear phenomenon, including general studies of lepton-nucleus scattering, investigating the effects of meson exchange currents, and extended superscaling analysis.

The E12-14-012 inclusive data is also expected to have a positive effect on upcoming and currently-running neutrino oscillation experiments such as DUNE, T2K, NOvA, and MINERνA. Approximately a quarter of the citations referenced above mention neutrinos, or neutrino oscillations, in the titles or abstracts.

The superscaling data collected in this experiment can be used to predict the electromagnetic nuclear responses for nuclei with mass numbers between $A = 12$ and $A = 48$. Two nuclei of particular interest to neutrino oscillation experiments are oxygen ($A = 16$) and chlorine ($A = 35$)[65]. The electromagnetic nuclear response of oxygen is important to the T2K experiment, as water is the radiation medium in the giant Super-Kamiokande Cherenkov detector used by T2K[100]. Similarly, the nuclear response of chlorine is important to the NOvA experiment, as the two-component scintillators employed by NOVA use a liquid scintillator contained within polyvinyl chloride extrusions[101].

The first paper based on the exclusive analysis was published in Physical Review C in March of 2021 (see Ref. [24]). This paper presented the exclusive differential cross sections as functions of missing energy and missing momentum at K_{in1} for argon and titanium. The data published in Ref. [24] represents the first $(e, e'p)$ scattering data on argon and titanium in the kinematical range of import to neutrino oscillation experiments.

The $(e, e'p)$ scattering data collected in this experiment is expected to lead to multiple future publications. The E12-14-012 collaboration is currently preparing a manuscript for publication, presenting the spectroscopic factors, mean energy, and width (FWHM) for each shell extracted from fits to the argon missing energy and missing momentum distributions.

Overall, comparison between the E12-14-012 data and theoretical calculations confirms that the impulse approximation, including contributions from meson exchange currents and final state interactions, is the proper theoretical basis in which to describe quasi-elastic electron scattering[62].

A Supplementary Mathematics

A.1 The Dirac Delta Function

The *Dirac delta function* $\delta(x)$ for $x \in \mathbb{R}$ is a generalized function, or distribution, defined by the piece-wise equation

$$\delta(x) = \begin{cases} 0 & x \in \mathbb{R} \setminus \{0\} \\ \infty & x \in \{0\} \end{cases}, \quad (\text{A.1})$$

and is normalized to unity on the real line. The definition of the delta function can be extended to n -dimensional vectors x as an integral over the imaginary exponential function,

$$\delta^n(x) = \int_{\mathbb{R}^n} \frac{d^n p}{(2\pi)^n} e^{-ip \cdot x}. \quad (\text{A.2})$$

The composite function $(\delta \circ g)(x)$ for some smooth function $g(x)$ can be related to its derivative g' through

$$\delta(g(x)) = \frac{\delta(x - x_0)}{|g'(x_0)|}, \quad (\text{A.3})$$

where x_0 is a real root of $g(x)$. This identity is used in §3.6.1 to calculate the y -scaling function.

A.2 The Dilogarithm Function

The *dilogarithm function* $\text{Li}_2(z)$ for some complex number $z \in \mathbb{C}$ is defined by the integral

$$\text{Li}_2(z) = - \int_0^z dt \frac{\log |1 - t|}{t}. \quad (\text{A.4})$$

The dilogarithm function is sometimes referred to as the *Spence function*, and is denoted $\Phi(z)$. This out-dated notation is often encountered in the older literature. The dilogarithm function appears in §3.7 in the expression for the effective non-radiative cross section, and is part of the Schwinger correction, defined in §B.6.

A useful identity gives the sum of two dilogarithm functions in terms of the standard *natural logarithm* as

$$\text{Li}_2(1 - z) + \text{Li}_2(1 - z^{-1}) = -\frac{1}{2} \log^2 z. \quad (\text{A.5})$$

This identity was used in the derivation of the radiative correction function $F(Q^2, T)$, defined in §3.7 Eq. 3.99.

A.3 The Gamma Function

The *Gamma function* $\Gamma(z)$ for $z \in \mathbb{C}$ is defined by the improper integral

$$\Gamma(z) = \int_0^{\infty} dx x^{z-1} e^{-x}. \quad (\text{A.6})$$

The reciprocal of the Gamma function $\Gamma(1 + bx)$ can be expanded in a Taylor series around $x \approx 0$ as

$$\frac{1}{\Gamma(1 + bx)} \approx 1 + \gamma bx + \frac{b^2}{12}(6\gamma^2 - \pi^2)x^2 + \dots \quad (\text{A.7})$$

for some constant b . The number $\gamma \approx 0.57721$ is the *Euler-Mascheroni constant*, which is defined by the improper integral

$$\gamma = - \int_0^{\infty} dx e^{-x} \log x. \quad (\text{A.8})$$

The series expansion in Eq. A.7 is used in §3.7 to calculate the function $F(Q^2, T)$, defined in Eq. 3.99.

B Supplementary Theoretical Analysis

B.1 Three-Flavor Neutrino Oscillations

The three generations of neutrinos can be classified into either flavor (ν_e, ν_μ, ν_τ) or mass (ν_1, ν_2, ν_3) eigenstates. Neutrinos are created in definite flavor eigenstates, which are linear combinations of the mass eigenstates which diagonalize the free particle Hamiltonian. That is, the flavor eigenstates $|\nu_\ell\rangle$ are related to the mass eigenstates $|\nu_m\rangle$ through

$$|\nu_\ell\rangle = \sum_m \mathbb{U}_{\ell m}^* |\nu_m\rangle, \quad (\text{B.1})$$

where the coefficients $\mathbb{U}_{\ell m}^*$ are elements of the unitary lepton mixing matrix \mathbb{U} , known as the Pontecorvo-Maki-Nakagawa-Sakata (PMNS) matrix. Since the PMNS matrix is 3×3 and unitary, its nine elements can be written in terms of three mixing angles ($\theta_{12}, \theta_{23}, \theta_{13}$) and six phase factors. Assuming the neutrino is a Dirac fermion, properties of the quantum neutrino fields $\nu_\ell(x)$ allow five phase-factors to be removed from \mathbb{U} [102]. The remaining

phase factor accounts for possible charge-parity (CP) violation. In this case, the PMNS mixing matrix is given by

$$\mathbb{U} = \begin{bmatrix} c_{12}c_{13} & c_{13}s_{12} & e^{-i\delta}s_{13} \\ -c_{23}s_{12} - e^{i\delta}c_{12}s_{13}s_{23} & c_{12}c_{23} - e^{i\delta}s_{12}s_{13}s_{23} & c_{13}s_{23} \\ s_{12}s_{23} - e^{i\delta}c_{12}c_{23}s_{13} & -e^{i\delta}c_{23}s_{12}s_{13} - c_{12}s_{23} & c_{13}c_{23} \end{bmatrix}, \quad (\text{B.2})$$

where $c_{ij} = \cos \theta_{ij}$, $s_{ij} = \sin \theta_{ij}$, and δ is the CP-violating phase. However, if the neutrino is a Majorana fermion, an additional diagonal matrix \mathbb{P} containing two additional Majorana phase factors is appended to the PMNS matrix ($\mathbb{U} \rightarrow \mathbb{U}\mathbb{P}$)[102].

The probability of a $\nu_\ell \rightarrow \nu_{\ell'}$ oscillation after a time t is obtained by calculating

$$P(\nu_\ell \rightarrow \nu_{\ell'}) = |\langle \nu_{\ell'} | \nu_\ell(t) \rangle|^2 = \left| \sum_j \mathbb{U}_{\ell'j} \mathbb{U}_{\ell j}^* e^{-iE_j t} \right|^2, \quad (\text{B.3})$$

where the energy of the j^{th} mass eigenstate is given by $E_j = \sqrt{p^2 + m_j^2} \approx p + m_j^2/2E$, assuming $p \approx E$. With this assumption, the oscillation probability is given by

$$\begin{aligned} P(\nu_\ell \rightarrow \nu_{\ell'}) &= \delta_{\ell\ell'} - 4 \sum_{i < j} \Re \{ \mathbb{U}_{\ell i} \mathbb{U}_{\ell' i}^* \mathbb{U}_{\ell j}^* \mathbb{U}_{\ell' j} \} \sin^2 \left(\frac{\Delta m_{ji}^2 L}{4E} \right) \\ &\quad + 2 \sum_{i < j} \Im \{ \mathbb{U}_{\ell i} \mathbb{U}_{\ell' i}^* \mathbb{U}_{\ell j}^* \mathbb{U}_{\ell' j} \} \sin^2 \left(\frac{\Delta m_{ji}^2 L}{2E} \right) \end{aligned} \quad (\text{B.4})$$

where $\Delta m_{ji}^2 = m_j^2 - m_i^2$ is the squared mass difference, and $L \approx ct$ is the distance traveled. Equation B.4 ties the existence of neutrino oscillations directly to the neutrino masses. If neutrinos were massless, as originally thought, or all had the same mass, then $\Delta m_{ji}^2 = 0$, and Eq. B.4 would vanish identically for $\ell \neq \ell'$. Experimental observation of neutrino oscillations is proof that neutrinos are indeed massive. Oscillation experiments, however, provide no insight into the individual values of the neutrino masses, only their squared difference. The oscillation probability also depends on the existence of CP-violation. If the CP-violating phase is zero, then the sum over the imaginary components of the PMNS matrix in Eq. B.4 vanishes.

There are three probabilities that can be calculated from Eq. B.4. Assuming an initial electron-neutrino, there is the probability to oscillate into a muon-neutrino $P(\nu_e \rightarrow \nu_\mu)$, the probability to oscillate into a tau-neutrino $P(\nu_e \rightarrow \nu_\tau)$, and the probability to remain an electron-neutrino $P(\nu_e \rightarrow \nu_e)$,

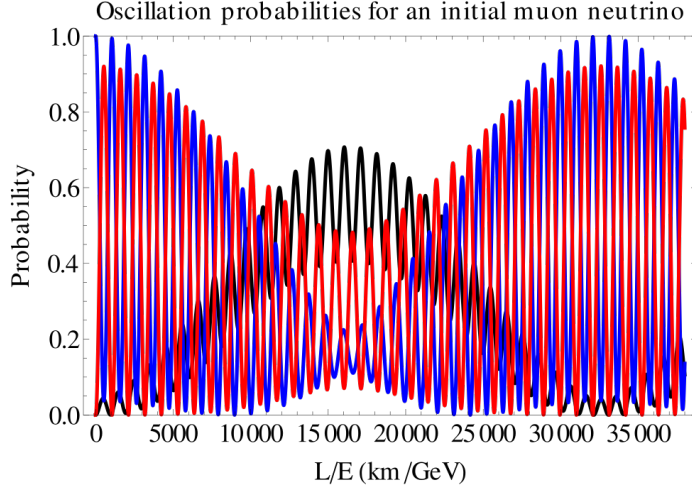


Figure 118: Neutrino oscillation probabilities from Eq. B.4 assuming an initial muon-neutrino[5]. The black line represents the probability to oscillate into an electron-neutrino $P(\nu_\mu \rightarrow \nu_e)$, and the red line represents the probability to oscillate into a tau-neutrino $P(\nu_\mu \rightarrow \nu_\tau)$. The blue line represents the survival probability $P(\nu_\mu \rightarrow \nu_\mu)$.

also known as the survival probability. Plots of these probabilities as functions of L/E are shown in §1.3.1 Fig. 2. Similarly, the oscillation probabilities derived from Eq. B.4 assuming an initial muon-neutrino and initial tau-neutrino are shown in Fig. 118 and Fig. 119, respectively. These plots, obtained from Ref. [5], were generated by a code simulating Eq. B.4, and do not represent experimental data.

B.2 The Rosenbluth Cross Section

The differential cross section for elastic electron-nucleon scattering is called the *Rosenbluth cross section*, and is given by

$$\frac{d\sigma}{d\Omega} = \sigma_M \frac{E'}{E_0} \left[\left(F_1^2 + \frac{Q^2}{4M^2} F_2^2 \right) + \frac{Q^2}{2M^2} (F_1 + F_2)^2 \tan^2 \frac{\theta}{2} \right]. \quad (\text{B.5})$$

where $F_{1,2}(Q^2)$ are the nuclear form factors. The Rosenbluth formula can also be written in terms of the electric and magnetic form factors $G_{E,M}(Q^2)$ as

$$\frac{d\sigma}{d\Omega} = \sigma_M \frac{E'}{E_0} \left[\left(\frac{G_E^2 + \tau G_M^2}{1 + \tau} \right) + 2\tau G_M^2 \tan^2 \frac{\theta}{2} \right]. \quad (\text{B.6})$$

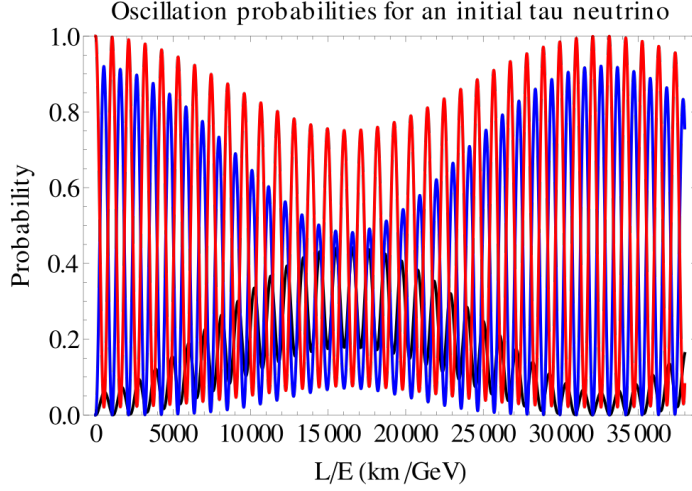


Figure 119: Neutrino oscillation probabilities from Eq. B.4 assuming an initial tau-neutrino[5]. The black line represents the probability to oscillate into an electron-neutrino $P(\nu_\tau \rightarrow \nu_e)$, and the blue line represents the probability to oscillate into a muon-neutrino $P(\nu_\tau \rightarrow \nu_\mu)$. The red line represents the survival probability $P(\nu_\tau \rightarrow \nu_\tau)$.

The $G_{E,M}$ are linear combinations of the $F_{1,2}$,

$$G_E = F_1 - \tau F_2 \quad (\text{B.7a})$$

$$G_M = F_1 + F_2 \quad (\text{B.7b})$$

The factor σ_M is the *Mott cross section*, and is given by

$$\sigma_M = \frac{\alpha^2 \cos^2 \frac{\theta}{2}}{4E_0^2 \sin^4 \frac{\theta}{2}} = \frac{4\alpha^2}{Q^4} E'^2 \cos^2 \frac{\theta}{2}. \quad (\text{B.8})$$

The Mott cross section considers the proton as a point charge with no internal structure.

B.3 Calculating The Inclusive Cross Section

Starting from the general expression of Eq. 3.17, the inclusive cross section can be written in a more understandable form by carrying out the tensor contraction $L^{\mu\nu} W_{\mu\nu}$. Using Eq. 3.9 for the leptonic tensor and Eq. 3.35 for the target response tensor, the contraction yields

$$\frac{d^3\sigma}{d\Omega' dE'} = \frac{\alpha^2 E'}{Q^4 E_0} \left[4(k \cdot k') W_1 + \frac{W_2}{M^2} (4(k \cdot P)(k' \cdot P) - 2M^2(k \cdot k')) \right] \quad (\text{B.9})$$

for the cross section. The four-vector products can easily be carried out, giving $k \cdot P = E_0 M$, $k' \cdot P = E' M$, and $k \cdot k' = 2E_0 E' \sin^2 \frac{\theta}{2}$. Plugging these into Eq. B.9 gives the inclusive differential cross section as

$$\frac{d^3 \sigma}{d\Omega' dE'} = \frac{4\alpha^2}{Q^4} E'^2 \cos^2 \frac{\theta}{2} \left[W_2(Q^2, \omega) + 2W_1(Q^2, \omega) \tan^2 \frac{\theta}{2} \right]. \quad (\text{B.10})$$

B.4 y -Scaling in PWIA Supplement

This section is meant to supplement the material in §3.6.1 on y -scaling by giving mathematical expressions for important quantities discussed in the text. Although definitions of these quantities can be found in Ref. [28], they are included here for convenience and completeness.

The nuclear excitation parameter \mathcal{E} is defined as

$$\mathcal{E}(\vec{\mathbf{p}}) = \sqrt{M_{A-1}^{*2} + |\vec{\mathbf{p}}|^2} - \sqrt{M_{A-1}^2 + |\vec{\mathbf{p}}|^2}. \quad (\text{B.11})$$

The asterisk on the mass in the first term indicates the $A - 1$ system is in an excited state. The energy of the struck nucleon, written as a function of the excitation parameter \mathcal{E} , is given by

$$E(\vec{\mathbf{p}}, \mathcal{E}) = M_A - \sqrt{M_{A-1}^2 + |\vec{\mathbf{p}}|^2} - \mathcal{E}. \quad (\text{B.12})$$

The function Ω used to simplify the argument of the delta function in Eq. 3.76 is given by

$$\begin{aligned} \Omega(\vec{\mathbf{p}}, \vec{\mathbf{q}}, \cos \theta_{pq}, \mathcal{E}) = & \left(\sqrt{M^2 + |\vec{\mathbf{p}} + \vec{\mathbf{q}}|^2} - M \right) \\ & + \left(\sqrt{M_{A-1}^2 + |\vec{\mathbf{p}}|^2} - M_{A-1} \right) + \mathcal{E} + E_s, \end{aligned} \quad (\text{B.13})$$

where $E_s = M_{A-1} + M - M_A$ is the nuclear *separation energy* (different than the removal energy)[28]. The term $|\partial\Omega/\partial \cos \theta_{pq}|^{-1}$ in Eq. 3.78 can be easily evaluated from the expression for Ω above. Only the first term in Eq. B.13 contains $\cos \theta_{pq}$, so all other terms vanish with the derivative. The derivative is calculated as

$$\frac{\partial\Omega}{\partial \cos \theta_{pq}} = \frac{|\vec{\mathbf{p}}||\vec{\mathbf{q}}|}{\sqrt{M^2 + (\vec{\mathbf{p}} + \vec{\mathbf{q}})^2}} \quad (\text{B.14})$$

As mentioned in the text, the factor of $|\vec{\mathbf{p}}|$ cancels, giving the kinematic factor K appearing in Eq. 3.80 as

$$K = |\vec{\mathbf{p}}| \left| \frac{\partial \Omega}{\partial \cos \theta_{pq}} \right|^{-1} = \frac{\sqrt{M^2 + (\vec{\mathbf{p}} + \vec{\mathbf{q}})^2}}{|\vec{\mathbf{q}}|}. \quad (\text{B.15})$$

The limits of integration over the momentum in Eq. 3.78 are given by

$$y(\vec{\mathbf{q}}, \omega) = \left[(M_A + \omega) \sqrt{\Lambda^2 - M_{A-1}^2 W^2} - |\vec{\mathbf{q}}| \Lambda \right] / W^2 \quad (\text{B.16a})$$

$$Y(\vec{\mathbf{q}}, \omega) = \left[(M_A + \omega) \sqrt{\Lambda^2 - M_{A-1}^2 W^2} + |\vec{\mathbf{q}}| \Lambda \right] / W^2 \quad (\text{B.16b})$$

with

$$W = \sqrt{(M_A + \omega)^2 - |\vec{\mathbf{q}}|^2} \quad (\text{B.17a})$$

$$\Lambda = (M_{A-1}^2 - M^2 + W^2) / 2. \quad (\text{B.17b})$$

The upper limit of the \mathcal{E} -integration in Eq. 3.78 is given by

$$\begin{aligned} \mathcal{E}_M(\vec{\mathbf{q}}, y; |\vec{\mathbf{p}}|) = & \sqrt{M^2 + (|\vec{\mathbf{q}}| + y)^2} - \sqrt{M^2 + |\vec{\mathbf{q}} - \vec{\mathbf{p}}|^2} \\ & + \sqrt{M_{A-1}^2 + y^2} - \sqrt{M_{A-1}^2 + |\vec{\mathbf{p}}|^2}. \end{aligned} \quad (\text{B.18})$$

In the limit that $|\vec{\mathbf{q}}| \rightarrow \infty$, the expression becomes

$$\mathcal{E}_M^\infty = y + |\vec{\mathbf{p}}| - \left(\sqrt{M_{A-1}^2 + |\vec{\mathbf{p}}|^2} - \sqrt{M_{A-1}^2 + y^2} \right). \quad (\text{B.19})$$

B.5 Correlated Spectral Function

The parameter γ in the correlated spectral function of Eq. 3.63 is given by

$$\gamma = \frac{3(A-1)}{4\langle \vec{\mathbf{p}}_{MF}^2 \rangle (A-2)}, \quad (\text{B.20})$$

where $\langle \vec{\mathbf{p}}_{MF}^2 \rangle$ is the mean-square of the mean-field momentum, defined by

$$\langle \vec{\mathbf{p}}_{MF}^2 \rangle = \frac{\int d^3 \vec{\mathbf{p}} |\vec{\mathbf{p}}|^2 n_N^{MF}(\vec{\mathbf{p}})}{\int d^3 \vec{\mathbf{p}} n_N^{MF}(\vec{\mathbf{p}})}. \quad (\text{B.21})$$

The minimum and maximum momenta that appear in Eq. 3.63 are defined by

$$|\vec{\mathbf{p}}_{min}|^2 = \left[\left(\frac{A-2}{A-1} \right) |\vec{\mathbf{p}}| - \sqrt{\frac{2M(A-2)}{(A-1)} (E - E^{(2)} - K_{A-1})} \right]^2 \quad (\text{B.22a})$$

$$|\vec{\mathbf{p}}_{max}|^2 = \left[\left(\frac{A-2}{A-1} \right) |\vec{\mathbf{p}}| + \sqrt{\frac{2M(A-2)}{(A-1)} (E - E^{(2)} - K_{A-1})} \right]^2 \quad (\text{B.22b})$$

where K_{A-1} is the recoil energy and $E^{(2)} \approx M_{A-2} + 2M - M_A$ is the average excitation energy of the $A - 2$ nuclear system[23].

B.6 Radiative Corrections Supplement

This section is meant to supplement the material in §3.7 on radiative corrections by giving mathematical expressions to quantities defined in the text.

The quantity b , described as a number “very close to 4/3” [42], is defined as $b = \frac{4}{3} + a$, with the quantity a given by the expressions

$$a = \frac{1}{9} \frac{Z+1}{Z+\zeta} \frac{1}{\log(191Z^{-1/3}) - 1.2(\alpha Z)^2} \quad (\text{B.23a})$$

$$\zeta = \frac{\log(1440Z^{-2/3})}{\log(191Z^{-1/3}) - 1.2(\alpha Z)^2} \quad (\text{B.23b})$$

The Schwinger correction is given by the sum of the following terms[42],

$$\delta_{\text{inf}}(Q^2) = -\frac{2\alpha}{\pi} \left(\log \frac{Q^2}{M^2} - 1 \right) \log \left(\frac{E}{\Delta E} \right), \quad (\text{B.24a})$$

$$\delta_{\text{ver}}(Q^2) = \frac{2\alpha}{\pi} \left(\frac{1}{3} \log \frac{Q^2}{m^2} - \frac{5}{9} \right), \quad (\text{B.24b})$$

$$\delta_{\text{vac}}(Q^2) = \frac{2\alpha}{\pi} \left(\frac{3}{4} \log \frac{Q^2}{m^2} - 1 \right), \quad (\text{B.24c})$$

plus an additional term involving the dilogarithm function[103]. The Schwinger correction for relativistic electron energies is given by

$$\delta_S = -\frac{2\alpha}{\pi} \left(\left[\log \frac{E_1}{\Delta E} - \frac{13}{12} \right] \left[\log \frac{Q^2}{m^2} - 1 \right] + \frac{17}{36} + \frac{1}{2} \left[\frac{\pi^2}{6} - \text{Li}_2 \left(\cos^2 \frac{\theta}{2} \right) \right] \right). \quad (\text{B.25})$$

The equivalent radiator t is defined as

$$t = \frac{2\alpha}{\pi} \left(\log \frac{Q^2}{m^2} - 1 \right). \quad (\text{B.26})$$

B.7 The SIMC Cross Section as a Surface

This section discusses an alternative method to obtain the exclusive differential cross section from SIMC as a two-dimensional histogram binned in missing energy and missing momentum. Although not used in this analysis, a lot of effort was put into developing this method, so it is included in the appendix of this dissertation.

First, the (P_{miss}, E_{miss}) space must be discretized into bins of uniform size. Let the indices i, j represent each bin of P_{miss} and E_{miss} respectively. Then, for each bin (ij) , the exclusive cross section is given by

$$\sigma_{ij} = \frac{Y_{ij} \cdot R}{Q \cdot L \cdot \varepsilon_{HRS} \cdot V_{ij}} \quad (\text{B.27})$$

where Q is the accumulated charge, L is the integrated luminosity, ε_{HRS} is the efficiency of both HRS arms (including the deadtime correction), and V_{ij} is the phase space volume of the bin (ij) . The yield for the bin (ij) is represented by Y_{ij} , and R is a factor to account for radiative corrections.

Unfortunately, this method was never used to extract an exclusive cross section from the data, and was only used initially with the SIMC output. However, the exclusive cross sections presented in the upcoming paper[89] based on the E12-14-012 analysis are presented as two-dimensional histograms.

B.7.1 Calculation of the Generated Phase Space

As the $(e, e'p)$ cross section is six-fold differential, SIMC must generate a six-dimensional phase space in the kinematic variables $E_{e'}$, $\Omega_{e'}(\theta_{e'}, \phi_{e'})$, $E_{p'}$,

and $\Omega_{p'}(\theta_{p'}, \phi_{p'})$. The total volume of the SIMC generated phase space is given by

$$\Delta E_{e'} \Delta \Omega_{e'} \Delta E_{p'} \Delta \Omega_{p'}. \quad (\text{B.28})$$

The ranges of the kinematic variables generated by SIMC are specified in one of the input files. The phase space volume of each bin (ij) is given by

$$V_{ij} = \frac{N_{ij}^{\text{SIMC}}}{N_{gen}^{\text{SIMC}}} \Delta E_{e'} \Delta \Omega_{e'} \Delta E_{p'} \Delta \Omega_{p'}, \quad (\text{B.29})$$

where N_{ij}^{SIMC} is the number of SIMC points in bin (ij), and N_{gen}^{SIMC} is the total number of *generated* monte-carlo events. This is different from the number of *accepted* monte-carlo events, which are those events that pass the select-events criterion. In the following calculations, all subscripts denoting particle type will be dropped, as the calculation is the same for both electrons and protons.

The quantity ΔE is the range of final state energies generated by SIMC. The user specified the upper and lower bounds of the fractional momentum interval $\Delta dp = [dp^{min}, dp^{max}]$. The particle momentum is given in terms of the fractional momentum and the spectrometer central momentum P_0 as $p = P_0(1 + dp)$. Thus, the minimum and maximum final state energies are given by

$$E^{min} = \sqrt{P_0^2(1 + dp^{min})^2 + M^2} \quad (\text{B.30a})$$

$$E^{max} = \sqrt{P_0^2(1 + dp^{max})^2 + M^2}. \quad (\text{B.30b})$$

From this, the quantity ΔE is easily calculated as

$$\Delta E = |E^{max} - E^{min}|. \quad (\text{B.31})$$

While Eqs. B.30 are certainly valid for the electron, they can be simplified at high-energies by invoking the ultra-relativistic approximation for the electron, and ignoring its mass. In this case, Eq. B.31 is simplified to

$$\Delta E_{e'} = |E_{e'}^{max} - E_{e'}^{min}| \approx |p_{e'}^{max} - p_{e'}^{min}|. \quad (\text{B.32})$$

The phase-space quantity $\Delta \Omega$ represents the range of solid angle subtended by the intervals $\Delta \theta$ and $\Delta \phi$, *i.e.* the integral

$$\Delta \Omega \longrightarrow \int_{\Delta \phi} \int_{\Delta \theta} d\Omega \quad (\text{B.33})$$

where $d\Omega = d\phi d\theta \sin \theta$ is the differential of solid angle. The SIMC input angles are given in the target coordinate system, and hence both of the angular

intervals are symmetric about the z_{tg} -axis. A slight change of variables is made, $\theta \rightarrow \tilde{\theta}$, so that the interval becomes

$$\Delta\theta \rightarrow \Delta\tilde{\theta} = [0, \tilde{\theta}_{max}], \quad (\text{B.34})$$

where $\tilde{\theta}_{max} = 2\theta_{max} = 2|\theta_{min}|$. Making this change of variables in Eq. B.33, the integral becomes

$$\Delta\Omega \equiv \int_{\Delta\phi} d\phi \int_0^{\tilde{\theta}_{max}} d\tilde{\theta} \sin\tilde{\theta} = \Delta\phi(1 - \cos\tilde{\theta}_{max}). \quad (\text{B.35})$$

Back substitution to the original θ and use of the half-angle trigonometric identities gives

$$\Delta\Omega = 2\Delta\phi \sin^2 \theta_{max} \quad (\text{B.36})$$

as the angular phase-space volume. Combining the expressions of Eq. B.31 and Eq. B.36, one obtains an expression for the SIMC phase space volume as

$$\Delta E_{e'} \Delta\Omega_{e'} \Delta E_{p'} \Delta\Omega_{p'} = \Delta E_{e'} \Delta\phi_{e'} \Delta E_{p'} \Delta\phi_{p'} 4 \sin^2(\theta_{e'}^{max}) \sin^2(\theta_{p'}^{max}). \quad (\text{B.37})$$

C Supplementary Data Analysis

C.1 ROOT Tree/NTUPLE Histograms

All data presented in this dissertation was analyzed using the C++ based ROOT analysis system developed at CERN by R. Brun and F. Rademakers. This section is meant to serve as a reference and guide to the ROOT histograms used in the data analysis, and referenced in this dissertation.

The JLab ESPACE program (§7.1) stores the data in histograms which are then stored in an object often called an NTUPLE. The labelling syntax for the histograms is defined by `HRS.detector.quantity`. The first label `HRS`, replaced with either `L` or `R`, represents the spectrometer arm (left or right) from which the data was collected. Negatively charged particles (electrons) are collected in the left arm, while positively charged particles (protons) are collected in the right arm. The second label represents the `detector` on the specified HRS stack. The third label represents the `quantity` measured by the detector. Consider the histogram `L.pr11.e` as an example. This histogram represents the energy (`e`) measured by the first layer of the calorimeter (`pr11`) on the left arm of the HRS (`L`).

Histograms that are also arrays have an index [j] attached. An additional label separated by an underscore (-) represents a variation on the quantity. Consider the histogram `L.cer.a[j]` as an example. This histogram represents the ADC spectra (a) collected from the PMT's in the Cherenkov detector (cer) on the left arm of the spectrometer (L). The spectrum from an individual PMT is accessed with the index j. The addition of the label `_p` represents the ADC spectrum with the pedestal subtracted.

The sections on the data analysis and efficiency calculations make many references to these histograms, or combinations thereof. Important histograms referred to in this dissertation, along with descriptions, are listed in Tab. 18. Whenever possible, a reference to an ESPACE histogram is replaced with a symbolic expression. For example, `L.tr.tg.th`, the reconstructed out-of-plane angle from the LHRS, is replaced by the symbol θ_{tg}^e in the text. Histograms and their symbolic representations used in the text are listed in Tab. 19. Certain cuts on the histograms are also represented symbolically in the text. A list of cuts and associated symbolic notation are given in Tab. 20.

C.2 Data to SIMC Comparison

As mentioned in §6.3.3, comparing the data to Monte-Carlo simulation was a large part of the initial data analysis effort. Part of this process was to ensure that the SIMC was accurately modeling the acceptance of the HRS.

Histograms of the acceptance variables at Kin2 are shown in Fig. 122 for argon, and Fig. 123 for titanium. Overall, the SIMC accurately models the general shape of the acceptance histograms, with some exceptions being θ_{tg}^e and ϕ_{tg}^e for titanium, and dp_{tg}^e for both targets. Figure 123 also shows the background (blue), which is to be subtracted from the data histogram. Subtraction of the background events increases the accuracy of the SIMC acceptance.

Clearly the SIMC yield (red) overestimates the data yield (black), but this was to be expected, as discussed in §6.3.3. The difference in yields was measured by comparing the integrals of the data and SIMC histograms between the cut lines. The ratio should be constant across all the histograms for each kinematic setting, and was expected to be approximately 70%.

Also of importance was modeling the reconstructed target vertex z_{tg} , shown in Fig. 120 for argon and titanium at Kin2. A cut of $|z_{tg}^e| \leq 0.1 m$ was applied to the argon histogram, while no cut was applied to the titanium z_{tg}^e distribution. Histograms of the β_{HRS}^R distributions for argon and titanium at Kin2 are shown in Fig. 121. Even though the SIMC prediction

Histogram	Description
L.pr11.e	Energy deposited in the first layer of the LHRS calorimeter.
L.pr12.e	Energy deposited in the second layer of the LHRS calorimeter.
L.cer.a[j]	Raw ADC spectrum from j^{th} LHRS Cherenkov PMT.
L.cer.a_p[j]	Pedestal-subtracted ADC spectrum from j^{th} LHRS Cherenkov PMT.
L.cer.a_c[j]	Fully calibrated ADC spectrum from j^{th} LHRS Cherenkov PMT.
L.cer.asum_c	Sum of calibrated LHRS Cherenkov PMT signals.
L.tr.beta	Reconstructed LHRS β .
R.tr.beta	Reconstructed RHRS β .
L.tr.n	Number of reconstructed tracks in the LHRS VDC.
R.tr.n	Number of reconstructed tracks in the RHRS VDC.
L.tr.p	Reconstructed LHRS particle momentum.
R.tr.p	Reconstructed RHRS particle momentum.
L.gold.p	LHRS <i>golden</i> momentum.
L.s0.time	Timing spectrum of the LHRS S0 scintillator.
R.s0.time	Timing spectrum of the RHRS S0 scintillator.
L.s0.lt	
L.s0.rt	
L.s2.lt	
L.s2.rt	
DR.t1	

Table 18: ESPACE histogram names with descriptions used in the E12-14-012 analysis.

Symbol	Histogram
$\theta_{tg}^{e,p}$	L.tr.tg_th, R.tr.tg_th
$\phi_{tg}^{e,p}$	L.tr.tg_ph, R.tr.tg_ph
$dp_{tg}^{e,p}$	L.tr.tg_dp, R.tr.tg_dp
$z_{tg}^{e,p}$	L.tr.tg_z, R.tr.tg_z
$y_{tg}^{e,p}$	L.tr.tg_y, R.tr.tg_y
N_{tracks}^L	L.tr.n
β_{HRS}^R	R.tr.beta
p_{HRS}^R	R.tr.p
Δt_{coinc}	L.s0.time - R.s0.time
$\Delta\beta(m)$	R.tr.beta - R.tr.p/ $\sqrt{(R.tr.p)^2 + m^2}$
E/p	(L.pr11.e + L.pr12.e)/(L.gold.p*1000)

Table 19: ESPACE histogram names with corresponding symbolic representations used in the data analysis.

Cut Name	Cut Description
Acceptance _L	$\theta_{tg}^e \in [l, u] \wedge \phi_{tg}^e \in [l, u] \wedge dp_{tg}^e \in [l, u]$
Acceptance _R	$\theta_{tg}^p \in [l, u] \wedge \phi_{tg}^p \in [l, u] \wedge dp_{tg}^p \in [l, u]$
Acceptance	Acceptance _L \wedge Acceptance _R
Cherenkov	L.cer.asum.c \geq #
E/p	$E/p \geq$ #
PID	Cherenkov \wedge E/p
DR.t1	$l \leq \text{DR.t1} \leq u$
Beam	$ I_{beam} - I_{avg} \leq 4\sigma$
$N_{tracks} = 1$	L.tr.n == 1 \wedge R.tr.n == 1
Target	$l \leq z_{tg}^e \leq u$ or $ y_{tg}^e - y_{avg} \leq 2\sigma$
T1	DR.evtypebits >> 1&1
T2	DR.evtypebits >> 2&1
T3	DR.evtypebits >> 3&1
T5	DR.evtypebits >> 5&1

Table 20: Histogram cuts with descriptions used in the E12-14-012 data analysis. The quantities l and u represent the *lower* and *upper* bounds of the cut intervals. A quantity with the subscript *avg*, and σ , are the mean and standard deviation, respectively, from a Gaussian fit.

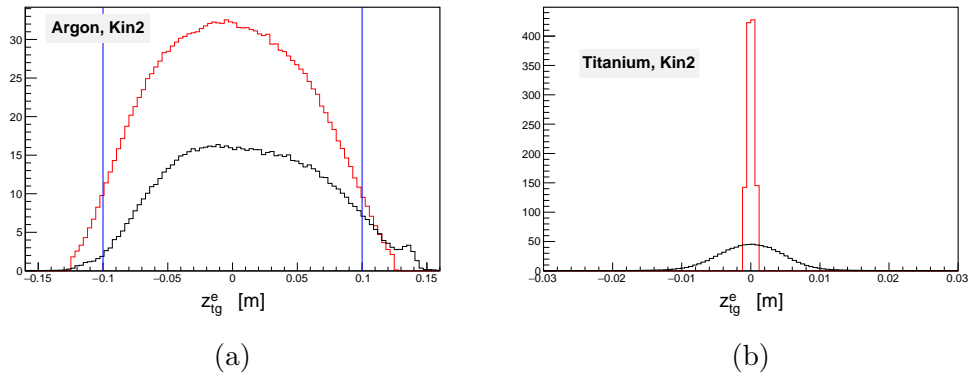


Figure 120: Histograms of z_{tg}^e distributions (black line) for (a) argon and (b) titanium targets at Kin2, with the SIMC prediction (red line).

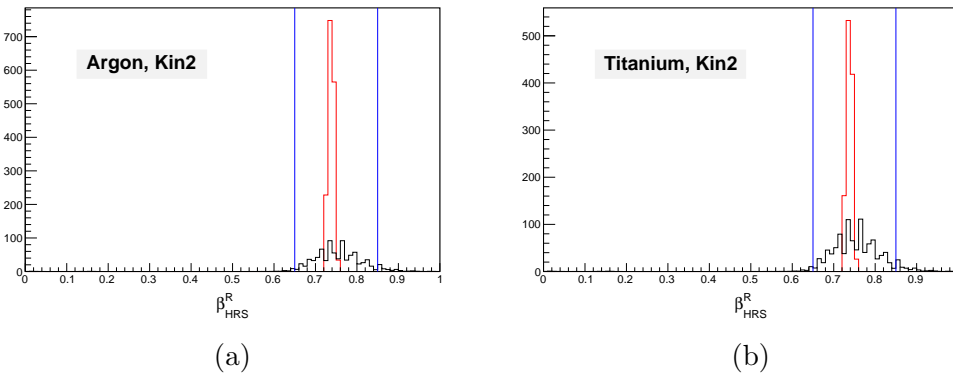


Figure 121: Histograms of β_{HRS}^R distributions (black line) for (a) argon and (b) titanium targets at Kin2, showing the full SIMC prediction (red line).

looks nothing like the data distribution, the integral ratio is consistent with the other histograms.

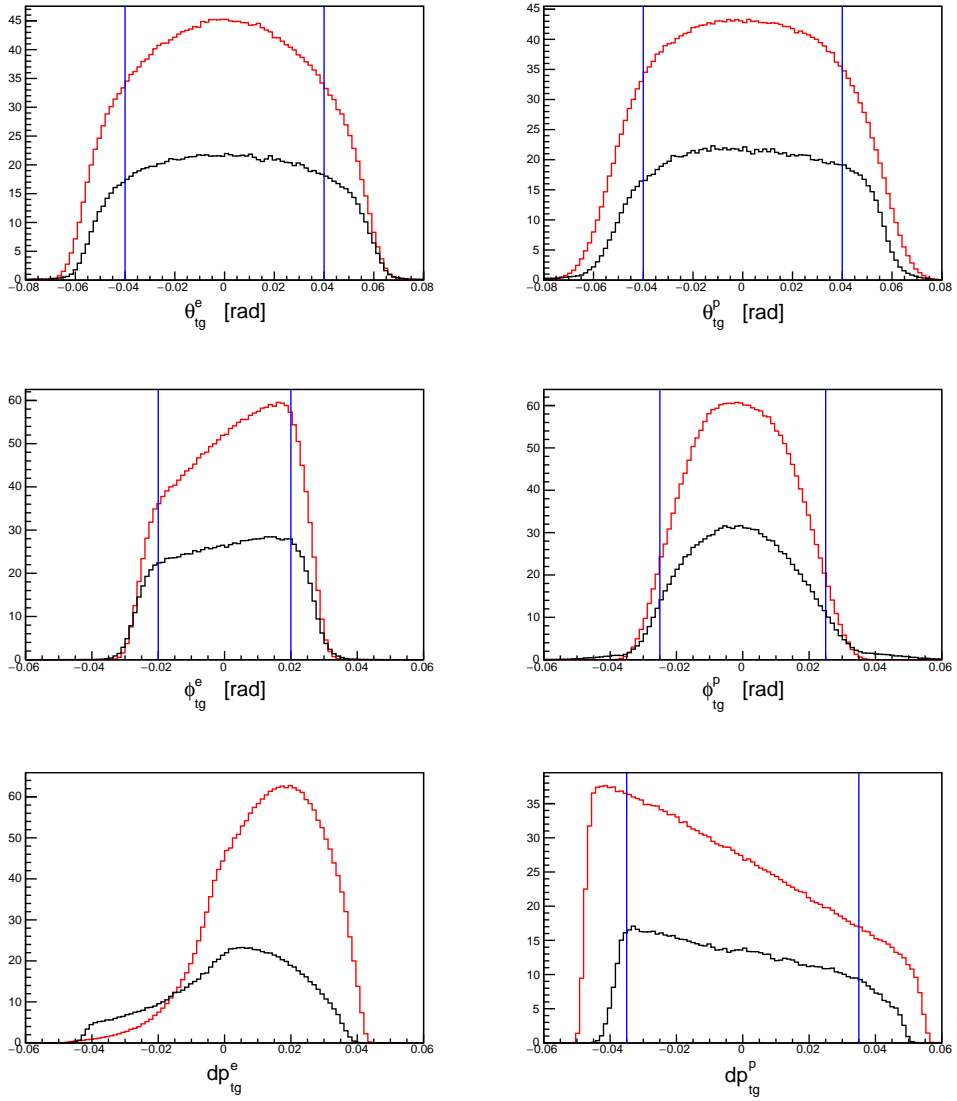


Figure 122: Histograms of data (black) and SIMC (red) acceptance variables at Kin2.

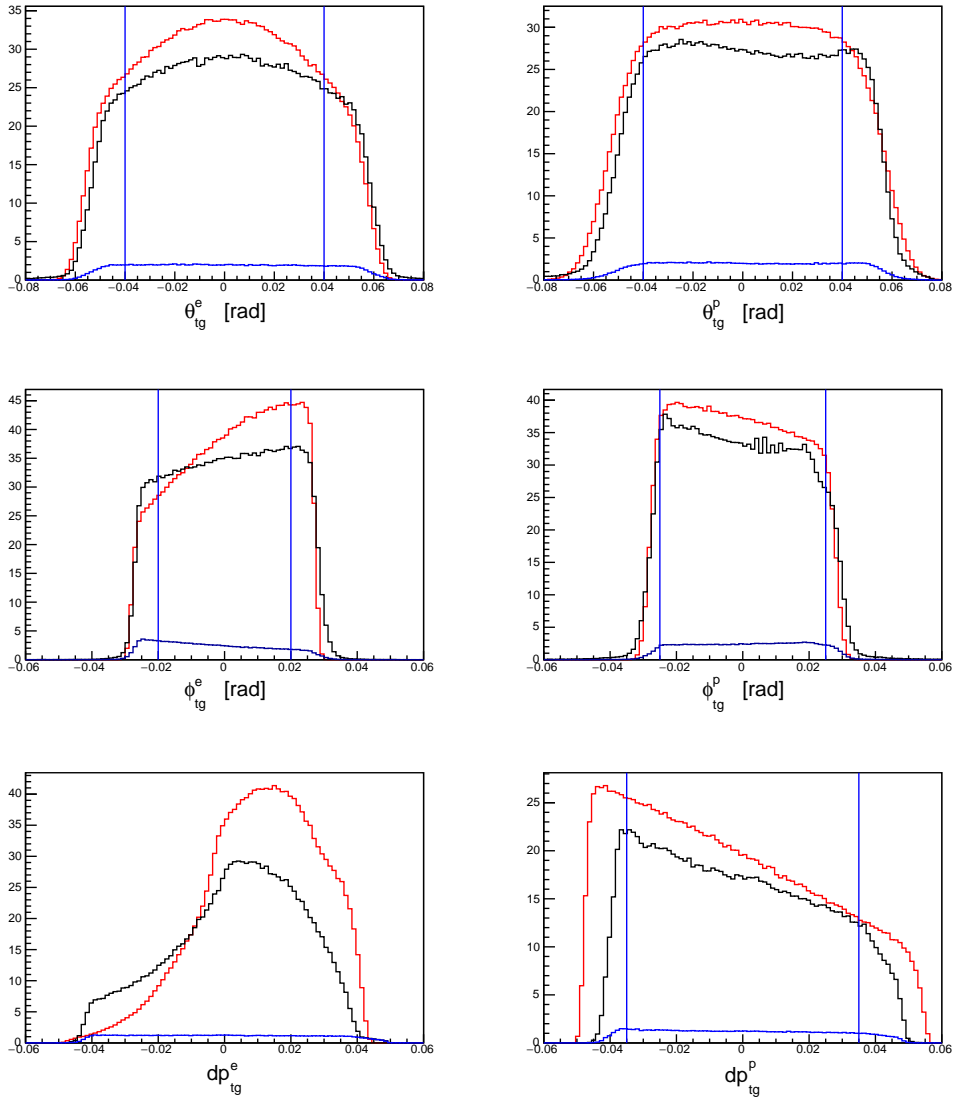


Figure 123: Histograms of data (black, before background subtraction), background noise (blue), and SIMC (red) acceptance variables at Kin2.

References

- [1] O. Benhar, G. M. Urciuoli, C. Mariani, C.-M. Jen, J. M. Link, M. L. Pitt, D. B. Day, D. G. Crabb, D. Keller, R. Lindgren, N. Liyanage, O. A. Rondon, J. Zhang, D. W. Higinbotham, D. Gaskell, O. Hansen, C. E. Keppel, L. Myers, B. Sawatzky, S. Wood, A. Ankowski, M. Sakuda, C. Giusti, A. Meucci, G. Garvey, X. Jiang, G. B. Mills, P. A. Souder, R. Holmes, and R. Beminiwattha. Measurement of the Spectral Function of ^{40}Ar through the $(e, e'p)$ reaction. JLab proposal PR12-14-012, [arXiv:1406.4080 [nucl-ex]], 2014.
- [2] K. B. Mather and P. Swan. *Nuclear Scattering*. Cambridge Monographs on Physics. Cambridge University Press, London, 1958.
- [3] V. Pandey, D. Abrams, S. Alsalmi, A. M. Ankowski, J. Bane, O. Benhar, H. Dai, D. B. Day, D. W. Higinbotham, C. Mariani, M. Murphy, and D. Nguyen. Probing electron-argon scattering for liquid-argon based neutrino-oscillation program. In *International Workshop on $(e, e'p)$ Processes*, 2017.
- [4] P. A. Zyla *et al.* (Particle Data Group). Review of particle physics. *Prog. Theor. Exp. Phys.*, 083C01, 2020.
- [5] Neutrino oscillation. Wikipedia, https://en.wikipedia.org/wiki/Neutrino_oscillation, Accessed November, 2021.
- [6] C. Grupen. *Particle Detectors*, volume 5 of *Cambridge Monographs on Particle Physics, Nuclear Physics and Cosmology*. Cambridge University Press, Cambridge, 1996.
- [7] LBNF/DUNE: An international flagship neutrino experiment. <http://www.fnal.gov/pub/science/lbnf-dune/index.html>, Accessed Oct. 2019.
- [8] O. Benhar, N. Farina, H. Nakamura, M. Sakuda, and R. Seki. Electron- and neutrino-nucleus scattering in the impulse approximation regime. *Phys. Rev. D*, 72(5), 2005.
- [9] L. Alvarez-Ruso, M. Sajjad Athar, M. B. Barbaro, D. Cherdack, M. E. Christy, P. Coloma, T. W. Donnelly, S. Dytman, A. de Gouvêa, R. J. Hill, P. Huber, Jachowicz N, T. Katori, A. S. Kronfeld, K. Mahn, M. Martini, J. G. Morfín, J. Nieves, G. Perdue, R. Petti, D. G. Richards, F. Sánchez, T. Sato, J. T. Sobczyk, and G. P. Zeller.

NuSTEC White Paper: Status and Challenges of Neutrino-Nucleus Scattering. *Prog. Part. Nucl. Phys.*, 100:1–68, 2017.

- [10] Hongxia Dai. *Measurement of the (e, e') cross section for ^{12}C , ^{48}C , ^{27}Al and ^{40}Ar* . PhD thesis, Virginia Polytechnic Institute and State University, 2019.
- [11] M. Anghinolfi, M. Ripani, R. Cenni, P. Corvisiero, A. Longhi, L. Mazzaschi, V. Mokeev, G. Ricco, M. Taiuti, A. Teglia, A. Zucchiatti, N. Bianchi, A. Fantoni, V. Muccifora, P. LeviSandri, V. Lucherini, E. Polli, A. R. Reolon, P. Rossi, and S. Simula. Inclusive electron scattering from an oxygen and argon jet target. *J. Phys. G: Nucl. Part. Phys.*, 21, 1995.
- [12] J. Heisenberg, J. S. McCarthy, and I. Sick. Inelastic Electron Scattering from Several Ca, Ti and Fe Isotopes. *Nucl. Phys. A*, 164:353–366, 1971.
- [13] E. F. Romberg, N. S. Wall, D. Blum, J. W. Lightbody, and S. Penner. Elastic Scattering of 60-120 MeV Electrons from $^{46,48,50}\text{Ti}$. *Nucl. Phys. A*, 173:124–128, 1971.
- [14] A. M. Selig, C. de Vries, P. K. A. de witt Huberts, and I. E. Zacharov. Effective Electro-magnetic Operators of ^{50}Ti Investigated with the (e, e') Reaction. *Nucl. Phys. A*, 476:413–447, 1988.
- [15] S. Boffi, C. Giusti, F. D. Pacati, and M. Radici. *Electromagnetic Response of Atomic Nuclei*. Clarendon Press, Oxford University Press, New York, 1996.
- [16] J. M. Blatt and V. F. Weisskopf. *Theoretical Nuclear Physics*. John Wiley & Sons, Inc., New York, 1952.
- [17] S. M. Dolfini, R. Beck, L. S. Cardman, R. M. Laszewski, J. B. Mandeville, C. N. Papanicolas, S. E. Williamson, R. Alarcon, M. M. Farkhondeh, J. Zumbro, W. Bertozzi, and W. Boeglin. Design of an 830 MeV/c out-of-plane spectrometer. *Nucl. Instrum. Methods Phys. Res. A*, 344(3):571–582, 1994.
- [18] M. E. Peskin and D. V. Schroeder. *An Introduction to Quantum Field Theory*. Addison-Wesley, USA, 1995.
- [19] Joaquin Lopez Herraiz. *Study of the $(e, e'p)$ Quasielastic Reaction in Complex Nuclei: Theory and Experiment*. PhD thesis, Universidad Complutense de Madrid, 2010.

- [20] A. E. L. Dieperink and P. K. A. de Witt Huberts. On high resolution ($e, e'p$) reactions. *Annu. Rev. Nucl. Part. Sci.*, 40(40):239–284, 1990.
- [21] O. Benhar, D. Day, and I. Sick. Inclusive quasi-elastic electron-nucleus scattering. *Rev. Mod. Phys.*, 80(1):189–224, 2008.
- [22] S. Frullani and J. Mougey. *Single-Particle Properties of Nuclei Through ($e, e'p$) Reactions*, volume 14 of *Advances in Nuclear Physics*. Plenum Press, New York, 1984.
- [23] A. M. Ankowski and J. T. Sobczyk. Construction of spectral functions for medium-mass nuclei. *Phys. Rev. C*, 77(4), 2008.
- [24] L. Gu, D. Abrams, L. Jiang, B. Aljawrneh, S. Alsalmi, J. Bane, A. Batz, S. Barcus, M. Barroso, O. Benhar, V. Bellini, J. Bericic, D. Biswas, A. Camsonne, J. Castellanos, J.-P. Chen, M. E. Christy, K. Craycraft, R. Cruz-Torres, H. Dai, D. Day, S.-C. Dusa, E. Fuchey, T. Gautam, C. Giusti, J. Gomez, C. Gu, T. Hauge, J.-O. Hansen, F. Hauenstein, D. W. Higinbotham, C. Hyde, C. Keppel, S. Li, R. Lindgren, H. Liu, C. Mariani, R. E. McClellan, D. Meekins, R. Michaels, M. Mihovilovic, M. Murphy, D. Nguyen, M. Nycz, L. Ou, B. Pandey, V. Pandey, K. Park, G. Perera, A. J. R. Puckett, S. N. Santiesteban, S. Širca, T. Su, L. Tang, Y. Tian, N. Ton, B. Wojtsekhowski, S. Wood, Z. Ye, and J. Zhang. Measurement of the Ar($e, e'p$) and Ti($e, e'p$) cross sections in Jefferson Lab Hall A. *Phys. Rev. C*, 103(3), 2021.
- [25] S. A. Kulagin and R. Petti. Global study of nuclear structure functions. *Nucl. Phys. A*, 765(1-2):126–187, 2006.
- [26] F. E. Close. *An Introduction to Quarks and Partons*. Academic Press, London/New York, 1979.
- [27] Matthew C. Osborn. Kinematic scaling in quasielastic electron scattering. Master's thesis, Massachusetts Institute of Technology, 1995.
- [28] D. B. Day, J. S. McCarthy, T. W. Donnelly, and I. Sick. Scaling in inclusive electron-nucleus scattering. *Ann. Rev. Nucl. Part. Sci.*, 40(1):357–409, 1990.
- [29] I. Sick, D. Day, and J. S. McCarthy. Nuclear high-momentum components and y scaling in electron scattering. *Phys. Rev. Lett.*, 45(11):871–874, 1980.

- [30] C. Maieron, T. W. Donnelly, and I. Sick. Extended superscaling of electron scattering from nuclei. *Phys. Rev. C*, 65(2), 2002.
- [31] E. Pace and G. Salme. The nuclear scaling function and quasi-elastic electron scattering by nuclei. *Phys. Lett.*, 110B(5):411–414, 1982.
- [32] H. Dai, M. Murphy, V. Pandey, D. Abrams, D. Nguyen, B. Aljawrneh, S. Alsalmi, A. M. Ankowski, J. Bane, S. Barcus, O. Benhar, V. Bellini, J. Bericic, D. Biswas, A. Camsonne, J. Castellanos, J.-P. Chen, M. E. Christy, K. Craycraft, R. Cruz-Torres, D. Day, S.-C. Dusa, E. Fuchey, T. Gautam, C. Giusti, J. Gomez, C. Gu, T. Hauge, J.-O. Hansen, F. Hauenstein, D. W. Higinbotham, C. Hyde, C. M. Jen, C. Keppel, S. Li, R. Lindgren, H. Liu, C. Mariani, R. E. McClellan, D. Meekins, R. Michaels, M. Mihovilovic, M. Nycz, L. Ou, B. Pandey, K. Park, G. Perera, A. J. R. Puckett, S. N. Santiesteban, S. Širca, T. Su, L. Tang, Y. Tian, N. Ton, B. Wojtsekhowski, S. Wood, Z. Ye, and J. Zhang. First measurement of the $\text{Ar}(e, e')\text{X}$ cross section at Jefferson Laboratory. *Phys. Rev. C*, 99(5), 2019.
- [33] C. Cioffi degli Atti, D. Faralli, and G. B. West. Nuclear y and x scaling. *arXiv:nucl-th/9812078v1*, 1998.
- [34] D. B. Day, J. S. McCarthy, Z. E. Meziani, R. Minehart, R. Sealock, S. T. Thornton, J. Jourdan, I. Sick, B. W. Filippone, R. D. McKeown, R. G. Milner, D. H. Potterveld, and Z. Szalata. Inclusive electron-nucleus scattering at high momentum transfer. *Phys. Rev. C*, 48(4):1849–1863, 1993.
- [35] W. M. Alberico, A. Molinari, T. W. Donnelly, E. L. Kronenberg, and J. W. Van Orden. Scaling in electron scattering from a relativistic fermi gas. *Phys. Rev. C*, 38(4):1801–1810, 1988.
- [36] T. W. Donnelly and I. Sick. Superscaling of inclusive electron scattering from nuclei. *Phys. Rev. C*, 60(6), 1999.
- [37] M. B. Barbaro, R. Cenni, A. De Pace, T. W. Donnelly, and A. Molinari. Relativistic y -scaling and the coulomb sum rule in nuclei. *Nucl. Phys. A*, 643(2):137–160, 1998.
- [38] T. W. Donnelly and I. Sick. Superscaling in inclusive electron-nucleus scattering. *Phys. Rev. Lett.*, 82(16):3212–3215, 1999.
- [39] E. A. Allton. Bremsstrahlung in electron-proton scattering. *Phys. Rev. B*, 135(2):570–576, 1964.

- [40] G. Miller. Inelastic Electron Scattering at Large Angles. SLAC-129 UC-34, 1971.
- [41] G. Miller, E. D. Bloom, G. Buschorn, D. H. Coward, H. DeStaebler, J. Drees, C. L. Jordan, L. W. Mo, R. E. Taylor, J. I. Friedman, G. C. Hartmann, H. W. Kendall, and R. Verdier. Inelastic Electron-Proton Scattering at Large Momentum Transfers and the Inelastic Structure Functions of the Proton. *Phys. Rev. D*, 5(3):528–544, 1972.
- [42] L. W. Mo and Y. S. Tsai. Radiative Corrections to Elastic and Inelastic ep and μp Scattering. *Rev. Mod. Phys.*, 41(1):205–235, 1969.
- [43] Y.-S. Tsai. Radiative corrections to electron-proton scattering. *Phys. Rev.*, 122(6):1898–1906, 1961.
- [44] Y.-S. Tsai. Radiative Corrections to Electron Scatterings. SLAC-PUB-848, 1971.
- [45] T. de Forest. Off-Shell electron Nucleon Cross-Sections. The Impulse Approximation. *Nucl. Phys. A*, 392:232–248, 1983.
- [46] The Hall A Beam Line. <https://hallaweb.jlab.org/12GeV/Documents/beam.ps>, Accessed Oct. 2021.
- [47] B. Povh, K. Rith, C. Scholz, and F. Zetsche. *Particles and Nuclei: An Introduction to the Physical Concepts*. Springer, Berlin, 1995.
- [48] CEBAF at 12 GeV Schematic. Jefferson Lab flickr account, <https://www.flickr.com/photos/jeffersonlab/12599705145>, Accessed Oct. 2021.
- [49] R. W. Lourie, W. Bertozzi, L. Weinstein, A. Saha, and The Hall A Collaboration. Study of the Quasielastic $(e, e'p)$ Reaction in ^{16}O at High Recoil Momenta. JLab proposal PR-89-003, 1989.
- [50] M. B. Epstein, R. W. Lourie, J. Mougey, A. Saha, and The Hall A Collaboration. Selected Studies of the ^3He and ^4He nuclei through electrodisintegration at high momentum transfer. JLab proposal PR-89-044, 1989.
- [51] C. E. Hyde-Wright, A. Klein, S. Kuhn, B. Raue, P. E. Ulmer, L. Weinstein, M. Epstein, J. M. Finn, R. Ent, J. LeRose, R. Michaels, J. Mitchell, A. Saha, Z. Papandreou, R. Madey, B. Anderson, R. Madey, G. Petratos, W. Bertozzi, S. Gilad, V. Punjabi, R. Gilman,

- C. Glashausser, C. C. Chang, P. Markowitz, J. Calarco, G. Huber, G. Lolos, R. W. Lourie, and The Hall A Collaboration. In-plane Separations and High Momentum Structure in $d(e, e'p)n$. Proposal submitted to the CEBAF Program Advisory Committee 8, 1994.
- [52] J. A. Templon, F. T. Baker, J. Hines, J. P. Chen, J. H. Mitchell, J. J. LeRose, A. Sarty, E. Jans, L. Lapikás, M. Epstein, M. Sargsian, L. L. Howell, S. A. Sofianos, and The Hall A Collaboration. Systematic Probe of Short-Range Correlations *via* the Reaction ${}^4\text{He}(e, e'p){}^3\text{H}$. Proposal submitted to the Jefferson Lab PAC, 1997.
- [53] A. Saha, W. Bertozzi, L. B. Weinstein, K. G. Fissum, and The Hall A Collaboration. Testing the Limits of the Single Particle Model in ${}^{16}\text{O}(e, e'p)$: An Update to E89-003. Proposal submitted to the Jefferson Lab PAC, 2000.
- [54] N. Benmouna, B. L. Berman, B. Briscoe, G. Feldman, Y. Ilieva, S. Strauch, R. Gilman, C. Glashausser, X. Jiang, G. Kumbartzki, K. McCormick, R. D. Ransome, J. Arrington, C. F. Perdrisat, R. Ent, D. W. Higinbotham, M. K. Jones, D. G. Meekins, B. Reitz, V. Punjabi, C. E. Hyde-Wright, P. E. Ulmer, L. B. Weinstein, F. Butaru, S. Choi, Z. E. Meziani, K. Silfer, P. Solvignon, H. Yao, J. R. M. Annand, D. Hamilton, D. G. Ireland, J. D. Kellie, K. Livingston, D. Protopopescu, G. Rosner, D. P. Watts, J. J. Kelly, and The Hall A Collaboration. Probing the Limits of the Standard Model of Nuclear Physics with the ${}^4\text{He}(\vec{e}, e'\vec{p}){}^3\text{H}$ Reaction. Proposal submitted to the Jefferson Lab PAC, 2003.
- [55] K. A. Aniol, M. B. Epstein, D. J. Margaziotis, J. M. Udias, J. R. Vignote, J. L. Herraiz, R. Feuerbach, D. Higinbotham, C. W. de Jager, J. Leroise, B. Reitz, A. Saha, E. Voutier, O. Gayou, S. Gilad, P. E. C. Markowitz, R. Lindgren, S. Sirca, F. Garibaldi, E. Cisbani, F. Cusanno, S. Frullani, M. Iodice, G. M. Urciuoli, R. De Leo, L. Lagamba, S. Marrone, R. Gilman, and The Hall A Collaboration. Impulse Approximation limitations to the $(e, e'p)$ Reaction on ${}^{208}\text{Pb}$, identifying correlations and relativistic effects in the nuclear medium. Proposal submitted to the Jefferson Lab PAC, 2005.
- [56] K. G. Fissum, W. Bertozzi, J. P. Chen, D. Dale, H. C. Fenker, J. Gao, A. Gavalya, S. Gilad, C. R. Leathers, N. Liyanage, R. O. Michaels, E. A. J. M. Offermann, J. Segal, J. A. Templon, R. Wechsler, B. Wojtsekhowski, and J. Zhao. Vertical drift chambers for the Hall A high-

- resolution spectrometers at Jefferson Lab. *Nucl. Instrum. Methods Phys. Res. A*, 474:108–131, 2001.
- [57] Jefferson Lab. Photograph of JLab Hall A and Spectrometers.
- [58] J. Alcorn *et al.* Basic instrumentation for Hall A at Jefferson Lab. *Nucl. Instrum. Methods Phys. Res. A*, 522:294–346, 2004.
- [59] Particle Data Group website. <https://pdg.lbl.gov/2012/AtomicNuclearProperties/>, Accessed Oct. 2021.
- [60] Jefferson Lab Hall A Tritium Target. https://wiki.jlab.org/jlab-tritium-target-wiki/index.php/Main_Page, Accessed Oct. 2021.
- [61] H. Dai. Unpublished internal analysis document.
- [62] H. Dai, M. Murphy, V. Pandey, D. Abrams, D. Nguyen, B. Aljawrneh, S. Alsalmi, A. M. Ankowski, J. Bane, S. Barcus, O. Benhar, V. Bellini, J. Bericic, D. Biswas, A. Camsonne, J. Castellanos, J.-P. Chen, M. E. Christy, K. Craycraft, R. Cruz-Torres, D. Day, S.-C. Dusa, E. Fuchey, T. Gautam, C. Giusti, J. Gomez, C. Gu, T. Hauge, J.-O. Hansen, F. Hauenstein, D. W. Higinbotham, C. Hyde, C. M. Jen, C. Keppel, S. Li, R. Lindgren, H. Liu, C. Mariani, R. E. McClellan, D. Meekins, R. Michaels, M. Mihovilovic, M. Nycz, L. Ou, B. Pandey, K. Park, G. Perera, A. J. R. Puckett, S. Širca, T. Su, L. Tang, Y. Tian, N. Ton, B. Wojtsekhowski, S. Wood, Z. Ye, and J. Zhang. First measurement of the $Ti(e, e')X$ cross section at Jefferson Lab. *Phys. Rev. C*, 98(1), 2018.
- [63] H. Dai and S. N. Santiesteban. Target boiling study. Unpublished internal analysis document.
- [64] S. N. Santiesteban and H. Dai. Ti density study. Unpublished internal analysis document, 2018.
- [65] M. Murphy, H. Dai, L. Gu, D. Abrams, A. M. Ankowski, B. Aljawrneh, S. Alsalmi, J. Bane, S. Barcus, O. Benhar, V. Bellini, J. Bericic, D. Biswas, A. Camsonne, J. Castellanos, J.-P. Chen, M. E. Christy, K. Craycraft, R. Cruz-Torres, D. Day, S.-C. Dusa, E. Fuchey, T. Gautam, C. Giusti, J. Gomez, C. Gu, T. Hauge, J.-O. Hansen, F. Hauenstein, D. W. Higinbotham, C. Hyde, C. M. Jen, C. Keppel, S. Li, R. Lindgren, H. Liu, C. Mariani, R. E. McClellan, D. Meekins, R. Michaels, M. Mihovilovic, D. Nguyen, M. Nycz, L. Ou, B. Pandey, V. Pandey, K. Park, G. Perera, A. J. R. Puckett, S. N. Santiesteban,

- S. Širca, T. Su, L. Tang, Y. Tian, N. Ton, B. Wojtsekhowski, S. Wood, Z. Ye, and J. Zhang. Measurement of the cross sections for inclusive electron scattering in the E12-14-012 experiment at Jefferson Lab. *Phys. Rev. C*, 100(5), 2019.
- [66] N. Liyanage. Optics Calibration of the Hall A High Resolution Spectrometers Using the New Optimizer. JLAB-TN-02-012, 2002.
- [67] C. Gu. Spectrometer Optics Study for E08-27. University of Virginia technical note, 2016.
- [68] D. W. Higinbotham, T. Keppel, and The Hall A Collaboration. *Jefferson Lab Hall A Standard Equipment Manual*. Thomas Jefferson National Accelerator Facility, 2019.
- [69] M. Iodice, E. Cisbani, S. Colilli, R. Crateri, S. Frullani, F. Garibaldi, F. Giuliani, M. Gricia, M. Lucentini, A. Mostarda, L. Pierangeli, F. Santavenere, G.M. Urciuoli, R. De Leo, L. Lagamba, A. Leone, R. Perrino, S. Kerhoas, I.C. Lugol, B. Mazeav, P. Vernin, and A. Zaccarian. The CO₂ Gas Cherenkov Detectors for the Jefferson Lab Hall-A Spectrometers. *Nucl. Instr. and Meth. A*, 411(2-3):223–237, 1998.
- [70] J. Gomez. Shower Counter for the SLAC 8 GeV/c Spectrometer. NPAS-TN-84-1, 1984.
- [71] V. Mamyan. Energy calibration and reconstruction algorithms of the rcs electromagnetic calorimeter. JLab technical note, 2005.
- [72] Fatiha Benmokhtar. *Measurement of the $^3\text{He}(e, e'p)pn$ Reaction at High Missing Energies and Momenta*. PhD thesis, Rutgers University, 2004.
- [73] P. Bosted. Empirical fit to the nucleon electromagnetic form factors. *Phys. Rev. C*, 51(1):409–411, 1995.
- [74] Y.-S. Tsai. Pair production and bremsstrahlung of charged leptons. *Rev. Mod. Phys.*, 46(4):815–851, 1974.
- [75] P. Bosted and M. Christy. Empirical fit to inelastic electron-deuteron and electron-neutron resonance region transverse cross sections. *Phys. Rev. C*, 77, 2008.
- [76] M. E. Christy and P. E. Bosted. Empirical fit to precision inclusive electron-proton cross sections in the resonance region. *arXiv:0712.3731v1 [hep-ph]*, 2007.

- [77] H. de Vries, C. W. de Jager, and C. de Vries. Nuclear Charge-Density-Distribution Parameters from Elastic Electron Scattering. *At. Data Nucl. Data Tables*, 36:495–536, 1987.
- [78] Monte-Carlo code `event.f`.
- [79] E. D. Cooper, S. Hama, B. C. Clark, and R. L. Mercer. Global dirac phenomenology for proton-nucleus elastic scattering. *Phys. Rev. C*, 47(1):297–311, 1993.
- [80] E. D. Cooper, S. Hama, and B. C. Clark. Global dirac optical potential from helium to lead. *Phys. Rev. C*, 80(3), 2009.
- [81] G. S. Blanpied, B. G. Ritchie, M. L. Barlett, R. W. Ferguson, J. A. McGill, and B. H. Wildenthal. Elastic and inelastic scattering of 0.8 GeV protons from ^{40}Ar . *Phys. Rev. C*, 37(3):1304–1306, 1988.
- [82] A. Meucci, C. Giusti, and F. D. Pacati. Relativistic corrections in $(e, e'p)$ knockout reactions. *Phys. Rev. C*, 64(1), 2001.
- [83] SIMC Monte-Carlo. https://hallcweb.jlab.org/wiki/index.php/SIMC_Monte_Carlo.
- [84] D. Gaskell and J. Arrington. JLab Hall A Analysis Meeting, 2009.
- [85] R. Cruz Torres and B. A. Schmookler. *Simc*. Thomas Jefferson National Accelerator Facility.
- [86] M. E. Christy. Extraction of inclusive cross sections. JLab analysis workshop presentation.
- [87] P. K. Sinervo. Definition and treatment of systematic uncertainties in high energy physics and astrophysics. In L. Lyons, R. Mount, and R. Reitmeyer, editors, *Proceedings of the Conference on Statistical Problems in Particle Physics, Astrophysics and Cosmology*, Stanford, California, 2003. SLAC.
- [88] T. Ullrich and Z. Xu. Treatment of errors in efficiency calculations. *arXiv:physics/0701199v1*, 2007.
- [89] The Jefferson Lab Hall A Collaboration. Measurements of the $\text{Ar}(e, e'p)$ reduced cross sections and Ar spectroscopic factors in Jefferson Lab Hall A. Paper to be submitted for publication.

- [90] I. Brock. Statistical Methods in Particle Physics, Part II. Heidelberg+LHCb Workshop, 2012.
- [91] Nadia Fomin. *Inclusive Electron Scattering From Nuclei at $x > 1$ and High Q^2 With A 5.75 GeV Beam*. PhD thesis, University of Virginia, 2008.
- [92] A. Bohr, B. R. Mottelson, and D. Pines. Possible Analogy Between the Excitation Spectra of Nuclei and Those of the Superconducting Metallic State. *Phys. Rev.*, 110(4):936–938, 1958.
- [93] P. Finelli, N. Kaiser, D. Vretenar, and W. Weise. Relativistic nuclear energy density functional constrained by low-energy QCD. *Nucl. Phys. A*, 770:1–31, 2006.
- [94] P. Finelli, N. Naiser, D. Vretenar, and W. Weise. Relativistic nuclear model with point-couplings constrained by QCD and chiral symmetry. *Nucl. Phys. A*, 735:449–481, 2004.
- [95] T. Nikšić, N. Paar, D. Vretenar, and P. Ring. DIRHB-A relativistic self-consistent mean-field framework for atomic nuclei. *Comput. Phys. Commun.*, 185:1808–1821, 2014.
- [96] L. Jiang. Evaluation of Systematic Uncertainty from Final State Interaction in Electron Scattering. Unpublished internal analysis document, 2020.
- [97] P. Bosted, R. G. Arnold, S. Rock, and Z. Szalata. Nuclear Scaling in Inelastic Electron Scattering from d , ^3He , and ^4He . *Phys. Rev. Lett.*, 49(19):1380–1383, 1982.
- [98] R. M. Sealock, K. L. Giovanetti, S. T. Thornton, Z. E. Meziani, O. A. Rondon-Aramayo, S. Auffret, J.-P. Chen, D. G. Christian, D. B. Day, J. S. McCarthy, R. C. Minehart, L. C. Dennis, K. W. Kemper, B. A. Mecking, and J. Morgenstern. Electroexcitation of the $\Delta(1232)$ in Nuclei. *Phys. Rev. Lett.*, 62(12):1350–1353, 1989.
- [99] J. S. O’Connell, W. R. Dodge, J. W. Lightbody Jr., X. K. Maruyama, J.-O. Adler, K. Hansen, B. Schröder, A. M. Bernstein, K. I. Blomqvist, B. H. Cottman, J. J. Comuzzi, R. A. Miskimen, B. P. Quinn, J. H. Koch, and N. Ohtsuka. Electromagnetic excitation of the delta resonance in nuclei. *Phys. Rev. C*, 35(3):1063–1071, 1987.

- [100] K. Abe *et al.* Search for CP Violation in Neutrino and Antineutrino Oscillations by the T2K Experiment with 2.2×10^{21} Protons on Target. *Phys. Rev. Lett.*, 121(17):1802, 2018.
- [101] R. L. Talaga, J. J. Grudzinski, S. Phan-Budd, A. Pla-Dalmau, J. E. Fagan, and C. Grozis. PVC extrusion development and production for the NOvA neutrino experiment. *Nucl. Instrum. Methods Phys. Res. A*, 861:77–89, 2017.
- [102] C. Giganti, S. Lavignac, and M. Zito. Neutrino oscillations: the rise of the PMNS paradigm. *arXiv:1710.00715v2 [hep-ex]*, 2017.
- [103] H. Uberall. *Electron Scattering From Complex Nuclei*, volume 36B of *Pure and Applied Physics*. Academic Press, Inc., New York, 1971.

Index

- Δ baryon, 116
- Δ -production peak, 20, 153
- $\Delta(1232)$ resonance, 20, 87
- ψ -scaling, 37, 42

- Acceptance correction method, 136
- Acceptance function, 136
- Accidental coincidence, 118
- $^{27}\text{Al}(e, e')$ data
 - cross section, 41, 155, 156
 - scaling function, 41, 158–160
- Aluminum target, 58
- Angular peaking approximation, 47
- Anti-parallel kinematics, 64
- Argon target, 58, 59
- $^{40}\text{Ar}(e, e'p)$ data
 - cross section, 163–165
- $^{40}\text{Ar}(e, e')$ data
 - cross section, 8, 27, 155, 156
 - scaling function, 159–161
- $^{40}\text{Ar}(p, p')$ data
 - cross section, 94

- Bardeen-Cooper-Schrieffer theory, 149
- Binding correction, 40
- Binomial distribution, 140
 - restricted, 141
- Bjorken scaling, 36
- Bjorken- x , 36, 63
- Born approximation, 9, 12, 13
- Bremsstrahlung, 43, 44
 - external, 47
 - internal, 47

- Calorimeter, 77, 79
 - calibration, 79
 - efficiency, 124, 127, 129, 130

- $^{12}\text{C}(e, e')$ data
 - cross section, 154, 156
 - scaling function, 158–161
- Carbon comparison method, 138
- Carbon target, 60
- CC1, 52, *see also* Structure functions, off shell
- CC2, 53, *see also* Structure functions, off shell
- CDWBA, 26
- CEBAF, 53, 54
- Charge-symmetric background, 115, 116
- Cherenkov detector, 75
 - calibration, 76, 77
 - efficiency, 123, 125, 126
- Cherenkov radiation, 75
- CODA, 104
- Coincidence scattering, 2, 11, 111
- Coincidence time, 112
 - cut, 112
 - efficiency, 131, 135
- Complete distorted wave Born approximation, 25
- Coordinate system
 - detector, 65, 66
 - focal plane, 67, 68
 - hall, 63, 65
 - target, 68, 69
 - transport, 66, 67
- CP-violating phase, 7, 171

- de Broglie wavelength (reduced), 10
- Dead time, 81
- Deep inelastic scattering, 10, 20
- Delta function, 169
- Delta scan, 63
- Density correction factor, 60, 61

Dilogarithm function, 50, 169
 Dip region, 20, 88, 153
 Dirac-Hartree-Bogoliubov model, 150
 Distorted wave impulse approximation, 26
 DR.t1 cut, 114
 Dummy target, 58, *see also* Aluminum target
 DUNE, 5, 6, 167
 E12-14-012, 1, 8, 62–64, 115
 Efficiency, 119
 beta cut, 135, 136
 calorimeter, 124, 127, 129, 130
 Cherenkov, 123, 125, 126
 coincidence time, 131, 135
 scintillator, 121–123
 trigger, 121
 VDC, 128, 133, 134
 Elastic cross section, 88
 Elastic scattering, 10
 Electron beam, 54, 110, 112, 113
 Electron scattering, 9, 10
 Energy peaking approximation, 47
 Equivalent radiator, 177
 ESPACE, 104, 179, 181, 182
 Exclusive cross section, 16, 139
 Exclusive scattering, 11
`externals_all_new.f`, 83
 Fermi gas model, 1, 40
 Fermi motion, 20
 Final state interactions, 24, 25, 63, 92, 94, 99, 149, 157, 160
 Form factors
 inelastic, 88
 Gamma function, 170
 Gaussian distribution, 105
 Hall A, 54–57, 71
 High resolution spectrometer, 70, 71
 High-resolution spectrometer, 56
 Impulse approximation, 6
 Inclusive cross section, 16, 19, 83, 136
 Inclusive scattering, 11
 Independent particle shell model, 28
 Inelastic cross section, 86
 Inelastic scattering, 10
 Kinematic settings, 62, 63
 LArTPC detector, 5
 LBNE, 5
 Leptonic tensor, 14
 Live time, 81
 computer, 81
 electronic, 81
 Local density approximation, 30
 Longitudinal momentum
 distribution, 40, 86, 87
 Luminosity (integrated), 90
 Maxwell-Boltzmann distribution, 31
`mc_hrs_single.f`, 96
`mc_hrs1.f`, 97
 Meson exchange currents, 88
 MINER ν A, 1, 167
 Missing energy, 23, 99
 distribution function, 28, 32, 99
 Missing momentum, 23, 98
 distribution function, 28, 31
 Monte-Carlo, 1, 96, 97
 Mott cross section, 42, 52, 173
 Neutrino oscillation, 4–6, 171–173
 Normal distribution, *see* Gaussian distribution

NOvA, 167
 Nuclear transparency, 99, 162
 Optical potential, 25, 92, 93
 democratic fit, 93, 94
 EDAD fits, 93, 94
 Optics target, 62
 $^{16}\text{O}(e, e')$ data
 cross section, 8
 Pairing mechanism, 150
 Parallel kinematics, 62, 64
 Particle identification, 109, 110
 Pauli suppression factors, 85
 Photomultiplier tube, 71, 76
 ADC spectrum, 78
 Plane wave impulse
 approximation, 22, 23
 Pontecorvo-Maki-Nakagawa-Sakata matrix,
 170
 Q^2 , 11
 Quasi-elastic cross section, 83
 Quasi-elastic peak, 20, 153
 Quasi-elastic scattering, 8, 10
 Radiation length, 55, 57
 Radiative correction factor, 89
 Radiative corrections, 43, 144, 176
`rc_mod.f`, 89
 Reaction plane, 11
`recon_mc.f`, 90
 Reduced cross section, 92, 95
 Reduced cross sections, 95
 Rosenbluth cross section, 172
 off shell correction, 51
 Scaling, 33
 of the first kind, 36, 41
 of the second kind, 37
 Scaling function, 37
 of the first kind, 39, 153
 of the second kind, 42, 43
 Scattering angle, 11, 63
 Scattering plane, 11
 Schwinger correction, 45, 50, 176,
 177
 Scintillator, 71
 efficiency, 122, 123
 Self-energy correction, 44, 45
 Shell model, 2
 Shower detector, 77
 SIMC, 94, 97–99, 162
 Spectral function, 2, 3, 6, 24, 27,
 139, 162
 correlated, 30, 175
 distorted, 26
 mean field, 29
 surface plot, 34, 35
 Spectroscopic factors, 29
 Spence function, *see also*
 Dilogarithm function
 Statistical uncertainty, 140, 147,
 148, 152
 Straggling function, 47
 Structure functions
 elastic, 88
 inelastic, 86
 off shell, 52, 53
 quasi-elastic, 85
 Superscaling, 37
 Systematic uncertainty, 142,
 146–148
 T2K, 167
 Target boiling, 60
 Target ladder, 55
 Target response tensor, 15, 17, 18
 Time projection chamber, 5
 Titanium target, 60
 $^{48}\text{Ti}(e, e'p)$ data
 cross section, 163, 164, 166

$^{48}\text{Ti}(e, e')$ data
 cross section, 154, 156
 scaling function, 159, 160
Trigger, 80
Vacuum polarization, 44, 46
VDC, *see* Vertical drift chamber
Vertex correction, 44, 46
Vertical drift chamber, 72
 efficiency, 128, 133, 134
Wilson score interval, 141, 142
Yield, 60, 136
Yield ratio method, 137
y-scaling, 36–38, 41, 83, 174, *see*
 also Scaling, of the first
 kind